ISSN 2074-272X

науково-практичний 2025/6 [[

ELEJOHOXIIKA I

Tectrical Engineering & Tectromechanics

Електричні машини та апарати Електротехнічні комплекси та системи Промислова електроніка

Журнал включено до найвищої категорії «А» Переліку фахових видань України

3 2019 рь журнал Індексується у Scopus

8 2015 p. myphan lithercycusca y Web of Science Core Collections Emerging Sources Citation Index



Electrical Engineering & Electromechanics

Scientific Journal was founded in 2002

Co-founders: National Technical University «Kharkiv Polytechnic Institute» (Kharkiv, Ukraine);

Anatolii Pidhornyi Institute of Power Machines and Systems of NAS of Ukraine (Kharkiv, Ukraine)

EDITORIAL BOARD

Sokol Ye.I. Editor-in-Chief, Professor, Corresponding member of NAS of Ukraine,

National Technical University «Kharkiv Polytechnic Institute» (NTU «KhPI»), Ukraine

Bolyukh V.F. Deputy Editor, Professor, NTU «KhPI», Ukraine Korytchenko K.V. Deputy Editor, Professor, NTU «KhPI», Ukraine

Rozov V.Yu. Deputy Editor, Professor, Corresponding member of NAS of Ukraine, Anatolii Pidhornyi Institute of

Power Machines and Systems of NAS of Ukraine (IEMS of NAS of Ukraine), Kharkiv, Ukraine

Abu-Siada A. Professor, Curtin University, Perth, Australia

Babak V.P. Professor, academician of NAS of Ukraine, General Energy Institute of NAS of Ukraine, Kyiv, Ukraine

Baltag O. Professor, Grigore T. Popa University Medicine and Pharmacy, Romania

Baranov M.I. Senior Researcher, NTU «KhPI», Ukraine

Batygin Yu.V. Professor, Kharkiv National Automobile and Highway University, Ukraine

Bezprozvannych G.V. Professor, NTU «KhPI», Ukraine

Bíró O. Professor, Institute for Fundamentals and Theory in Electrical Engineering, Graz, Austria

Boiko M.I. Professor, NTU «KhPI», Ukraine

Bouktir T. Professor, Ferhat Abbas University, Setif 1, Algeria

Buriakovskyi S.G. Professor, NTU «KhPI», Ukraine

Butkevych O.F. Professor, Institute of Electrodynamics of NAS of Ukraine, Kyiv, Ukraine

Colak I. Professor, Nisantasi University, Istanbul, Turkey
Cruz S. Professor, University of Coimbra, Portugal
Danylchenko D.O. Associate Professor, NTU «KhPI», Ukraine

Doležel I. Professor, University of West Bohemia, Pilsen, Czech Republic

Féliachi M. Professor, Technological Institute of Saint-Nazaire, University of Nantes, **France Grinchenko V.S.** Chief Researcher, General Energy Institute of NAS of Ukraine, Kyiv, **Ukraine**

Guerrero J.M. Professor, Aalborg University, Denmark

Hammarström T. Professor, Chalmers University of Technology, Sweden

Ida N. Professor, The University of Akron, Ohio, USA

Izykowski J. Professor, Wroclaw University of Science and Technology, Poland

Kildishev A.V. Associate Research Professor, Purdue University, USA

Klepikov V.B. Professor, NTU «KhPI», Ukraine

Korzeniewska E. Professor, Lodz University of Technology, Poland Kuznetsov B.I. Professor, IEMS of NAS of Ukraine, Kharkiv, Ukraine

Kyrylenko O.V. Professor, academician of NAS of Ukraine, Institute of Electrodynamics of NAS of Ukraine, Kyiv, Ukraine

Malik O.P. Professor, University Of Calgary, Canada

Maslov V.I. Professor, National Science Center «Kharkiv Institute of Physics and Technology», Ukraine

Mikhaylov V.M. Professor, NTU «KhPI», Ukraine

Miljavec D. Professor, University of Ljubljana, Slovenia

Milykh V.I. Professor, NTU «KhPI», Ukraine

Nacke B. Professor, Gottfried Wilhelm Leibniz Universitat, Institute of Electrotechnology, Hannover, Germany
Oleschuk V. Professor, Institute of Power Engineering of Technical University of Moldova, Republic of Moldova

Petrushin V.S. Professor, Odessa National Polytechnic University, Ukraine

Podoltsev A.D. Senior Researcher, Institute of Electrodynamics of NAS of Ukraine, Kyiv, Ukraine

Reutskiy S.Yu. Senior Researcher, IEMS of NAS of Ukraine, Kharkiv, Ukraine

Rezinkina M.M. Professor, NTU «KhPI», Ukraine

Rusanov A.V. Professor, academician of NAS of Ukraine, IEMS of NAS of Ukraine, Kharkiv, Ukraine

Sikorski W. Professor, Poznan University of Technology, Poland
Strzelecki R. Professor, Gdansk University of Technology, Poland
Suemitsu W. Professor, Universidade Federal Do Rio de Janeiro, Brazil

Trichet D. Professor, Institut de Recherche en Energie Electrique de Nantes Atlantique, France

Vaskovskyi Yu.M. Professor, National Technical University of Ukraine «Igor Sikorsky Kyiv Polytechnic Institute», Kyiv, Ukraine

Vazquez N. Professor, Tecnológico Nacional de México en Celaya, Mexico

Vinnikov D. Professor, Tallinn University of Technology, Estonia

Yagup V.G. Professor, Kharkiv National Automobile and Highway University, Ukraine

Yamnenko Yu.S. Professor, National Technical University of Ukraine «Igor Sikorsky Kyiv Polytechnic Institute», Kyiv, Ukraine

Yatchev I. Professor, Technical University of Sofia, Bulgaria

Zagirnyak M.V. Professor, academician of NAES of Ukraine, Kremenchuk M.Ostrohradskyi National University, Ukraine

Zgraja J. Professor, Lodz University of Technology, **Poland**

Grechko O.M. Executive Managing Editor, Associate Professor, NTU «KhPI», Ukraine

From no. 1 2019 Journal «Electrical Engineering & Electromechanics» is indexing in Scopus

and from no. 1 2005 Journal is indexing in Web of Science Core Collection: Emerging Sources Citation Index (ESCI)

Also included in DOAJ (Directory of Open Access Journals), in EBSCO's database, in ProQuest's databases – Advanced Technologies & Aerospace Database and Materials Science & Engineering Database, in Gale/Cengage Learning databases.

Editorial office address:

National Technical University «Kharkiv Polytechnic Institute», Kyrpychova Str., 2, Kharkiv, 61002, Ukraine

phone: +380 67 3594696, e-mail: a.m.grechko@gmail.com (Grechko O.M.)

ISSN (print) 2074-272X ISSN (online) 2309-3404 © Anatolii

© National Technical University «Kharkiv Polytechnic Institute», 2025 © Anatolii Pidhornyi Institute of Power Machines and Systems of NAS of Ukraine, 2025



Electrical Engineering & Electromechanics



Scientific Journal

no. 6, 2025

Table of Contents

Electrical Machines and Apparatus

Diboune Y., Hachelaf R., Kouchih D. Effect of short-circuit in stator windings on the operation of doubly-fed Electrotechnical Complexes and Systems Bessaad T., Benbouali A., Khelifi Otmane K., Taleb R., Sahraoui H., Iqbal A. Inverter fuzzy speed control of multimachine system series-connected fed by a single five-phase an asymmetrical 19-level inverter with less number of switches 8 Bouhadouza B., Sadaoui F. Optimal power flow analysis under photovoltaic and wind power uncertainties using Guizani S., Nayli A., Ben Ammar F. Fault-tolerant control of a double star induction machine operating in active Hamdi N., Babaa F., Touil A., Merabet N. Robust fault-tolerant sliding mode control and advanced fault diagnosis Kuznetsov B.I., Nikitina T.B., Bovdui I.V., Chunikhin K.V., Kolomiets V.V., Kobylianskyi B.B. Synthesis of combined shielding system for overhead power lines magnetic field normalization in residential building space....... 40 Laamari Y., Boukhennoufa N., Benderradji H., Allaoui S. Fuzzy logic-based vector control of permanent magnet Makhlouf M., Laouar O. New adaptive modified perturb and observe algorithm for maximum power point tracking Nhi V.T.K., Quy B.T., Nghia H.H.B., Dai L.V. A robust hybrid control strategy for enhancing torque stability and Rezgui S.E., Darsouni Z., Benalla H. Nonlinear vector control of multiphase induction motor using linear quadratic Sabry S.S., Al-Yozbaky O.Sh. Enhanced siting and sizing of distributed generation in radial distribution networks Tran C.D., Kuchar M., Nguyen P.D. Improved speed sensorless control for induction motor drives using rotor flux

Industrial Electronics

angle estimation 93

Toualbia A., Djilali A.B., Taleb R., Mansour N., Souaihia M., Saidi H. Application perturb and observe maximum power point tracking with interconnection and damping assignment passive-based control for photovoltaic system using boost converter.

Y. Diboune, R. Hachelaf, D. Kouchih

Effect of short-circuit in stator windings on the operation of doubly-fed induction generators operating in a wind power system

Introduction. Wind energy has been a clean and renewable source of electricity in recent decades, making a significant addition to overall generation, and wind power is one of the most popular sources of renewable energy. Problem. Accurate modeling of wind turbine generators is critical to improve the efficiency of power systems. Doubly-fed induction generator (DFIG) stands out for its economic advantages associated with the use of frequency converters and induction machines. Increasing operating and maintenance costs of wind turbines highlight the need for early fault identification to optimize costs and ensure reliable operation. The goal of this work is to develop a simplified yet effective model for analyzing stator winding short-circuits in DFIGs operating in wind turbines. The model uses line-to-line voltages as inputs and explicitly considers the neutral-point voltage variation under fault conditions. Methodology. The problem was solved using spectral analysis, the model was implemented for 4 kW DFIG wind turbine in MATLAB to validate its effectiveness. Results. The simulation results confirm the effectiveness of the proposed approach for timely fault detection and analysis. It demonstrates computational simplicity by accurately capturing the main fault characteristics, which is preferable to traditional methods such as symmetrical components and FEM. The scientific novelty of the work lies in a methodology for modeling DFIG during stator short-circuits, integrating the effect of elevated neutral voltage during faults using line-to-line voltages in the base model. It also takes into account phenomena such as magnetic saturation, gap effects, and skin effects. The simplicity of the model makes it suitable for condition monitoring and validation of fault-tolerant control algorithms, which distinguishes it from more complex methods such as symmetrical components or the FEM. Practical value. The proposed model offers a pragmatic and reliable approach for monitoring and analyzing defects in DFIG wind turbines. Its versatility and efficiency improve the optimization of maintenance costs and reliability of renewable energy systems. References 27, tables 2, figures 8.

Key words: doubly-fed induction generator, short-circuit fault, wind turbine.

Вступ. Вітроенергетика є екологічно чистим та відновлюваним джерелом електроенергії в останні десятиліття, роблячи значний внесок у загальну генерацію енергії, і є одним із найпопулярніших джерел відновлюваної енергії. Проблема. Точне моделювання вітрогенераторів ϵ критично важливим для підвищення ефективності енергосистем. Асинхронний генератор з подвійним живленням (DFIG) відрізняється економічними перевагами, пов'язаними з використанням перетворювачів частоти та асинхронних машин. Зростання витрат на експлуатацію та технічне обслуговування вітрогенераторів призводить до необхідності раннього виявлення несправностей для оптимізації витрат та забезпечення надійної роботи. Метою даної роботи є розробка спрощеної, але ефективної моделі для розрахунку короткого замикання обмотки статора DFIG, що працює у вітрогенераторі. Модель використовує значення лінійної напруги та враховує підвищення напруги в нейтральній точці у разі несправностей. Методика. Завдання вирішено за допомогою спектрального аналізу. Модель реалізована у MATLAB для вітрогенератора DFIG потужністю 4 кВт для підтвердження її ефективності. **Результати** моделювання підтверджують ефективність запропонованого підходу до своєчасного виявлення та аналізу несправностей. Модель демонструє обчислювальну простоту, точно фіксуючи основні характеристики несправностей, що краще традиційних методів, таких як симетричні компоненти та метод скінченних елементів (МСЕ). Наукова новизна роботи полягає в методології моделювання DFIG при коротких замиканнях статора, що враховує вплив підвищеної напруги нейтралі при коротких замиканнях з використанням лінійних напруг базової моделі. Модель також враховує такі явища, як магнітне насичення, вплив зазору та скін-ефект. Простота моделі робить її придатною для моніторингу стану та валідації алгоритмів стійкості до відмови, що відрізняє її від складніших методів, таких як симетричні компоненти або МСЕ. Практична значимість. Розроблена модель пропонує практичний та надійний підхід до моніторингу та аналізу дефектів у вітрових турбінах з DFIG. Її універсальність та ефективність сприяють оптимізації витрат на технічне обслуговування та підвищенню надійності систем відновлюваної енергетики. Бібл. 27, табл. 2, рис. 8.

Ключові слова: асинхронний генератор з подвійним живленням, коротке замикання, вітрова турбіна.

Introduction. Wind energy is recognized as one of the most efficient and resilient renewable energy sources. In modern power systems, the configuration of variable-speed wind turbines is widely adopted to maximize energy capture and operational flexibility. Among the components of wind energy conversion systems, doubly-fed induction generators (DFIGs) are preferred due to their capability for variable-speed constant-frequency operation and high system efficiency [1].

The stator windings of DFIGs are subjected to thermal, electrical, and mechanical stresses, which can affect the performance and reliability of the generator and associated components [2, 3]. Inter-turn short circuit faults in the stator windings are particularly critical because they disturb voltage and current symmetry, potentially destabilizing the entire system [4]. Compared to other generator types used in wind energy, squirrel-cage induction generators operate only at fixed speed and lack controllability [5], while permanent magnet synchronous generators offer high efficiency but

require full-scale converters and are more expensive [6]. DFIGs remain a practical compromise for medium and high power applications due to their partial converter rating and grid compatibility.

Several techniques have been developed for detecting inter-turn short-circuit faults in the stator windings of DFIG-based wind energy systems. Signal-based methods remain prevalent, where fault diagnosis is performed by monitoring deviations in physical quantities such as external leakage flux [7], wideband frequency response [8], flux density distribution [9], and vibration analysis [10]. However, selecting an appropriate monitoring signal remains a key challenge, especially in distinguishing stator asymmetries. Observer-based approaches have also been applied [11], yet they may suffer from parameter sensitivity and false positives. Recently, artificial intelligence methods including neural networks [12], deep learning [13] and decision trees [14] have shown potential for fault

© Y. Diboune, R. Hachelaf, D. Kouchih

classification, although they are often complex and require extensive training data. For modeling stator winding short-circuit faults, classical techniques such as the symmetrical components method [15] and finite element method (FEM) [16–18] are commonly used. However, both approaches tend to overlook the neutral-point voltage rise during fault conditions and require considerable simulation time.

This study focuses on small-scale wind energy systems using DFIGs rated at 4 kW [19], primarily designed for stand-alone applications or isolated consumers.

The **goal** of this work is to develop a simplified yet effective model for analyzing stator winding short-circuits in DFIGs operating in wind turbines. The model uses line-to-line voltages as inputs and explicitly considers the neutral-point voltage variation under fault conditions.

This formulation enables efficient fault detection and analysis, supporting the development of condition monitoring strategies and fault-tolerant control schemes. Spectrum analysis is used to extract key harmonic indicators related to stator faults and validate the model through simulation on a 4 kW system.

Turbine modeling. The blades of a wind turbine capture the kinetic energy of the wind and transmit it to the rotor of a DFIG via a gearbox [20]. The wind turbine's power is calculated as:

$$P_{v} = \frac{1}{2} \cdot \rho \cdot S \cdot v^{2} \,, \tag{1}$$

where P_{ν} is the wind turbine's power; S is the surface swept by the blades of the turbine; ρ is the air density; ν is the wind speed.

The wind turbine's mechanical power is expressed as [21, 22]:

$$P_t = \frac{1}{2} \cdot \rho \cdot S \cdot C_p(\lambda, \beta) \cdot v^3, \qquad (2)$$

where P_t is the mechanical power; $C_p(\lambda, \beta)$ is referred to as the power coefficient, indicating the turbine aerodynamic efficiency. It depends on the tip speed ratio λ , defined as the quotient of the blade tip speed to the wind speed, and the blade pitch angle β .

The ratio λ can be articulated as [23, 24]:

$$\lambda = R \cdot \Omega_t / v \,, \tag{3}$$

where Ω_l is the rotational speed of the turbine; R is the blade radius.

The function of the power coefficient is (4):

$$C_p(\lambda, \beta) = 0.35 - 0.0167(\beta - 2)\sin\left(\frac{\pi \cdot (\lambda + 0.1)}{14.34 - 0.3(\beta - 2)}\right).$$
 (4)

Aerodynamic torque T_t is produced when aerodynamic power is transformed into mechanical power [25]:

$$T_t = \frac{P_t}{\Omega_t} = \frac{1}{2 \cdot \Omega_t} \cdot \rho \cdot S \cdot C_p(\lambda, \beta) \cdot v^3.$$
 (5)

The gearbox is a speed adapter from that of the turbine to that of the generator [26]:

$$G = T_t / T_m = \Omega_m / \Omega_t , \qquad (6)$$

where Ω_m is the mechanical speed; T_m is the mechanical torque.

Finally applying the fundamental relation of the dynamic, the model is completed as:

$$J\frac{\mathrm{d}\Omega_m}{\mathrm{d}t} = T_m - T_{em} - f_v \cdot \Omega_m, \tag{7}$$

where J is the total inertia; T_{em} is the electromagnetic torque; f_v is the viscous friction.

DFIG modeling. Under asymmetrical conditions, the stator voltages are unknown and deviate from the network phase voltages due to fluctuations in the neutral point voltage. This effect entails utilizing line-to-line voltages as inputs in the state model of the DFIG [19]. Thus, the stator voltage is indicated as:

$$\frac{\mathrm{d}[\boldsymbol{\Phi}_{sc}]}{\mathrm{d}t} = [\boldsymbol{U}_{sc}] + [\boldsymbol{R}_{sc}] \cdot [\boldsymbol{i}_{sc}], \tag{8}$$

where $[\boldsymbol{\Phi}_{sc}]$ is the stator fluxes vector; $[\boldsymbol{U}_{sc}] = [U_{ab}, U_{bc}, U_{ca}, 0]^T$ is the line voltages vector; $[\boldsymbol{i}_{sc}] = [i_{as}, i_{bs}, i_{cs}, i_{d}]^T$ is the line currents vector; $[\boldsymbol{R}_{sc}]$ is the stator windings resistances matrix:

$$\begin{bmatrix} R_{sc} \end{bmatrix} = \begin{bmatrix} r_{as} & -r_{bs} & 0 & 0 \\ 0 & r_{bs} & -r_{cs} & 0 \\ -r_{as} & 0 & r_{cs} & 0 \\ 0 & 0 & 0 & r_{d} \end{bmatrix}.$$
(9)

A short-circuit between 2 distinct places in the stator windings creates an alternative short-circuited phase, designated as *«d»* [27]. The novel phase is represented as:

$$r_d \cdot i_d + \frac{\mathrm{d}\Phi_d}{\mathrm{d}t} = 0 , \qquad (10)$$

where r_d , i_d , Φ_d are the resistance, the current and the magnetizing flux of the faulty phase.

We determine the short-circuit factor k_{cc} as:

$$k_{cc}[\%] = \frac{n_{cc}}{N_s} \cdot 100\%$$
, (11)

where N_s is the number of stator-turns; n_{cc} is the number of short-circuited turns.

The stator fluxes matrix is:

$$[\boldsymbol{\Phi}_{sc}] = [T_c] \cdot [\boldsymbol{\Phi}_s], \tag{12}$$

with

$$[T_c] = \begin{bmatrix} 1 & -1 & 0 & 0 \\ 0 & 1 & -1 & 0 \\ -1 & 0 & 1 & 0 \\ 0 & 0 & 0 & 1 \end{bmatrix};$$
 (13)

$$[\boldsymbol{\Phi}_{s}] = -[\boldsymbol{L}_{ss}] \cdot [\boldsymbol{i}_{sc}] - [\boldsymbol{L}_{sr}] \cdot [\boldsymbol{i}_{r}], \qquad (14)$$

where $[T_c]$ is the transformation matrix; $[L_{ss}]$ is the matrix of the stator inductances; $[L_{sr}]$ is the matrix of the stator and rotor mutual inductances; $[i_r]$ is the rotor currents vector.

In the case of an inter-turn fault in phase A, the stator and mutual inductances are given as:

stator and mutual inductances are given as:
$$\begin{bmatrix} \boldsymbol{L_{ss}} \end{bmatrix} = \begin{bmatrix} b^2 \cdot L_s & -b \cdot \frac{L_{ms}}{2} & -b \cdot \frac{L_{ms}}{2} & b \cdot f_a \cdot Lm_s \\ -b \cdot \frac{L_{ms}}{2} & L_s & -\frac{L_{ms}}{2} & -f_a \cdot \frac{L_{ms}}{2} \\ -b \cdot \frac{L_{ms}}{2} & -\frac{L_{ms}}{2} & L_s & -f_a \cdot \frac{L_{ms}}{2} \\ b \cdot f_a \cdot L_{ms} & -f_a \cdot \frac{L_{ms}}{2} & -f_a \cdot \frac{L_{ms}}{2} & f_a^2 \cdot L_s \end{bmatrix}; (15)$$

$$\begin{bmatrix} \boldsymbol{L_{sr}} \end{bmatrix} = L_{sr} \cdot \begin{bmatrix} M \\ f_a \end{bmatrix}, \tag{16}$$

with

$$[\mathbf{M}] = \begin{bmatrix} b \cdot \cos(\theta) & b \cdot \cos\left(\theta + \frac{2 \cdot \pi}{3}\right) & b \cdot \cos\left(\theta - \frac{2 \cdot \pi}{3}\right) \\ \cos\left(\theta - \frac{2 \cdot \pi}{3}\right) & \cos(\theta) & \cos\left(\theta + \frac{2 \cdot \pi}{3}\right) \\ \cos\left(\theta + \frac{2 \cdot \pi}{3}\right) & \cos\left(\theta - \frac{2 \cdot \pi}{3}\right) & \cos(\theta) \end{bmatrix}; (17)$$

$$[f_{\theta}] = \left[f_a \cdot \cos(\theta) \quad f_a \cdot \cos\left(\theta + \frac{2 \cdot \pi}{3}\right) \quad f_a \cdot \cos\left(\theta - \frac{2 \cdot \pi}{3}\right) \right]; (18)$$

$$b = (1 - f_a); L_s = (L_{ms} + L_{ls}),$$
 (19)

where L_{ls} is the leakage inductance of the stator windings; L_{ms} is the stator magnetization inductance; L_{sr} is the maximum of the stator and rotor mutual inductances; f_a is the short-circuit factor.

The rotor voltages equation, based on equivalent rotor variables, is formulated as:

$$\frac{\mathrm{d}[\boldsymbol{\phi}_r]}{\mathrm{d}t} = [\boldsymbol{V}_r] + [\boldsymbol{R}_r] \cdot [\boldsymbol{i}_r], \qquad (20)$$

where $[V_r]$ is the rotor voltages vector; $[R_r]$ is the rotor winding resistances matrix; $[\boldsymbol{\Phi}_r]$ is the rotor fluxes vector:

$$[\boldsymbol{\Phi}_{r}] = -[\boldsymbol{L}_{rs}] \cdot [\boldsymbol{i}_{s}] - [\boldsymbol{L}_{rr}] \cdot [\boldsymbol{i}_{r}], \tag{21}$$

where $[L_{rs}] = [L_{sr}]^T$ is the rotor and stator mutual inductances matrix; $[L_{rr}]$ is the rotor inductances matrix.

The stator currents vector comprises 4 interdependent values, with only 3 independent components required for its calculation. The current vector is defined with 3 components: i_{as} , i_{bs} , and i_d yielding the following matrix representation:

$$[i_{sc}] = [B_{sc}] \cdot [i_{abds}]. \tag{22}$$

The stator flux is represented by a vector consisting of 3 independent components, defined as follows:

$$[\boldsymbol{\Phi}_{abds}] = [A_{sc}] \cdot [\boldsymbol{\Phi}_{s}], \tag{23}$$

with

$$\begin{bmatrix} \boldsymbol{A_{sc}} \end{bmatrix} = \begin{bmatrix} 1 & -1 & 0 & 0 \\ 0 & 1 & -1 & 0 \\ 0 & 0 & 0 & 1 \end{bmatrix}; \ \begin{bmatrix} \boldsymbol{B_{sc}} \end{bmatrix} = \begin{bmatrix} 1 & 0 & 0 \\ 0 & 1 & 0 \\ -1 & -1 & 0 \\ 0 & 0 & 1 \end{bmatrix}.$$

Using (15), (22) and (23), we obtain:

$$\begin{cases}
[\boldsymbol{\Phi}_{abds}] = [\boldsymbol{M}_{sc}] \cdot [\boldsymbol{i}_{abds}] + [\boldsymbol{M}_{src}] \cdot [\boldsymbol{i}_{r}]; \\
[\boldsymbol{\Phi}_{r}] = [\boldsymbol{M}_{tsc}] \cdot [\boldsymbol{i}_{abds}] + [\boldsymbol{L}_{rr}] \cdot [\boldsymbol{i}_{r}];
\end{cases} (24)$$

with

$$\begin{cases}
[M_{sc}] = [A_{sc}] \cdot [L_{ss}] \cdot [B_{sc}]; \\
[M_{src}] = [A_{sc}] \cdot [L_{sr}]; \\
[M_{rsc}] = [L_{rs}] \cdot [B_{sc}],
\end{cases} (25)$$

Based on (24), we get:

$$\begin{cases}
[i_{abds}] = [C_{sc}] \cdot [\boldsymbol{\Phi}_{sr}]; \\
[i_r] = [C_{rc}] \cdot [\boldsymbol{\Phi}_{rs}],
\end{cases}$$
(26)

with

$$\begin{bmatrix}
[C_{sc}] = -([M_{sc}] - [M_{src}] \cdot [L_{rr}]^{-1} \cdot [M_{rsc}])^{-1}; \\
[C_{rc}] = -([L_{rr}] - [M_{rsc}] \cdot [M_{sc}]^{-1} \cdot [M_{src}])^{-1}; \\
[\boldsymbol{\Phi}_{sr}] = ([\boldsymbol{\Phi}_{abds}] - [M_{src}] \cdot [L_{rr}]^{-1} \cdot [\boldsymbol{\Phi}_{r}]) \\
[\boldsymbol{\Phi}_{rs}] = ([\boldsymbol{\Phi}_{r}] - [M_{rsc}] \cdot [M_{sc}]^{-1} \cdot [\boldsymbol{\Phi}_{abds}])
\end{bmatrix}$$

Finally, by using (7), (8), (20) and (26), we obtain the state model of DFIG:

$$\frac{d\left[\frac{\boldsymbol{\Phi}_{sc}}{dt}\right]}{dt} = \left[\boldsymbol{R}_{sc}\right] \cdot \left[\boldsymbol{B}_{sc}\right] \cdot \left[\boldsymbol{C}_{sc}\right] \cdot \left[\boldsymbol{\Phi}_{sr}\right] + \left[\boldsymbol{V}_{s}\right];$$

$$\frac{d\left[\boldsymbol{\Phi}_{r}\right]}{dt} = \left[\boldsymbol{R}_{r}\right] \cdot \left[\boldsymbol{C}_{rc}\right] \cdot \left[\boldsymbol{\Phi}_{rs}\right] + \left[\boldsymbol{V}_{r}\right];$$

$$\frac{d\Omega_{m}}{dt} = \frac{1}{J} \cdot \left(T_{em} - T_{m} - f_{v} \cdot \Omega_{m}\right).$$
(28)

The electromagnetic torque expression is:

$$T_{em} = p \cdot [\mathbf{i}_s]^t \cdot \frac{\partial [\mathbf{L}_{sr}]}{\partial \theta} \cdot [\mathbf{i}_r], \tag{29}$$

where p is the pole pairs number; θ is the mechanical angle (angle of the body rotation due to torque T_{em}).

Results. The simulations of the whole system were performed with MATLAB software. The wind turbine and DFIG parameters are given in Table 1, 2 with a short-circuit factor of 5 % on phase A. The wind speed and mechanical speed are shown in Fig. 1, 2. Figures 3–5 illustrate the stator currents, voltages and magnetic flux, while Fig. 6–8 show the spectrum analysis of the stator current I_{as} , voltage V_{as} and flux Φ_{as} .

Table 1

Di 10 parameters	
Rated power P_s , kW	4
Mutual inductance L_m , H	0.258
Stator inductance L_s , H	0.274
Rotor inductance L_r , H	0.303
Stator resistance R_s , Ω	4.85
Rotor resistance R_r , Ω	3.805
Number of pole pairs p	2
Moment of the inertia J , kg·m ²	0.045
Viscous friction f_v , kg·m ² ·s ⁻¹	0.0038

Table 2

Wind turbine parameters

wind turbine parameters				
Radius R, m	3			
Gear box ratio G	5.4			
Number of blades n_p	3			
Nominal wind speed v, m/s	12 m/s			

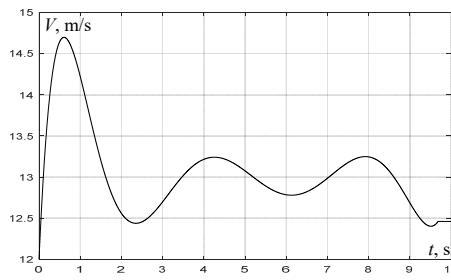
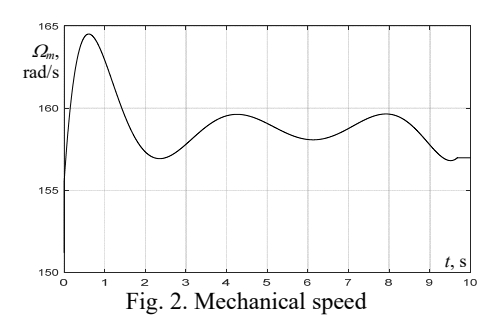


Fig. 1. Wind speed



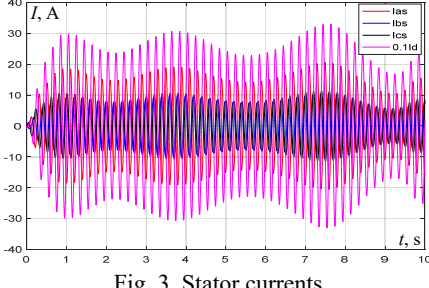


Fig. 3. Stator currents

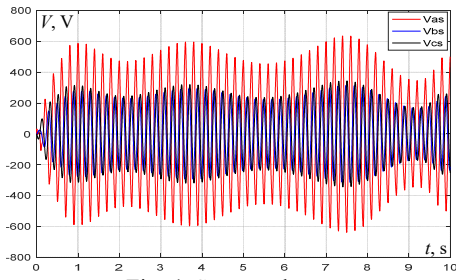


Fig. 4. Stator voltages

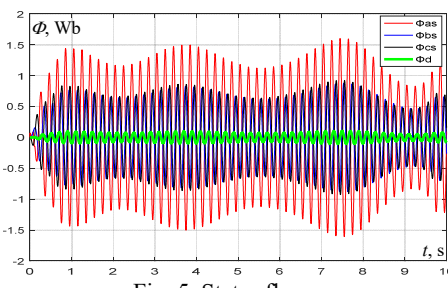


Fig. 5. Stator fluxes

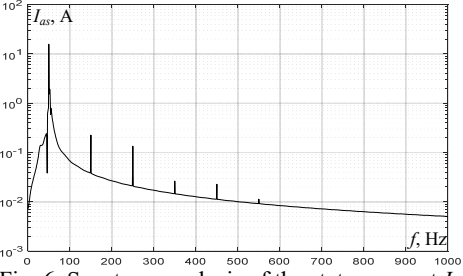


Fig. 6. Spectrum analysis of the stator current I_{as}

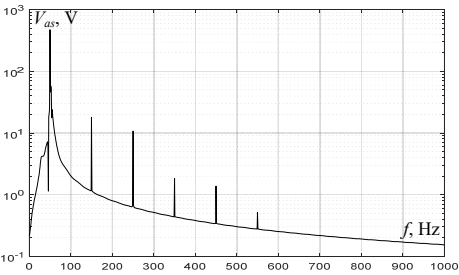


Fig. 7. Spectrum analysis of the stator voltage V_{as}

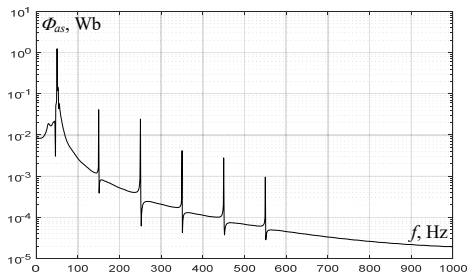


Fig. 8. Spectrum analysis of the stator flux Φ_{as}

Spectral analysis of these magnetic fluxes reveals significant variations when a 5 % inter-turn short-circuit occurs in phase A. At the same time, high-frequency components appear in the stator currents, producing acoustic noise and vibration. These phenomena induce additional stresses in the gearbox and turbine blades, reducing their service life. The stator current spectrum analysis reveals the emergence of distinct harmonics at frequencies of 150 Hz, 250 Hz and 350 Hz. These harmonics resemble those of stator flux and voltage. Harmonic components in the stator currents lead to the production of pulsating torques. As a result, significant consequences such as overheating occur, indicating that overcurrent is generated among the short-circuited turns and the stator windings, especially within the defective winding. Moreover, unbalanced voltages are generated in the stator windings as a result of the asymmetry of the stator fluxes. This asymmetry can adversely affect the control algorithms of the DFIG and disrupt the maximum power point tracking leading to a reduction in energy efficiency and stability.

Conclusions. This study analyzed the effect of stator inter-turn short-circuit faults on the operation of DFIGs in wind power systems, using a simplified electromagnetic model that includes the rise of neutral point voltage.

The model, based on line-to-line voltages, proved effective in identifying key fault-related harmonics through spectral analysis, confirming its diagnostic capability.

Simulation results showed that such faults lead to electromagnetic imbalances, which cause mechanical vibrations and control instability, ultimately reducing system reliability.

The proposed modeling approach offers a practical tool for condition monitoring and lays the groundwork for further studies on other fault types in DFIG-based wind turbines.

Conflict of interest. The authors declare that they have no conflicts of interest.

REFERENCES

- 1. Ma Y., Zhu D., Zou X., Kang Y., Guerrero J.M. Transient Characteristics and Quantitative Analysis of Electromotive Force for DFIG-based Wind Turbines during Grid Faults. Chinese Journal of Electrical Engineering, 2022, vol. 8, no. 2, pp. 3-12. doi: https://doi.org/10.23919/CJEE.2022.000010.
- 2. Rolan A., Bogarra S., Bakkar M. Integration of Distributed Energy Resources to Unbalanced Grids Under Voltage Sags With Grid Code Compliance. IEEE Transactions on Smart Grid, 13, 2022, vol. no. 1. pp. 355-366. https://doi.org/10.1109/TSG.2021.3107984.
- 3. Husari F., Seshadrinath J. Incipient Interturn Fault Detection and Severity Evaluation in Electric Drive System Using Hybrid HCNN-SVM Based Model. IEEE Transactions on Industrial Informatics, 2022, vol. 18, no. 3, pp. 1823-1832. doi: https://doi.org/10.1109/TII.2021.3067321.
- 4. Chen Y., Rehman A.U., Zhao Y., Wang L., Wang S., Zhang M., Zhao Y., Cheng Y., Tanaka T. Numerical Modeling, Electrical Characteristics Analysis and Experimental Validation of Severe Inter-Turn Short Circuit Fault Conditions on Stator Winding in DFIG of Wind Turbines. IEEE Access, 2021, vol. 9, pp. 13149-13158. doi: https://doi.org/10.1109/ACCESS.2021.3050876.
- 5. Sotoudeh A., Rezaei M.M. An adaptive control strategy for grid-forming of SCIG-based wind energy conversion systems. Energy Reports, 2023, vol. 10, pp. 114-122. https://doi.org/10.1016/j.egyr.2023.06.030

- 6. Huang S., Wang J., Huang C., Zhou L., Xiong L., Liu J., Li P. A fixed-time fractional-order sliding mode control strategy for power quality enhancement of PMSG wind turbine. *International Journal of Electrical Power & Energy Systems*, 2022, vol. 134, art. no. 107354. doi: https://doi.org/10.1016/j.ijepes.2021.107354.
- 7. Zhao S., Chen Y., Rehman A.U., Liang F., Wang S., Zhao Y., Deng W., Ma Y., Cheng Y. Detection of Interturn Short-Circuit Faults in DFIGs Based on External Leakage Flux Sensing and the VMD-RCMDE Analytical Method. *IEEE Transactions on Instrumentation and Measurement*, 2022, vol. 71, pp. 1-12. doi: https://doi.org/10.1109/TIM.2022.3186061.
- 8. Sarma N., Tuohy P.M., Djurovic S. Stator Electrical Fault Detection in DFIGs Using Wide-Band Analysis of the Embedded Signals From the Controllers. *IEEE Transactions on Energy Conversion*, 2021, vol. 36, no. 2, pp. 800-811. doi: https://doi.org/10.1109/TEC.2020.3017443.
- 9. Gurusamy V., Capolino G.-A., Akin B., Henao H., Romary R., Pusca R. Recent Trends in Magnetic Sensors and Flux-Based Condition Monitoring of Electromagnetic Devices. *IEEE Transactions on Industry Applications*, 2022, vol. 58, no. 4, pp. 4668-4684. doi: https://doi.org/10.1109/TIA.2022.3174804.
- 10. Botha S., Gule N. Vibrational Analysis of an Unbalanced Brushless Doubly Fed Induction Machine. 2023 IEEE International Electric Machines & Drives Conference (IEMDC), 2023, pp. 1-6. doi: https://doi.org/10.1109/IEMDC55163.2023.10239081.
- 11. Sahin I., Keysan O. Model Predictive Controller Utilized as an Observer for Inter-Turn Short Circuit Detection in Induction Motors. *IEEE Transactions on Energy Conversion*, 2021, vol. 36, no. 2, pp. 1449-1458. doi: https://doi.org/10.1109/TEC.2020.3048071.
- 12. Abid M., Laribi S., Larbi M., Allaoui T. Diagnosis and localization of fault for a neutral point clamped inverter in wind energy conversion system using artificial neural network technique. *Electrical Engineering & Electromechanics*, 2022, no. 5, pp. 55-59. doi: https://doi.org/10.20998/2074-272X.2022.5.09.
- 13. Alipoor G., Mirbagheri S.J., Moosavi S.M.M., Cruz S.M.A. Incipient detection of stator inter-turn short-circuit faults in a doubly-fed induction generator using deep learning. *IET Electric Power Applications*, 2023, vol. 17, no. 2, pp. 256-267. doi: https://doi.org/10.1049/elp2.12262.
- 14. Toshani H., Abdi S., Hosseini N.K., Abdi E. Fault Diagnosis of Squirrel Cage Induction Generator for Wind Turbine Applications Using a Hybrid Deep Neural Network and Decision Tree Approach. 2021 International Conference on Electrical, Computer and Energy Technologies (ICECET), 2021, pp. 1-6. doi: https://doi.org/10.1109/ICECET52533.2021.9698556.
- 15. St-Onge X.F., Cameron J., Saleh S., Scheme E.J. A Symmetrical Component Feature Extraction Method for Fault Detection in Induction Machines. *IEEE Transactions on Industrial Electronics*, 2019, vol. 66, no. 9, pp. 7281-7289. doi: https://doi.org/10.1109/TIE.2018.2875644.
- 16. Mellah H., Arslan S., Sahraoui H., Hemsas K.E., Kamel S. The Effect of Stator Inter-Turn Short-Circuit Fault on DFIG Performance Using FEM. Engineering, Technology & Applied Science Research, 2022, vol. 12, no. 3, pp. 8688-8693. doi: https://doi.org/10.48084/etasr.4923.
- 17. Ahmadpour A., Dejamkhooy A., Shayeghi H. Fault Diagnosis of HTS–SLIM Based on 3D Finite Element Method and Hilbert–Huang Transform. *IEEE Access*, 2022, vol. 10, pp. 35736-35749. doi: https://doi.org/10.1109/ACCESS.2022.3159693.

- 18. Grechko O.M. Influence of the poles shape of DC electromagnetic actuator on its thrust characteristic. *Technical Electrodynamics*, 2024, no. 1, pp. 38-45. doi: https://doi.org/10.15407/techned2024.01.038.
- 19. Diboune Y., Hachelaf R., Kouchih D. Theoretical and experimental analysis of unbalanced doubly fed induction generators. *IAES International Journal of Robotics and Automation (IJRA)*, 2024, vol. 13, no. 4, pp. 476-484. doi: https://doi.org/10.11591/ijra.v13i4.pp476-484.
- 20. Alphan H. Modelling potential visibility of wind turbines: A geospatial approach for planning and impact mitigation. Renewable and Sustainable Energy Reviews, 2021, vol. 152, art. no. 111675. doi: https://doi.org/10.1016/j.rser.2021.111675.
- 21. Sajan C., Satish Kumar P., Virtic P. Enhancing grid stability and low voltage ride through capability using type 2 fuzzy controlled dynamic voltage restorer. *Electrical Engineering & Electromechanics*, 2024, no. 4, pp. 31-41. doi: https://doi.org/10.20998/2074-272X.2024.4.04.
- **22.** Nid A., Sayah S., Zebar A. Power fluctuation suppression for grid connected permanent magnet synchronous generator type wind power generation system. *Electrical Engineering & Electromechanics*, 2024, no. 5, pp. 70-76. doi: https://doi.org/10.20998/2074-272X.2024.5.10.
- 23. Muthukaruppasamy S., Dharmaprakash R., Sendilkumar S., Parimalasundar E. Enhancing off-grid wind energy systems with controlled inverter integration for improved power quality. *Electrical Engineering & Electromechanics*, 2024, no. 5, pp. 41-47. doi: https://doi.org/10.20998/2074-272X.2024.5.06.
- 24. Kaddache M., Drid S., Khemis A., Rahem D., Chrifi-Alaoui L. Maximum power point tracking improvement using type-2 fuzzy controller for wind system based on the double fed induction generator. *Electrical Engineering & Electromechanics*, 2024, no. 2, pp. 61-66. doi: https://doi.org/10.20998/2074-272X.2024.2.09.
- 25. Mousavi Y., Bevan G., Kucukdemiral I.B., Fekih A. Sliding mode control of wind energy conversion systems: Trends and applications. *Renewable and Sustainable Energy Reviews*, 2022, vol. 167, art. no. 112734. doi: https://doi.org/10.1016/j.rser.2022.112734.
- **26.** Kong X., Ma L., Liu X., Abdelbaky M.A., Wu Q. Wind Turbine Control Using Nonlinear Economic Model Predictive Control over All Operating Regions. *Energies*, 2020, vol. 13, no. 1, art. no. 184. doi: https://doi.org/10.3390/en13010184.
- 27. L'Hadj Said M., Ali Moussa M., Bessaad T. Control of an autonomous wind energy conversion system based on doubly fed induction generator supplying a non-linear load. *Electrical Engineering & Electromechanics*, 2025, no. 4, pp. 3-10. doi: https://doi.org/10.20998/2074-272X.2025.4.01.

Received 09.02.2025 Accepted 26.05.2025 Published 02.11.2025

Y. Diboune¹, PhD Student,

R. Hachelaf¹, Assistant Professor,

D. Kouchih¹. PhD. Associate Professor.

Automatic and Electrotechnics Department,

Electrical Systems and Remote-Control Laboratory (LabSET), Faculty of Technology, University of Blida 1, Algeria, e-mail: yaakoubd479@gmail.com (Corresponding Author);

haclefr@yahoo.fr; djkouchih@yahoo.fr

How to cite this article:

Diboune Y., Hachelaf R., Kouchih D. Effect of short-circuit in stator windings on the operation of doubly-fed induction generators operating in a wind power system. *Electrical Engineering & Electromechanics*, 2025, no. 6, pp. 3-7. doi: https://doi.org/10.20998/2074-272X.2025.6.01

T. Bessaad, A. Benbouali, K. Khelifi Otmane, R. Taleb, H. Sahraoui, A. Iqbal

Inverter fuzzy speed control of multi-machine system series-connected fed by a single five-phase an asymmetrical 19-level inverter with less number of switches

Introduction. 5-phase permanent magnet synchronous machines (PMSMs) are widely used in modern electric drive systems due to their superior torque density, improved fault tolerance, and reduced torque ripple. These characteristics make them ideal for demanding applications such as electric vehicles, aerospace systems, and industrial automation. Problem. Despite their advantages, conventional multimachine systems using multilevel inverters and PI controllers suffer from sensitivity to parameter variations, high torque ripple, and increased cost and complexity due to the large number of power switches. The goal of this work is to design and validate a compact robust drive system that enables independent vector control of two series-connected 5-phase PMSMs using a reduced switch count asymmetrical 19-level inverter and fuzzy logic controllers. Methodology. The proposed system is modeled in the phase domain and transformed using Clarke and Park transformations to enable decoupled control. Mamdani-type fuzzy logic controllers are implemented for both speed and current regulation. The system is simulated in MATLAB/Simulink to evaluate performance under dynamic conditions and parameter variations. Results. The fuzzy logic controller significantly outperforms the conventional PI controller, achieving a settling time of 0.06 s versus 0.15 s, a steady-state speed error of 0.4 % compared to 1.9 %, and a torque ripple reduction of 47 %. Under robustness testing with doubled inertia, the fuzzy controller maintains stable and accurate control, whereas the PI controller fails. Additionally, the inverter achieves near-sinusoidal output with a total harmonic distortion of less than 4.5 %, and the switch count is reduced by 66 % compared to traditional 36-switch designs. Scientific novelty. This work presents the first implementation of independent vector control for two seriesconnected PMSMs using a single 12-switch asymmetrical 19-level inverter and model-free fuzzy logic control, offering a simpler and more efficient alternative to existing approaches. Practical value. The proposed system provides a highly efficient and cost-effective solution for electric drive applications where space, reliability, and control robustness are essential, such as in electric transportation, avionics, and compact industrial systems. References 26, tables 4, figures 9.

Key words: multi-machine system, fuzzy logic controller, independent vector control, asymmetric inverter.

Вступ. П'ятифазні синхронні машини з постійними магнітами (PMSMs) широко використовуються в сучасних системах електроприводу завдяки високій щільності і зменшеній пульсації крутного моменту, та підвищеній відмовостійкості. Ці характеристики роблять їх ідеальними для багатьох застосувань — електромобілі, аерокосмічні системи та промислова автоматика. Проблема. Незважаючи на переваги, традиційні багатомашинні системи, що використовують багаторівневі інвертори та Π І-регулятори, ϵ чутливими до змін параметрів, високої пульсації крутного моменту, а також високій вартості і складності через велику кількість силових ключів. Метою роботи є розробка та валідація компактної надійної системи приводу, яка забезпечує незалежне векторне керування двома послідовно з'єднаними п'ятифазними PMSM з використанням асиметричного 19-рівневого інвертора зі зменшеною кількістю ключів та нечітких логічних контролерів. Методологія. Запропонована система моделюється у фазовій області з використанням перетворень Кларка та Парка для забезпечення розв'язаного керування. Реалізовано нечіткі логічні контролери типу Мамдані для регулювання швидкості і струму. Система моделюється в MATLAB/Simulink для оцінки продуктивності в динамічних умовах та зміни параметрів. Результати. Нечіткий логічний регулятор значно перевершує традиційний ПІ-регулятор, досягаючи часу встановлення 0,06 с проти 0,15 с, помилки швидкості 0,4 % проти 1,9 % і зниження пульсацій крутного моменту на 47 %. При випробуванні на надійність з подвоєним моментом інерції нечіткий логічний регулятор підтримує стабільне та точне керування, тоді як ПІ-регулятор виходить з ладу. Крім того, інвертор досягає майже синусоїдального вихідного сигналу із загальним коефіцієнтом гармонічних спотворень менше 4,5%, а кількість перемикачів скорочено на 66% порівняно з традиційними конструкціями з 36 перемикачами. Наукова новизна. У роботі представлена перша реалізація незалежного векторного управління для двох послідовно з'єднаних PMSMs з використанням одного асиметричного 19-рівневого інвертора з 12 перемикачами та нечіткого логічного управління без моделі, що пропонує більш просту та ефективну альтернативу існуючим підходам. **Практична значимість**. Пропонована система ϵ високоефективним та економічним рішенням для електроприводів, де важливі компактність, надійність і стійкість управління, наприклад, в електротранспорті, авіоніці та компактних промислових системах. Бібл. 26, табл. 4, рис. 9.

Ключові слова: багатомашинна система, контролер нечіткої логіки, незалежне векторне керування, асиметричний інвертор.

Introduction. Multi-phase machines have attracted growing interest due to their numerous advantages over conventional 3-phase systems. These include reduced current ripple [1], improved stability and fault tolerance [2], higher torque density [3, 4], and lower torque pulsations [5, 6]. Such characteristics make them well-suited for demanding applications such as electric aircraft, marine propulsion, robotics, and hybrid/electric vehicles [7, 8]. Among the various configurations, dual-machine drive systems, where two multi-phase machines are connected in series or parallel and powered by voltage- and frequency-controlled sources, typically multilevel inverters (MLIs), have proven particularly promising [9, 10]. These systems support independent motor operation under different load and speed conditions, enabling flexible control strategies and the use of various motor types [11].

Effective control of such systems requires managing additional stator current components beyond those needed for single-machine vector control. When the stator windings are connected in series, each machine can effectively operate as though it were supplied by an independent multi-phase voltage source [12], as demonstrated in 5-phase systems powered by a single inverter [13, 14]. To meet high-voltage demands in electric traction applications, MLIs have emerged as the preferred solution [14], with typical topologies including neutral point clamped inverters [15], flying capacitor inverters [16], and cascaded H-bridge inverters [17]. While cascaded H-bridge architectures offer benefits such as modularity and reduced voltage stress [18], increasing the number of output levels usually requires more switching devices, which adds to system complexity and cost [19].

© T. Bessaad, A. Benbouali, K. Khelifi Otmane, R. Taleb, H. Sahraoui, A. Iqbal

introduced Recent advances have 19-level asymmetrical inverter architectures that use significantly fewer switches, such as 9-switch or 12-switch designs, without compromising output quality [20]. The present study proposes a compact 19-level asymmetrical 5-phase inverter architecture that drives two series-connected 5-phase permanent magnet synchronous machines (PMSMs) using only 12 switches, while maintaining high-quality voltage output [21]. To control the system, we employ fuzzy logic control (FLC) for both speed and current regulation. Unlike traditional methods, FLC does not require an accurate mathematical model and is inherently robust to parameter variations. Comparative results demonstrate that the proposed FLC significantly outperforms conventional PI control under dynamic load conditions, while also reducing total harmonic distortion (THD).

The **goal** of this work is to design and validate a compact robust drive system that enables independent vector control of two series-connected 5-phase PMSMs using a reduced-switch-count asymmetrical 19-level inverter and fuzzy logic controllers.

Asymmetrical MLI with uniform step configuration. A detailed schematic of the partial cells is shown in Fig. 1, which also shows the main notation conventions adopted throughout this study. The switching states of the transistor pairs S_{jx}/S'_{jx} (for x=1,2 and j=1 to k) are controlled by binary signals M_{jx} , and M'_{jx} , respectively. These Boolean control functions are subject to the following logical constraints:

$$M_{ix} + M'_{ix} = 1$$
. (1)

A dedicated conversion function F_j maps the switching states to their corresponding voltage levels:

$$F_i = M_{ix} - M'_{ix} \Rightarrow F_i \in \{-1, 0, +1\}.$$
 (2)

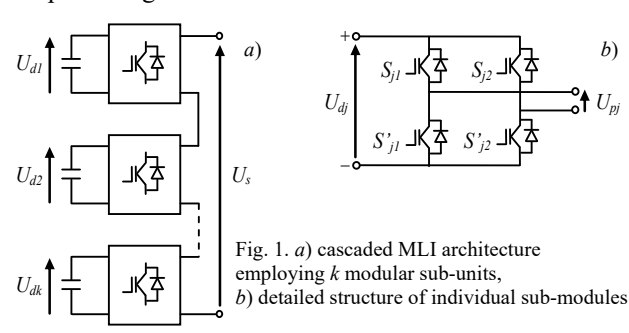
The output voltage generated by each power cell is defined as:

$$U_{pj} = F_j \cdot U_{dj} \Rightarrow U_{pj} \in \left\{ -U_{dj}, 0, +U_{dj} \right\}, \quad (3)$$

which illustrates the ternary voltage-level generation capability of each individual partial cell. When combined, the total output voltage of the complete MLI is:

$$U_s = U_{p1} + U_{p2} + \cdots U_{pk}, \qquad (4)$$

where $U_{p1} - U_p$ are the output voltages from each partial inverter cell (or module); U_s is the total synthesized output voltage at the inverter terminal.



The asymmetric configuration of MLIs is defined by the use of non-uniform DC input voltages, where at least one partial inverter is supplied with a different voltage level from its series-connected counterparts. In regular-step asymmetric MLI topologies, 3 design criteria must be satisfied to achieve equal voltage steps (ΔU) across all

output levels. Importantly, this uniform step size is directly determined by the smallest DC voltage source in the system, denoted as U_{d1} [22].

Successful operation of the asymmetrical MLI depends on satisfying the following design conditions:

- 1) monotonic ordering of DC inputs. The DC voltage sources must be arranged in a strictly monotonically increasing sequence, such that: $U_{d(h-1)} \le U_{dh}$, $\forall h = 2...k$;
- 2) voltage ratio constraint. The ratio between 2 consecutive DC sources must satisfy: $U_{dh}/U_{d(h-1)} = \delta_h$, $\delta_h \in N^*$;
- 3) dedicated DC source per cell. Each j^{th} cell in the cascaded structure must be supplied with a distinct DC voltage U_{dj} , such that:

$$U_{dj} \le 1 + 2\sum_{l=1}^{j-1} U_{dl} . {5}$$

If all these conditions are fulfilled, the inverter can generate an output voltage waveform U_s consisting of N equally spaced voltage levels:

$$N = 1 + 2\sum_{i=1}^{k} \left(U_{dj} / U_{d1} \right).$$
 (6)

For k=3 in (6), the 13-level output voltage waveform can be synthesized using 2 distinct sets of DC source configurations, i.e., $(U_{d1}, U_{d2}, U_{d3}) \in \{(1, 1, 4), (1, 2, 3)\}.$ Figure 2 shows the complete set of output voltage combinations achievable by the 3 partial cells (k=3) in the 9-level inverter topology. The corresponding DC voltage values for the 3 cells are: $U_{d1} = 1$ p.u., $U_{d2} = 1$ p.u., $U_{d3} = 2$ p.u. Each partial inverter generates one of 3 possible output voltage levels: $U_{p1} \in \{-1, 0, 1\}, U_{p2} \in \{-1, 0, 1\}$ and $U_{p3} \in \{-2, 0, 2\}$. This configuration enables the proposed topology to -1, 0, 1, 2, 3, 4. Certain output voltage values can be obtained using multiple switching combinations. For example, the 2 p.u. output voltage can be achieved through the following 4 distinct switching states: $(U_{p1}, U_{p2}, U_{p3}) \in \{(-1, 1, 2), (0, 0, 2), (0, 2$ (1, -1, 2), (1, 1, 0). The existence of multiple voltage synthesis paths, including redundant switching states for the same output level, introduces degrees of freedom that can be strategically exploited. These degrees of freedom enhance the performance of the uniform step asymmetrical MLI in terms of efficiency, reliability, and power quality [23].

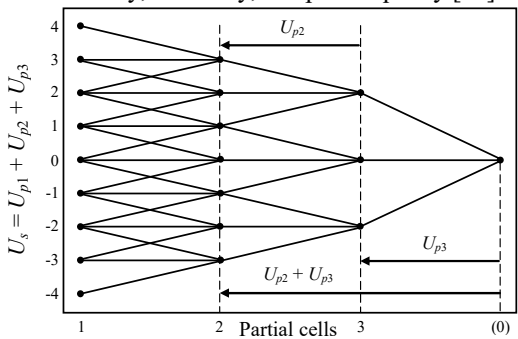


Fig. 2. In a 3-cell cascaded H-bridge topology producing 9 voltage levels, the possible output states per partial inverter are: $(U_{d1} = 1 \text{ p.u.}; U_{d2} = 1 \text{ p.u.}; U_{d3} = 2 \text{ p.u.})$

Asymmetrical MLIs offer the user a high degree of design flexibility, particularly through the ability to select different intermediate voltage levels and the availability of redundancy in these choices.

The approach utilizes two fundamental control variables [21, 24]: Modulation index m and modulation rate r:

$$m = f_c / f_r \; ; \tag{7}$$

$$r = 2A_r/(N-1)A_c$$
 (8)

Table 1 shows representative DC voltage configurations along with their corresponding output voltage level capabilities. The case study focuses on a 3-stage (k=3) series-connected single-phase inverter topology for each phase leg.

Table 1
Voltage imbalance phenomena in 3-cell uniform step
asymmetrical MLI systems

N	1/ 10 11	11 . 10 11	11 . D.II
	u_{d1} , p.u	u_{d2} , p.u	u_{d3} , p.u
7	1	1	1
9	1	1	2
11	1	1	3
11	1	2	2
13	1	1	4
13	1	2	3
	1	1	5
15	1	2	4
	1	3	3
	1	1	6
17	1	2	5
	1	3	4
	1	1	7
19	1	2	6
19	1	3	5
	1	4	4

The multi-machine system (Fig. 3) consists of two 5-phase PMSMs connected in series. A single 5-phase inverter supplies power to both machines. Each machine exhibits a spatial phase shift of 72° between 2 successive stator phases.

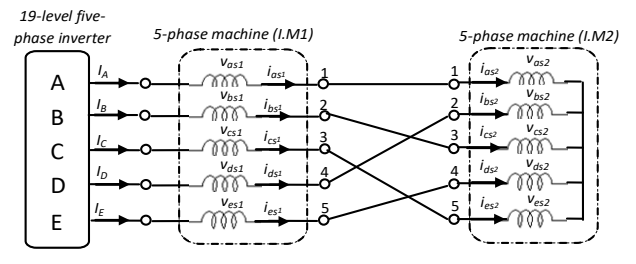


Fig. 3. Diagram of coupling the phase windings in series of the stator of the multi-motors (a 5-phase inverter powers the system)

In the analysis, it is assumed that both machines have identical electrical parameters. The electrical circuit of the system is described as:

$$[V_{ABCDE}] = [R_S][i_{ABCDE}] + \frac{\mathrm{d}}{\mathrm{d}t}[\varphi_{ABCDE}], \qquad (9)$$

where V_{ABCDE} is the vector of stator voltages each phase (A to E); i_{ABCDE} is the vector of phase currents; R_s is the stator resistance (assumed equal for all phases); φ_{ABCDE} is the vector of stator flux linkages.

Figure 3 illustrates the relationship between the stator winding voltages and the source currents for two 5-phase PMSMs connected in series. The stator winding phases (A-E) and the neutral point (N) correspond to the inverter's output terminals.

The stator voltages of the 2 machines are given by:

$$[V_{s}] = \begin{bmatrix} v_{A} \\ v_{B} \\ v_{C} \\ v_{D} \\ v_{E} \end{bmatrix} = \begin{bmatrix} v_{as1} + v_{as2} \\ v_{bs1} + v_{cs2} \\ v_{cs1} + v_{es2} \\ v_{ds1} + v_{bs2} \\ v_{es1} + v_{ds2} \end{bmatrix},$$
 (10)

where $v_{as1,2}$, $v_{bs1,2}$, $v_{cs1,2}$, $v_{ds1,2}$, $v_{es1,2}$ are the phase voltages of 2 machines.

The following equation represents the stator currents of the two 5-phase machines connected in series. Phases A–E and the neutral point N correspond to the MLI's output. Figure 3 also shows the connection between each machine's source and stator currents:

$$[i_{s}] = \begin{bmatrix} i_{A} \\ i_{B} \\ i_{C} \\ i_{D} \\ i_{E} \end{bmatrix} = \begin{bmatrix} i_{as1} \\ i_{bs1} \\ i_{cs1} \\ i_{ds1} \\ i_{es1} \end{bmatrix} = \begin{bmatrix} i_{as2} \\ i_{cs2} \\ i_{es2} \\ i_{bs2} \\ i_{ds2} \end{bmatrix},$$
 (11)

where $i_{as1,2}$, $i_{bs1,2}$, $i_{cs1,2}$, $i_{ds1,2}$, $i_{es1,2}$ are the currents of 2 machines.

The power-invariant Clarke decoupling transformation matrix is:

$$\begin{bmatrix} C \end{bmatrix}^{T} = \sqrt{\frac{2}{5}} \begin{bmatrix} 1 & \cos(\alpha) & \cos(2\alpha) & \cos(3\alpha) & \cos(4\alpha) \\ 0 & \sin(\alpha) & \sin(2\alpha) & \sin(3\alpha) & \sin(4\alpha) \\ 1 & \cos(2\alpha) & \cos(4\alpha) & \cos(6\alpha) & \cos(8\alpha) \\ 0 & \sin(2\alpha) & \sin(4\alpha) & \sin(6\alpha) & \sin(8\alpha) \\ 1/\sqrt{2} & 1/\sqrt{2} & 1/\sqrt{2} & 1/\sqrt{2} & 1/\sqrt{2} \end{bmatrix}.$$
(12)

Moving to the new variables system (α, β, x, y, o) from the original system (A-E), we have:

$$f(\alpha \beta xy) = [C] \cdot f(ABCDE),$$

where [C] is the power-invariant transformation matrix.

The voltages and currents of the 5-phase inverter (α, β) and (x, y) axes are defined as:

$$\begin{bmatrix} v_{\alpha}^{inv} \\ v_{\beta}^{inv} \\ v_{\beta}^{inv} \\ v_{\gamma}^{inv} \\ v_{\rho}^{inv} \\ v_{\rho}^{inv} \\ v_{\rho}^{inv} \\ v_{\rho}^{inv} \end{bmatrix} = \begin{bmatrix} C \\ v_{A} \\ v_{B} \\ v_{C} \\ v_{D} \\ v_{E} \end{bmatrix} = \begin{bmatrix} C \\ v_{as1} + v_{as2} \\ v_{bs1} + v_{cs2} \\ v_{cs1} + v_{es2} \\ v_{ds1} + v_{bs2} \\ v_{es1} + v_{ds2} \end{bmatrix} = \begin{bmatrix} C \\ v_{\alpha s1} + v_{xs2} \\ v_{\beta s1} + v_{\gamma s2} \\ v_{\gamma s1} + v_{\beta s2} \\ v_{\gamma s1} + v_{\beta s2} \\ 0 \end{bmatrix}; (13)$$

$$\begin{cases} i_{\alpha}^{inv} = i_{\alpha s_1} = i_{xs_2}; \\ i_{\beta}^{inv} = i_{\beta s_1} = -i_{ys_2}; \\ i_{x}^{inv} = i_{xs_1} = i_{\alpha s_2}; \\ i_{y}^{inv} = i_{ys_1} = i_{\beta s_2}, \end{cases}$$
(14)

where v_{α}^{inv} , v_{β}^{inv} , v_{x}^{inv} , v_{y}^{inv} and i_{α}^{inv} , i_{β}^{inv} , i_{x}^{inv} , i_{y}^{inv} are the inverter voltage and currents in the $\alpha\beta$ and xy axes.

Since the two subspaces $\alpha\beta$ and xy are orthogonal (Fig. 3) the chosen series connection strategy enables independent vector control of the two machines.

The zero-sequence component of the MLI can be neglected. The electromagnetic part of the drive system is described by 8 first-order equations. Equations (15), (16) represent the 4 inverter/stator voltage expressions:

$$\begin{cases} v_{\alpha}^{inv} = (R_{s1} + R_{s2})i_{\alpha}^{inv} + (L_{sl1} + \frac{5}{2}M_{s1})\frac{d}{dt}i_{\alpha}^{inv} + \\ + L_{sl2}\frac{d}{dt}i_{\alpha}^{inv} - \sqrt{\frac{5}{2}}\Omega_{1}\phi_{f1}\sin\theta_{1}; \\ v_{\beta}^{inv} = (R_{s1} + R_{s2})i_{\beta}^{inv} + (L_{sl1} + \frac{5}{2}M_{s1})\frac{d}{dt}i_{\beta}^{inv} + \\ + L_{sl2}\frac{d}{dt}i_{\beta}^{inv} + \sqrt{\frac{5}{2}}\Omega_{1}\phi_{f1}\cos\theta_{1}; \\ \begin{cases} v_{x}^{inv} = (R_{s1} + R_{s2})i_{x}^{inv} + (L_{sl2} + \frac{5}{2}M_{s2})\frac{d}{dt}i_{x}^{inv} + \\ + L_{sl1}\frac{d}{dt}i_{x}^{inv} - \sqrt{\frac{5}{2}}\Omega_{2}\phi_{f2}\sin\theta_{2}; \\ v_{y}^{inv} = (R_{s1} + R_{s2})i_{y}^{inv} + (L_{sl2} + \frac{5}{2}M_{s2})\frac{d}{dt}i_{y}^{inv} + \\ + L_{sl1}\frac{d}{dt}i_{y}^{inv} + \sqrt{\frac{5}{2}}\Omega_{2}\phi_{f2}\cos\theta_{2}, \end{cases}$$
(16)

where $L_{sl1,2}$, $M_{s1,2}$ are the inductance and mutual inductance in the rotating frame; $\Omega_{1,2}$, $\phi_{f1,2}$, $\theta_{1,2}$ are the mechanical speed, flux and electrical speed, respectively.

To achieve a more compact representation, the stator parameters are transformed into a φ -rotated (dq) synchronous reference frame from the stationary $(\alpha\beta)$ frame using the transformation matrix [D]:

$$[\mathbf{D}] = \begin{bmatrix} \cos \theta & \sin \theta & . \\ \sin \theta & \cos \theta & . \\ . & . & [I]^{3 \times 3} \end{bmatrix} .$$
 (17)

The torque equations for the 2 series-connected machines are:

$$\begin{cases} T_{em1} = p_1[(L_d - L_q)i_d^{inv} \cdot i_q^{inv} + \sqrt{\frac{5}{2}\phi_{f1}} \cdot i_q^{inv}]; \\ T_{em2} = p_2[(L_x - L_y)i_x^{inv} \cdot i_y^{inv} + \sqrt{\frac{5}{2}\phi_{f2}} \cdot i_y^{inv}], \end{cases}$$
(18)

where p_1 , p_2 are the number of pole pairs for 2 machines.

From the previous equations it is clear that the torqueproducing current components i_{sd} , i_{sq} in the 1st machine are set to 0. As a result, the torque is generated by the 2nd machine through the current components i_{sx} , i_{sy} . This configuration allows both machines to be independently controlled using a single voltage source inverter.

Interconnected 5-phase PMSM set in series configuration with independent control loops. The torque control strategy derived in (18) relies on the i_{sd} , i_{sq} currents for the 1st machine, and a similar current-controlled method is applied to the 2nd machine using i_{sx} , i_{sy} . A common strategy in such systems is to set i_{sd} and i_{sx} to 0, ensuring that torque is controlled exclusively by i_{sq} and i_{sy} .

For the 1st machine:

$$\begin{cases} v_d^{inv} = (R_{s1} + R_{s2})i_d^{inv} + (L_{sl1} + \frac{5}{2}M_{s1})\frac{d}{dt}i_d^{inv} + \\ + L_{sl2}\frac{d}{dt}i_d^{inv} - \Omega_1(L_{sl1} + \frac{5}{2}M_{s1})i_q^{inv}; \\ v_q^{inv} = (R_{s1} + R_{s2})i_q^{inv} + (L_{sl1} + \frac{5}{2}M_{s1})\frac{d}{dt}i_q^{inv} + \\ + L_{sl2}\frac{d}{dt}i_q^{inv} - \Omega_1(L_{sl1} + \frac{5}{2}M_{s1})i_d^{inv} + \sqrt{\frac{5}{2}}\Omega_1\phi_{f1}. \end{cases}$$
(19)

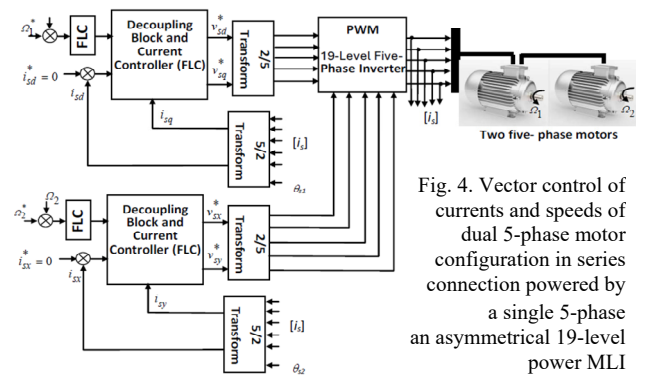
For the 2nd machine:

$$\begin{vmatrix} v_x^{inv} = (R_{s1} + R_{s2})i_x^{inv} + (L_{sl1} + \frac{5}{2}M_{s2})\frac{d}{dt}i_x^{inv} + \\ + L_{sl1}\frac{d}{dt}i_x^{inv} - \Omega_2(L_{sl2} + \frac{5}{2}M_{s2})i_y^{inv}; \\ v_y^{inv} = (R_{s1} + R_{s2})i_y^{inv} + (L_{sl1} + \frac{5}{2}M_{s2})\frac{d}{dt}i_y^{inv} + \\ + L_{sl1}\frac{d}{dt}i_y^{inv} - \Omega_2(L_{sl2} + \frac{5}{2}M_{s2})i_x^{inv} + \sqrt{\frac{5}{2}}\Omega_2\phi_{f2}. \end{aligned}$$
 (20)

The overall voltage references are generated based on the schematic shown in Fig. 4, and are defined as [11]:

$$\begin{bmatrix} V_a^* \\ V_b^* \\ V_c^* \\ V_d^* \\ V_e^* \end{bmatrix} = \begin{bmatrix} v_{as1}^* + v_{as2}^* \\ v_{bs1}^* + v_{cs2}^* \\ v_{cs1}^* + v_{es2}^* \\ v_{ds1}^* + v_{bs2}^* \\ v_{es1}^* + v_{ds2}^* \end{bmatrix}, \tag{21}$$

where symbol «*» indicates a reference value provided to the controller.



Machines parameters are listed in Table 2.

Table 2

Machines parameters							
R_s , Ω	$L_d = L_q$, H	J_k , kg/m ²	p	φ _f , Wb	f, Hz	F_r , kg·m ² ·s ⁻¹	
3.6	0.0021	0.0011	2	0.25	50	0.0014	

Fuzzy logic controller (FLC). FLCs are widely used in the speed control of electric machines due to their simplicity, intuitive design, and model-free nature. Unlike conventional control techniques, FLCs do not require an accurate mathematical model of the system or a complex feedback loop to achieve effective performance.

In an FLC, the input and output variables are defined using membership functions within a common universe of discourse. The controller's performance depends heavily on the appropriate selection of scaling factors (gains) and the careful tuning of its parameters. These settings are often optimized empirically through trial-and-error methods to enhance control quality [25, 26].

A fuzzy logic controller typically consists of 4 main components: a rule base, an inference engine, a fuzzification module, and a defuzzification module. In this study, Mamdani's inference method is applied using the max—min composition technique. To convert fuzzy outputs into crisp control actions, the center of area method is used for defuzzification.

The architecture of the proposed fuzzy speed controller is shown in Fig. 5. It processes 2 input variables – the speed error E and its derivative ΔE . Based

on these inputs, the controller generates an output signal representing the torque increment ΔT_{em} . Integration of this signal provides the electromagnetic torque command T_{em} .

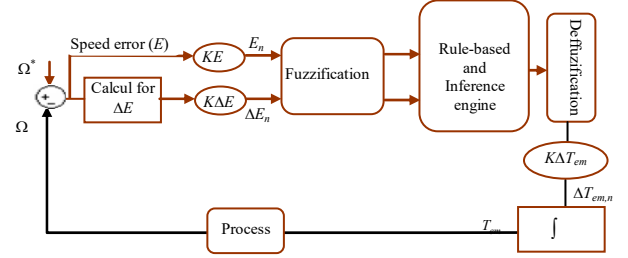


Fig. 5. Block diagram of the fuzzy speed controller

The fuzzy speed controller employs a complete rule base of 49 If—Then rules, covering all possible combinations of input conditions. As shown in Fig. 6, all variables – namely, the speed error E, its time derivative (ΔE), and the output signal – use triangular membership functions. Each variable is divided into 7 linguistic categories: Negative High (NH); Negative Moderate (NM); Negative Low (NS); Neutral (ZE); Positive Low (PS); Positive Moderate (PM); Positive High (PH).

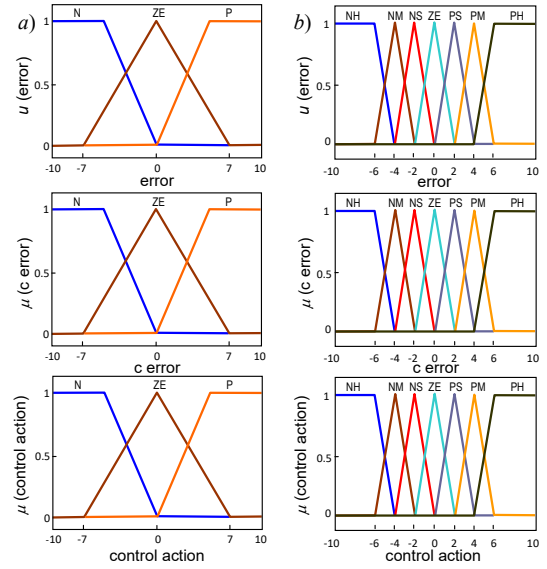


Fig. 6. Membership functions of input/output variables: *a*) current; *b*) speed

The fuzzy inference system uses a 49-rule decision matrix (Table 3) to determine the controller's output response based on the inputs E and ΔE . Each rule is expressed in standard If—Then format and governs the control action accordingly.

Table 3
The rule base for controlling the speed

	The full base for controlling the speed							
ΔE	NH	NM	NS	ZE	PS	PM	РН	
NH	NH	NH	NH	NH	NM	NS	ZE	
NM	NH	NH	NH	NM	NS	ZE	PS	
NS	NH	NH	NM	NS	ZE	PS	PM	
ZE	NH	NM	NS	ZE	PS	PM	PH	
PS	NM	NS	ZE	PS	PM	PH	PH	
PM	NS	ZE	PS	PM	PH	PH	PH	
PH	7 F	PS	PM	PН	PН	PН	PH	

Some of the rules in Table 3 can be interpreted as follows: for example, if the speed error E is PM and its derivation ΔE is also PM, then the torque increment ΔT_{em} should be PH. In this case, both the error and its rate of

change indicate a moderate increase in speed, and a fast corrective action is required – hence, a high positive torque increment is needed.

The same methodology used to design the speed controller is applied to develop the current controller, with appropriate adaptations to account for the different control objectives. The current controller includes the following features.

The input error E: instead of being equal to $E = \Omega^* - \Omega$, it will be equal with $E = i_{ds}^* - i_{ds}$ for the 1st fuzzy controller of current i_{ds} and $E = i_{qs}^* - i_{qs}$ for the 2nd fuzzy controller of current i_{qs} .

The fuzzy controller outputs are V_{ds} for the i_{ds} current controller and V_{qs} for the i_{qs} current controller.

The inner current control loop operates with faster dynamics than the outer speed loop, maintaining the required cascade control hierarchy.

As shown in Fig. 6,b, both input variables (the error E and its derivative ΔE) are triangular membership functions, which are divided into 3 fuzzy subsets: Positive (P), Negative (N), and Zero (ZE). This control strategy uses a compact 9-rule inference system (Table 4) to determine the appropriate output response for all possible combinations of input conditions. This minimalist fuzzy partitioning ensures high computational efficiency while maintaining accurate and robust current regulation.

Table 4
The rule case for controlling the currents $\begin{array}{|c|c|c|c|c|}
\hline
E & N & ZE & P \\
\hline
\end{array}$

ΔE E	N	ZE	P
N	N	N	ZE
ZE	N	ZE	P
P	ZE	P	P

Discussion of simulation. Using MATLAB/Simulink, simulations were conducted to evaluate the vector speed control of the 2 series-connected machines in the multimachine system. The simulation results demonstrate the dynamic responses of the multi-machine system under various operating conditions. To verify that both machines can be controlled independently despite their series connection, a sequence of simulation tests was performed. The speed, current, and torque responses of the 2 unloaded machines are presented in Fig. 7, 8.

In the 1st test, machine 1 was commanded to change speed from +150 rad/s to -150 rad/s at t = 0.5 s, while machine 2 was initially set to run at +200 rad/s, then reversed to -200 rad/s at the same instant (t = 0.5 s).

Both machines were subjected to load torques equal to 100 % of the rated torque corresponding to their reference speeds, applied in the interval t = [0.15-0.3] s. Additionally, load steps were applied at t = 0.2 s for machine 1 and at t = 0.4 s for machine 2.

Figure 8 presents the simulation results for the 2nd test scenario, in which the reference speeds are reversed: machine 1 switches from +200 rad/s to -200 rad/s, and machine 2 – from -200 rad/s to +200 rad/s. These reversals are initiated at t = 0.7 s. Additionally, load torques are applied to both machines during the interval t = [0.2-0.4] s.

From Fig. 7, 8 it is evident that decoupled control is successfully maintained. The independent operation of each machine remains unaffected by the other, with no observable interference or degradation in performance.

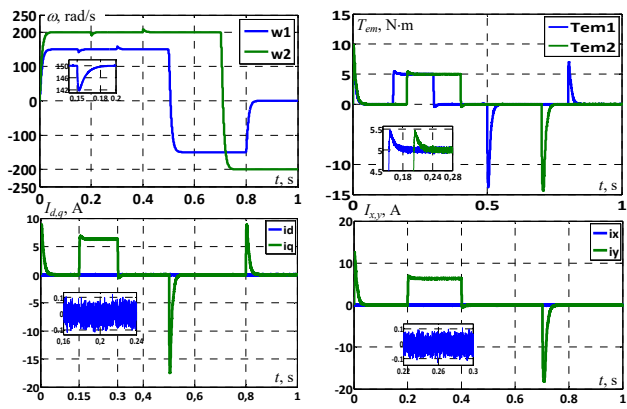


Fig. 7. The PMSM system's dynamic behavior under a 5 N⋅m load applied during intervals [0.15–3] s and [0.2–0.4] s with subsequent step changes in speed reference

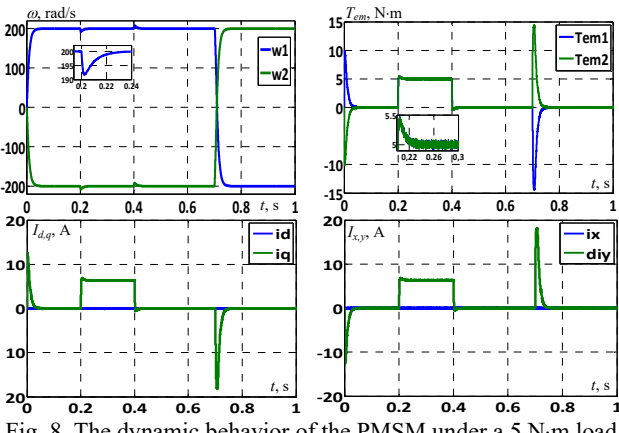
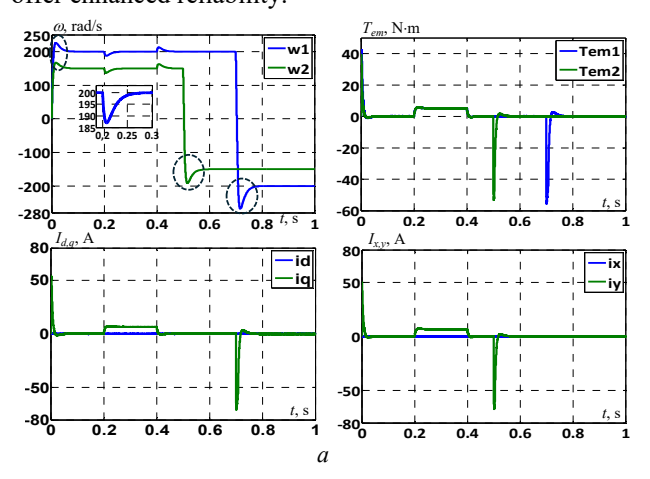


Fig. 8. The dynamic behavior of the PMSM under a 5 N·m load applied during the interval [0.2–0.4] s followed by step variations in speed reference for both machines

Test of robustness. To evaluate the impact of parameter variations on control performance, a robustness test was conducted (Fig. 9). In this test, the motors operate at their nominal reference speeds, while the inertia parameters J_1 and J_2 of both machines are doubled to assess the controllers resilience under mechanical changes. Figure 9 shows the resulting speed and torque responses. The results clearly indicate that parameter variations have a more significant effect on the performance of the classical PI controller compared to the FLC. The FLC demonstrates superior robustness, maintaining stable speed tracking and torque control despite the increased inertia. These findings confirm that the proposed fuzzy controllers are more tolerant of system variations and offer enhanced reliability.



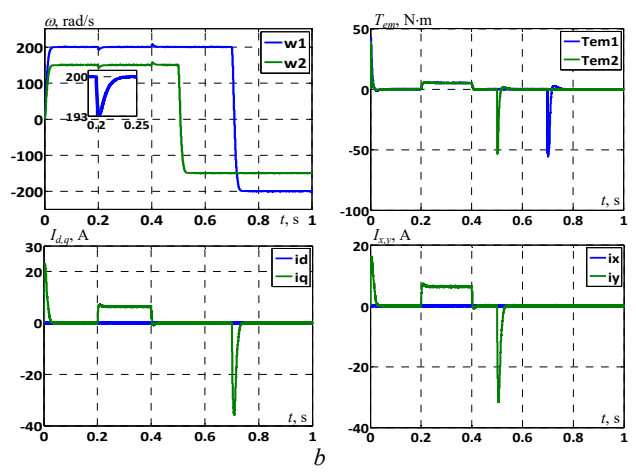


Fig. 9. PMSM's responses at J_k variations for both machines: a – with PI controllers; b – with FLC controllers

Conclusions. This paper presents a dual 5-phase drive system powered by a 12-switch asymmetrical 19-level inverter and controlled using fuzzy logic. The proposed approach enables independent vector control of 2 seriesconnected machines with reduced hardware complexity.

Simulation results show that the fuzzy controller significantly outperforms the conventional PI controller, achieving a settling time of 0.06 s compared to 0.15 s, a speed error of 0.4 % versus 1.9 %, and a 47 % torque ripple reduction. It also maintains stability under doubled inertia, where PI fails. The inverter achieves THD below 4.5 % and reduces the switch count by 66 %, confirming the system's efficiency, robustness, and suitability for compact, high-performance applications.

Conflict of interest. The authors declare that they have no conflicts of interest.

REFERENCES

- *I.* Park H., Kim T., Suh Y. Fault-Tolerant Control Methods for Reduced Torque Ripple of Multiphase BLDC Motor Drive System Under Open-Circuit Faults. *IEEE Transactions on Industry Applications*, 2022, vol. 58, no. 6, pp. 7275-7285. doi: https://doi.org/10.1109/TIA.2022.3191633.
- **2.** Bhuvaneswari G., Nagaraju. Multi-Level Inverters A Comparative Study. *IETE Journal of Research*, 2005, vol. 51, no. 2, pp. 141-153. doi: https://doi.org/10.1080/03772063.2005.11416389.
- 3. Nageswar Rao B., Suresh Y., Aditya K., Naik B.S., Karunakaran E. Design and implementation of novel multilevel inverter with full DC-utilization. *International Journal of Electronics*, 2025, vol. 112, no. 6, pp. 1212-1231. doi: https://doi.org/10.1080/00207217.2024.2370904.
- 4. Gopinath B., Suresh S., Jayabaskaran G., Geetha M. Renewable energy resource integrated multilevel inverter using evolutionary algorithms. *Automatika*, 2024, vol. 65, no. 3, pp. 1061-1078. doi: https://doi.org/10.1080/00051144.2024.2329494.
- 5. Sagvand F., Siahbalaee J., Koochaki A. An Asymmetrical 19-Level Inverter with a Reduced Number of Switches and Capacitors. *Electronics*, 2023, vol. 12, no. 2, art. no. 338. doi: https://doi.org/10.3390/electronics12020338.
- 6. EL Magri A., Lajouad R., Kissaoui M., Chakir M., Bouattane O., Chakir F. Design and analysis of a new multilevel inverter topology with a reduced number of switches and controlled by PDPWM technique. *International Journal of Electrical and Computer Engineering Systems*, 2023, vol. 14, no. 5, pp. 593-600. doi: https://doi.org/10.32985/ijeces.14.5.11.
- 7. Kakar S., Ayob S.B.M., Iqbal A., Nordin N.M., Arif M.S.B., Gore S. New Asymmetrical Modular Multilevel Inverter Topology With Reduced Number of Switches. *IEEE Access*,

- 2021, no. 9, pp. 27627-27637. doi: https://doi.org/10.1109/ACCESS.2021.3057554.
- 8. Djafer L., Taleb R., Mehedi F. Dspace implementation of real-time selective harmonics elimination technique using modified carrier on three phase inverter. *Electrical Engineering & Electromechanics*, 2024, no. 5, pp. 28-33. doi: https://doi.org/10.20998/2074-272X.2024.5.04.
- **9.** Ebrahimi F., Wndarko N.A., Gunawan A.I. Wild horse optimization algorithm implementation in 7-level packed U-cell multilevel inverter to mitigate total harmonic distortion. *Electrical Engineering & Electromechanics*, 2024, no. 5, pp. 34-40. doi: https://doi.org/10.20998/2074-272X.2024.5.05.
- 10. Nouaoui T., Dendouga A., Bendaikha A. Speed control of PMSM using a fuzzy logic controller with deformed MFS tuned by a novel hybrid meta-heuristic algorithm. *Electrical Engineering*, 2024, vol. 106, no. 6, pp. 6927-6939. doi: https://doi.org/10.1007/s00202-024-02404-w.
- 11. Thakre K., Mohanty K.B., Kommukuri V.S., Chatterjee A., Nigam P., Gupta S.K. Modified cascaded multilevel inverter for renewable energy systems with less number of unidirectional switches. *Energy Reports*, 2022, no. 8, pp. 5296-5304. doi: https://doi.org/10.1016/j.egyr.2022.03.167.
- 12. Antar R.K., Hussein T.A., Abdullah A.M. Design and implementation of reduced number of switches for new multilevel inverter topology without zero-level state. International Journal of Power Electronics and Drive Systems (IJPEDS), 2022, vol. 13, no. 1, pp. 401-410. doi: https://doi.org/10.11591/ijpeds.v13.i1.pp401-410.
- 13. Fnaiech M.A., Betin F., Capolino G.-A., Fnaiech F. Fuzzy Logic and Sliding-Mode Controls Applied to Six-Phase Induction Machine With Open Phases. *IEEE Transactions on Industrial Electronics*, 2010, vol. 57, no. 1, pp. 354-364. doi: https://doi.org/10.1109/TIE.2009.2034285.
- 14. Hadjidj N., Benbrahim M., Ounnas D., Mouss L.H. Global maximum power point tracking method for photovoltaic systems using Takagi-Sugeno fuzzy models and ANFIS approach. *Electrical Engineering & Electromechanics*, 2025, no. 2, pp. 31-38. doi: https://doi.org/10.20998/2074-272X.2025.2.05.
- *15.* Ali A.R., Antar R.K., Abdulghafoor A.G.A. Harmonics mitigation technique for asymmetrical multilevel inverter fed by photovoltaic sources. *Bulletin of Electrical Engineering and Informatics*, 2024, vol. 13, no. 2, pp. 865-873. doi: https://doi.org/10.11591/eei.v13i2.6607.
- **16.** Li Z., Jiang D., Sun W. Zero Common-Mode Voltage Overmodulation Strategy for Flying Capacitor Three-Level Inverter With Capacitor Voltage Control. *IEEE Journal of Emerging and Selected Topics in Power Electronics*, 2025, vol. 13, no. 5, pp. 6575-6587. doi: https://doi.org/10.1109/JESTPE.2025.3589774.
- 17. Memon M.A., Siddique M.D., Mekhilef S., Mubin M. Asynchronous Particle Swarm Optimization-Genetic Algorithm (APSO-GA) Based Selective Harmonic Elimination in a Cascaded H-Bridge Multilevel Inverter. IEEE Transactions on Industrial Electronics, 2022, vol. 69, no. 2, pp. 1477-1487. doi: https://doi.org/10.1109/TIE.2021.3060645.
- 18. Sadoughi M., Pourdadashnia A., Farhadi-Kangarlu M., Galvani S. PSO-Optimized SHE-PWM Technique in a Cascaded H-Bridge Multilevel Inverter for Variable Output Voltage Applications. *IEEE Transactions on Power Electronics*, 2022, vol. 37, no. 7, pp. 8065-8075. doi: https://doi.org/10.1109/TPEL.2022.3146825.

- 19. Jahan H.K., Abapour M., Zare K., Hosseini S.H., Blaabjerg F., Yang Y. A Multilevel Inverter With Minimized Components Featuring Self-Balancing and Boosting Capabilities for PV Applications. IEEE Journal of Emerging and Selected Topics in Power Electronics, 2023, vol. 11, no. 1, pp. 1169-1178. doi: https://doi.org/10.1109/JESTPE.2019.2922415.
- 20. Foti S., Scimone T., Oteri A., Scelba G., Testa A. A Reduced Switch Count, Self-Balanced, 13-Level Inverter Based on a Dual T-Type Configuration. *IEEE Transactions on Power Electronics*, 2023, vol. 38, no. 9, pp. 11010-11022. doi: https://doi.org/10.1109/TPEL.2023.3281679.
- 21. Benkahla M., Taleb R., Boudjema Z. A new robust control using adaptive fuzzy sliding mode control for a DFIG supplied by a 19-level inverter with less number of switches. *Electrical Engineering & Electromechanics*, 2018, no. 4, pp. 11-19. doi: https://doi.org/10.20998/2074-272X.2018.4.02.
- 22. Rodriguez J., Franquelo L.G., Kouro S., Leon J.I., Portillo R.C., Prats M.A.M., Perez M.A. Multilevel Converters: An Enabling Technology for High-Power Applications. *Proceedings of the IEEE*, 2009, vol. 97, no. 11, pp. 1786-1817. doi: https://doi.org/10.1109/JPROC.2009.2030235.
- 23. Song-Manguelle J., Mariethoz S., Veenstra M., Rufer A. A generalized design principle of a uniform step asymmetrical multilevel converter for high power conversion. *European Conference on Power Electronics and Applications (EPE'01)*, 2001, Graz, Austria.
- 24. Srinivasan G.K., Rivera M., Loganathan V., Ravikumar D., Mohan B. Trends and Challenges in Multi-Level Inverter with Reduced Switches. *Electronics*, 2021, vol. 10, no. 4, art. no. 368. doi: https://doi.org/10.3390/electronics10040368.
- 25. Bessaad T., Taleb R., Chabni F., Iqbal A. Fuzzy adaptive control of a multimachine system with single inverter supply. *International Transactions on Electrical Energy Systems*, 2019, vol. 29, no. 10, art. no. e12070. doi: https://doi.org/10.1002/2050-7038.12070.
- **26.** Ayada A., Guiza D., Ounnas D., Tidjani N. Design and control of a DC-DC buck converter using discrete Takagi-Sugeno fuzzy models. *Electrical Engineering & Electromechanics*, 2025, no. 3, pp. 53-58. doi: https://doi.org/10.20998/2074-272X.2025.3.08.

Received 20.05.2025 Accepted 06.07.2025 Published 02.11.2025

T. Bessaad ¹, Associate Professor,

A. Benbouali¹, Associate Professor,

K. Khelifi Otmane², Associate Professor,

R. Taleb¹, Professor,

H. Sahraoui¹, Associate Professor,

A. Iqbal³, Professor,

¹ Electrical Engineering Department, Faculty of Technology, Laboratoire Génie Electrique et Energies Renouvelables (LGEER), Hassiba Benbouali University, Chlef, Algeria,

e-mail: t.bessaad@univ-chlef.dz (Corresponding Author).

² Automatic and Electrotechnical Department.

Saad Dahlab University - Blida 1, Blida, Algeria,

³ Electrical Engineering Department,

Qatar University, Doha, Qatar.

How to cite this article:

Bessaad T., Benbouali A., Khelifi Otmane K., Taleb R., Sahraoui H., Iqbal A. Inverter fuzzy speed control of multi-machine system series-connected fed by a single five-phase an asymmetrical 19-level inverter with less number of switches. *Electrical Engineering & Electromechanics*, 2025, no. 6, pp. 8-14. doi: https://doi.org/10.20998/2074-272X.2025.6.02

B. Bouhadouza, F. Sadaoui

Optimal power flow analysis under photovoltaic and wind power uncertainties using the blood-sucking leech optimizer

Introduction. Optimal power flow (OPF) is a fundamental task in modern power systems, aiming to ensure cost-effective generation dispatch and efficient energy distribution. The increasing integration of renewable energy sources such as photovoltaic (PV) and wind turbines (WT), alongside conventional thermal units, introduces significant variability and uncertainty into system operations. Problem. The OPF problem is nonlinear, constrained by complex technical limits, and further complicated by the stochastic nature of PV and WT power generation. Efficiently addressing these uncertainties while maintaining system optimality remains a major challenge. The goal of this study is to solve the OPF problem in power networks that integrate PV and WT systems, while accounting for the uncertainty in their power outputs. Methodology. The stochastic behavior of PV and WT units is modeled using probability distribution functions. A novel bio-inspired metaheuristic, the Blood-Sucking Leech Optimizer (BSLO), is proposed and benchmarked against two well-established algorithms: Particle Swarm Optimization (PSO) and Grey Wolf Optimizer (GWO). Simulations are conducted on both the IEEE 30-bus test system and a real Algerian transmission network. Results. The BSLO algorithm consistently outperforms PSO and GWO in minimizing generation cost, power losses, and voltage deviation across all tested scenarios. Scientific novelty. This work considers both single and multi-objective OPF formulations, whereas most previous studies focus solely on single-objective approaches. It integrates renewable generation uncertainty through probabilistic modeling and introduces a novel metaheuristic (BSLO). Validation on a real Algerian power grid confirms the method's robustness and practical relevance. Practical value. The results confirm the BSLO algorithm as a promising and effective tool for solving complex, renewable-integrated OPF problems in real-world power systems, contributing to more reliable, economical, and flexible grid operation. References 48, tables 13, figures 17.

Key words: blood-sucking leech optimizer, optimal power flow, stochastic renewable energy sources, power systems.

Вступ. Оптимальний розподіл потужності (OPF) ϵ фундаментальним завданням у сучасних енергосистемах, спрямованим на забезпечення економічно ефективного розподілу та генерації енергії. Зростаюча інтеграція відновлюваних джерел енергії, таких як фотоелектричні (PV) та вітрові турбіни (WT), поряд з традиційними тепловими установками, вносить значну мінливість та невизначеність у роботу системи. **Проблема**. Завдання OPF ϵ нелінійним зі складними технічними обмеженнями та додатково ускладненим стохастичною природою генерації електроенергії РV та WT установками. Ефективне вирішення ших невизначеностей за збереження оптимальності системи залишається серйозною проблемою. **Метою** роботи є вирішення завдання *OPF* в енергомережах з інтегрованими PV та WT системами з урахуванням невизначеності їхньої вихідної потужності. Методика. Стохастична поведінка PV та WT установок моделюється з використанням функцій розподілу ймовірностей. Запропоновано новий біоінспірований метаевристичний алгоритм на основі поведінки п'явки (BSLO), який порівнюється з двома алгоритмами, що добре зарекомендували себе: метод рою частинок (PSO) і метод сірого вовка (GWO). Моделювання проводилося як у тестовій системі IEEE з 30 шинами, так і у реальній алжирській мережі електропередачі. Результати. Алгоритм BSLO стабільно перевершує PSO та GWO щодо мінімізації вартості генерації, втрат потужності та відхилень напруги у всіх протестованих сценаріях. Наукова новизна. У цій роботі розглядаються як однокритеріальні, так і багатокритеріальні формулювання ОРГ, тоді як більшість попередніх досліджень фокусувалися виключно на однокритеріальних підходах. Це враховує невизначеність генерації відновлюваних джерел енергії за допомогою імовірнісного моделювання і представляє новий метаевристичний алгоритм (BSLO). Перевірка на реальній алжирській енергосистемі підтверджує надійність та практичну значущість методу. **Практична значимість**. Результати підтверджують, що алгоритм BSLO є перспективним та ефективним інструментом для вирішення складних завдань ОРГ, інтегрованих з відновлюваними джерелами енергії, у реальних енергосистемах, сприяючи більш надійній, економічній та гнучкішій роботі мережі. Бібл. 48, табл. 13, рис. 17.

Ключові слова: оптимізатор на основі поведінки п'явки, оптимальний розподіл потужності, стохастичні відновлювані джерела енергії, енергетичні системи.

Introduction. Power flow analysis is the essential tool used to assess the performance of electrical networks. It focuses on several key parameters, including voltage profiles, line power flows, the balance between generation and load powers, and losses. In contrast, optimal power flow (OPF) analysis plays a critical role in the design and operational planning of electrical grids. OPF helps identify potential design weaknesses, improves the reliability of energy supply, and ensures efficient system operation [1–3]. The main goal of OPF is to define the best set of decision variables that optimize a predefined objective function. One of its most common applications is the economic dispatch of power supply, aiming to minimize the overall generation cost and satisfy operational and safety constraints [4–10].

Conventionally, power generation has relied heavily on fossil fuel-based thermal units. However, the integration of photovoltaic (PV) and wind turbines (WT) generators offers considerable benefits, reduced greenhouse gas emissions and decreased dependence on fossil fuels [11, 12]. Despite these advantages, renewable energy sources introduce new challenges due to their power uncertainty. Indeed, the power generation of PV and WT systems is highly dependent on changing weather conditions, specifically wind speed and solar irradiance. Therefore, it is essential to address the OPF problem while considering the stochastic nature of renewable energy generation to maintain grid stability and achieve economic efficiency [13, 14].

Traditional methods for solving OPF problems, such as the Newton-based method, linear and nonlinear programming, and others [15–20], often struggle to converge to the global optimum. This limitation stems from the highly nonlinear, non-convex, and complex form of the power system equations, and the presence of multiple operational constraints. Consequently, conventional optimization techniques may fail to provide reliable or accurate solutions for large-scale or modernized power grids. To address these challenges, researchers have

© B. Bouhadouza, F. Sadaoui

increasingly turned to advanced optimization strategies, particularly metaheuristic algorithms, which have gained significant attention in recent decades for their robustness and flexibility in handling complex and multi-objective OPF problems [21–23].

Metaheuristic algorithms, including standard, improved, and hybrid variants, are widely employed to address complex, non-linear, and high-dimensional optimization challenges in power systems, such as OPF problem, unit commitment, and renewable energy integration. These methods overcome the limitations of traditional approaches by efficiently exploring large search spaces and avoiding local optima. Standard metaheuristic algorithms are population-based and rely on stochastic search processes. Papers [24, 25] demonstrate the superiority of the Grey Wolf Optimizer (GWO) and Hamiltonian methods, respectively, in reducing power losses in electrical networks, compared to Particle Swarm Optimization (PSO) and Genetic Algorithms (GA). In [26], the author applies GWO to solve the OPF problem for different test systems, achieving lower generation costs compared to those obtained with GA and PSO. The authors in [27] introduce Differential Evolution (DE) to minimize cost, emissions, and real power losses in IEEE 30 and 118 bus systems, demonstrating improved performance over conventional methods.

The improved and hybrid methods are enhanced versions of standard metaheuristic algorithms, often combining 2 or more techniques to leverage their respective strengths. The authors in [28] improve the cuckoo optimization algorithm by incorporating a Gaussian mixture model, which improves convergence, accuracy, and robustness in systems with solar and wind sources. A stochastic optimization framework is presented in [29], combining probabilistic modeling with mathematical programming to handle renewable energy uncertainties and maintain system stability. In [30], a DE variant enhanced with fitness-distance balance adaptive guidance shows superior convergence efficiency. The paper [31] proposes a hybrid of the GWO and the crisscross search algorithm, which outperforms PSO, GA and DE algorithms.

The **goal** of the paper is to solve the OPF problem in power networks that integrate PV and WT systems; while accounting for the uncertainty in their power outputs. This uncertainty is modeled using probability distribution function (PDF) and the Monte Carlo simulation. 3 single-objective functions are considered: generation cost, active power losses and voltage deviation, as well as a multi-objective function combining these single objectives. The proposed approach, based on the Blood-Sucking Leech Optimizer (BSLO) algorithm, is evaluated on the standard IEEE 30-bus test system and in a real South-East Algerian Network (SEAN). The effectiveness of BSLO is assessed in terms of convergence characteristics, optimal solutions, and statistical indicators, and is compared to that of the PSO and GWO algorithms.

Problem formulation. The OPF problem consists in determining the optimal control variables that optimize an objective function and satisfy the system's constraints, and is formulated as follows:

$$\min F(x,u); \tag{1}$$

$$\begin{cases} g(x,u) = 0; \\ h(x,u) \le 0, \end{cases}$$
 (2)

where F is the OPF objective function; g, h are the equality and inequality constrains of the system.

The vector *x* contains all state variables, given by the following:

$$x = [P_{Th_1}, V_{L_1}, ..., V_{L_{NPQ}}, Q_{Th_1}, ..., Q_{Th_{NTh}}, ...$$

$$...Q_{WT_1}, ..., Q_{WT_{NWT}}, Q_{PV_1}, ..., Q_{PV_{NPV}}, S_{L_1}, ..., S_{L_{NL}}],$$
(3)

where P_{Th_1} is the real power generation of the slack generator; V_L is the voltage of the load bus; S_L is the apparent power in the transmission lines; Q_{Th} , Q_{WT} , Q_{PV} correspond to the reactive power outputs of thermal units, WT and PV systems, respectively; NL, NPQ, NWT, NPV, NTh indicate the number of transmission lines, load buses, WT, PV units and thermal plants, respectively.

The control variable vector u is defined as follows:

$$u = [P_{Th_2}, ..., P_{Th_{NTh}}, P_{WT_1}, ..., P_{WT_{NWT}}, ...$$

$$...P_{PV_1}, ..., P_{PV_{NPV}}, V_{G_1}, ..., V_{G_{NG}}],$$
(4)

where P_{Th} , P_{WT} , P_{PV} are the real powers generated by thermal generators, WT, and PV units, respectively; V_G is the voltage of the generation bus; N_G is the number of generators.

Fuel cost model of thermal generators. The total fuel cost of thermal generators is modeled using the following quadratic function [12, 23]:

$$F_{C1}(P_{Th}) = \sum_{i=1}^{NTh} a_i + b_i P_{Th_i} + c_i P_{Th_i}^2 , \qquad (5)$$

where a_i , b_i , c_i are the cost coefficients of the i^{th} generator.

For thermal units equipped with multi-valve steam turbines, the fuel cost model accounts for fluctuations in the cost function caused by the valve-point effect (VPE). This effect is modeled as a sinusoidal function integrated into the basic cost function, as shown in (5), yielding the total fuel cost (\$/h) [12, 32, 33]:

$$F_{C2}(P_{Th}) = \sum_{i=1}^{NTh} a_i + b_i P_{Th_i} + c_i P_{Th_i}^2 + \left| d_i \sin(e_i (P_{Th_i}^{\min} - P_{Th_i})) \right|, (6)$$

where d_i , e_i are the VPE coefficients.

Wind and solar's direct cost. Solar PV systems and WTs operate without requiring fuel, incurring only basic maintenance and operational costs. The direct cost model for PV and WT units is represented as a linear function of the planned power energy [12, 34]:

$$DC_{WT_i} = C_{DWT_i} P_{WTs_i}; (7)$$

$$DC_{PV_i} = C_{DPV_i} P_{PVs_i} , \qquad (8)$$

where P_{PVs_i} , P_{WTs_i} are the planned powers from the i^{th} PV and WT units; C_{DPV_i} , C_{DWT_i} are the direct cost coefficients for the i^{th} PV and WT generators.

Uncertainty of WTs and PVs cost functions. Depending on the power generated by the WTs, 2 scenarios can arise. If the generated power exceeds the planned power, an overestimation cost is applied. Conversely, if the generated power is lower than the planned power, an underestimation cost is applied. The expressions for these costs for the *i*th WT are formulated as follows [12, 34]:

$$UC_{WT_{i}} = C_{UWT_{i}}(P_{WTa_{i}} - P_{WTs_{i}}) =$$

$$= C_{UWT_{i}} \int_{P_{WTs_{i}}} (P_{WT_{i}} - P_{WTs_{i}}) f_{WT}(P_{WT_{i}}) dP_{WT_{i}};$$
(9)

$$OC_{WT_{i}} = C_{OWT_{i}}(P_{WTs_{i}} - P_{WTa_{i}}) = P_{WTs_{i}}$$

$$= C_{OWT_{i}} \int_{0}^{P_{WTs_{i}}} (P_{WTs_{i}} - P_{WT_{i}}) f_{WT}(P_{WT_{i}}) dP_{WT_{i}},$$
(10)

where UC_{WT_i} , OC_{WT_i} are the underestimation and overestimation costs; C_{UWT_i} , C_{OWT_i} are the uncertainty cost coefficients; P_{WTs_i} , P_{WTa_i} , P_{WTr_i} are the scheduled, available and rated powers of the i^{th} wind unit.

For PV units, the uncertainty cost models are formulated as follows [12, 34]:

$$UC_{PV_{i}} = C_{UPV_{i}}(P_{PVa_{i}} - P_{PVS_{i}}) =$$

$$= C_{UPV_{i}} f_{PV}(P_{PVa_{i}} > P_{PVS_{i}}) [E(P_{PVa_{i}} > P_{PVS_{i}}) - P_{PVS_{i}}];$$
(11)

$$OC_{PV_i} = C_{OPV_i}(P_{PVS_i} - P_{PVa_i}) =$$

$$= C_{OPV_i} f_{PV}(P_{PVa_i} < P_{PVS_i}) [P_{PVS_i} - E(P_{PVa_i} > P_{PVS_i})],$$
(12)

where UC_{PV_i} , OC_{PV_i} are the underestimation and overestimation cost values, C_{UPV_i} , C_{OPV_i} are the uncertainty cost coefficients; P_{PVS_i} , P_{PVa_i} are the planned and available powers of the i^{th} PV unit.

Total cost function. The first objective F_1 aims to reduce the total cost, which includes the fuel cost of thermal units with VPE, as well as the costs associated with PV and WT units. The function F_1 is expressed as [35]:

$$F_{1} = \sum_{i=1}^{NTh} a_{i} + b_{i} P_{Th_{i}} + c_{i} P_{Th_{i}}^{2} + \left| d_{i} \sin(e_{i} (P_{Th_{i}}^{\min} - P_{Th_{i}})) \right| + \sum_{i=1}^{NWT} DC_{WT_{i}} + UC_{WT_{i}} + OC_{WT_{i}} + \sum_{i=1}^{NPV} DC_{PV_{i}} + UC_{PV_{i}} + OC_{PV_{i}}.$$
(13)

When the VPE is neglected, the objective function simplifies to:

$$F_{1} = \sum_{i=1}^{NTh} a_{i} + b_{i} P_{Th_{i}} + c_{i} P_{Th_{i}}^{2} + \sum_{i=1}^{NWT} DC_{WT_{i}} + UC_{WT_{i}} + OC_{WT_{i}} + \sum_{i=1}^{NPV} DC_{PV_{i}} + UC_{PV_{i}} + OC_{PV_{i}}.$$

$$(14)$$

Active power losses function. The second objective function F_2 aims to reduce the total active power losses, as formulated below [23, 36, 37]:

$$F_2 = \sum_{i=1}^{NTh} G_{ij}(n)(V_i^2 + V_j^2 - 2V_I V_J \cos \delta_{ij}), \qquad (15)$$

where $G_{ij}(n)$ is the conductance of the n^{th} branch; δ_{ij} is the voltage angle difference between buses i and j.

Voltage deviation function. The third objective function F_3 aims to reduce the voltage deviation and is expressed as follows [29, 38, 39]:

$$F_3 = \sum_{i=1}^{NPQ} |V_i - 1|. \tag{16}$$

Multi-objective function. The fourth objective function F_4 originates from a multi-objective optimization problem that simultaneously considers total cost, active power losses and voltage deviation. These criteria are aggregated into a single scalar function using predefined weighting factors. It is described as follows:

$$F_4 = F_1 + \omega_1 F_2 + \omega_2 F_3, \tag{17}$$

where the total cost component is assigned a fixed weight of 1; ω_1 =100 and ω_2 =40 are the weighting factors for active power losses and voltage deviation. These values were chosen to ensure a balanced contribution of all objectives in the scalarized function. The weighting factors used in this study are the same as those adopted in previous works where a multi-objective function is constructed by combining single objectives such as cost, loss and voltage deviation [32].

Equality constraints. The solution to the OPF problem must satisfy the equality constraints defined as follows [40, 41]:

$$P_{G_i} = P_{D_i} + V_i \sum_{j=1}^{NB} V_j (G_{ij} \cos \delta_{ij} - B_{ij} \sin \delta_{ij}); \quad (18)$$

$$Q_{G_i} = Q_{D_i} + V_i \sum_{j=1}^{NB} V_j (G_{ij} \sin \delta_{ij} - B_{ij} \cos \delta_{ij}), \quad (19)$$

where P_{G_i} , Q_{G_i} are the real and reactive powers of the i^{th} generator, including thermal, WT and PV units; P_{D_i} , Q_{D_i} are the real and reactive loads.

Inequality constraint. Operational limits on power output and voltage levels for all generators are defined as constraints:

$$P_{Th_i}^{\min} \le P_{Th_i} \le P_{Th_i}^{\max}, \quad i = 1,...,NTh ;$$
 (20)

$$P_{WT_i}^{\min} \le P_{WT_i} \le P_{WT_i}^{\max}, \quad i = 1,, NWT;$$
 (21)

$$P_{PV_i}^{\min} \le P_{PV_i} \le P_{PV_i}^{\max}, \quad i = 1,...,NPV ;$$
 (22)

$$Q_{Th_{i}}^{\min} \leq Q_{Th_{i}} \leq Q_{Th_{i}}^{\max}, i = 1,, NTh;$$
 (23)

$$Q_{WT_i}^{\min} \le Q_{WT_i} \le Q_{WT_i}^{\max}, \quad i = 1,, NWT;$$
 (24)

$$Q_{PV_i}^{\min} \le Q_{PV_i} \le Q_{PV_i}^{\max}, \quad i = 1,...., NPV;$$
 (25)

$$V_{G_i}^{\min} \le V_{G_i} \le V_{G_i}^{\max}, \quad i = 1, ..., NG.$$
 (26)

The voltage at the PQ bus must remain within the specified limits:

$$V_{L_i}^{\min} \le V_{L_i} \le V_{L_i}^{\max}, \quad i = 1, ..., NPQ.$$
 (27)

The apparent power flow in each network branch must not exceed its allowable limits.

$$S_{L_i} \le S_{L_i}^{\text{max}}, \quad i = 1,, NS_L .$$
 (28)

Mathematical modeling of WT power uncertainty. The power of a WT is affected by wind speed variability and is represented by the Weibull PDF, as expressed in the following equation [34, 42]:

$$f_{v}(v) = \left(\frac{k}{c}\right) \cdot \left(\frac{v}{c}\right)^{k-1} e^{-\left(\frac{v}{c}\right)^{k}}; \tag{29}$$

where c is the scale parameter; k is the shape parameter.

The power supplied by a WT system is modeled as follows [34, 39]:

$$P_{WT}(v) = \begin{cases} 0; & \text{if } v_{out} < v; \ v_{in} < v; \\ P_{WTr} \left(\frac{v - v_{in}}{v_r - v_{in}} \right); & \text{if } v_r \le v \le v_{out}; \\ P_{WTr}; & \text{if } v_{in} \le v \le v_r, \end{cases}$$
(30)

where v_r , v_{out} , v_{in} are the rated, cut-out and cut-in wind speeds, which are equal to 16, 25 and 3 m/s.

Mathematical modeling of PV power uncertainty. The uncertainty in solar irradiance is modeled using a lognormal PDF, as defined in [34]:

$$f_{G_{PV}}(G_{PV}) = \frac{1}{G_{PV}\sigma\sqrt{2\pi}} \exp\left[-\frac{(\ln(G_{PV}) - \mu)^2}{2\sigma^2}\right] e^{\left(-\frac{V}{c}\right)^k}, (31)$$

where σ , μ are the standard deviations and mean values.

The power supplied by the PV system can be determined using the following equation [34, 43]:

$$P_{PV}(G_{PV}) = \begin{cases} P_{PVr} \left(\frac{G_{PV}^2}{G_{std} R_C} \right); & \text{if } 0 < G_{PV} \le R_C; \\ P_{PVr} \left(\frac{G_{PV}}{G_{std}} \right); & \text{if } G_{PV} \ge R_C, \end{cases}$$
(32)

where P_{PVr} is the rated power; R_c is the irradiance constant (set to 120 W/m²); G_{std} is the standard solar irradiance.

Blood-sucking leech optimizer is a recently introduced swarm intelligence algorithm proposed in [44]. This approach draws inspiration from the feeding mechanisms of blood-sucking leeches, particularly those observed in rice farming environments, where they attach to and feed on the blood of diverse hosts, including humans. The algorithm mimics the leeches' ability to locate prey using sensory receptors that detect stimuli like water waves. The behavioral dynamics of leeches are mathematically modeled by classifying them into 2 distinct categories. The first category, referred to as directional leeches, accurately processes the stimuli emitted by their prey, allowing them to advance incrementally toward the target with each iteration. In contrast, the second category, termed directionless leeches, misinterprets these signals and consequently moves away from the prey.

Initialization phase. The population of bloodsucking leeches is initialized randomly, as described in the following equation:

$$X = \operatorname{rand}(1, D)(ub - lb) + lb, \qquad (33)$$

where X is the position of all leeches; rand is the random number in the interval [0, 1]; D is the dimension of the optimization problem; ub, lb are the upper and lower bounds.

Exploration approach of directional leeches. During the exploration phase, the N_1 directional leeches move toward their prey at an angle α determined by their response to a circular wave stimulus. As these leeches approach the prey, the length L of the green arc, illustrated in Fig. 1 [44], gradually decreases. The number N_1 is calculated using the following equation:

$$N_1 = floor \left(N \left(m + (1 - m) \left(\frac{t}{T} \right)^2 \right) \right), \tag{34}$$

where t, T are the current and maximum iterations;

N is the population size. The MATLAB function *floor* is employed to round each element to the nearest integer that is less than or equal to the original value m, which is set to 0.8, serves as the ratio parameter.

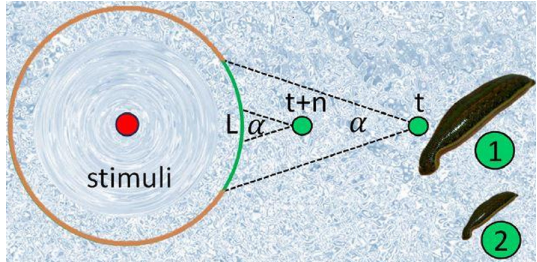


Fig. 1. Feeding mechanism of blood-sucking leeches [44]

The equations governing the exploration phase are:

$$x_{(i,j)}^{t+1} = \begin{cases} x_{(i,j)}^{t} + C \cdot x_{(i,j)}^{t} - L_{1}, & \text{if } r < a \text{ and } \left| x_{prey(j)} \right| > \left| x_{(i,j)}^{t} \right|; \\ x_{(i,j)}^{t} + C \cdot x_{(i,j)}^{t} + L_{1}, & \text{if } r < a \text{ and } \left| x_{prey(j)} \right| < \left| x_{(i,j)}^{t} \right|; \\ x_{(i,j)}^{t} + C \cdot x_{(i,j)}^{t} - L_{2}, & \text{if } r > a \text{ and } \left| x_{prey(j)} \right| > \left| x_{(i,j)}^{t} \right|; \\ x_{(i,j)}^{t} + C \cdot x_{(i,j)}^{t} + L_{2}, & \text{if } r > a \text{ and } \left| x_{prey(j)} \right| < \left| x_{(i,j)}^{t} \right|, \end{cases}$$

where a is the parameter of the BSLO method, assigned a value of 0.97. The term C represents the disturbance coefficient, which is defined as follows:

$$C = b \cdot \left(1 - \frac{t}{T}\right) \cdot 0.5 \cdot levy ; \tag{36}$$

$$levy = 0.01 \cdot \frac{\mu \cdot \sigma}{\left|\omega^{1/\beta}\right|}; \tag{37}$$

$$\sigma = \left(\frac{\Gamma(1+\beta) \cdot \sin(\pi\beta/2)}{\Gamma((1+\beta)/2) \cdot \beta \cdot 2^{(\beta-1)/2}}\right)^{1/\beta}; \quad (38)$$

$$\beta = -0.5 \cdot (t/T)^6 + (t/T)^4 + 1.5, \qquad (39)$$

where levy is the Levy flight distribution function; b, which is set to 0.001, is the parameter of the BSLO algorithm; μ , ω are the random numbers uniformly distributed within the interval [0, 1].

The lengths L_1 and L_2 are expressed as follows:

$$L_{1} = r_{1} \cdot \left| x_{prey(j)} - x_{(i,j)}^{t} \right| \cdot PD \cdot (1 - k_{1}/N); \tag{40}$$

$$L_2 = \left| x_{prey(j)} - x_{(i,k)}^t \right| \cdot PD \cdot \left(1 - r_1^2 \cdot \frac{k_1}{N} \right), \tag{41}$$

where k_1 is the random integer in the range [1, floor(N·(1 + t/T))]; k is the random integer in [1, m], while PD is the perceived distance. This parameter reflects the distance estimated by directional leeches from their prey and is calculated as:

$$PD = s \cdot r_2 \cdot (1 - t/T). \tag{42}$$

The value of *s* is given by the following expression:
$$s = \begin{cases} 8 - \left(-\left(t/T\right)^2 + 1\right) & \text{if } r < 0.5; \\ 8 - 7 \cdot \left(-\left(t/T\right)^2 + 1\right) & \text{else.} \end{cases}$$
(43)

Exploitation method Throughout this phase, the directional leeches progressively move closer to their prey, eventually reaching zones characterized by heightened stimulus intensity. The updated positions of these leeches are determined using the equations provided below:

$$x_{(i,j)}^{t+1} = \begin{cases} x_{(i,j)}^{t} + C \cdot x_{(i,j)}^{t} - L_{3}, & \text{if } r < a \text{ and } \left| x_{prey(j)} \right| > \left| x_{(i,j)}^{t} \right|; \\ x_{(i,j)}^{t} + C \cdot x_{(i,j)}^{t} + L_{3}, & \text{if } r < a \text{ and } \left| x_{prey(j)} \right| < \left| x_{(i,j)}^{t} \right|; \\ x_{(i,j)}^{t} + C \cdot x_{(i,j)}^{t} - L_{4}, & \text{if } r > a \text{ and } \left| x_{prey(j)} \right| > \left| x_{(i,j)}^{t} \right|; \\ x_{(i,j)}^{t} + C \cdot x_{(i,j)}^{t} + L_{4}, & \text{if } r > a \text{ and } \left| x_{prey(j)} \right| < \left| x_{(i,j)}^{t} \right|. \end{cases}$$

The value of b is set to 0.001 when (t<0.1T), and to 0.00001 in all other cases. This ensures that the distribution coefficient decreases progressively over successive iterations, allowing the BSLO algorithm to converge toward an optimal solution. The arc lengths L_3 and L_4 are defined as follows:

$$L_3 = \left| x_{prey(j)} - x_{(i,j)}^t \right| \cdot PD \cdot \left(1 - r_3^2 \cdot \frac{k_1}{N} \right); \quad (45)$$

$$L_4 = \left| x_{prey(j)} - x_{(i,k)}^t \right| \cdot PD \cdot \left(1 - r_3^2 \cdot \frac{k_1}{N} \right), \quad (46)$$

where the variables r, r_1 , r_2 and r_3 are the random numbers within the range [-1, 1].

Strategies transitioning between exploration and exploitation phases. The perceived distance PD acts as a critical decision-making parameter for directional leeches, facilitating their transition between the exploration and exploitation phases. $|PD| \ge 1$, a significant portion of the leeches are located at a distance from the prey, indicating that the BSLO algorithm is operating in the exploration phase. On the other hand, |PD| < 1, the leeches converge toward the prey, showing that the algorithm has entered the exploitation phase.

Search way of directionless leeches. The N_2 directionless leeches, calculated as $N_2 = N - N_1$, incorrectly respond to stimuli and move away from the target. Over successive iterations, their population size steadily diminishes, and their updated positions are determined as:

$$s = \begin{cases} \frac{t}{T} \cdot \left| x_{prey(j)} - x_{(i,j)}^t \right| \cdot 0.5 \cdot levy \cdot x_{(i,j)}^t, & \text{if } r < 0; \\ \frac{t}{T} \cdot \left| x_{prey(j)} - x_{(i,j)}^t \right| \cdot 0.5 \cdot levy \cdot x_{prey(j)}^t, & \text{else.} \end{cases}$$
(47)

Re-tracking approach. Following multiple iterations t_1 and after undergoing various phases of exploitation and exploration, certain leeches successfully located their prey (humans) and fed on their blood. Subsequently, the humans removed these leeches by returning them to the rice field. The updated positions of these leeches are mathematically expressed as follows:

$$X_i = \text{rand}(1, D) \cdot (ub - lb) + lb;$$

if $t > t_1$ and $F(X_i^t) = F(X_{prey}^{t-t_2}).$ (48)

The parameters t_1 and t_2 are assigned a value of 20. This approach ensures that the BSLO algorithm avoids becoming stuck in local optima. Figure 2 shows the flowchart of BSLO.

Simulations results. In this study, the performance and efficiency of the proposed BSLO algorithm were evaluated for solving the OPF problem in power systems integrating PV and WT systems. The tests were conducted on an IEEE 30-bus network, as described in [45], which includes 3 thermal generators at buses 1, 2, 8, one PV unit at bus 13, and 2 WT units at buses 5, 11. Additionally, the cost

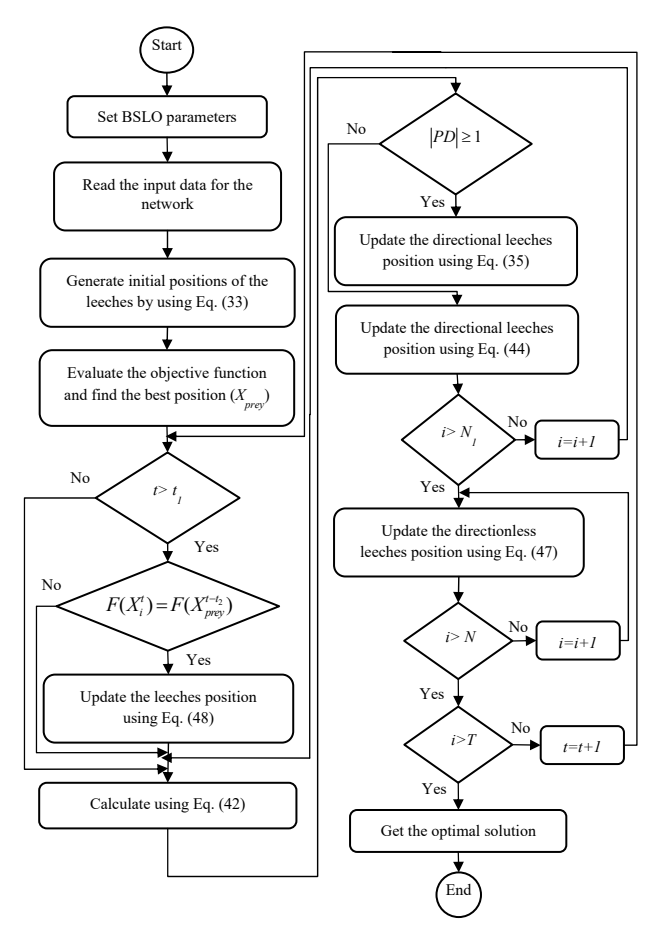


Fig. 2. BSLO flowchart

coefficients of the thermal generators, PV and WT units are detailed in [12, 29]. The second power system analyzed was the SEAN [46], consisting of 12 buses, 2 thermal generators, and 13 branches (including 2 transformers), with a total power demand of 297.5 MW and 39 MVAr. To assess the impact of renewable energy integration in this real network, a PV unit was incorporated at bus 8. Table 1 summarizes the main characteristics of the studied networks.

Table 1 Characteristics of the studied power systems

enarations of the station power systems						
Item	IEEE 3	0-bus network	SEAN system			
Helli	Quantity	Details	Quantity	Details		
Branches	41	[29]	13	[46]		
Buses	30	[29]	12	[46]		
Thermal units	3	buses: 1, 2, 8	2	buses: 1, 2		
PV units	1	bus: 13	1	bus: 8		
WT units	2	buses: 5, 11	_	_		
Slack bus	1	bus: 1	bus: 1 1			
Control variables	11	Real power at the PV buses and the voltage at the generator buses	5	Real power at the PV buses and the voltage at the generator buses		
Rated power loads	_	283.4 MW, 126.2 MVAr	_	297.5 MW, 39 MVAr		
PQ bus	24	[0.95-1.05] p.u.	8	[0.9–1.1] p.u.		

Power flow analysis was performed using the MATPOWER [45]. The proposed BSLO algorithm was compared with PSO [47] and GWO [48]. To ensure a robust and consistent evaluation, 20 independent trial runs were conducted for all test cases. The population size (*N*=50) and the maximum number of iterations (*T*=300) were kept constant across all 3 optimization methods: BSLO, GWO and PSO.

The uncertainties in the power generated by the PV and WT units were considered in our study. The Monte Carlo simulation method was employed to generate 8000 values for both irradiation and wind speed. Tables 2, 3 present the cost coefficients of the thermal generators and the PV unit for the SEAN system.

Cost coefficients of thermal units for the SEAN system

Gen	Bus	а	b	c			
1	1	0	2.5	0.017			
2	2	0	2.5	0.017			

Table 3

Cost coefficients of PV units for the SEAN system

			,
Bus	C_{DPV}	OC_{PV}	UC_{PV}
8	1.6	3	1.5

Table 4 presents the Weibull PDF parameters of the WT units for the IEEE 30-bus network, while Table 5 reports the lognormal PDF parameters of the PV units for the IEEE 30-bus and SEAN systems.

Table 4

Weibull PDF parameters of WT units

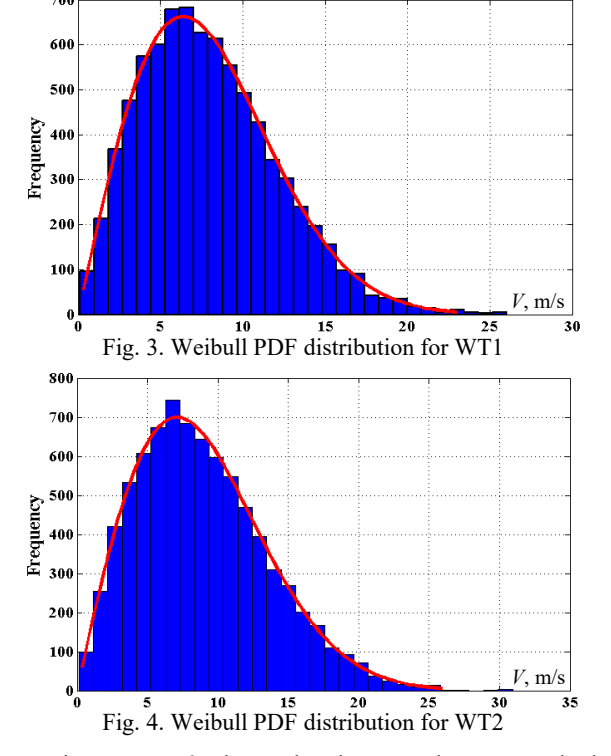
	r en reconstruction of the second						
	IEEE 30-bus network						
Wind No. of Rated power Weibull PDF							
farm	turbines	P_{WTr} , MW	parameters				
WT1	25	75	c = 9, k = 2				
WT2	20	60	c = 10, k = 2				

Table 5

Lognormal PDF parameters of the PV units

Network	Rated power P_{PVr} , MW	Lognormal PDF parameters
IEEE30-bus	50 (bus 13)	$\mu = 6, \sigma = 0.6$
SEAN system	100 (bus 8)	$\mu = 6, \sigma = 0.6$

Figures 3, 4 show the Weibull fitting and the wind speed frequency distribution for the wind power plants that replaced thermal generators at buses 5 (WT1) and 11 (WT2) in the IEEE 30-bus network. These results were obtained after performing 8000 Monte Carlo simulations.



Figures 5, 6 show the lognormal PDF and the irradiance frequency distribution obtained from Monte Carlo

simulations with 8000 iterations. These results correspond to the PV unit installed at bus 13, which replaces the thermal generator in the IEEE 30-bus system, and the additional PV unit integrated at bus 8 of the SEAN system.

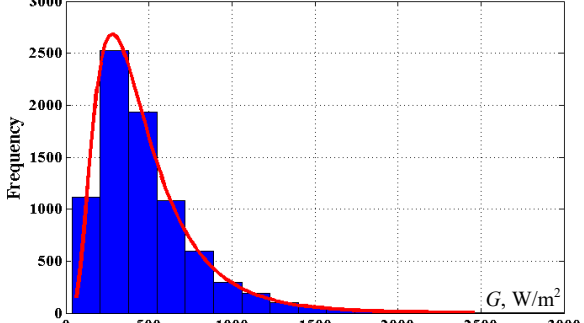
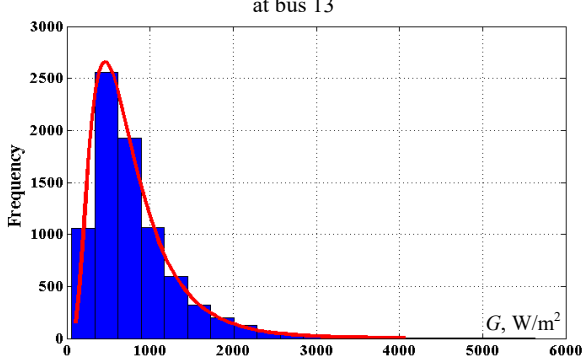


Fig. 5. Lognormal PDF for the solar PV in the IEEE 30-bus system at bus 13



0 1000 2000 3000 4000 5000 6000 Fig. 6. Lognormal PDF for the solar PV in the SEAN system at bus 8

Figures 7, 8 illustrate the stochastic output power of the PV units in each of the power systems under study. This distribution is used to calculate the overestimation and underestimation costs of the solar PV units based on their scheduled power output.

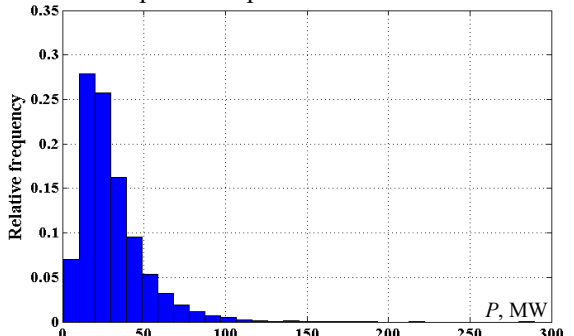


Fig. 7. Real power distribution of the PV unit in the IEEE 30-bus network at bus 13

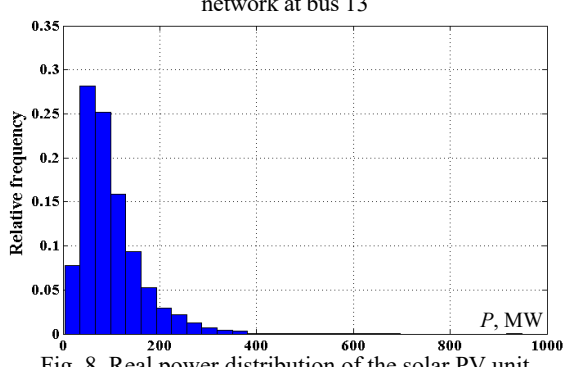


Fig. 8. Real power distribution of the solar PV unit in the SEAN system at bus 8

Test results of the IEEE30-bus system. Total cost minimizing. The first case study aims to reduce the total

cost function (F_1) with VPE as signaled in (13), and includes wind, solar and conventional power generation. The direct costs of wind and solar energy are calculated using (7), (8). Additionally, the underestimation and overestimation costs for wind and solar energy are determined using (9), (11) and (10), (12), respectively.

Table 6 presents the optimal results for the decision variables, reactive power of generators, total generation cost, power losses and total voltage deviation obtained using the BSLO, GWO and PSO algorithms. The table also includes the mean, standard deviation (Std) and worst value of the total generation cost. Additionally, the minimum and maximum values of the real and reactive power of the generators, as well as the voltage amplitude, are provided in Table 6 and are identical across all scenarios considered for the IEEE 30-bus system.

Table 6 Simulation results for total cost reduction

Simulation	Simulation results for total cost reduction							
Item	min	max	PSO	GWO	BSLO			
$P_{\mathrm{Th1}},\mathrm{MW}$	50	140	76.7121	71.6108	64.2158			
P_{Th2} , MW	20	80	35.8849	37.87	38.7185			
$P_{\mathrm{Th3}},\mathrm{MW}$	10	35	24.6507	33.1131	35			
P_{WTs1} , MW	0	75	68.5834	66.3579	68.7485			
P_{WTs2} , MW	0	60	42.4412	41.7435	44.9998			
$P_{\text{PVs1}}, \text{MW}$	0	50	38.3328	35.6942	34.442			
V_1 , p.u.	0.95	1.1	1.0239	1.0277	1.0268			
V_2 , p.u.	0.95	1.1	1.0154	1.0199	1.0198			
V_5 , p.u.	0.95	1.1	0.9973	1.0037	1.0076			
V_8 , p.u.	0.95	1.1	0.9982	1.0062	1.0077			
V ₁₁ , p.u.	0.95	1.1	1.0082	1.0358	1.0234			
V ₁₃ , p.u.	0.95	1.1	1.0307	1.0167	1.0166			
Q_{Th1} , MVAr	-20	150	1.2899	0.7484	0.8544			
Q_{Th2} , MVAr	-20	60	20.6716	18.7892	16.13			
Q_{Th3} , MVAr	-15	40	38.7294	39.4339	40			
Q_{WTs1} , MVAr	-30	35	21.3278	22.7235	25.4271			
Q_{WTs2} , MVAr	-10	30	1.044	8.1244	7.0903			
Q_{PVs1} , MVAr	-20	25	4.8243	-3.2843	-3.2947			
Total cost, \$/h, best	_	_	785.4689	785.8805	781.22			
P_{Loss} , MW	_	_	5.9874	6.4032	5.798			
VD, p.u.	_	_	0.5054	0.4957	0.7169			
Mean	_	_	796.4208	806.673	781.5035			
Worst	_	_	816.4433	837.7390	782.1341			
Std	_	_	7.2581	16.9356	0.2328			

The results show that the BSLO algorithm achieves the lowest total generation cost among the compared methods, with a value of 781.22 \$/h, compared to 785.4689 \$/h for PSO and 785.8805 \$/h for GWO. Moreover, the standard deviation for BSLO is notably low (0.2328) compared to PSO (7.2581) and GWO (16.9356), indicating that the results obtained by BSLO exhibit minimal dispersion across the 20 simulations conducted. This demonstrates the algorithm's stable convergence and enhanced reliability. Furthermore, as shown in Fig. 9, the BSLO algorithm converges to the optimal solution in less iteration, highlighting its efficiency and fast convergence behavior.

Total active power losses minimizing. This case study focuses on minimizing total active transmission losses in the IEEE 30-bus system using the BSLO, GWO and PSO algorithms. As shown in Table 7, the BSLO algorithm achieves the lowest power losses with a value of 2.0369 MW, compared to 2.5869 MW for PSO and 2.7671 MW for GWO, and demonstrates strong performance in terms of both the mean and standard deviation.

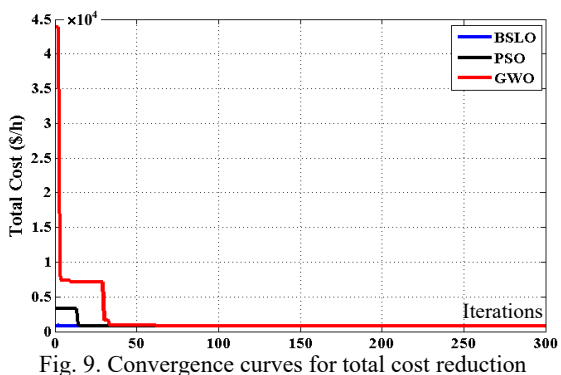


Table 7
Simulation results for total active power losses reduction

Item	PSO	GWO	BSLO
$P_{\mathrm{Th1}},\mathrm{MW}$	56.7554	76.0841	50
P_{Th2} , MW	43.7425	33.4933	29.4619
$P_{\mathrm{Th3}},\mathrm{MW}$	32.1789	28.1790	35
P_{WTs1} , MW	71.2795	74.9682	75
P_{WTs2} , MW	55.484	49.0042	59.9997
$P_{\mathrm{PVs1}},\mathrm{MW}$	26.5466	24.4383	35.9753
V_1 , p.u.	1.0359	1.0398	1.0399
V_2 , p.u.	1.0264	1.0311	1.0339
V_5 , p.u.	1.016	1.02	1.0232
V_8 , p.u.	1.0102	1.0212	1.0287
<i>V</i> ₁₁ , p.u.	1.0604	1.0726	1.0684
V_{13} , p.u.	0.989	1.0485	1.048
$Q_{Th1}, MVAr$	10.4175	-0.2533	-0.3096
Q_{Th2} , MVAr	12.1398	9.9067	11.2841
Q_{Th3} , MVAr	35.8329	37.2458	39.8119
Q_{WTs1} , MVAr	27.4807	22.2697	21.3692
Q_{WTs2} , MVAr	17.319	14.1711	12.7728
Q_{PVs1} , MVAr	-14.5685	0.7956	-0.6847
Total cost, \$/h	874.3381	864.1246	879.3848
P_{Loss} , MW, best	2.5869	2.7671	2.0369
VD, p.u.	0.2398	0.6	0.6595
Mean	3.1307	3.8534	2.0654
Worst	4.4579	6.2984	2.1569
Std	0.4426	0.8314	0.0294

Figure 10 presents the convergence curves corresponding to the best results obtained with PSO, GWO and BSLO, highlighting the evolution of minimal active power line losses. It is evident that the objective function value decreases rapidly and stabilizes in fewer than 20 iterations when using the BSLO algorithm, confirming its fast convergence capability.

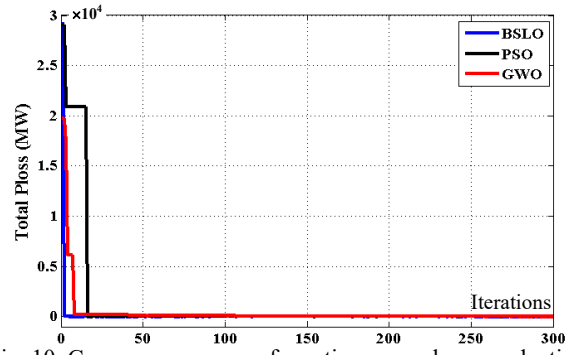


Fig. 10. Convergence curves for active power losses reduction

Load voltage deviation minimizing. This case interests on controlling the voltage magnitudes of load buses by minimizing their deviations from the reference value ($V_{ref} = 1$ p.u.), as defined in (16). Table 8 summarizes

the simulation results voltage deviation reduction, highlighting that the BSLO algorithm achieves the lowest value (0.1913 p.u.), compared to 0.208 p.u. for PSO and 0.2014 p.u. for GWO. The convergence curves of the evaluated methods are illustrated in Fig. 11. Furthermore, the BSLO algorithm converges to the global solution with a smaller number of iterations.

Table 8 Simulation results for voltage deviation reduction

Simulation results for voltage deviation reduction			
Item	PSO	GWO	BSLO
$P_{\mathrm{Th1}},\mathrm{MW}$	88.2113	119.1021	55.2959
P_{Th2} , MW	45.6265	29.9804	80
P_{Th3} , MW	27.2619	28.7075	35
P_{WTs1} , MW	70.0671	69.8552	74.4709
P_{WTs2} , MW	36.6761	25.5604	41.9836
$P_{\mathrm{PVs1}},\mathrm{MW}$	19.3226	15.0478	0
V_1 , p.u.	1.0308	1.0325	1.0256
V_2 , p.u.	1.0301	1.0303	1.0322
V_5 , p.u.	1.0098	1.0163	1.0165
V_8 , p.u.	1.0048	1.0052	1.0067
V ₁₁ , p.u.	1.0166	1.0123	1.0023
V_{13} , p.u.	1.0079	1.0157	1.0181
Q_{Th1} , MVAr	-14.4918	-19.4105	-19.9972
Q_{Th2} , MVAr	44.6989	45.4807	45.9197
Q_{Th3} , MVAr	39.2687	39.3375	40
Q_{WTs1} , MVAr	22.4846	28.859	26.2698
Q_{WTs2} , MVAr	2.058	-0.5398	-2.6237
Q_{PVs1} , MVAr	-5.1563	-2.5165	0.374
Total cost, \$/h	862.069	849.3795	958.0732
P_{Loss} , MW	3.7656	4.8534	3.3503
VD, p.u., best	0.208	0.2014	0.1913
Mean	0.2224	0.2113	0.1924
Worst	0.2422	0.2245	0.1962
Std	0.0083	0.0074	0.0011

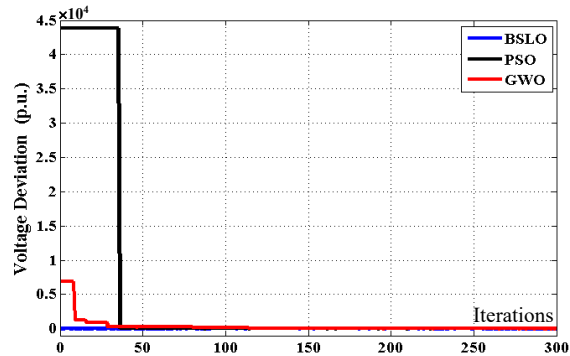


Fig. 11. Convergence curves for voltage deviation reduction

Multi-objective function minimizing. The objective is to minimize the multi-objective function defined in (17), which includes the total generation cost, active power losses and load voltage deviation. Table 9 presents the OPF solutions obtained using the BSLO, GWO and PSO algorithms. The BSLO algorithm demonstrates superior performance compared to the other methods. Moreover, the convergence curve of the objective function is illustrated in Fig. 12. The evolution of the multi-objective function using BSLO also shows the most favorable behavior among the evaluated algorithms.

The superiority of the BSLO algorithm is particularly evident in the multi-objective optimization case. Unlike PSO and GWO, which show significant variability between runs, with standard deviations of 19.5146 and 46.9889 and large gaps between worst and

best objective values (1064.8796 versus 993.1464 for PSO, and 1180.1231 versus 996.7087 for GWO, BSLO exhibits remarkable consistency. It achieves a worst-case value of 985.8281, a best-case value of 985.3818, and a very low standard deviation of 0.1058, confirming its robustness and reliability. In this case, using BSLO, the total active losses are 2.2949 MW, the voltage drop (*VD*) is 0.2252 p.u., and the generation cost is \$871.0642 \$/h.

Simulation results for multi-objective function minimization

Item	PSO	GWO	BSLO
$P_{\mathrm{Th1}},\mathrm{MW}$	60.258	76.0573	50
$P_{\mathrm{Th2}},\mathrm{MW}$	34.9418	34.4584	35.4247
P_{Th3} , MW	24.6371	23.8389	35
P_{WTs1} , MW	74.0053	72.7683	73.722
P_{WTs2} , MW	51.2131	42.651	50.3174
$P_{\mathrm{PVs1}},\mathrm{MW}$	41.0924	36.6089	41.2308
V_1 , p.u.	1.037	1.0252	1.0208
V_2 , p.u.	1.0252	1.0196	1.0151
<i>V</i> ₅ , p.u.	1.0226	1.007	1.005
V_8 , p.u.	1.01	1.0052	1.0063
<i>V</i> ₁₁ , p.u.	1.0151	1.0522	1.0365
V_{13} , p.u.	1.025	1.0095	1.0184
Q_{Th1} , MVAr	12.8347	-5.4173	0.34
Q_{Th2} , MVAr	3.6808	21.8226	13.8981
Q_{Th3} , MVAr	36.645	39.1846	40
Q_{WTs1} , MVAr	34.107	24.016	24.6231
Q_{WTs2} , MVAr	1.0662	13.8226	9.4904
Q_{PVs1} , MVAr	-1.1077	-6.3064	-2.0071
Total cost, \$/h	862.5596	850.8861	871.0642
P_{Loss} , MW	2.648	3.0731	2.2949
VD, p.u.	0.2467	0.229	0.2252
Multi-objective function F_4 , best	993.1464	996.7087	985.3818
Mean	1021.5482	1043.9233	985.4953
Worst	1064.8796	1180.1231	985.8281
Std	19.5146	46.9889	0.1058

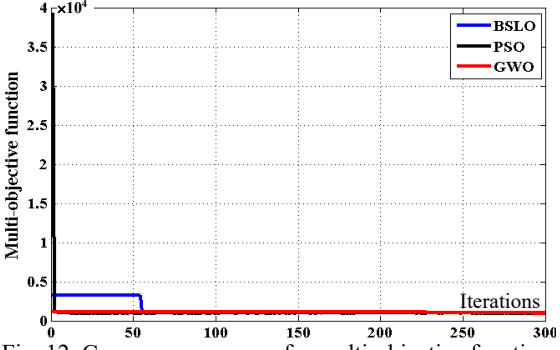
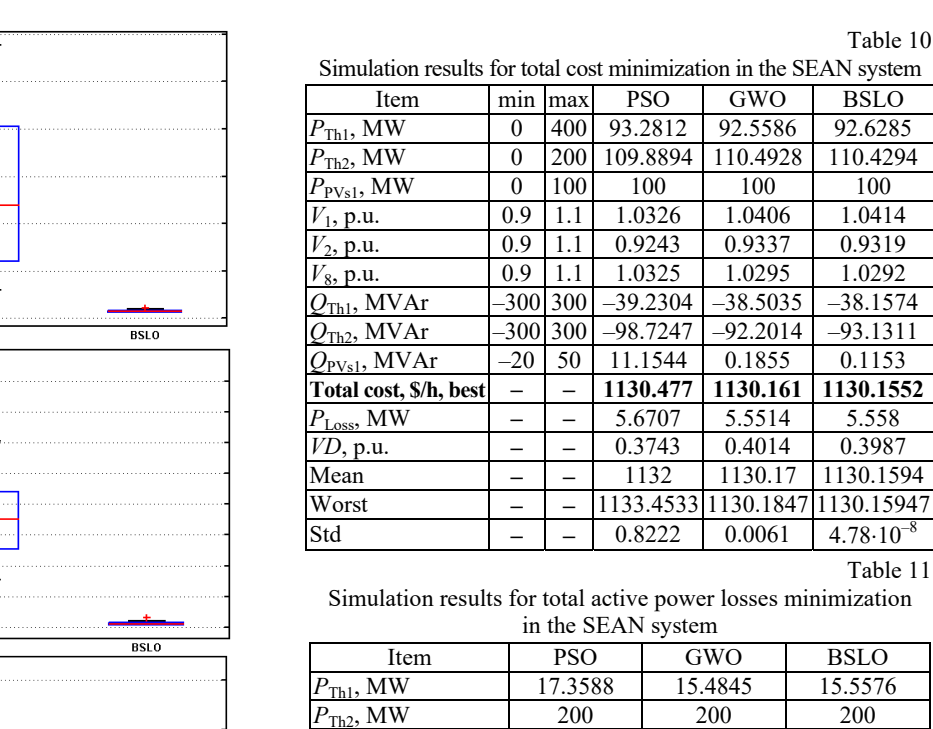


Fig. 12. Convergence curves for multi-objective function minimization

To assess the performance of the BSLO algorithm, the results of 20 independent runs conducted for each method are presented as boxplots in Fig. 13, offering a clear visual comparison of result dispersion, stability, and robustness. The analysis shows that BSLO achieves significantly lower dispersion than the other algorithms, indicating more stable convergence and greater reliability. BSLO consistently produces results that are less affected by variations in the initial decision variables. Note that each algorithm includes a population initialization phase, which is inherently random and can significantly influence the algorithm's ability to find the global optimum of the problem.



 $P_{\text{Th2}}, \overline{\text{MW}}$ $P_{\mathrm{PVs1}}, \mathrm{MW}$ 81.8412 83.7122 83.6391 V_1 , p.u. 0.9883 0.983 0.9822 0.9495 V_2 , p.u. 0.9422 0.9418 1.038 1.0321 1.0313 V_8 , p.u. 49.5131 48.2966 48.3258 $Q_{\text{Th1}}, M\text{VAr}$ $Q_{\text{Th2}}, \overline{\text{MVAr}}$ 75.7063 -75.2507 -74,4846 $Q_{\text{PVs1}}, \overline{\text{MVAr}}$ -0.6789 -0.8503 0.985 Total cost, \$/h 1446.8353 1445.6603 1445.6729 $P_{\text{Loss}}, \overline{\text{MW}}, \text{best}$ 1.6967 1.6967 1.7 VD, p.u. 0.3824 0.3284 0.3222 Mean 1.7129 1.6969 1.6967 Worst 1.697 1.69677 1.7643 0.0166 Std $6.8336 \cdot 10^{-1}$ 5.2117.10

Table 12

OPF simulation results for voltage deviation minimization in the SEAN system

Item	PSO	GWO	BSLO
$P_{\mathrm{Th1}},\mathrm{MW}$	198.3750	208.1016	212.7295
P_{Th2} , MW	74.3085	98.7613	43.0739
$P_{\mathrm{PVs1}},\mathrm{MW}$	51.4712	20.4118	72.4242
V_1 , p.u.	0.9838	0.9875	0.9898
V_2 , p.u.	0.9744	0.9749	0.9883
V_8 , p.u.	1.0015	1.0026	1.0011
Q_{Th1} , MVAr	-0.5315	6.333	9.6434
Q_{Th2} , MVAr	-26.5009	-23.7497	-13.5178
Q_{PVs1} , MVAr	8.8667	19.0264	2.8416
Total cost, \$/h	1610.6879	1820.7532	1642.4949
P_{Loss} , MW	26.6548	29.7748	30.7277
VD, p.u., best	0.01526	0.01469	0.01386
Mean	0.0202	0.0239	0.0141
Worst	0.03014	0.0398	0.01517
Std	0.004	0.0074	$2.9827 \cdot 10^{-4}$

Multi-objective function in SEAN system. The multiobjective function of the OPF problem simultaneously considers the generation cost of both thermal generators and solar PV units, the voltage profile and power losses (Fig. 17). Table 13 summarizes the values of the decision parameters, the reactive power outputs of all generators, the objective function values, and the statistical performance indicators obtained using the PSO, GWO, and BSLO algorithms.

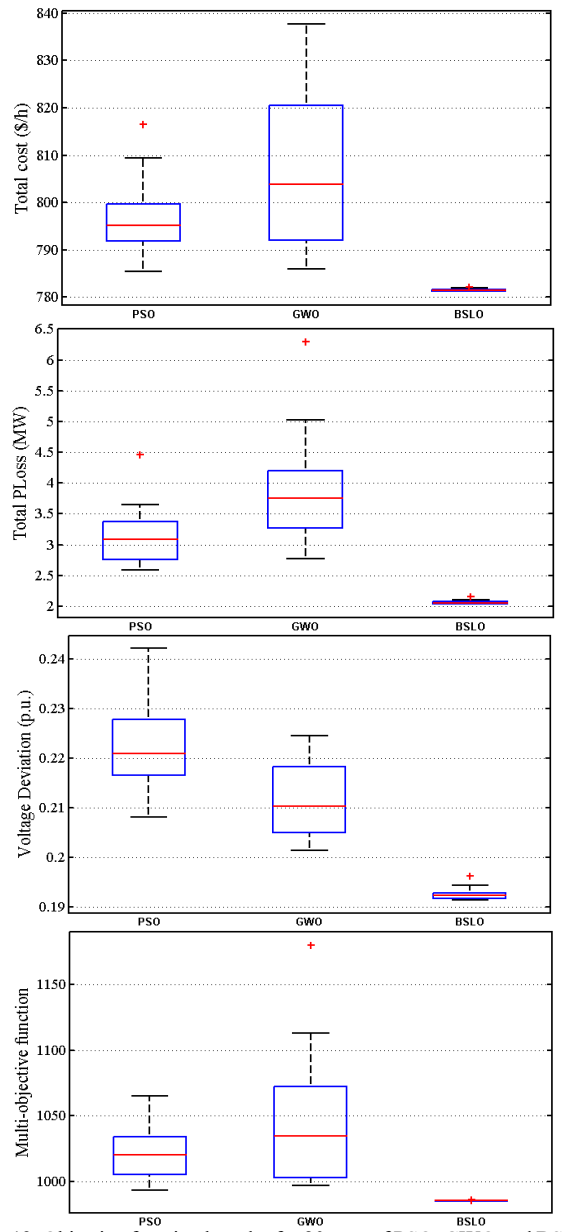
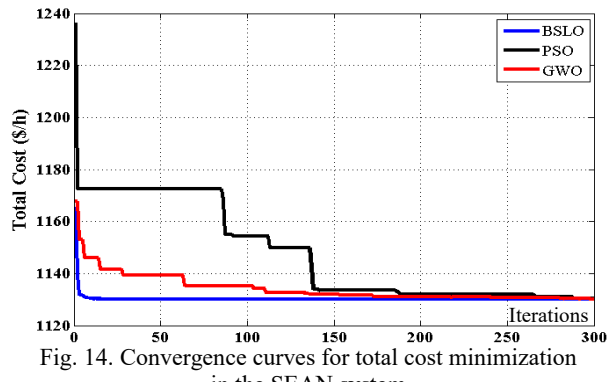


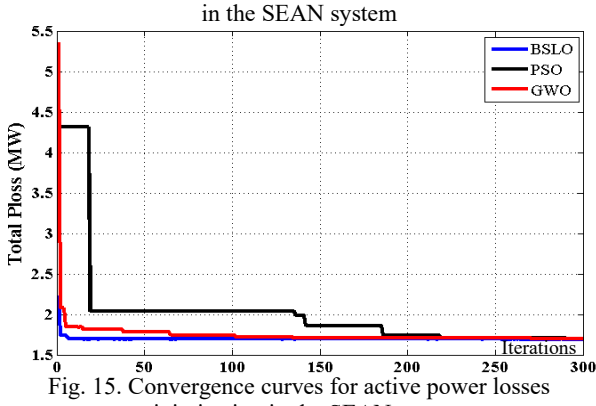
Fig. 13. Objective function boxplot for 20 runs of PSO, GWO and BSLO

Test results of the SEAN. Single objective function in SEAN system. In this section, the PSO, GWO and BSLO algorithms were applied to the real SEAN system to address 3 single objective functions: minimizing the total generation cost without VPE (case 1), minimizing total active power losses (case 2) and minimizing voltage deviation (case 3). The simulation results obtained using the different algorithms for the single objective optimization cases 1–3 are presented in Tables 10–12.

These results show that the BSLO method provides the best OPF solutions compared to the other methods. In case 1, which focuses on minimizing the total generation cost, the values obtained are 1130.477 \$/h, 1130.161 \$/h and 1130.1552 \$/h using the PSO, GWO and BSLO algorithms, respectively. In case 2, the BSLO algorithm achieves the lowest power losses at 1.6967 MW, and in case 3, it also provides the smallest voltage deviation at 0.01386 p.u. In all single objective function, the statistical performance indicators: best, mean, worst and standard deviation demonstrate that BSLO consistently outperforms both PSO and GWO. Also, the BSLO algorithm exhibits a faster convergence rate, as illustrated in Fig. 14–16.

In this case, the BSLO algorithm once again outperforms the other methods, achieving the lowest objective function value of 1333.8135.





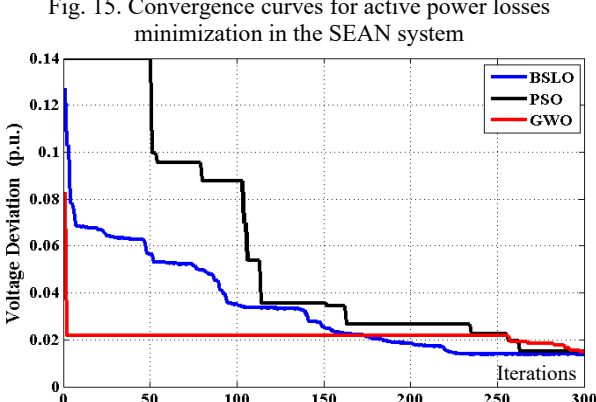


Fig. 16. Convergence curves for voltage deviation minimization in the SEAN system

Table 13 Simulation results for multi-objective function minimization in the SEAN system

in the SELL System			
Item	PSO	GWO	BSLO
$P_{\mathrm{Th1}},\mathrm{MW}$	0.5917	57.2208	57.4852
P_{Th2} , MW	141.4894	143.2943	143.0508
$P_{\mathrm{PVs1}},\mathrm{MW}$	100	100	100
V_1 , p.u.	0.9612	0.9668	0.9657
V_2 , p.u.	0.92	0.919	0.9201
V_8 , p.u.	1.001	1.0006	1.0001
Q_{Th1} , MVAr	-46.6739	-45.8008	-45.9652
Q_{Th2} , MVAr	-72.6615	-73.294	-72.2996
Q_{PVs1} , MVAr	-1.6825	-2.5963	-3.4911
Total cost, \$/h	1170.8346	1175.3552	1174.737
P_{Loss} , MW	3.1595	3.01522	3.0360
VD, p.u.	0.09741	0.1074	0.1056
Multi-objective function F ₄ , best	1334.1308	1333.8270	1333.8135
Mean	1341.4334	1333.8567	1333.8136
Worst	1360.9850	1333.9529	1333.8137
Std	7.3014	0.03114	6.0958×10 ⁻⁵

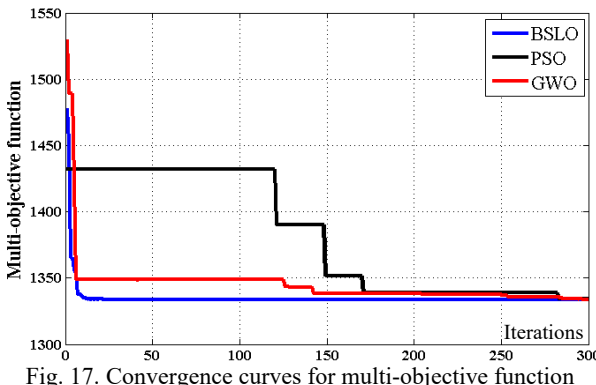


Fig. 17. Convergence curves for multi-objective function minimization in the SEAN system

In comparison to the IEEE-30 bus network, no significant difference in the best values is observed between the 3 algorithms for the various objective functions in the SEAN system. This is due to the fact that the number of decision variables is only 5 in the Algerian network, whereas it is 11 in the IEEE-30 bus network.

Conclusions. This paper presents a solution methodology for addressing the OPF problem in electrical grids integrating PV and WT generators. The inherent uncertainties of intermittent renewable energy sources are modeled using PDF and Monte Carlo simulations. To solve the OPF problem, BSLO algorithm was effectively employed, and its computational efficiency was compared against the PSO and GWO algorithms. Four distinct objective functions were considered:

- minimization of total generation costs from thermal and renewable sources;
 - reduction of active power losses;
 - voltage deviation minimization;
- a multi-objective function combining all 3 through a weighted sum.

The proposed approach was tested on the both the IEEE 30-bus test system, which includes stochastic wind and solar power units, and a real-world power system in the Southeast Algeria, incorporating the variability of PV generation. The results demonstrate that addressing the stochastic OPF problem significantly improves grid performances. Optimal integration of renewable energy sources leads to reduce the active power supplied by the thermal generators and minimizing overall generation costs. Moreover, the BSLO algorithm demonstrated superior convergence characteristics and solution quality compared to PSO and GWO algorithms across all case studies, achieving the most optimal solutions for the OPF problem. These findings highlight the effectiveness and robustness of the BSLO algorithm for solving complex stochastic OPF problems.

Conflict of interest. The authors declare that they have no conflicts of interest.

REFERENCES

- *I.* Carpentier J. Optimal power flows. *International Journal of Electrical Power & Energy Systems*, 1979, vol. 1, no. 1, pp. 3-15. doi: https://doi.org/10.1016/0142-0615(79)90026-7.
- 2. Capitanescu F., Martinez Ramos J.L., Panciatici P., Kirschen D., Marano Marcolini A., Platbrood L., Wehenkel L. State-of-the-art, challenges, and future trends in security constrained optimal power flow. *Electric Power Systems*

- Research, 2011, vol. 81, no. 8, pp. 1731-1741. doi: https://doi.org/10.1016/j.epsr.2011.04.003.
- 3. Naderi E., Narimani H., Pourakbari-Kasmaei M., Cerna F.V., Marzband M., Lehtonen M. State-of-the-Art of Optimal Active and Reactive Power Flow: A Comprehensive Review from Various Standpoints. *Processes*, 2021, vol. 9, no. 8, art. no. 1319. doi: https://doi.org/10.3390/pr9081319.
- 4. Lai L.L., Ma J.T., Yokoyama R., Zhao M. Improved genetic algorithms for optimal power flow under both normal and contingent operation states. *International Journal of Electrical Power & Energy Systems*, 1997, vol. 19, no. 5, pp. 287-292. doi: https://doi.org/10.1016/S0142-0615(96)00051-8.
- **5.** Abido M.A. Optimal power flow using particle swarm optimization. *International Journal of Electrical Power & Energy Systems*, 2002, vol. 24, no. 7, pp. 563-571. doi: https://doi.org/10.1016/S0142-0615(01)00067-9.
- **6.** Bakirtzis A.G., Biskas P.N., Zoumas C.E., Petridis V. Optimal power flow by enhanced genetic algorithm. *IEEE Transactions on Power Systems*, 2002, vol. 17, no. 2, pp. 229-236. doi: https://doi.org/10.1109/TPWRS.2002.1007886.
- 7. Roa-Sepulveda C.A., Pavez-Lazo B.J. A solution to the optimal power flow using simulated annealing. *International Journal of Electrical Power & Energy Systems*, 2003, vol. 25, no. 1, pp. 47-57. doi: https://doi.org/10.1016/S0142-0615(02)00020-0.
- 8. Somasundaram P., Kuppusamy K., Kumudini Devi R.P. Evolutionary programming based security constrained optimal power flow. *Electric Power Systems Research*, 2004, vol. 72, no. 2, pp. 137-145. doi: https://doi.org/10.1016/j.epsr.2004.02.006.
- 9. Si Tayeb A., Larouci B., Rezzak D., Houam Y., Bouzeboudja H., Bouchakour A. Application of a new hybridization to solve economic dispatch problem on an Algerian power system without or with connection to a renewable energy. *Diagnostyka*, 2021, vol. 22, no. 3, pp. 101-112. doi: https://doi.org/10.29354/diag/142060.
- 10. Marzbani F., Abdelfatah A. Economic Dispatch Optimization Strategies and Problem Formulation: A Comprehensive Review. *Energies*, 2024, vol. 17, no. 3, art. no. 550. doi: https://doi.org/10.3390/en17030550.
- 11. Sulaiman M.H., Mustaffa Z. Optimal power flow incorporating stochastic wind and solar generation by metaheuristic optimizers. *Microsystem Technologies*, 2021, vol. 27, no. 9, pp. 3263-3277. doi: https://doi.org/10.1007/s00542-020-05046-7.
- 12. Ghasemi M., Trojovský P., Trojovská E., Zare M. Gaussian bare-bones Levy circulatory system-based optimization for power flow in the presence of renewable units. Engineering Science and Technology, an International Journal, 2023, vol. 47, art. no. 101551. doi: https://doi.org/10.1016/j.jestch.2023.101551.
- 13. Naidji M., Boudour M. Stochastic multi-objective optimal reactive power dispatch considering load and renewable energy sources uncertainties: a case study of the Adrar isolated power system. *International Transactions on Electrical Energy Systems*, 2020, vol. 30, no. 6. doi: https://doi.org/10.1002/2050-7038.12374.
- 14. Kouadri R., Slimani L., Bouktir T., Musirin I. Optimal Power Flow Solution for Wind Integrated Power in presence of VSC-HVDC Using Ant Lion Optimization. *Indonesian Journal of Electrical Engineering and Computer Science*, 2018, vol. 12, no. 2, pp. 625-633. doi: https://doi.org/10.11591/ijeecs.v12.i2.pp625-633.
- 15. Wells D.W. Method for economic secure loading of a power system. Proceedings of the Institution of Electrical Engineers, 1968, vol. 115, no. 8, art. no. 1190. doi: https://doi.org/10.1049/piee.1968.0210.
- 16. Habibollahzadeh H., Luo G.-X., Semlyen A. Hydrothermal optimal power flow based on a combined linear and nonlinear programming methodology. *IEEE Transactions on Power Systems*, 1989, vol. 4, no. 2, pp. 530-537. doi: https://doi.org/10.1109/59.193826.

- 17. Ponnambalam K., Quintana V.H., Vannelli A. A fast algorithm for power system optimization problems using an interior point method. *IEEE Transactions on Power Systems*, 1992, vol. 7, no. 2, pp. 892-899. doi: https://doi.org/10.1109/59.141801.
- 18. Sun D., Ashley B., Brewer B., Hughes A., Tinney W. Optimal Power Flow By Newton Approach. *IEEE Transactions on Power Apparatus and Systems*, 1984, vol. PAS-103, no. 10, pp. 2864-2880. doi: https://doi.org/10.1109/TPAS.1984.318284. 19. Santos A., da Costa G.R.M. Optimal-power-flow solution by Newton's method applied to an augmented Lagrangian function.
- Newton's method applied to an augmented Lagrangian function. *IEE Proceedings: Generation, Transmission and Distribution*, 1995, vol. 142, no. 1, pp. 33-36. doi: https://doi.org/10.1049/ipgtd:19951586.
- 20. Nicholson H., Sterling M. Optimum Dispatch of Active and Reactive Generation by Quadratic Programming. *IEEE Transactions on Power Apparatus and Systems*, 1973, vol. PAS-92, no. 2, pp. 644-654. doi: https://doi.org/10.1109/TPAS.1973.293768.
- 21. Diab A.A.Z., Abdelhamid A.M., Sultan H.M. Comprehensive analysis of optimal power flow using recent metaheuristic algorithms. *Scientific Reports*, 2024, vol. 14, no. 1, art. no. 13422. doi: https://doi.org/10.1038/s41598-024-58565-y.
- 22. Surender Reddy S., Bijwe P.R. Efficiency improvements in meta-heuristic algorithms to solve the optimal power flow problem. *International Journal of Electrical Power & Energy Systems*, 2016, vol. 82, pp. 288-302. doi: https://doi.org/10.1016/j.ijepes.2016.03.028.
- 23. Nassef A.M., Abdelkareem M.A., Maghrabie H.M., Baroutaji A. Review of Metaheuristic Optimization Algorithms for Power Systems Problems. *Sustainability*, 2023, vol. 15, no. 12, art. no. 9434. doi: https://doi.org/10.3390/su15129434.
- 24. Abbas M., Alshehri M.A., Barnawi A.B. Potential Contribution of the Grey Wolf Optimization Algorithm in Reducing Active Power Losses in Electrical Power Systems. *Applied Sciences*, 2022, vol. 12, no. 12, art. no. 6177. doi: https://doi.org/10.3390/app12126177.
- 25. Tehzeeb-Ul-Hassan H., Tahir M.F., Mehmood K., Cheema K.M., Milyani A.H., Rasool Q. Optimization of power flow by using Hamiltonian technique. *Energy Reports*, 2020, vol. 6, pp. 2267-2275. doi: https://doi.org/10.1016/j.egyr.2020.08.017.
- **26.** Pradhan M., Roy P.K., Pal T. Grey wolf optimization applied to economic load dispatch problems. *International Journal of Electrical Power & Energy Systems*, 2016, vol. 83, pp. 325-334. doi: https://doi.org/10.1016/j.ijepes.2016.04.034.
- 27. Varadarajan M., Swarup K.S. Solving multi-objective optimal power flow using differential evolution. *IET Generation, Transmission & Distribution*, 2008, vol. 2, no. 5, pp. 720-730. doi: https://doi.org/10.1049/iet-gtd:20070457.
- 28. Alghamdi A.S., Zohdy M.A. Boosting cuckoo optimization algorithm via Gaussian mixture model for optimal power flow problem in a hybrid power system with solar and wind renewable energies. *Heliyon*, 2024, vol. 10, no. 11, art. no. e31755. doi: https://doi.org/10.1016/j.heliyon.2024.e31755.
- **29.** Biswas P.P., Suganthan P.N., Amaratunga G.A.J. Optimal power flow solutions incorporating stochastic wind and solar power. *Energy Conversion and Management*, 2017, vol. 148, pp. 1194-1207. doi: https://doi.org/10.1016/j.enconman.2017.06.071.
- *30.* Guvenc U., Duman S., Kahraman H.T., Aras S., Katı M. Fitness–Distance Balance based adaptive guided differential evolution algorithm for security-constrained optimal power flow problem incorporating renewable energy sources. *Applied Soft Computing*, 2021, vol. 108, art. no. 107421. doi: https://doi.org/10.1016/j.asoc.2021.107421.
- *31.* Meng A., Zeng C., Wang P., Chen D., Zhou T., Zheng X., Yin H. A high-performance crisscross search based grey wolf optimizer for solving optimal power flow problem. *Energy*, 2021, vol. 225, art. no. 120211. doi: https://doi.org/10.1016/j.energy.2021.120211.
- 32. Ebeed M., Abdelmotaleb M.A., Khan N.H., Jamal R., Kamel S., Hussien A.G., Zawbaa H.M., Jurado F., Sayed K. A Modified

- Artificial Hummingbird Algorithm for solving optimal power flow problem in power systems. *Energy Reports*, 2024, vol. 11, pp. 982-1005. doi: https://doi.org/10.1016/j.egyr.2023.12.053.
- 33. Mezhoud N., Ayachi B., Amarouayache M. Multi-objective optimal power flow based gray wolf optimization method. *Electrical Engineering & Electromechanics*, 2022, no. 4, pp. 57-62. doi: https://doi.org/10.20998/2074-272X.2022.4.08.
- 34. Jamal R., Khan N.H., Ebeed M., Zeinoddini-Meymand H., Shahnia F. An improved pelican optimization algorithm for solving stochastic optimal power flow problem of power systems considering uncertainty of renewable energy resources. *Results in Engineering*, 2025, vol. 26, art. no. 104553. doi: https://doi.org/10.1016/j.rineng.2025.104553.
- 35. Hassan M.H., Kamel S., Alateeq A., Alassaf A., Alsaleh I. Optimal Power Flow Analysis With Renewable Energy Resource Uncertainty: A Hybrid AEO-CGO Approach. *IEEE Access*, 2023, vol. 11, pp. 122926-122961. doi: https://doi.org/10.1109/ACCESS.2023.3328958.
- **36.** Laifa A., Ayachi B. Application of whale algorithm optimizer for unified power flow controller optimization with consideration of renewable energy sources uncertainty. *Electrical Engineering & Electromechanics*, 2023, no. 2, pp. 69-78. doi: https://doi.org/10.20998/2074-272X.2023.2.11.
- *37.* Nagarajan K., Rajagopalan A., Bajaj M., Raju V., Blazek V. Enhanced wombat optimization algorithm for multi-objective optimal power flow in renewable energy and electric vehicle integrated systems. *Results in Engineering*, 2025, vol. 25, art. no. 103671. doi: https://doi.org/10.1016/j.rineng.2024.103671.
- 38. Nassef A.M., Abdelkareem M.A., Maghrabie H.M., Baroutaji A. Review of Metaheuristic Optimization Algorithms for Power Systems Problems. *Sustainability*, 2023, vol. 15, no. 12, art. no. 9434. doi: https://doi.org/10.3390/su15129434.
- 39. Mohamed A.A., Kamel S., Hassan M.H., Domínguez-García J.L. Optimal Power Flow Incorporating Renewable Energy Sources and FACTS Devices: A Chaos Game Optimization Approach. *IEEE Access*, 2024, vol. 12, pp. 23338-23362. doi: https://doi.org/10.1109/ACCESS.2024.3363237.
- 40. Nguyen T.T., Nguyen H.D., Duong M.Q. Optimal Power Flow Solutions for Power System Considering Electric Market and Renewable Energy. *Applied Sciences*, 2023, vol. 13, no. 5, art. no. 3330. doi: https://doi.org/10.3390/app13053330.
- 41. Gurumoorthi G., Senthilkumar S., Karthikeyan G., Alsaif F. A hybrid deep learning approach to solve optimal power flow

- problem in hybrid renewable energy systems. *Scientific Reports*, 2024, vol. 14, no. 1, art. no. 19377. doi: https://doi.org/10.1038/s41598-024-69483-4.
- 42. Adhikari A., Jurado F., Naetiladdanon S., Sangswang A., Kamel S., Ebeed M. Stochastic optimal power flow analysis of power system with renewable energy sources using Adaptive Lightning Attachment Procedure Optimizer. *International Journal of Electrical Power & Energy Systems*, 2023, vol. 153, art. no. 109314. doi: https://doi.org/10.1016/j.ijepes.2023.109314.
- 43. Laouafi F. Improved grey wolf optimizer for optimal reactive power dispatch with integration of wind and solar energy. *Electrical Engineering & Electromechanics*, 2025, no. 1, pp. 23-30. doi: https://doi.org/10.20998/2074-272X.2025.1.04.
- 44. Bai J., Nguyen-Xuan H., Atroshchenko E., Kosec G., Wang L., Abdel Wahab M. Blood-sucking leech optimizer. *Advances in Engineering Software*, 2024, vol. 195, art. no. 103696. doi: https://doi.org/10.1016/j.advengsoft.2024.103696.
- **45.** MATPOWER. Free, open-source tools for electric power system simulation and optimization. Available at: https://matpower.org/about/ (accessed on 27 April 2024).
- **46.** Bouhadouza B., Bouktir T., Bourenane A. Transient Stability Augmentation of the Algerian South-Eastern Power System including PV Systems and STATCOM. *Engineering, Technology & Applied Science Research*, 2020, vol. 10, no. 3, pp. 5660-5667. doi: https://doi.org/10.48084/etasr.3433.
- 47. Kennedy J., Eberhart R. Particle swarm optimization. *Proceedings of ICNN'95 International Conference on Neural Networks*, 1995, vol. 4, pp. 1942-1948. doi: https://doi.org/10.1109/ICNN.1995.488968.
- **48.** Mirjalili S., Mirjalili S.M., Lewis A. Grey Wolf Optimizer. *Advances in Engineering Software*, 2014, vol. 69, pp. 46-61. doi: https://doi.org/10.1016/j.advengsoft.2013.12.007.

Received 06.06.2025 Accepted 16.08.2025 Published 02.11.2025

B. Bouhadouza¹, Senior Lecturer,

F. Sadaoui¹, Professor,

¹Department of Electrical Engineering, Faculty of Applied Sciences, University of Kasdi Merbah Ouargla, Algeria,

e-mail: bouhadouza.boubekeur@univ-ouargla.dz

(Corresponding Author); sadaoui.fares@univ-ouargla.dz

How to cite this article:

Bouhadouza B., Sadaoui F. Optimal power flow analysis under photovoltaic and wind power uncertainties using the blood-sucking leech optimizer. *Electrical Engineering & Electromechanics*, 2025, no. 6, pp. 15-26. doi: https://doi.org/10.20998/2074-272X.2025.6.03

S. Guizani, A. Nayli, F. Ben Ammar

Fault-tolerant control of a double star induction machine operating in active redundancy

Introduction. The operating safety of a variable-speed drive is of paramount importance in industrial sectors, such as electric propulsion for ships, rail transport, electric cars, and aircraft, where reliability, maintainability, and safety are top priorities. Problem. One solution to improve the availability of a variable-speed drive is the use of a double star induction machine (DSIM). This machine can provide active or passive redundancy. Redundancy is active if both converters operate simultaneously, and the failure of one of them does not affect system operation. Passive redundancy is passive if only one converter is operating and the 2nd is on standby; the latter will only operate if the first fails. Goal. Improving the availability of a DSIM by the operation in active redundant of the machine supply system. Methodology. Use scalar control to control the machine power system in active redundancy. Simulation results with this scalar control demonstrated the need to equip this control with a decoupling of the variables responsible for machine magnetization and torque production. Field-oriented control (FOC) is then used to ensure the reconnection of a converter after a failure for active redundancy operation, without the risk of significant torque ripples. Scientific novelty. To increase the availability of the variable speed drive, an original control strategy for reintegrating the repaired faulty inverter is implemented to allow the repaired inverter to resume operation of the drive motor. This strategy control is based on the specific use of FOC to resynchronize the output frequency of the repaired inverter with the motor speed. Results. The results demonstrated the value of vector control in each star power supply system to avoid transient over currents at the input of the 2nd converter, by synchronizing the frequency of the 2 converters to the rotor speed. Practical value. An experimental model around a DSIM is set up to validate the active redundancy operation of the system. Active redundancy provides the variable speed drive with an increase in the reliability of the variable speed drive and significantly improves the availability rate of the driven load, since the disconnection of one of the 2 converters following a failure does not affect the operation of the machine. References 17, tables 2, figures 13. Key words: double star induction machine, active redundancy, field-oriented control, reliability.

Вступ. Безпека експлуатації частотно-регульованого приводу має першорядне значення в таких галузях промисловості, як електроприводи для суден, залізничного транспорту, електромобілів та літаків, де надійність, ремонтопридатність та безпека ϵ головними пріоритетами. **Проблема**. Одним із рішень для підвищення готовності частотно-регульованого приводу ϵ використання асинхронного двигуна з подвійною зіркою (DSIM). Цей двигун може забезпечувати активне чи пасивне резервування. Резервування активно, якщо обидва перетворювачі працюють одночасно, і відмова одного з них не впливає на роботу системи. Пасивне резервування пасивне, якщо працює лише один перетворювач, а другий перебуває у резерві; останній працюватиме лише у разі відмови першого. **Мета**. Підвищення готовності DSIM завдяки роботі в режимі активного резервування системи живлення машини. Методика. Використання скалярного керування для управління системою живлення машини в режимі активного резервування. Результати моделювання з використанням скалярного управління показали необхідність оснашення управління поділом змінних, що відповідають за намагнічування машини та створення крутного моменту. Далі використовується полеорієнтоване управління (FOC) для забезпечення повторного підключення перетворювача після відмови для роботи в режимі активного резервування без ризику значних пульсацій крутного моменту. Наукова новизна. Для підвищення готовності перетворювача частоти реалізовано оригінальну стратегію управління для повторного підключення відремонтованого несправного перетворювача, що дозволяє відремонтованому перетворювачу відновити роботу приводного двигуна. Ця стратегія управління заснована на специфічному використанні FOC для повторної синхронізації вихідної частоти відремонтованого перетворювача зі швидкістю двигуна. Результати продемонстрували цінність векторного управління в кожній зіркоподібній системі електропостачання для запобігання перехідним струмам на вході другого перетворювача шляхом синхронізації частоти двох перетворювачів зі швидкістю ротора. Практична цінність. Створено експериментальну модель на основі DSIM для перевірки роботи системи в режимі активного резервування. Активне резервування забезпечує підвищення надійності перетворювача частоти і значно покращує коефіцієнт готовності навантаження, оскільки відключення одного з двох перетворювачів після відмови не впливає на роботу машини. Бібл. 17, табл. 2, рис. 13.

Ключові слова: асинхронна машина з подвійною зіркою, активне резервування, полеорієнтоване управління, надійність.

Introduction. In the speed drive applications (pumps, fans, extruders, railway traction, drive of the compressors in the methane tankers, electric propulsion of the ships etc.) [1–3], the use of multiphase or multi-stars asynchronous machine offers multiple redundancy degrees [4–6], since the loss of one star does not stop the machine. For motors and drives for surface ship propulsion, particular attention is paid to the separation of the phases, motor and inverter connection scheme [7]. As consequence of complete separation between the phases, the loss of any motor or inverter phase will not jeopardize the remaining phases and continue operation at reduced load.

In the case of 6 phase induction machine, different configurations are possible. In Fig. 1,*a* the stator can be realized with a single star point with a 6 independent armature currents [8, 9]. As shown in Fig. 1,*b*, to avoid the 3rd harmonics, the 6 stator windings can be combined into 2 three phase windings; the star points are kept isolated with 2 pairs of independent stator currents.

In the asymmetrical stator windings structure the 2 three phase windings are spatially shifted by 30°.

The symmetrical winding structure with displacement between any 2 consecutive stator phases is

60° [10, 11]. It's shown by that non shifted star windings are preferred to have a weak magnetic coupling between stars. Figure 1,c shows the configuration in which each phase is electrically insulated from the others for independent control; each phase is supplied with H-bridge voltage source inverter (VSI). In Fig. 1,d the 2 stator windings are not mutually coupled, this aim can be accomplished if the 2 stator windings are designed with a different number of poles.

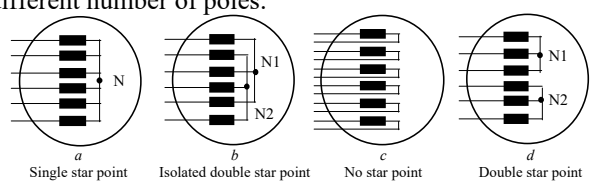
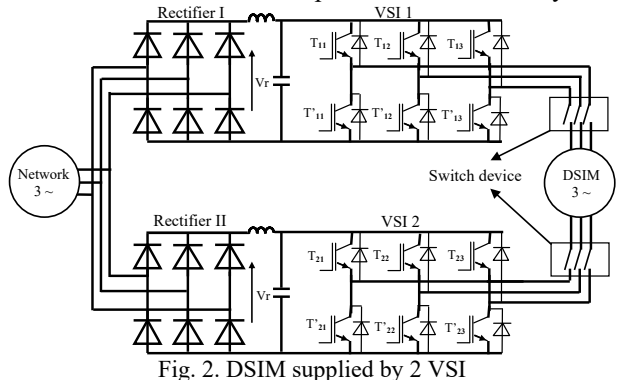


Fig. 1. Six phases induction machine

As shown in Fig. 2, the drive-motor configuration employs 2 identical pulse-width modulation VSIs to supply the double star induction machine (DSIM) [12–14]. The failure that may involve VSI can take place either in the diodes of the rectifier, in the DC link capacitors and the switches of the inverter or in their gate control circuit.

© S. Guizani, A. Nayli, F. Ben Ammar

Note that the reliability level is increased if the IGBT driver uses differential signal processing to provide a high level of signal integrity and high noise rejection. For example, with the over voltages, especially those that occur during a short-circuit turn-off, are reduced by the IGBT driver like Skyper 52 of Semikron, using intelligent turn-off control to switch the power transistor slowly.



To detect the failure inverter, the controller receives feedback from each gate drive IGBT signals. If the fault is detected, then the inverter can be disconnected and electrically isolated from the corresponding star stator winding while continuing to operate using the healthy inverter. In case of failure in one inverter the motor will be driven with up to half of maximal torque. The faulty inverter can be repaired or replaced and reintegrated into the system without over-voltage or over-current.

The **goal** of this work is to improve the availability of a DSIM by the operation in active redundant of the machine supply system.

The scalar control. Figure 3 shows the simulation for a load torque of the form $T_r = kn$. We considered the disconnection of converter 2 following a failure, then its reintegration into the machine power supply.

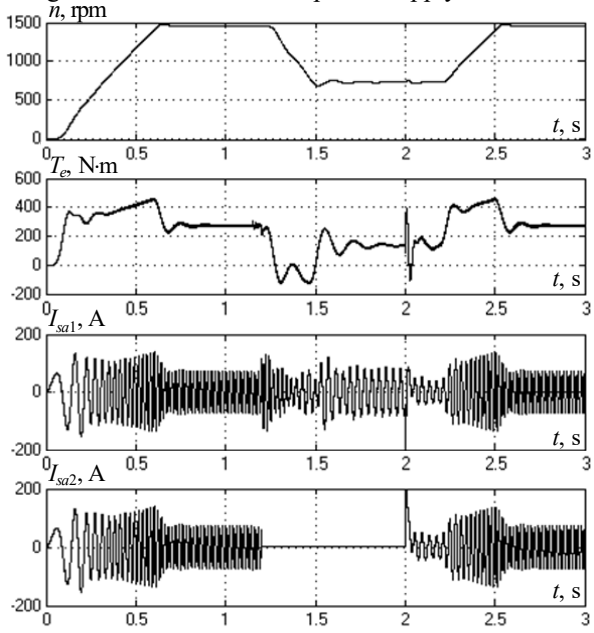


Fig. 3. Simulation of the converter 2 reconnection after the power supply failure of star 2 for a load torque $T_r = kn$

The operation consists of a start cycle between t = 0 and t = 0.6 s. At t = 1.2 s we disconnected converter 2 supplying the 2nd star following a failure. The speed is then reduced to 50 % of the nominal speed. At time t = 2.5 s, we simulated the reconnection of converter 2.

The parameters of DSIM are: R_r , R_s are the rotor and stator resistances; M_{ss} is the mutual inductance between 2 stars of the stator; M_{sr1} is the mutual cyclic inductance between star 1 and rotor; M_{sr2} is the mutual cyclic inductance between star 2 and rotor; L_s , L_r are the stator and rotor cyclic inductances; T_e is the electromagnetic torque; T_L is the load torque; p is the number of pole pairs.

Preliminary results have shown significant ripples in the torque and stator currents during the reconnection of the 2nd star. Scalar redundancy therefore does not allow for the reintegration of the repaired converter.

To increase the availability of the variable speed drive, an **original control strategy** for reintegrating the repaired faulty inverter is implemented to allow the repaired inverter to resume operation of the drive motor. This strategy control is based on the specific use of field-oriented control (FOC) to resynchronize the output frequency of the repaired inverter with the motor speed.

The model obtained by using Park's transformation (Fig. 4) is undoubtedly the best adapted for the description of the DSIM behavior at the transient, as well as steady state operation [14–16]. The control strategy and fault manager software of the double stator supplied by redundant VSIs are realized in the field rotating (d, q) orthogonal axes reference frame running at ω_{dq} . The decoupling between the torque and the flux are be accomplished by properly aligning the rotor flux vector along the d-axis.

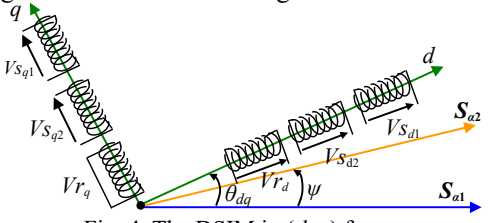


Fig. 4. The DSIM in (d, q) frame

The mathematical flux model is written in (d, q) reference frame, and described as:

$$\begin{cases} \frac{\mathrm{d}X(t)}{\mathrm{d}t} = \left[A(\omega, \omega_{dq})\right][X(t)] + [B]U(t); \\ Y(t) = [C]X(t), \end{cases}$$
(1)

where $X(t) = [\Phi_{sd1}, \Phi_{sq1}, \Phi_{sq2}, \Phi_{sd2}, \Phi_{rd}, \Phi_{rq}]^t$ is the state vector; $U(t) = [U_1, U_2]^t = [V_{sd1}, V_{sq1}, V_{sd2}, V_{sq2}]^t$ is the control vector; $Y(t) = [I_{sd1}, I_{sq1}, I_{sd2}, I_{sq2}]^t$ is the output vector; Φ_{rd}, Φ_{rq} are the direct and orthogonal components of the rotor flux; $I_{sd1}, I_{sq1}, I_{sd2}, I_{sq2}$ are the direct and orthogonal components of star 1 and star 2 current; $\Phi_{sd1}, \Phi_{sq1}, \Phi_{sd2}, \Phi_{sq2}$ are the direct and orthogonal components of star 1 and star 2 flux; $V_{sd1}, V_{sq1}, V_{sd2}, V_{sq2}$ are the direct and orthogonal components of star 1 and star 2 voltages; ψ is the shifting angle between 2 stars of the stator; θ_{dq} is the displacement between d-axis and the α_1 -axis of the star 1 of the stator; $\theta_{dq} - \psi$ is the displacement between d-axis and the α_2 -axis of the star 2 of the stator; $\theta_{dq} - \theta$ is the displacement between d-axis and the α_2 -axis of the rotor.

The state matrix is determined as:

$$[A(\omega, \omega_{dq})] = -([R][L_{d,q}]^{-1} + [W]);$$

$$[C] = [L_{d,q}]^{-1};$$

$$(3)$$

$$\begin{bmatrix} L_s & 0 & M_{ss} & 0 & M_{sr1} & 0\\ 0 & L_s & 0 & M_{ss} & 0 & M_{sr1}\\ M_{ss} & 0 & L_s & 0 & M_{sr2} & 0\\ 0 & M_{ss} & 0 & L_s & 0 & M_{sr2}\\ M_{sr1} & 0 & M_{sr2} & 0 & L_r & 0\\ 0 & M_{sr1} & 0 & M_{sr2} & 0 & L_r \end{bmatrix}.$$
(4)

In case of failure in VSI 1, it could be disconnected from star 1 of stator winding. In the inductance matrix $[L_{d,q}]_{f1}$ the terms involving M_{sr1} and M_{ss} can be ignored.

Similarly, in the inductance matrix $[L_{d,q}]_{f2}$ the terms involving M_{sr2} and M_{ss} can be ignored in case of the disconnection of star 2 stator winding:

Fig. 5. The block diagram of DSIM with FOC strategy

The feedback regulators are working in coordinates which rotates synchronously with the rotor flux in all operating modes; the direction of axis d is always coincident with the rotor flux representative vector. The

measurements stators current are transformed to field-oriented quantities I_{sd1} , I_{sq1} and I_{sd2} , I_{sq2} . In a large speed range, rotor flux Φ_{rd} is kept at constant nominal values controlling direct axis currents i_{sd1} and/or i_{sd2} .

Table 1 shows speed and rotor flux references in different operating inverter states.

Speed and rotor flux references in different operating

speed and rotor max references in different operating			
State of motor drive	Speed reference	Rotor flux references	
Inverter 1 up Inverter 2 up	$egin{aligned} \omega_{ref1} &= \omega_n \ \omega_{ref2} &= \omega_n \end{aligned}$	$ \Phi_{rdref1} = \Phi_n/2 $ $ \Phi_{rdref2} = \Phi_n/2 $	
Inverter 1 up Inverter 2 down	$\omega_{ref} = \omega_n/2 \text{ if } T_L = k\omega$ $\omega_{ref} = \omega_n/\sqrt{2} \text{ if } T_L = k\omega^2$	$\Phi_{rdref1} = \Phi_n$	
Inverter 1 down Inverter 2 up	$\omega_{ref} = \omega_n/2$ if $T_L = k\omega$ $\omega_{ref} = \omega_n/\sqrt{2}$ if $T_L = k\omega^2$	$ \Phi_{rdref2} = \Phi_n $	
Inverter 1 down Inverter 2 down	0	0	

Table 2 shows the electromagnetic torque, the speed of rotor flux vector and the magnitude of rotor flux in all operating configurations.

Table 2 Electromagnetic torque and rotor flux in (d, q) plane aligned with the rotor flux in 4 operating inverters states

with the rotor riux in 4 operating inverters states			
State of motor	Electromagnetic torque T_e ;	Rotor flux $\Phi_{rd}(p)$	
drive	Field speed ω_{dq}		
Inverter 1 up Inverter 2 up	$T_e = \frac{3M_{sr}p \Phi_{rd}}{2L_r} \left(I_{sq1} + I_{sq2} \right)$ $\omega_{dq} = \omega + \frac{M_{sr}}{T_r \Phi_{rd}} \left(I_{sq1} + I_{sq2} \right)$	$\frac{M_{sr1}}{1+T_rp} \left(I_{sd1} + I_{sq2} \right) (p)$	
Inverter 1 up Inverter 2 down	$T_e = \frac{3M_{sr1}p\Phi_{rd}}{2L_r}I_{sq1}$ $\omega_{dq} = \omega + \frac{M_{sr}}{T_r\Phi_{rd}}I_{sq1}$	$\frac{M_{sr1}}{1 + T_r p} I_{sd1}(p)$	
Inverter 1 down Inverter 2 up	$T_e = \frac{3M_{sr2}p\Phi_{rd}}{2L_r}I_{sq2}$ $\omega_{dq} = \omega + \frac{M_{sr}}{T_r\Phi_{rd}}I_{sq2}$	$\frac{M_{sr2}}{1+T_rp}I_{sd2}(p)$	
Inverter 1 down Inverter 2 down	0	0	

The results simulation (Fig. 6) shows the active redundancy operation of the system using the reconfiguration and reintegration control strategy of the repaired inverter is based on the special use of the FOC [14–16]. The operating description is as follows:

- 1) for $0 \le t < 0.2$ s: machine fluxing provided by the 2 currents I_{sd1} , I_{sd2} the reference fluxes are $\Phi_{rdref1} = \Phi_{rdref2} = 0.5 \Phi_n$.
- 2) for $0.2 \le t < 0.8$ s: acceleration from 0 to 1460 rpm.
- 3) for $0.8 \le t < 1.49$ s: machine operation at nominal speed.
- 4) at t = 1.49 s: fault in converter 2.

DSIM

- 5) for $1.49 \le t < 1.59$ s: the current I_{sd1} of the healthy star winding is controlled to impose the required rotor flux. The motor must be controlled at half speed.
- 6) for $1.59 \le t < 2.1$ s: deceleration from 1460 to 730 rpm.
- 7) for $2.48 \le t < 3.1$ s: once the faulty converter is replaced or repaired, it will attempt to return to normal operation. The prerequisite for the repaired converter to return to a healthy state is for the output frequency to be resynchronized with the motor speed.
- 8) for $t \ge 3.1$ s: machine operation at nominal speed.

In active redundancy operation, the converters are sized for a power 0.5*P*. Thus, in degraded mode, the speed

is reduced to 50 % or 70 % of the nominal speed depending on whether the torque is in the form of kn or kn^2 .

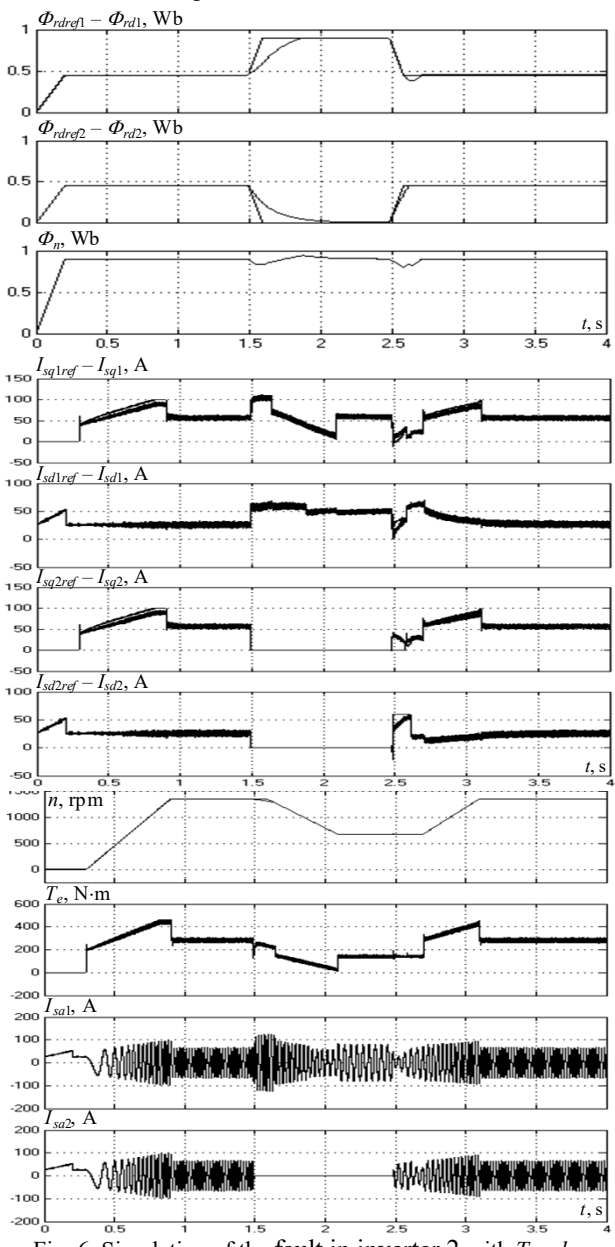


Fig. 6. Simulation of the fault in inverter 2 with $T_r = kn$

Experimental results. In Fig. 7 the experimental platform shows the DSIM shifted by 30 el. degrees of 1.5 kW power feeding by 2 VSI using Spartan 3E FPGA board [17].

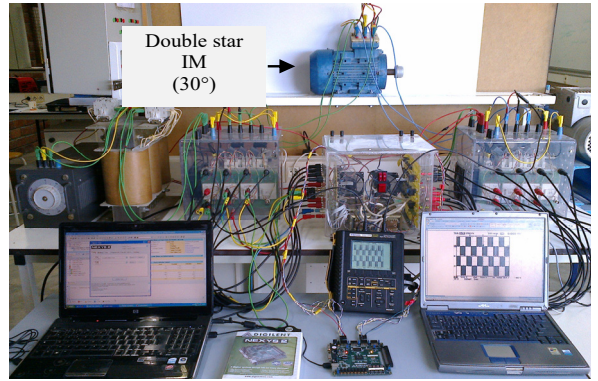


Fig. 7. Experimental platform

The obtained experimental results of the active redundant operating mode of supply system of the DSIM

are shown in Fig. 8–13. The voltage between 2 phases of the 1st and the 2nd star before and after fails and after reintegration of inverter 2 are shown in Fig. 8.

The voltage between 2 phases of the 1st star and stator current in the 2nd star after fails and after reintegrated of inverter 2 are given in Fig. 9.

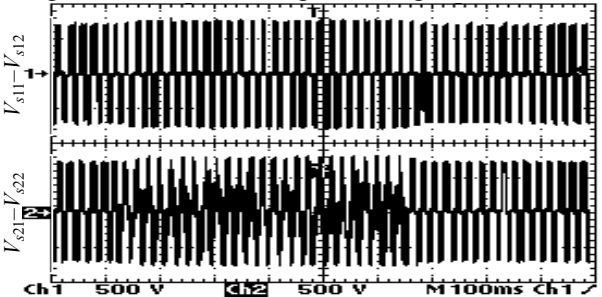


Fig. 8. Voltage between 2 phases of the 1st star and the 2nd star before and after fails and after reintegration of inverter 2

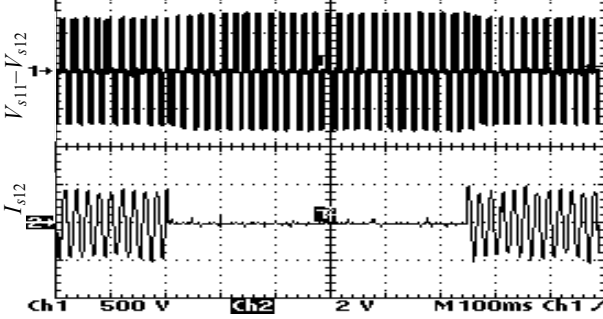


Fig. 9. Voltage between 2 phases of the 1st star and stator current in the 2nd star before and after fails and after reintegration of inverter 2

The voltage between 2 phases of the 1st star and stator current in the 2nd star after fails and after reintegrated of inverter 2 are shown respectively in Fig. 10, 11.

The voltage between 2 phases and stator current in the 2nd stator after fails of inverter 2 are given in Fig. 12.

The voltage between 2 phases and stator current in the 2nd stator after reintegrated of inverter 2 are given in Fig. 13.

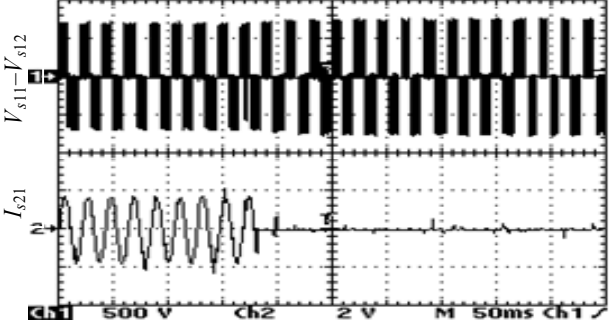


Fig. 10. Voltage between 2 phases of the 1st star and stator current in the 2nd stator before and after fails

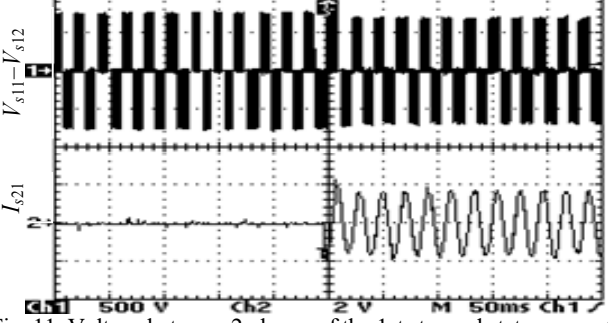


Fig. 11. Voltage between 2 phases of the 1st star and stator current in the 2nd stator before and after reintegrated of inverter 2

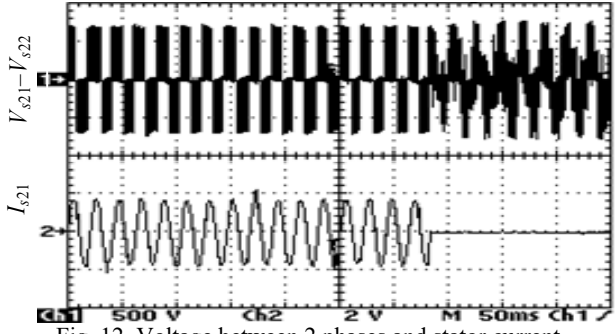
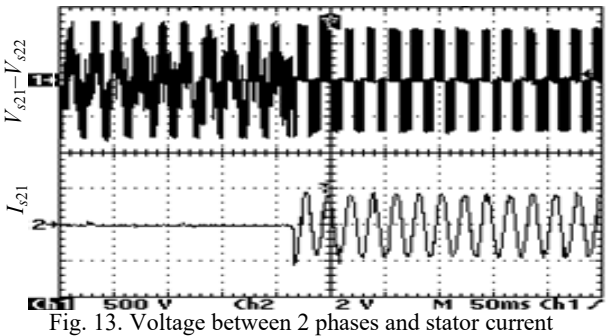


Fig. 12. Voltage between 2 phases and stator current in the 2nd stator before and after fails of inverter 2



in the 2nd stator before and after reintegrated of inverter 2

Conclusions. The aim of this work was the DSIM supplied by redundant VSIs improves reliability, availability and safety of the system since the loss of a one star does not stop the motor. A control strategy by reintegration of the repaired faulty inverter increases system survivability by allowing the faulty inverter to resume operation of the drive motor. The 1st strategy based on scalar control demonstrated its weaknesses in terms of torque and stator current during converter reintegration. To address these weaknesses, the 2nd strategy was used. This reintegration control strategy relies on the specific use of FOC to resynchronize the output frequency of the repaired inverter with the motor speed. Simulation results of FOC of the active redundancy operation of the DSIM power supply demonstrated a good solution for fault-tolerant control. Indeed, the reintegration of repaired inverter gave for the 1st control strategy a current peak of 200 A (maximum value) whereas with the faulttolerant control strategy, the current gradually goes from 0 to 100 A (maximum value), then it stabilizes at its nominal value. This is also true for the torque.

Experimental results on a 1.5 kW DSIM are performed to demonstrate the ability of a fault-tolerant architecture to improve availability.

Conflict of interest. The authors declare that they have no conflicts of interest.

REFERENCES

- 1. Nemouchi B., Rezgui S.E., Benalla H., Nebti K. Fractional-based iterative learning-optimal model predictive control of speed induction motor regulation for electric vehicles application. Electrical Engineering & Electromechanics, 2024, no. 5, pp. 14-19. doi: https://doi.org/10.20998/2074-272X.2024.5.02.
 Chaib Ras A., Bouzerara R., Bouzeria H. An adaptive controller for
- power quality control in high speed railway with electric locomotives with asynchronous traction motors. Electrical Engineering & *Electromechanics*, 2024, no. 2, https://doi.org/10.20998/2074-272X.2024.2.04. pp.
- 3. Khemis A., Boutabba T., Drid S. Model reference adaptive system speed estimator based on type-1 and type-2 fuzzy logic sensorless control of electrical vehicle with electrical differential. Electrical

Engineering & Electromechanics, 2023, no. 4, pp. 19-25. doi: https://doi.org/10.20998/2074-272X.2023.4.03.

- 4. Guizani S., Nayli A., Ben Ammar F. Comparison between star winding and open-end winding induction machines. *Electrical* Engineering, 2016, vol. 98, no. https://doi.org/10.1007/s00202-016-0359-4. 219-232. no. 3, pp.
- 5. Sun J., Zheng Z., Li C., Wang K., Li Y. Optimal Fault-Tolerant Control of Multiphase Drives Under Open-Phase/Open-Switch Faults Based on DC Current Injection. IEEE Transactions on Power Electronics, 2022, vol. 37, no. 5, https://doi.org/10.1109/TPEL.2021.3135280. pp. 5928-5936. doi:
- Letellier P. Electrical propulsion motors. Electric Propulsion. The Effective Solution. Paper 7. London, IMarE, 1995.
- Mitcham A.J., Cullen J.J.A. Motors and drives for surface ship propulsion: comparison of technologies. Proceeding of 1995 Electric Propulsion Conference, 1995, vol. 4, pp. 88-89.
- 8. Abdel-Khalik A.S., Masoud M.I., Williams B.W. Vector controlled multiphase induction machine: Harmonic injection using optimized constant gains. Electric Power Systems Research, 2012, vol. 89, pp. 116-128. doi: https://doi.org/10.1016/j.epsr.2012.03.001.
- Abdelwanis M.I., Zaky A.A. Maximum power point tracking in a perovskite solar pumping system with a six-phase induction motor. Revue Roumaine des Sciences Techniques — Série Électrotechnique et 2024, vol. 69, no. 1. Énergétique, pp. 15-20. https://doi.org/10.59277/RRST-EE.2024.1.3.
- 10. Lim C.S., Lee S.S., Levi E. Continuous-Control-Set Model Predictive Current Control of Asymmetrical Six- Phase Drives Considering System Nonidealities. IEEE Transactions on Industrial 2023, vol. 70, no. 8, pp. 7615-7626. Electronics, https://doi.org/10.1109/TIE.2022.3206703.
- 11. Hammad R., Dabour S.M., Rashad E.M. Asymmetrical six-phase induction motor drives based on Z-source inverters: Modulation, design, fault detection and tolerance. Alexandria Engineering Journal, 2022, 61, no. 12, pp. 10055-10070. https://doi.org/10.1016/j.aej.2022.02.058.
- 12. Boukhalfa G., Belkacem S., Chikhi A., Benaggoune S. Genetic algorithm and particle swarm optimization tuned fuzzy PID controller on direct torque control of dual star induction motor. Journal of Central South University, 2019, vol. 26, no. https://doi.org/10.1007/s11771-019-4142-3. 7, pp. 1886-1896. doi:
- 13. Chaabane H., Khodja D.E., Chakroune S., Hadji D. Model reference adaptive backstepping control of double star induction machine with extended Kalman sensorless control. *Electrical Engineering & Electromechanics*, 2022, no. 4, pp. 3-11. doi: https://doi.org/10.20998/2074-272X.2022.4.01.
- 14. Zemmit A., Messalti S., Herizi A. New Direct Torque Control of Dual Star Induction Motor using Grey Wolf Optimization Technique. Przegląd Elektrotechniczny, 2024, no. 2, pp. 109-113. doi: https://doi.org/10.15199/48.2024.02.21
- 15. Abdelwanis M.I., Zaky A.A., Selim F. Direct torque control for a six phase induction motor using a fuzzy based and sliding mode controller. *Scientific Reports*, 2025, vol. 15, no. 1, art. no. 14874. doi: https://doi.org/10.1038/s41598-025-97479-1.
- 16. Moussaoui L. Performance enhancement of direct torque control induction motor drive using space vector modulation strategy. Electrical Engineering & Electromechanics, 2022, no. 1, pp. 29-37. doi: https://doi.org/10.20998/2074-272X.2022.1.04.
- 17. Aib A., Khodja D.E., Chakroune S., Rahali H. Fuzzy current analysis-based fault diagnostic of induction motor using hardware cosimulation with field programmable gate array. Electrical Engineering Electromechanics, 2023, 3-9. no. 6. pp. https://doi.org/10.20998/2074-272X.2023.6.01.

Received 11.05.2025 Accepted 16.07.2025 Published 02.11.2025

- S. Guizani¹, Professor of Electrical Engineering,
- A. Nayli², Doctor of Electrical Engineering,
- F. Ben Ammar³, Professor of Electrical Engineering,
- ¹ University of El Manar, IPEIEM, Tunisia.
- ²University of Gafsa, IPEIG, Tunisia,
- e-mail: abdelmonoem.nayli@gmail.com (Corresponding Author)
- MMA Laboratory, INSAT, University of Carthage, Tunisia.

How to cite this article:

Guizani S., Nayli A., Ben Ammar F. Fault-tolerant control of a double star induction machine operating in active redundancy. Electrical Engineering & Electromechanics, 2025, no. 6, pp. 27-31. doi: https://doi.org/10.20998/2074-272X.2025.6.04

N. Hamdi, F. Babaa, A. Touil, N. Merabet

Robust fault-tolerant sliding mode control and advanced fault diagnosis for doubly-fed induction generators

Introduction. Doubly-fed induction generators (DFIGs) have become the preferred technology in modern wind energy systems due to their high efficiency and flexible variable-speed operation capabilities. Problem. Despite their advantages, DFIGs face significant challenges related to grid-connected power converters, which are susceptible to operational instability caused by voltage imbalances and electrical faults. Goal. This study aims to develop and validate a novel Active Fault-Tolerant Sliding Mode Control (AFT-SMC) strategy that integrates real-time fault diagnosis to enhance the reliability and stability of DFIG systems during grid disturbances. Unlike existing approaches, this work specifically addresses the reduction of false fault detections during transient events and improves fault characterization through spectral analysis. Methodology. The proposed control framework combines a robust sliding mode controller with a model-based fault detection and isolation system that employs adaptive thresholds and diagnostic residuals for accurate fault identification. The approach has been thoroughly tested through high-fidelity simulations under severe voltage unbalance scenarios. Results. Simulation outcomes demonstrate the superior performance of the proposed strategy in maintaining system stability under a 30 % voltage unbalance scenario. Specifically, the controller achieves a voltage recovery time of 0.28 s, compared to 0.42 s with conventional vector control, and reduces electromagnetic torque oscillations by approximately 45 %. Furthermore, the integrated spectral diagnosis method reaches a fault classification accuracy of 94.6 %, confirming its effectiveness in enabling early and reliable fault detection. These results validate the advantages of the proposed AFT-SMC framework in both dynamic response and fault resilience. Scientific novelty. The key innovation lies in the integration of a self-correcting «detect-and-adapt» mechanism that mitigates false triggers during transient grid conditions, alongside a novel spectral decomposition method for precise detection and characterization of voltage imbalances through negative-sequence component analysis. Practical value. This strategy significantly reduces operational costs at pilot wind farms and sets a new benchmark for intelligent fault management in renewable energy systems, with broad applicability to other power electronic interfaces in smart grids. References 35, figures 12.

Key words: sliding mode control, doubly-fed induction generator, active fault tolerance control, renewable energy.

Вступ. Асинхронні генератори з подвійним живленням (DFIGs) стали поширеними технічними рішеннями в сучасних вітроенергетичних системах завдяки своїй високій ефективності та гнучкій роботі з регульованою швидкістю. Проблема. Незважаючи на свої переваги, DFIGs стикаються зі значними проблемами, пов'язаними з перетворювачами потужності, підключеними до мережі, які схильні до нестабільної роботи, спричиненої дисбалансом напруги та електричними несправностями. Мета. Дане дослідження спрямоване на розробку та перевірку нової стратегії активного відмовостійкого керування ковзним режимом (AFT-SMC), яка поєднує діагностику несправностей у реальному часі для підвищення надійності та стійкості систем DFIG при порушеннях у мережі. На відміну від існуючих підходів, дана робота спрямована на зниження помилкових виявлень несправностей під час перехідних процесів та покращення характеристики несправностей за допомогою спектрального аналізу. Методологія. Пропонована структура управління поєднує в собі надійний контролер ковзного режиму з системою виявлення та виділення несправностей на основі моделі, яка використовує адаптивні граничні значення та діагностичні залишки для точної ідентифікації несправностей. Даний підхід ретельно протестували за допомогою високоточного моделювання в умовах сильного дисбалансу напруги. Результати моделювання демонструють високу ефективність пропонованої стратегії підтримки стійкості системи в умовах 30 % несиметрії напруги. Зокрема, контролер досягає часу відновлення напруги 0,28 в порівнянні з 0,42 с при традиційному векторному управлінні і знижує коливання електромагнітного моменту приблизно на 45 %. Більш того, інтегрований метод спектральної діагностики досягає точності класифікації несправностей 94,6 %, що підтверджує його ефективність у забезпеченні раннього та надійного виявлення несправностей. Ці результати підтверджують переваги запропонованої структури AFT-SMC як з точки зору динамічного реагування, так і стійкості до несправностей. **Наукова** новизна. Ключове нововведення полягає в інтеграції механізму «виявлення та адаптації», що самокоректується, який знижує кількість помилкових спрацьовувань в перехідних режимах мережі, а також нового методу спектрального розкладання для точного виявлення і характеристики несиметрії напруги за допомогою аналізу компонентів зворотної послідовності. Практична цінність. Ця стратегія значно знижує експлуатаційні витрати на пілотних вітряних електростанціях та встановлює новий стандарт інтелектуального управління несправностями у системах відновлюваної енергії з широкою застосовністю до інших інтерфейсів силової електроніки в інтелектуальних мережах. Бібл. 35, рис. 12. Ключові слова: ковзне управління, асинхронний генератор з подвійним живленням, активне управління

відмовостійкістю, відновлювані джерела енергії.

Introduction. Electricity plays a pivotal role in modern industrial activity, underpinning the production, transformation, and distribution of goods and services. Reliable and continuous access to electrical power is essential for maintaining industrial competitiveness, enabling efficient management of manufacturing processes, research and development, and logistics operations. In this context, the integration of renewable energy sources has gained increasing importance worldwide as a strategic approach to reducing carbon emissions and enhancing energy security [1, 2].

Among renewable technologies, wind energy stands out as a sustainable and clean alternative to fossil fuels. The efficiency of wind power generation relies heavily on the performance of electrical machines that convert the kinetic energy of the wind into electrical energy suitable

for grid integration. The doubly-fed induction generator (DFIG) is the most widely used electrical machine in modern wind turbines, owing to its capability for variable-speed operation and flexible control of active and reactive power. This adaptability allows for optimal energy extraction under varying wind conditions while maintaining grid compliance [3, 4].

Despite these advantages, DFIGs are vulnerable to operational stresses, including mechanical, electrical, and environmental factors, which can degrade their performance and reliability over time. Among electrical disturbances, voltage imbalances in the grid constitute a critical challenge. Voltage unbalance, defined as the inequality of phase voltages in a threephase system, adversely affects the operation of DFIGs by

© N. Hamdi, F. Babaa, A. Touil, N. Merabet

inducing unbalanced rotor currents. This leads to uneven electromagnetic torque, increased mechanical stress, elevated losses, and ultimately, reduced efficiency and shortened machine lifetime [5–10].

Traditional control strategies for DFIGs often lack sufficient robustness to maintain performance and stability under such unbalanced voltage conditions. Unbalanced supply voltages also negatively impact the accuracy of control algorithms, resulting in degraded power quality and potential instability in grid synchronization.

Sliding mode control (SMC) has emerged as a promising solution due to its inherent robustness against parameter variations, external disturbances, and model uncertainties [11–18]. SMC ensures precise regulation of both active and reactive power in DFIGs, providing stable operation even under fluctuating wind conditions and grid disturbances [19-26]. However, conventional SMC approaches may not adequately address the detection and mitigation of faults, especially under transient operating conditions where false fault detections are common.

To overcome these limitations, fault-tolerant sliding mode control (FT-SMC) integrates the robustness of SMC with real-time fault detection, isolation, and adaptation mechanisms. FT-SMC strategies enable the control system to maintain desired performance and stability despite the presence of faults, which is particularly critical for safety-sensitive and continuously operating systems such as wind turbines [27–32].

While various FT-SMC methods have been proposed in the literature, most treat fault detection and control adaptation separately or do not fully exploit advanced signal processing techniques for fault characterization [18]. Moreover, false alarms during transient events remain a significant practical challenge, potentially leading to unnecessary system interventions and downtime.

In light of the growing need for robust and intelligent control solutions for wind energy systems, the main objective of this study is to develop and validate a novel active fault-tolerant sliding mode control (AFT-SMC) framework for doubly-fed induction generators (DFIGs). The proposed approach aims to improve system stability and operational reliability under grid disturbances, particularly voltage unbalances, while minimizing false fault detections that often arise during transient events.

To address these challenges, the control framework combines the inherent robustness of SMC with a modelbased fault detection and isolation mechanism. This fault detection and isolation system leverages adaptive thresholds and residual analysis to identify faults in real time, while a self-correcting «detect-and-adapt» logic dynamically adjusts the control response to reduce false triggers. Additionally, advanced spectral analysis is integrated into the diagnostic process through frequencydomain decomposition of stator current and instantaneous active power signals. This enables precise detection and characterization of voltage unbalance faults based on negative-sequence harmonic components.

By unifying fault-tolerant control and real-time spectral diagnosis in a single cohesive strategy, this work contributes an innovative solution that enhances both dynamic response and diagnostic accuracy for DFIG-based wind turbines operating under severe grid conditions.

DFIG mathematical model. In this study, the stator is directly linked to the grid, simplifying the system

design by removing the necessity for an additional statorside converter. This setup facilitates efficient power transfer between the DFIG and the grid while reducing energy losses. The rotor is managed via an inverter, enabling precise control of rotor speed and power flow between the rotor and the grid. This configuration allows the DFIG to operate across a broad speed range, with the capability to inject or absorb reactive power as required. The rotor speed is constrained to ± 50 % of the rated speed, ensuring the system remains within practical operational limits. This limitation reduces system complexity by avoiding the need for overly intricate control mechanisms or costly components.

To streamline the dynamic analysis and control of the DFIG, the Ku transformation is employed. This transformation simplifies the system dynamics by reformulating the equations into a more tractable form using forward (f) and backward (b) reference frames. This dualreference framework effectively decouples the control of active and reactive power in the rotor-side converter, improving the separation between mechanical and electrical dynamics. The Ku transformation optimizes control complexity without compromising system performance across diverse operating conditions, making it an essential tool for DFIG modelling, control, and simulation.

The machine equation system Ku transformation is:

$$\begin{cases} V_{sf} = R_{s}i_{sf} + L_{s}\frac{di_{sf}}{dt} + M\frac{di_{rf}}{dt} + j\frac{d\theta_{s}}{dt}\varphi_{sf}; \\ V_{sb} = R_{s}i_{sb} + L_{s}\frac{di_{sb}}{dt} + M\frac{di_{rb}}{dt} - j\frac{d\theta_{s}}{dt}\varphi_{sb}; \\ V_{rf} = R_{r}i_{rf} + L_{r}\frac{di_{rf}}{dt} + M\frac{di_{sf}}{dt} + j\frac{d\theta_{r}}{dt}\varphi_{rf}; \\ V_{rb} = R_{r}i_{rb} + L_{r}\frac{di_{rb}}{dt} + M\frac{di_{sb}}{dt} - j\frac{d\theta_{r}}{dt}\varphi_{rb}, \end{cases}$$

$$(1)$$

where V_{sf} , V_{sb} , V_{rf} , V_{rb} are the f- and b-axis components of the stator and rotor voltages; i_{sf} , i_{sb} , i_{rf} , i_{rb} are the f- and baxis components of the stator and rotor currents; $R_s R_r$ are the stator and rotor phase resistances; L_s , L_r are the stator and rotor phase inductances; M is the mutual inductance between the stator and rotor; p is the number of pole pairs; φ_{sf} , φ_{sb} , φ_{rf} , φ_{rb} are the f- and b-axis components of the stator and rotor fluxes.

The stator and rotor flux linkages are:

The stator and rotor flux linkages are:
$$\begin{bmatrix} \phi_{sofb} \end{bmatrix} = \begin{pmatrix} L_{so} & 0 & 0 \\ 0 & L_{s} & 0 \\ 0 & 0 & L_{s} \end{pmatrix} \begin{bmatrix} i_{sofb} \end{bmatrix} + \begin{pmatrix} 0 & 0 & 0 \\ 0 & M & 0 \\ 0 & 0 & M \end{pmatrix} \begin{bmatrix} i_{rofb} \end{bmatrix}; (2)$$

$$\begin{bmatrix} \phi_{rofb} \end{bmatrix} = \begin{pmatrix} L_{ro} & 0 & 0 \\ 0 & L_{r} & 0 \\ 0 & 0 & L_{r} \end{pmatrix} \begin{bmatrix} i_{rofb} \end{bmatrix} + \begin{pmatrix} 0 & 0 & 0 \\ 0 & M & 0 \\ 0 & 0 & M \end{pmatrix} \begin{bmatrix} i_{sofb} \end{bmatrix}, (3)$$

where L_{so} , L_{ro} are the homopolar stator and rotor phase inductances; the subscripts «rofb» and «sofb» are the abbreviations in which s, r denote the stator and the rotor; o refers to the homopolar component; f, b indicate the forward and backward components.

The use of the Ku transformation in the electromagnetic torque results in: $T_e = p \cdot M \cdot \left[i_{sb} \cdot i_{rf} - i_{sf} \cdot i_{rb} \right].$

$$T_{\rho} = p \cdot M \cdot |i_{sh} \cdot i_{rf} - i_{sf} \cdot i_{rh}|. \tag{4}$$

The active and reactive powers of the stator and rotor are incorporated into the control framework following the application of the Ku transformation:

$$\begin{cases} P_s = 2 \cdot V_{sf} \cdot i_{sf}; & P_r = 2 \cdot V_{rf} \cdot i_{rf}; \\ Q_s = 2 \cdot V_{sf} \cdot i_{sf}^*; & Q_r = 2 \cdot V_{rf} \cdot i_{rf}^*; \end{cases}$$
(5)

$$i_{rf} = \frac{P_r}{2 \cdot V_{rf}}; \quad i_{rb} = i_{rf}^* = \frac{Q_r}{2 \cdot V_{rf}},$$
 (6)

where i_{rf}^* is the conjugate of i_{rb} .

This transformation enables the decoupling of system dynamics, simplifying the independent control of power components in each reference frame. Consequently, the torque is expressed as:

$$T_e = 2 \cdot p \cdot M \cdot \left[i_{sf} \cdot i_{rf}^* \right]. \tag{7}$$

Advanced SMC strategy for DFIGs. SMC is a nonlinear control methodology renowned for its robustness against uncertainties and external disturbances. The technique involves driving the system state toward a predefined sliding surface and maintaining it on this surface to achieve desired performance metrics. In the context of a DFIG, the control objective is to regulate rotor currents to ensure the generator delivers the specified active power while maintaining operational stability. A sliding surface is designed based on the error between the measured and reference rotor currents. Additionally, the SMC approach offers a rapid dynamic response, making it particularly suitable for systems requiring swift and precise adjustments. The control scheme's simplicity and computational efficiency contribute to its practical implementation in realtime systems, where high performance and minimal computational load are essential. The sliding surface can be defined as:

$$S_i = x_i^{ref} - x_i \,. \tag{8}$$

The sliding surface associated with each controlled (state) variable is x_i . Then, slide surface is presented by:

$$S_i = 0. (9)$$

This formulation of the sliding surface ensures that ensuring that the dynamics of the controlled variables remain stable and the desired objectives are achieved with high precision. In the case of the reference x_i^{ref} is constant, the derivative of S_i in time-dependent is:

$$S_i = \frac{\mathrm{d}}{\mathrm{d}t} \left(x_i^{ref} - x_i \right) = -\frac{\mathrm{d}x_i}{\mathrm{d}t} \,. \tag{10}$$

Equation (10) can be rewritten as:

$$S_{i} = -\sum_{i=1}^{n} a_{ij} \cdot x_{i} - \sum_{k} b_{k}^{1} \cdot u_{k} , \qquad (11)$$

for a linear system of order n and in the absence of disturbances.

In the Ku framework, a single input u_i is directly associated with S_i , leading to the following relationship:

$$S_i = -\sum_{j=1}^n a_{ij} \cdot x_j - b_i \cdot u_i, \qquad (12)$$

where u_i is defined as:

$$u_{i} = \frac{1}{b_{i}} \left(-S_{i} - \sum_{i=1}^{n} a_{ij} \cdot x_{j} \right), \tag{13}$$

where $\sum_{j=1}^{n} a_{ij} \cdot x_j$ is the term that corresponding to the

control input required on the slide surface ($S_i = 0$) and S_i is the term which leads the regulated state variable towards the slide surface. To guarantee the stability we use the Lyapunov criterion that we apply to S_i :

$$S_i \cdot S_i < 0. \tag{14}$$

Then we have:

$$S_i = -q \cdot \operatorname{sign}(S_i) - k \cdot S_i , \qquad (15)$$

01

$$S_i = -k|S_i|^{\alpha} \cdot \text{sign}(S_i)$$
 with $0 < \alpha < 1$, (16)

where q is the positive (q>0) control gain related to the switching action; k is the positive (k>0) linear feedback gain that introduces a damping effect; α is the nonlinear exponent that modifies the surface dynamics, allowing finite-time convergence and further reduction of chattering effects.

A nonlinear sliding surface is defined as a function of the system's state variables, enabling the derivation of control inputs. The methodology involves designing an appropriate sliding surface and computing the equivalent nonlinear control values for each regulated variable. By leveraging the Ku transformation, the sliding surfaces for the rotor currents are formulated as follows:

$$\begin{cases} S(i_{rf}) = \left(i_{rf}^{ref} - i_{rf}\right); \\ S(i_{rb}) = S\left(i_{rf}^{*}\right). \end{cases}$$
(17)

The derived of the surfaces gives:

$$\begin{cases}
S(i_{rf}) = \begin{pmatrix} *ref - i_{rf}^* \\ i_{rf}^* - i_{rf}^* \end{pmatrix}; \\
S(i_{rb}) = \begin{pmatrix} i_{ref}^* - i_{rb}^* \\ i_{rb}^* - i_{rb}^* \end{pmatrix}.
\end{cases} (18)$$

After the calculation we have:

$$\begin{cases}
S(i_{rf}) = \left(i_{rf}^{*ref} + \frac{1}{L_r} \cdot \left(V_{rf} - R_r \cdot i_{rf} + j \cdot \omega_r \cdot \varphi_{rf}\right)\right); \\
S(i_{rb}) = S(i_{rf}^*)
\end{cases} (19)$$

We put $V_{rf} = V_{rf}^{eq} + V_{rf}^n$ and $V_{rb} = V_{rb}^{eq} + V_{rb}^n$ then the control becomes:

$$\begin{cases} S(i_{rf}) = i_{rf}^{*ref} + \frac{1}{L_r} \cdot \left(V_{rf}^{eq} + V_{rf}^n \right) - R_r \cdot i_{rf} + j \cdot \omega_r \cdot \varphi_{rf} \right); \\ S(i_{rb}) = S(i_{rf}^*) \end{cases}$$
(20)

In the steady state the sliding mode is:

$$S_i = 0$$
, $S(i) = 0$, $V_{rf}^n = 0$ and $V_{rb}^n = 0$.

Then the rotor voltage expression becomes:

$$\begin{cases} V_{rf} = V_{rf}^{eq} + V_{rf}^{n}; \\ V_{rb} = V_{rf}^{*}. \end{cases}$$
 (21)

Consequently, the commutation terms are:

$$\begin{cases} V_{rf}^{n} = k \cdot V_{rf} \cdot \operatorname{sign}(S(i_{rf})); \\ V_{rb}^{n} = V_{rf}^{n*}. \end{cases}$$
 (22)

Study of unbalanced voltage effects on DFIG operation.

1. Unbalanced supply voltage modelling. Modelling unbalanced supply voltage disturbances is essential to understanding their impact on systems like the DFIG. Voltage unbalance occurs when the three-phase voltages have unequal amplitudes or are not 120° out of phase, often due to phase loss, single-phase loads, or issues in

the power source. This unbalance can significantly reduce motor lifespan and lead to voltage drops, interrupting industrial processes. These transients, with varying amplitude and frequency, can degrade or destroy motor winding insulation. It is recommended to avoid operating motors with a voltage unbalance greater than 5 %, as this can cause a current unbalance of around 40 %. The calculation of unbalance can be approximated by the voltage unbalance factor (VUF, in %) equation that is the expression of the Standards [33–35]:

$$VUF = (V_n / V_p) \cdot 100 \%$$

 ${\rm VUF} = (V_n \, / \, V_p) \cdot 100 \, \%,$ where $V_p, \ V_n$ are the amplitudes of the positive and negative sequence, respectively.

The unbalanced supply voltage can be expressed as: $V_{unb}(t) = V_{ref} \cdot (1 + \delta(t)),$

where V_{ref} is the reference voltage underbalanced conditions; $\delta(t)$ is the voltage deviation due to the imbalance, which varies over time.

The total unbalance in the system can be quantified using VUF, which measures the degree of unbalance, with higher values indicating greater imbalance:

$$VUF = \frac{\sqrt{\left(\Delta V_a\right)^2 + \left(\Delta V_b\right)^2 + \left(\Delta V_c\right)^2}}{V_{ref}},$$
 (24)

where ΔV_a , ΔV_b , ΔV_c are the deviations in each phase due to the unbalance.

Voltage unbalance is assumed at the stator, directly connected to the grid, eliminating the need to reconfigure the machine's equations. Since control is applied at the rotor level, it remains unaffected by the unbalance, requiring no adjustments. Under unbalanced conditions, only the stator's electrical equation is modified to account for unbalanced voltages, while the rotor's electrical and mechanical equations remain unchanged:

$$V_{sf} = \sqrt{\frac{3}{2}} \left(V_{sd} e^{+i\omega t} + V_{si} e^{-i\omega t} \right), \tag{25}$$

where V_{sd} , V_{si} are the RMS values of the direct and inverse sequence voltages, respectively; and:

$$\begin{cases} i_{sf} = i_{sfd} + i_{sfi}; \\ i_{sb} = i_{sf}^*. \end{cases}$$
 (26)

Unbalanced supply voltage disturbances are a common issue in DFIGs used in wind energy systems. These disturbances can significantly impact system performance and stability, causing torque ripple, increased power losses, overheating of components, and a reduced system lifespan. Additionally, they impair the effectiveness of the voltage controller, leading to less efficient power generation.

2. Mathematical modelling of voltage imbalance impact on DFIG performance. To account for the voltage imbalance in the DFIG, the equations governing active and reactive power need to be adjusted.

Indeed, in the case of an unbalanced supply voltage, these equations must account for the voltage deviations ΔV_a , ΔV_b , ΔV_c , which will modify the power calculations and the control strategies used to maintain stability. After considering the unbalanced stator voltages $V_a^{'}$, $V_b^{'}$, $V_c^{'}$:

$$V_{a}^{'} = V_{a} + \Delta V_{a}; \quad V_{b}^{'} = V_{b} + \Delta V_{b}; \quad V_{c}^{'} = V_{c} + \Delta V_{c}. \quad (27)$$

The active power P and the reactive power Qprovided by the DFIG are expressed as:

$$\begin{cases}
P = \frac{3}{2} \left(V_a' \cdot I_a^* + V_b' \cdot I_b^* + V_c' \cdot I_c^* \right) \\
Q = \frac{3}{2} \left(V_a' \cdot I_a^{*'} + V_b' \cdot I_b^{*'} + V_c' \cdot I_c^{*'} \right)
\end{cases} (28)$$

where I_a^* , I_b^* , I_c^* are the complex conjugates of the currents in each phase; $I_a^{*'}$, $I_b^{*'}$, $I_c^{*'}$ are the phase currents in quadrature with the voltages.

The inclusion of ΔV_a , ΔV_b , ΔV_c , in the voltages leads to changes in the reactive power produced by the system. The electromagnetic torque T_{em} produced by the DFIG is directly related to the active power P and the rotor speed ω_r . Under balanced conditions, the torque can be expressed as:

$$T_{em} = P/\omega_r . (29)$$

The revised equation for the electromagnetic torque, taking into account the voltage deviations, can be expressed as:

$$T_{em}' = P'/\omega_r . ag{30}$$

Power losses P_{loss} in the system can increase due to unbalanced voltages, as they cause higher currents and additional losses in both the stator and rotor circuits:

$$P_{loss} = R_s \cdot I_s^2 + R_r \cdot I_r^2 \,, \tag{31}$$

 $P_{loss} = R_s \cdot I_s^2 + R_r \cdot I_r^2,$ where R_s , R_r are the stator and rotor resistances; I_s , I_r are the currents in the stator and rotor under unbalanced voltage conditions. These currents increase due to the imbalance, leading to higher losses. As a result, the efficiency η is reduced due to the increased losses.

$$\eta = \frac{P_{out}}{P_{in}} = \frac{P_{out}}{P_{out} + P_l},$$
 (32) where P_l is the mechanical output power; P_{in} , P_{out} are the

electrical input and output powers. Under unbalanced voltage conditions, as losses increase, the efficiency decreases.

3. Active fault-tolerant control description. The primary goal of the AFT-SMC strategy is to maintain the operational performance of the DFIG by enabling rapid fault detection and adaptive control adjustments to mitigate their impact, thereby ensuring high equipment availability and system reliability. AFT-SMC is particularly well suited to this application because of its robustness to disturbances and its ability to react quickly and effectively to faults. This rapid response reduces service interruptions and improves the overall resilience of the system, even in degraded conditions.

AFT-SMC is a strategy designed to maintain safe and effective system operation despite faults, which is crucial for critical systems like DFIGs in wind turbines. AFT-SMC consists of 4 key components (Fig. 1): fault detection, fault isolation, reconfiguration, and system adaptation. The fault detection block identifies anomalies in the system and activates the reconfiguration mechanism quickly.

The fault isolation block minimizes the impact of the typically through modularization. Finally, the reconfiguration mechanism adapts the controller to the system's behavior in both normal and faulty conditions. After detecting, locating, and identifying the fault, the system must adopt a strategy that ensures continued operation while providing accurate information about the faulty situation.

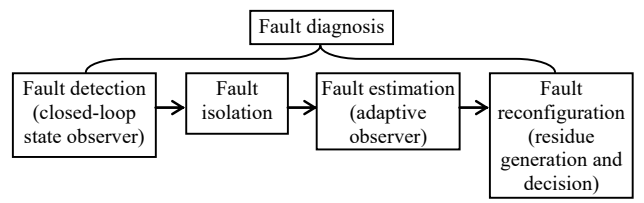


Fig. 1. AFT-SMC strategy scheme

Fault detection can be modelled using a criterion based on monitoring key system parameters. This approach involves tracking the deviation of parameter values from normal operating thresholds.

$$\delta(t) = |y(t) - y_{ref}(t)|, \qquad (33)$$

where y(t) is the system's output; $y_{ref}(t)$ is the reference value (the expected value). If $\delta(t)$ exceeds a critical threshold $\delta_{th}(t)$, a fault is detected. We have:

- fault detected if: $\delta(t) > \delta_{th}(t)$;
- no fault if: $\delta(t) \leq \delta_{th}(t)$.

Fault isolation identifies the specific location of a fault within the system, aiming to minimize deviation errors by precisely isolating the fault's origin. A common localization technique uses the deviation of outputs from each component to identify the origin of the fault. For a DFIG, fault isolation can be represented by the deviation between observed system values and those predicted under various fault scenarios, enabling precise identification of the fault location.

$$e(t) = \hat{y}(t) - \tilde{y}(t), \tag{34}$$

where $\hat{y}(t)$, $\tilde{y}(t)$ are the estimated and actual system outputs. The error is defined as the difference between them.

When an abnormality is detected and isolated, the controller is reconfigured to adapt to the changed operating conditions. This adjustment involves updating the control model to mitigate the impact of the fault. The active and reactive power control equations are therefore modified as:

$$\begin{cases} P = V_s \cdot I_s \cdot \cos(\theta_s - \theta_r); \\ Q = V_s \cdot I_s \cdot \sin(\theta_s - \theta_r), \end{cases}$$
(35)

where θ_s , θ_r are the respective angles of the stator and rotor voltages.

Indeed, the control must be adjusted to compensate for the loss of performance as well as the change in the system's behavior. This should be done by modifying the converter or generator control:

$$\begin{cases}
P_{re} = P + \Delta P; \\
Q_{re} = Q + \Delta Q,
\end{cases}$$
(36)

where P_{re} , Q_{re} are the active and reactive reconfigured power; ΔP , ΔQ are the necessary adjustments to maintain the system's balance after the fault.

When a fault is identified, the controller must modify its behavior in response to the diagnostic information to effectively handle the changed conditions. This adaptive controller is represented by a dynamic gain function that adjusts according to the system parameters:

$$u(t) = K(t) \cdot e(t), \tag{37}$$

where u(t) is the controller output (control signal); K(t) is an adaptive gain that depends on the system's operating conditions and the detected errors; e(t) is the error between the measured output and the reference output.

To mitigate the effects of voltage unbalance, the control system must dynamically adapt the operation of the generator and converter to maintain system stability and ensure efficient energy delivery. This is achieved through adjustments to the converter duty cycle, reconfiguration of control parameters, or compensation for the imbalance by modulating the generator output. Consequently, the stator active and reactive power equations are updated as:

$$\begin{cases} P_{s} = V_{sf} \cdot (i_{sfd} + i_{sfi}) + V_{sf}^{*} \cdot i_{sf}^{*}; \\ Q_{s} = V_{sf}^{*} \cdot (i_{sfd} + i_{sfi}) + V_{sf} \cdot i_{sf}^{*}. \end{cases}$$
(38)

In this transformation i_{sf} is the conjugate of i_{sb} . Then:

$$\begin{cases} P_s = 2 \cdot V_{sf} \cdot (i_{sfd} + i_{sfi}); \\ Q_s = 2 \cdot V_{sf}^* \cdot (i_{sfd} + i_{sfi}). \end{cases}$$
(39)

Simulation results and discussions.

1. Healthy condition. To demonstrate the effectiveness of the control approach, we use MATLAB. First, to confirm the effectiveness of the control, we represent the sliding surfaces (Fig. 2). We observe the fastest convergence time and the least amount of interference in the control.

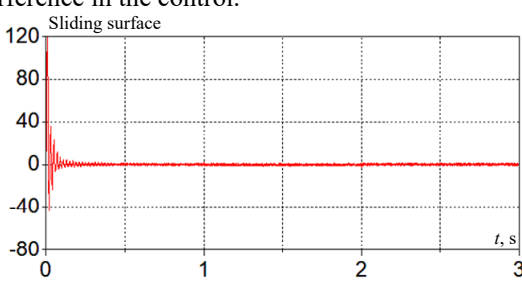


Fig. 2. Sliding surface in healthy situation

In Fig. 3, 4, the active and reactive powers in the output sliding mode control perfectly follow the desired variables. We note that the outputs are fast during the transient state, and the static error tends to zero. The results indicate that the control dynamics exhibit rapid response and accurately track the steady-state reference with negligible static error.

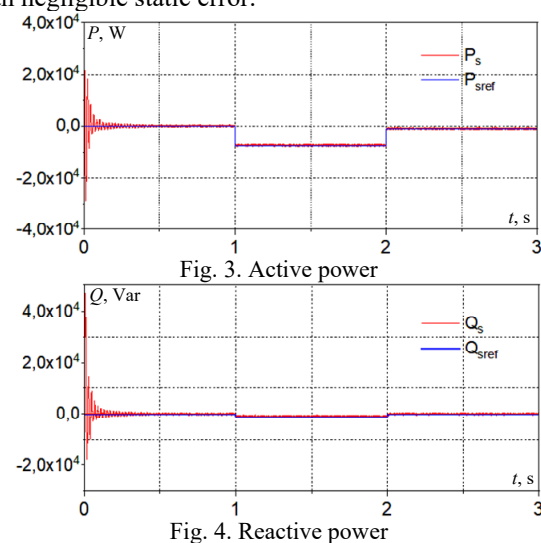
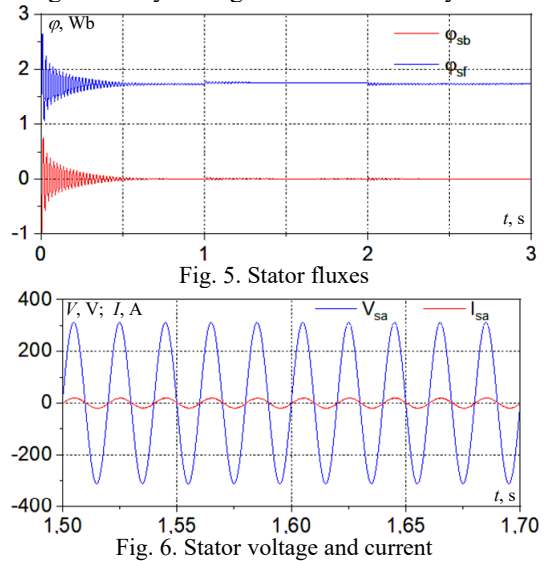


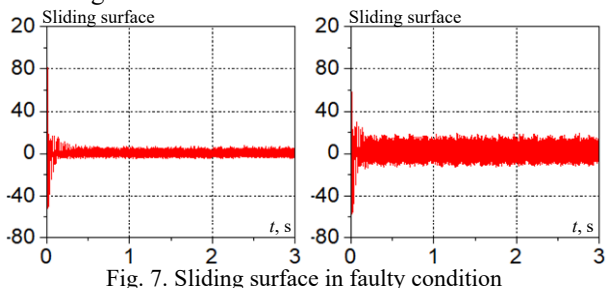
Figure 5 shows the stator fluxes curves, where the flux-oriented strategy is clearly observable. Figure 6 provides a detailed presentation of the generated stator

voltage (phase A) and its associated current. We notice that the generated stator voltage meets the desired amplitude and frequency. From these results, we can conclude that speed regulation by sliding mode is satisfactory.



2. Faulty condition. An unbalanced fault occurs in one phase of the machine's stator supply.

In Fig. 7 we observe the effect of the fault on the sliding surface. We note that the sliding surface of the machine with the fault is significantly larger compared to the sliding surface without the fault.



Indeed, unbalanced supply voltages can cause the DFIG to deviate from the desired sliding surface due to inaccuracies in the estimation of rotor currents or a mismatch between actual and reference values.

We also observe excessive oscillations when the fault occurs. These oscillations vary within a maximum interval, a phenomenon known as chattering. Despite these oscillations, the control remains accurate to its setpoint. Therefore, the control design is clearly independent of the disturbance applied to the system.

The fault-tolerant control performance of the DFIG is demonstrated in Fig. 8–10 under 30 % voltage unbalance. The strategy exhibits robustness, as evidenced by the consistent tracking of the reference set-point despite oscillations around the target value. To implement an adaptive fault-tolerant control scheme, residual signatures from the control parameters must be defined and analyzed. The key goal of fault-tolerant control is to identify and interpret fault-induced spectral characteristics within the system, enabling effective mitigation and adaptive system response. Indeed, to extract the specific fault signatures and highlight our results, a spectral analysis of the active power is conducted. The chosen diagnostic method is based on fast Fourier transform (FFT).

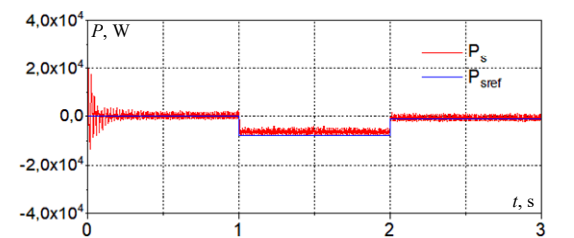


Fig. 8. Active power after unbalanced supply voltage condition

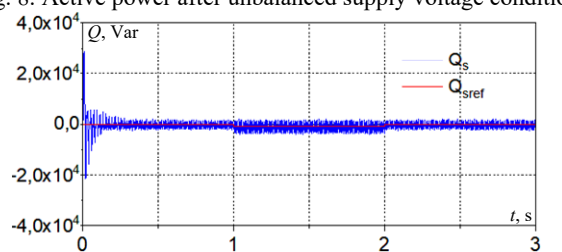


Fig. 9. Reactive power after unbalanced supply voltage condition

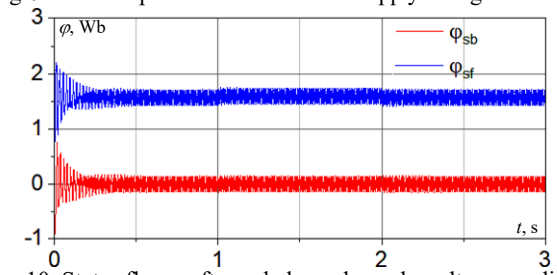


Fig. 10. Stator fluxes after unbalanced supply voltage condition

This model-based diagnostic approach involves detecting faults by studying certain frequency components that appear in the stator current and instantaneous stator power spectrums. The analysis of the spectral content of partial instantaneous power (the instantaneous power of a stator phase), as defined as the product of the line current, offers important insights for characterizing the voltage imbalance phenomenon in the machine.

Figure 11 shows the spectral characteristics of active power under voltage imbalance conditions.

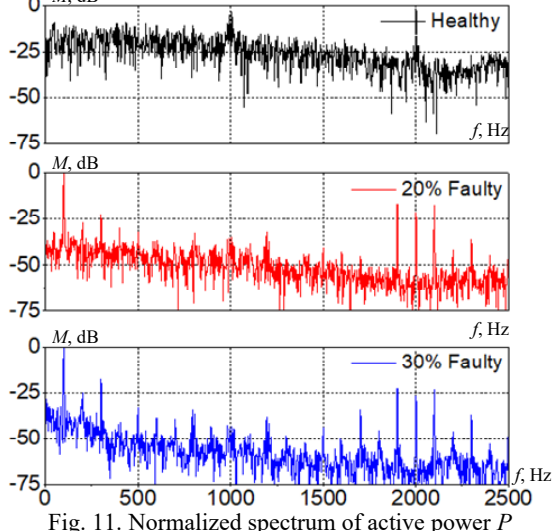
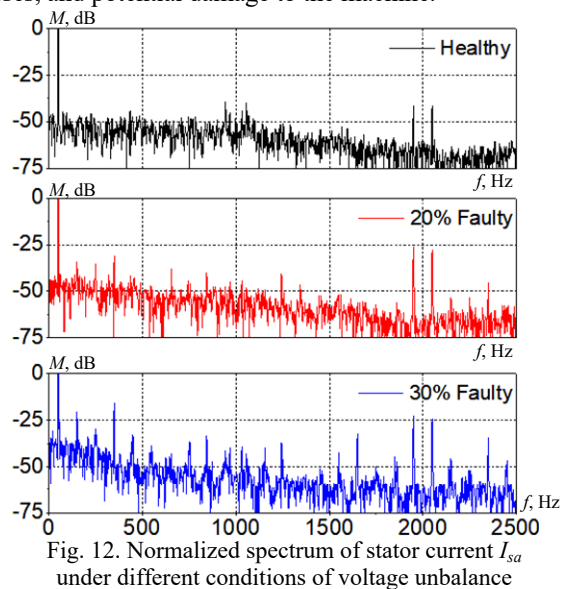


Fig. 11. Normalized spectrum of active power *P* under different conditions of voltage unbalance

Several frequency components may appear in the spectrum. The analysis reveals the existence of harmonic components at integer multiples of the fundamental frequency $(k \cdot f_s)$, arising due to disturbances within the system. In the presence of voltage imbalance, the amplitude

of the harmonics varies from phase to phase, leading to an asymmetrical harmonic content in the active power spectrum. Imbalance frequencies become clearly noticeable when different levels of fault are applied. Their severity is linked to the increase in fault severity applied to the system.

Figure 12 shows the spectral content of the stator current I_{sa} under unbalanced supply voltage conditions. Voltage imbalance refers to the uneven distribution or asymmetry of voltage levels between the machine's phases. The frequency components examined in the stator current signal show an increase in certain harmonics directly related to the fault, as well as the appearance of other frequencies that are multiples of the fundamental. These frequencies cause multiple impacts of voltage imbalance on machine performance, including torque ripple, increased losses, and potential damage to the machine.



Conclusions. This work introduces a robust active fault-tolerant strategy based on sliding mode control (AFT-SMC) for doubly-fed induction generators (DFIGs), combined with an advanced real-time spectral fault diagnosis system. The methodology addresses 2 major challenges in wind energy systems: maintaining system stability under severe grid disturbances, and accurately diagnosing electrical faults in real time.

Unlike conventional vector control schemes, the proposed AFT-SMC approach effectively mitigates the adverse effects of voltage unbalance, such as torque ripple and unstable current profiles, by dynamically adjusting the control surface based on fault severity. This is made possible by integrating a diagnostic module based on fast Fourier transform, which detects characteristic harmonic distortions in both the stator current and active power signals. These harmonic components are shown to correlate directly with fault magnitude, enabling a precise and adaptive fault response mechanism.

Extensive simulation results conducted under a realistic 30 % voltage unbalance scenario demonstrate the superior performance of the proposed strategy. The controller achieves a voltage recovery time of approximately 0.28 s, compared to 0.42 s with standard vector control, highlighting faster system stabilization. Moreover, electromagnetic torque oscillations are reduced by around 45 %, significantly lowering mechanical stress

and enhancing system lifespan. The integrated diagnostic system further achieves a fault classification accuracy of 94.6 %, ensuring early fault identification and improving operational reliability. These quantitative results confirm that the proposed AFT-SMC framework not only improves transient and steady-state performance but also advances fault resilience through embedded intelligence. By integrating control and diagnosis within a unified framework, the proposed methodology offers a powerful predictive maintenance, minimizing solution for downtime and significantly improving the operational reliability of wind turbine systems. This work establishes a solid foundation for future deployment in large-scale renewable energy infrastructures, where resilience to faults, autonomous operation, and efficiency are paramount. Although the current validation is based on detailed and realistic simulations, future research will focus on experimental implementation to assess the controller's performance under real-world conditions.

This progressive research pathway, from rigorous simulation to practical validation, reinforces the robustness, scalability, and technological relevance of the proposed strategy. In summary, the developed AFT-SMC approach represents a significant and practical advancement in fault-tolerant control of DFIG-based wind energy systems. It addresses key challenges in modern smart grids and holds strong promise for accelerating the integration of reliable, intelligent renewable energy technologies on a large scale.

Conflict of interest. The authors declare that they have no conflicts of interest.

REFERENCES

- *I.* Qazi A., Hussain F., Rahim N.A., Hardaker G., Alghazzawi D., Shaban K., Haruna K. Towards sustainable energy: a systematic review of renewable energy sources, technologies, and public opinions. *IEEE Access*, 2019, vol. 7, pp. 63837-63851. doi: https://doi.org/10.1109/ACCESS.2019.2906402.
- **2.** Ahmed M., Shimada K. The effect of renewable energy consumption on sustainable economic development: evidence from emerging and developing economies. *Energies*, 2019, vol. 12, no. 15, art. no. 2954. doi: https://doi.org/10.3390/en12152954.
- 3. Sun L., Mi Z., Yu Y., Wu T., Tian H. Active power and reactive power regulation capacity study of DFIG wind turbine. 2009 International Conference on Sustainable Power Generation and Supply, 2009, pp. 1-6. doi: https://doi.org/10.1109/SUPERGEN.2009.5348144.
- 4. Ghennam T., Berkouk E.M., Francois B. Modeling and control of a Doubly Fed Induction Generator (DFIG) based Wind Conversion System. 2009 International Conference on Power Engineering, Energy and Electrical Drives, 2009, pp. 507-512. doi: https://doi.org/10.1109/POWERENG.2009.4915230.
- 5. Kaddache M., Drid S., Khemis A., Rahem D., Chrifi-Alaoui L. Maximum power point tracking improvement using type-2 fuzzy controller for wind system based on the double fed induction generator. *Electrical Engineering & Electromechanics*, 2024, no. 2, pp. 61-66. doi: https://doi.org/10.20998/2074-272X.2024.2.09.
- **6.** Bouraghda S., Sebaa K., Bechouat M., Sedraoui M. An improved sliding mode control for reduction of harmonic currents in grid system connected with a wind turbine equipped by a doubly-fed induction generator. *Electrical Engineering & Electromechanics*, 2022, no. 2, pp. 47-55. doi: https://doi.org/10.20998/2074-272X.2022.2.08.
- 7. Kini P.G., Bansal R.C., Aithal R.S. A novel approach toward interpretation and application of voltage unbalance factor. *IEEE Transactions on Industrial Electronics*, 2007, vol. 54, no. 4, pp. 2315-2322. doi: https://doi.org/10.1109/TIE.2007.899935.
- 8. Jannati M., Idris N.R.N., Salam Z. A new method for modeling and vector control of unbalanced induction motors. 2012 IEEE Energy

- Conversion Congress and Exposition (ECCE), 2012, pp. 3625-3632. doi: https://doi.org/10.1109/ECCE.2012.6342483.
- 9. Touil A., Babaa F. Studying of unbalanced supply voltage effects on three-phase induction motor performances based on line neutral voltage analytical calculation. *Lecture Notes in Electrical Engineering*, 2024, vol. 1147 LNEE, pp. 455-467. doi: https://doi.org/10.1007/978-981-97-0045-5 41.
- 10. Maurer F., Toftevaag T.L., Noland J.K. An analytical prediction model of balanced and unbalanced faults in doubly fed induction machines. *IEEE Transactions on Industrial Electronics*, 2023, vol. 70, no. 1, pp. 189-199. doi: https://doi.org/10.1109/TIE.2022.3146540.
- *11.* Barambones O., Alkorta P. Position control of the induction motor using an adaptive sliding-mode controller and observers. *IEEE Transactions on Industrial Electronics*, 2014, vol. 61, no. 12, pp. 6556-6565. doi: https://doi.org/10.1109/TIE.2014.2316239.
- 12. Bennassar A., Banerjee S., Jamma M., Essalmi A., Akherraz M. Real time high performance of sliding mode controlled induction motor drives. *Procedia Computer Science*, 2018, vol. 132, pp. 971-982. doi: https://doi.org/10.1016/j.procs.2018.05.113.
- 13. Farhi S.E., Sakri D., Golea N. High-performance induction motor drive based on adaptive super-twisting sliding mode control approach. *Archives of Electrical Engineering*, 2022, vol. 71, no. 1, pp. 245-263. doi: https://doi.org/10.24425/aee.2022.140208.
- 14. Fetene Y., Shibeshi D. Fractional order sliding mode speed control of feedback linearized induction motor. Power Electronics and Drives, 2020, vol. 5, no. 1, pp. 109-122. doi: https://doi.org/10.2478/pead-2020-0010.
- 15. Lascu C., Argeseanu A., Blaabjerg F. Supertwisting sliding-mode direct torque and flux control of induction machine drives. *IEEE Transactions on Power Electronics*, 2020, vol. 35, no. 5, pp. 5057-5065. doi: https://doi.org/10.1109/TPEL.2019.2944124.
- 16. Jafarian M.J., Nazarzadeh J. Spectral analysis for diagnosis of bearing defects in induction machine drives. *IET Electric Power Applications*, 2019, vol. 13, no. 3, pp. 340-348. doi: https://doi.org/10.1049/iet-epa.2018.5226.
- 17. Boudali A., Negadi K., Boudiaf M., Berkani A., Marignetti F. Super twisting sliding mode controller of small hydropower plant energy generation based DFIG. *Przegląd Elektrotechniczny*, 2020, vol. 96, no. 10, pp. 136-143. doi: https://doi.org/10.15199/48.2020.10.25.
- 18. Begam S.R., Burthi L.R., Depuru S.R. Adaptive neuro-fuzzy sliding mode controller (ANF-SMC) to control speed, electromagnetic torque (EMT), stator current, and back EMF using PMBLDCmotor(PMBLDCM) in electric propulsion of electric vehicles. Przegląd Elektrotechniczny, 2023, no. 8, pp. 49-62. doi: https://doi.org/10.15199/48.2023.08.09.
- 19. Sakri D., Laib H., Farhi S.E., Golea N. Sliding mode approach for control and observation of a three phase AC-DC pulse-width modulation rectifier. *Electrical Engineering & Electromechanics*, 2023, no. 2, pp. 49-56. doi: https://doi.org/10.20998/2074-272X.2023.2.08.
- 20. Wang X., Wang Z., Xu Z., He J., Zhao W. Diagnosis and tolerance of common electrical faults in T-type three-level inverters fed dual three-phase PMSM drives. IEEE Transactions on Power Electronics, 2020, vol. 35, no. 2, pp. 1753-1769. doi: https://doi.org/10.1109/TPEL.2019.2920400.
- 21. Bolognani S., Zordan M., Zigliotto M. Experimental fault-tolerant control of a PMSM drive. *IEEE Transactions on Industrial Electronics*, 2000, vol. 47, no. 5, pp. 1134-1141. doi: https://doi.org/10.1109/41.873223.
- 22. Siddiqui K.M., Sahay K., Giri V.K. Stator Inter-turn fault detection in inverter fed induction motor drives. *International Journal of Applied Power Engineering (IJAPE)*, 2017, vol. 6, no. 2, pp. 89-102. doi: https://doi.org/10.11591/ijape.v6.i2.pp89-102.
- 23. Namdar A., Samet H., Allahbakhshi M., Tajdinian M., Ghanbari T. A robust stator inter-turn fault detection in induction motor utilizing Kalman filter-based algorithm. *Measurement*, 2022, vol. 187, art. no. 110181. doi: https://doi.org/10.1016/j.measurement.2021.110181.

- 24. Nikpayam M., Ghanbari M., Esmaeli A., Jannati M. Vector control methods for star-connected three-phase induction motor drives under the open-phase failure. *Journal of Operation and Automation in Power Engineering*, 2022, vol. 10, no. 2, pp. 155-164. doi: https://doi.org/10.22098/joape.2022.8802.1616.
- 25. Merabet A., Eshaft H., Tanvir A.A. Power-current controller based sliding mode control for DFIG-wind energy conversion system. *IET Renewable Power Generation*, 2018, vol. 12, no. 10, pp. 1155-1163. doi: https://doi.org/10.1049/iet-rpg.2017.0313.
- 26. Chavhan R., Kulkarni V.A. Negative sequence component for detection of inter-turn fault of transformer. *International Journal of Innovative Research in Science, Engineering and Technology*, 2017, vol. 6, no. 7, pp. 13950-13958. doi: https://doi.org/10.15680/IJIRSET.2017.0607172.
- 27. Huang G., Luo Y.-P., Zhang C.-F., Huang Y.-S., Zhao K.-H. Current sensor fault diagnosis based on a sliding mode observer for PMSM driven systems. *Sensors*, 2015, vol. 15, no. 5, pp. 11027-11049. doi: https://doi.org/10.3390/s150511027.
- 28. Jiang J., Yu X. Fault-tolerant control systems: a comparative study between active and passive approaches. *Annual Reviews in Control*, 2012, vol. 36, no. 1, pp. 60-72. doi: https://doi.org/10.1016/j.arcontrol.2012.03.005.
- **29.** Amin A.A., Hasan K.M. A review of fault tolerant control systems: advancements and applications. *Measurement*, 2019, vol. 143, pp. 58-68. doi: https://doi.org/10.1016/j.measurement.2019.04.083.
- 30. Moussaoui L., Aouaouda S., Rouaibia R. Fault tolerant control of a permanent magnet synchronous machine using multiple constraints Takagi-Sugeno approach. *Electrical Engineering & Electromechanics*, 2022, no. 6, pp. 22-27. doi: https://doi.org/10.20998/2074-272X.2022.6.04.
- *31.* Noura H., Sauter D., Hamelin F., Theilliol D. Fault-tolerant control in dynamic systems: application to a winding machine. *IEEE Control Systems Magazine*, 2000, vol. 20, no. 1, pp. 33-49. doi: https://doi.org/10.1109/37.823226.
- 32. Rahali H., Zeghlache S., Cherif B.D.E., Benyettou L., Djerioui A. Robust adaptive fuzzy type-2 fast terminal sliding mode control of robot manipulators in attendance of actuator faults and payload variation. *Electrical Engineering & Electromechanics*, 2025, no. 1, pp. 31-38. doi: https://doi.org/10.20998/2074-272X.2025.1.05.
- 33. IEEE Recommended Practice for Monitoring Electric Power Quality. IEEE Std 1159-2009, 26 June 2009, 94 p. doi: https://doi.org/10.1109/IEEESTD.2009.5154067.
- 34. IEC 61000-4-30:2015+AMD1:2021 CSV. Electromagnetic compatibility (EMC) Part 4-30: Testing and measurement techniques Power quality measurement methods, 2021, 292 p.
- 35. Standard NRS 048-2:2003. Electricity Supply Quality of Supply. Part 2: Voltage Characteristics, Compatibility Levels, Limits and Assessment Methods. Standards South Africa, 2013. 33 p.

Received 07.06.2025 Accepted 13.08.2025 Published 02.11.2025

- N. Hamdi 1, Doctor of Electrical Engineering,
- F. Babaa², Doctor of Electrical Engineering,
- A. Touil², Doctor of Electrical Engineering,
- N. Merabet², PhD,
- ¹ Laboratory of Electronics and New Technology,
- University of Oum El Bouaghi, Algeria,
- e-mail: hamdi naouel@yahoo.fr
- ² Electrical Laboratory of Constantine «LE»,
- University Freres Mentouri Constantine 1, Algeria,
- e-mail: babaa.fatima@yahoo.fr;
- abderrahim.touil@lec-umc.org (Corresponding Author); nacer.merabet1@doc.umc.edu.dz

How to cite this article:

Hamdi N., Babaa F., Touil A., Merabet N. Robust fault-tolerant sliding mode control and advanced fault diagnosis for doubly-fed induction generators. *Electrical Engineering & Electromechanics*, 2025, no. 6, pp. 32-39. doi: https://doi.org/10.20998/2074-272X.2025.6.05

B.I. Kuznetsov, T.B. Nikitina, I.V. Bovdui, K.V. Chunikhin, V.V. Kolomiets, B.B. Kobylianskyi

Synthesis of combined shielding system for overhead power lines magnetic field normalization in residential building space

Problem. Most studies of power frequency magnetic field reduced to safe level in residential buildings located near overhead power lines carried out based on two-dimensional magnetic field modeling, which does not allow studying of original magnetic field shielding effectiveness in residential building edges. The goal of the work is synthesis of combined active and multi-circuit passive shielding system to improve shielding efficiency of initial magnetic field to sanitary standards level in residential building edges generated by overhead power lines. Methodology. System synthesis methodology based on vector game solution, in which vector payoff calculated based on of Maxwell's equations solution in a quasi-stationary approximation using the COMSOL Multiphysics software. Vector game solution calculated based on hybrid optimization algorithm, which globally explores synthesis search space using Particle Swarm Optimization and gradient-based Sequential Quadratic Programming to rapidly calculated optimum synthesis point from Pareto optimal solutions taking into account binary preference relations. Results. During combined active and multi-circuit passive shielding system synthesisspatial arrangement coordinates of 16 contours of passive shield and two compensating windings, as well as windings currents and phases of active shield calculated. New scientific results are theoretical and experimental studies of synthesized combined active and multi-circuit passive shielding system efficiency for magnetic field created by overhead power lines. Scientific novelty. For the first time synthesis methodology for combined active and multi-circuit passive shielding system taking into account original field shielding effectiveness decrease in residential building edges for more effective reduction of industrial frequency magnetic field created by overhead power lines developed. Practical value. Practical recommendations for the reasonable choice of the spatial arrangement of a multi-circuit passive shield and two shielding windings of active shielding system for magnetic field created by overhead power lines are given. The possibility of reducing the initial magnetic field induction to the sanitary standards level is shown. References 42, figures 16. Key words: overhead power line, magnetic field, combined electromagnetic active and passive shielding system, synthesis computer simulation, experimental research.

Проблема. Більшість досліджень з зниження рівня магнітного поля промислової частоти в житлових будинках, що розташовані поблизу повітряних ліній електропередачі, до безпечного рівня, виконані на основі двовимірного моделювання магнітного поля, що не дозволяє вивчати ефективність екранування вихідного магнітного поля на краях житлових будинків. **Метою** роботи є синтез комбінованої активної та багатоконтурної пасивної електромагнітної екрануючої систем для підвишення ефективності екранування вихідного магнітного поля до рівня санітарних норм на краях житлових будинків, що генерується повітряними лініями електропередачі. Методологія. Методологія синтезу системи заснована на рішенні векторної гри, в якій векторний виграш розраховується на основі розв'язку рівнянь Максвелла в квазістаціонарному наближенні за допомогою програмного пакету COMSOL Multiphysics. Рішення векторної гри обчислюється на основі гібридного алгоритму оптимізації, яке глобально досліджує простір пошуку для синтезу за допомогою оптимізації роєм частинок та градієнтного послідовного квадратичного програмування для швидкого обчислення оптимальної точки синтезу з системи Парето оптимальних рішень з урахуванням бінарних відношень переваг. Результати. В процесі синтезу активної та багатоконтурної пасивної електромагнітної екрануючих систем розраховано координати просторового розташування 16 контурів пасивного екрану та двох компенсаційних обмоток системи активного екранування, а також струм та фази компенсуючих обмоток системи активного екранування. Новими науковими результатами є теоретичні та експериментальні дослідження ефективності синтезованої комбінованої активної та багатоконтурної пасивної електромагнітних екрануючих систем магнітного поля, що створюється повітряними лініями електропередачі. Наукова новизна. Вперше запропонована методологія синтезу комбінованих активних та багатоконтурних пасивних електромагнітних екрануючих систем з урахуванням ефективності екранування вихідного поля на краях житлових будинків з метою більш ефективного зниження магнітного поля промислової частоти, що генерується повітряними лініями електропередачі. Практична значимість. Надано практичні рекомендації щодо обтрунтованого вибору просторового розташування багатоконтурного пасивного екрана та двох екрануючих обмоток системи активного екранування магнітного поля, що генерується повітряними лініями електропередачі. Показана можливість зниження індукиїї вихідного магнітного поля до рівня санітарних норм. Бібл. 42, рис. 16.

Ключові слова: повітряна лінія електропередачі, магнітне поле, система комбінованого електромагнітного активного та пасивного екранування, синтез комп'ютерного моделювання, експериментальне дослідження.

Introduction. Protecting public health problem solving from electric power man-made electromagnetic field biological impact has high social significance and is extremely relevant and important task in population quality and life expectancy improving [1-3]. Reducing problem humanity priority of man-made electromagnetic fields influence has been confirmed by World Health Organization (WHO) and electromagnetic field influence on human body. A significant place in these studies occupied industrial-frequency electromagnetic created by power transmission lines. High-voltage overhead power lines located in residential areas are industrial-frequency magnetic fields main sources, which negatively affects on population in residential buildings located along power line routes [4-7]. The basis for substantiating these conclusions was identification of carcinogenic properties of industrial-frequency magnetic

field exposure with its weak but long-term effects on humans [1–3] and the development of recommendations for maximum possible reduction in magnetic fields induction level in residential areas located near power lines homes, to reduce likelihood of population cancer.

Carcinogenic properties identification and weak magnetic field action deadly danger with less than 1 μ T induction during its long-term exposure to people has led to gradual introduction for magnetic field induction level strict sanitary standards and these standards constant tightening of 50–60 Hz frequency magnetic field induction boundary levels with up to WHO recommended level 0.2–0.6 μ T [1–3].

Many residential buildings located in close proximity to high-voltage power lines, so that magnetic field induction level inside these buildings significantly exceeds modern sanitary standards.

© B.I. Kuznetsov, T.B. Nikitina, I.V. Bovdui, K.V. Chunikhin, V.V. Kolomiets, B.B. Kobylianskyi



Fig. 1. Residential buildings located close to power line

For example, shown in Fig. 1. residential buildings located close in proximity to main two-circuit power line 330 kV with split wires of 2 kA in each circuit. Next to this power line there is another double-circuit power line 110 kV 500 A of an older construction.

Numerous theoretical and experimental studies show [7–10] that the maximum permissible magnetic field level induction (0.5 $\mu T)$ can be exceeded by order of magnitude or more, which poses threat to health of hundreds of thousands of citizens living closer than 100 m from overhead power lines.

In addition, due to land plots price constant rise for development, the construction of residential, administrative and other public buildings and structures in places where existing high-voltage power lines pass through continues. This condition is typical for many leading countries of the world - the USA, Israel, Italy, Spain and many others and requires the adoption of urgent measures to reduce existing power lines magnetic field level by 3-5 times [4–7]. Therefore, in many leading countries of the world, methods and means of normalizing magnetic field in energy infrastructure, public buildings, and residential buildings are being intensively developed, and these means are being widely introduced [8–12].

Most effective technology is power lines reconstruction by moving them to safe distance from residential buildings, or replacing overhead power lines with cable line. However, such reconstruction requires enormous financial resources.

Existing power lines magnetic field shielding methods are less expensive. Active contour magnetic field shielding methods provided necessary efficiency. Currently, research is being intensively carried out all over the world and various systems for active shielding of man-made magnetic field of industrial frequency are being implemented [13–18].

Overhead power lines with phase wires «triangular» arrangement often pass in close proximity to older residential buildings. This power lines are one of most dangerous wire layout options for magnetic field sources. Overhead power lines with phase wires «triangular» arrangement created magnetic field with circle shape spatio-temporal characteristic. For effective active shielding of magnetic field with such a space-time characteristic, at least two compensation windings are required for active shielding system.

Active shielding requires external power sources used to generate compensating windings appropriate magnitude and phase currents to create compensating magnetic field directed opposite to power line original magnetic field, which is necessary to desired shielding effect implement.

Active shielding systems are capable of providing power lines initial magnetic field strong weakening [4].

However, this requires a rather complex automatic control system, in which, in addition to magnetic field sensors, it is necessary to install expensive high-power equipment, such as power supplies, power converters and control system that forms the currents supplied to compensating windings to achieve of original magnetic field required suppression. Active shielding systems are significantly more expensive to develop than passive methods [13–18].

Original magnetic field with passive shielding weakening achieved by compensating field generating according to Faraday law passive shield using. Multicircuit passive shields often used to increase initial magnetic field shielding efficiency [8]. However, passive shields have significantly lower shielding coefficient than active shields, so passive shields are often used as an addition to active shielding systems, so that hybrid active-passive shields simultaneously use both an active shielding system and passive shields of various designs [19].

In addition to solid electromagnetic shields [16], multicircuit passive shields also used as a passive screen [20].

The diagram of such combined electromagnetic active multi-circuit passive shielding system with multi-circuit passive shields shown in Fig. 2.

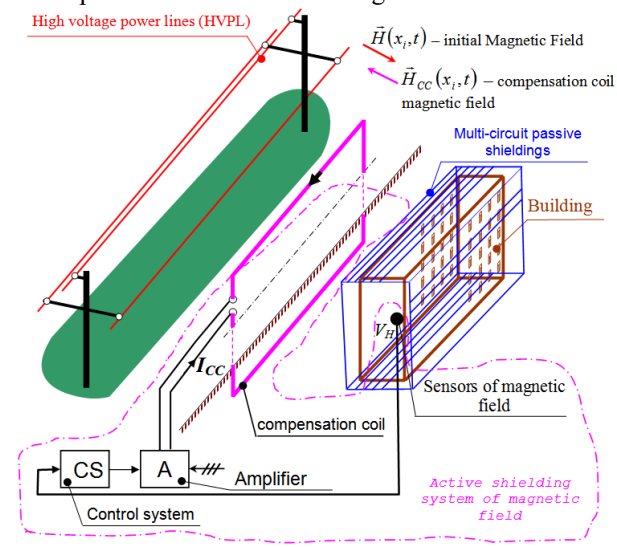


Fig. 2. Combined electromagnetic active and multi-circuit passive shielding system diagram

The active shielding system is a closed dynamic automatic control system with feedback. Using a magnetic field sensor installed in the shielding space, the resulting magnetic field measured to implement feedback.

The active shielding system generated a compensating magnetic field directed opposite to the original magnetic field using a compensating winding. The active shielding system also contains a control system and an amplifier.

With the help of a multi-circuit passive shielding system a magnetic field is generated opposite to the initial magnetic field according to the Faraday law. In this case, the initial magnetic field for the multi-circuit passive shielding system generated by power transmission line wires and compensating windings of the active shielding system.

Magnetic field induction level in residential buildings necessary reduced to safe level in apartments located at buildings edges. Most studies carried out based on two-dimensional magnetic field modeling, which does not allow studying effectiveness decrease of original field shielding in residential building edges [21–23]. Therefore, to effectively

shielding the original magnetic field throughout the entire space of a residential building, it is necessary to use a threedimensional model of the magnetic field.

The goal of the work is synthesis of combined active and multi-circuit passive shielding system to improve shielding efficiency of initial magnetic field to sanitary standards level in residential building edges generated by overhead power lines.

Definition of geometric forward magneto static problem for passive electromagnetic multi-circuit shield. Using a system of hybrid active and multi-loop passive shielding, it is necessary to generate such a compensating magnetic field in the entire shielding space that the vector of the instantaneous value of the induction of this compensating magnetic field is directed opposite to the vector of the instantaneous value of the induction of the original magnetic field generated by the power transmission line in residential building space.

To synthesize a combined active and multi-circuit passive shielding system, it is first necessary to solve three geometric direct problems of magnetostatics for three-dimensional overhead power lines magnetic field model. The first geometric direct problem of magnetostatics calculated the vector of the instantaneous value of the induction of the initial magnetic field generated by the power transmission line at a given point of the entire screening space.

The second geometric direct problem calculated the vector of the instantaneous value of the induction of the compensating magnetic field generated by the compensating windings of the active shielding system at a given point of the entire shielding space.

The third geometric direct problem of magnetostatics calculated the vector of the instantaneous value of the induction of the compensating magnetic field generated by the compensating windings of the multi-circuit passive shielding system at a given point of the entire shielding space.

Based on the solution of these three geometric direct magnetostatic problems, a geometric inverse magnetostatic problem formulated and solved for the synthesis of a hybrid active and multi-loop passive shield. This geometric inverse magnetostatic problem is an ill-posed mathematical problem and usually formulated in the form of an optimization problem. The components of the vector objective function of this optimization problem are the effective values of the resulting magnetic field induction at the points of the entire shielding space.

As result of solving this geometric inverse problem of magnetostatics, the coordinates of the «geometric» arrangement of the compensation windings of the active and multi-circuit passive shielding system, as well as the values of currents and phases in the compensation windings of the active shielding system calculated.

Three-dimensional mathematical modeling of electromagnetic field in general case comes down to boundary value problem solving for Maxwell partial differential equations system [7].

$$rot \ \mathbf{H} = \mathbf{j} + \partial_t \mathbf{D} + \mathbf{j}_{ex}; \tag{1}$$

$$rot \; \boldsymbol{E} = -\partial_t \boldsymbol{B} \;, \tag{2}$$

where E – electric field strength; H – magnetic field strength; D, B – electric and magnetic induction vectors; j – conduction current density; j_{ex} – density of external currents created by sources outside the region under consideration.

First equation (1) is generalized Ampere law – the total current density is magnetic field strength vortex.

Second equation (2) is Faraday law differential formulation that magnetic induction change over time generates vortex electric field.

Intermediate position between constant field and rapidly changing field occupied by quasi-stationary field – electromagnetic field in which displacement currents neglected in comparison with conduction currents. Maxwell equations for quasi-stationary field have form

$$rot \ \mathbf{H} = \mathbf{j} + \mathbf{j}_{ex}; \tag{3}$$

$$rot \ \mathbf{E} = -\partial_t \mathbf{B} \ . \tag{4}$$

From (3) follows that quasi-stationary magnetic field at any given time moment completely determined by electric currents distribution at the same time moment and founded from this distribution in exactly same way as is done in magnetostatics.

Power lines magnetic field calculated based on Biot-Savart law for elementary current

$$d\mathbf{H}(t) = \frac{\mathbf{I}(t)}{4\pi \mathbf{R}^3} (d\mathbf{I} \times \mathbf{R}), \qquad (5)$$

where R – vector directed from elementary segment; dI with total current I(t) to observation point Q. Total field strength vector calculated as:

$$\boldsymbol{H}(Q,t) = \frac{\boldsymbol{I}(t)}{4\pi} \int_{L} \frac{(\mathrm{d}\boldsymbol{I} \times \boldsymbol{R})}{\boldsymbol{R}^{3}}.$$
 (6)

This formula (6) widely used to calculate overhead power lines magnetic field instead of Maxwell equations system (3)–(4). Thus magnetic field induction dependence on current and described by (6).

Magnetic field quasi-stationary model varies with time according to sinusoidal law calculated as

$$H(Q,t) = A(Q) \exp j(\omega t), \tag{7}$$

where A(Q) – magnetic field strength amplitude.

Consider design of magnetic field mathematical model created by a multi-circuit passive shield, which is hybrid active-passive shield part [19]. In works [13–15] passive shield parameters considered given. These parameters calculated during active-passive shielding system design. Therefore, in contrast to works [13–15], we set initial values vector \mathbf{X}_p of geometric dimensions, thickness and material of multi-circuit passive shield.

In works [12–15] power line currents parameters (8) considered known and do not change over time. However, power line currents magnitudes have daily, weekly and seasonal changes. Therefore, unlike works [12–15], we introduce of of the initial uncertainties parameters vector $\boldsymbol{\delta}$ of hybrid active-passive shielding system designing problem with power line wires currents and phases values uncertainties components, as well as other uncertainty parameters of electromagnetic hybrid active-passive screen, which, firstly, are initially known inaccurately, and, secondly, can changed during system operation [24–28].

Then, for given induction vector $\mathbf{B}_{Ra}(Q_i, \mathbf{X}_a, \boldsymbol{\delta}, t)$ of resulting magnetic field, created by power line and only windings of active part of hybrid active-passive shield, as well as of geometric dimensions vector values \mathbf{X}_p of multicircuit passive contour shield, magnetic flux $\boldsymbol{\Phi}_l(\mathbf{X}_a, \mathbf{X}_p, \boldsymbol{\delta}, t)$ piercing contour l of multi-circuit passive shield calculated

$$\boldsymbol{\Phi}_{l}(\boldsymbol{X}_{a}, \boldsymbol{X}_{p}, \boldsymbol{\delta}, t) = \int_{S} \boldsymbol{B}_{Ra}(\boldsymbol{X}_{a}, \boldsymbol{\delta}, t) dS.$$
 (8)

Current $I_{Pl}(X_a, X_p, \delta, t)$ in complex form, induced in circuit l of multi-circuit passive shield calculated according to Ohm law and in integral form of Faraday law [9]:

$$I_{Pl}(X_a, X_p, \boldsymbol{\delta}, t) = -j\omega \boldsymbol{\Phi}(X_a, X_p, \boldsymbol{\delta}, t) / \dots$$

$$\dots / (\boldsymbol{R}_l(X_p) + j\omega \boldsymbol{L}_l(X_p),$$
(9)

where $R_l(X_p)$ – active resistance and inductance $L_l(X_p)$ of circuit l of multi-circuit passive shield calculated for passive shield geometric dimensions vector values X_p .

Then, for calculated values currents $I_{Pl}(X_a, X_p, \delta, t)$ in circuits l of multi-circuit passive shield [13–15] and for passive contour screen geometric dimensions vector values X_p magnetic field induction vector $B_p(Q_l, X_a, X_p, \delta, t)$ created by all circuits l of multi-circuit passive shield calculated according to Bio-Savart law (6). This passive shield magnetic field induction vector $B_p(Q_l, X_a, X_p, \delta, t)$, based on Faraday law directed opposite to original magnetic field generated by power line and only by windings of active part of hybrid active-passive shield.

With help of passive part of hybrid active-passive shield, resulting magnetic field that remains uncompensated after operation of only active part of hybrid active-passive screen shielded.

Definition of geometric forward magneto static problem for overhead power lines and compensating winding magnetic field. Let's consider three-dimensional quasi-static magnetic field model created by overhead power lines. Let us set power transmission line wires currents amplitudes A_i and phases φ_i of industrial frequency ω . Let us write expressions for power transmission line wires currents in complex form

$$I_i(t) = A_i \exp j(\omega t + \varphi_i). \tag{10}$$

Then initial magnetic field induction vector $\mathbf{B}_L(Q_i, \delta, t)$ calculated according to Biot-Savart law based on (6) in magnetic field induction vectors sum form created by all power line wires at shielding space point Q_i [9]

$$B_L(Q_i, \delta, t) = \sum_{i=1}^{n} B_l(Q_i, \delta, t).$$
 (11)
Consider design magnetic field mathematical model

Consider design magnetic field mathematical model created by compensation windings of hybrid shield active part. Let us set vector X_a of spatial location and geometric dimensions of compensation windings of hybrid shield active part, as well as compensation windings currents amplitude A_{ai} and phase φ_{ai} [29–33]. Let us write expressions for compensation windings wires currents in complex form

$$I_{ai}(t) = A_{ai} \exp j(\omega t + \varphi_{ai}). \tag{12}$$

Then magnetic field induction vector $\mathbf{B}_a(Q_i, \mathbf{X}_a, t)$ created by all compensating windings wires of active part of hybrid shield $\mathbf{B}_{ai}(Q_i, \mathbf{X}_a, t)$ in shielding space point Q_i calculated based on (6), according to the Biot-Savart law [6]

$$\boldsymbol{B}_{a}(Q_{i},\boldsymbol{X}_{a},t) = \sum \boldsymbol{B}_{ai}(Q_{i},\boldsymbol{X}_{a},t). \tag{13}$$

Then resulting magnetic field induction vector $\mathbf{B}_{Ra}(Q_i, \mathbf{X}_a, \boldsymbol{\delta}, t)$ created by all power line wires and all windings of hybrid shield active part calculated as sum

$$\mathbf{B}_{Ra}(Q_i, \mathbf{X}_a, \boldsymbol{\delta}, t) = \mathbf{B}_L(Q_i, \boldsymbol{\delta}, t) + \mathbf{B}_a(Q_i, \mathbf{X}_a, t). \tag{14}$$

Then resulting magnetic field induction vector $\mathbf{B}_R(Q_i, \mathbf{X}_a, \mathbf{X}_p, \boldsymbol{\delta}, t)$ calculated as sum of magnetic field induction vector $\mathbf{B}_L(Q_i, \boldsymbol{\delta}, t)$ created by all power line wires, magnetic field induction vector $\mathbf{B}_a(Q_i, \mathbf{X}_a, t)$ created by all compensating windings of the of the hybrid shield active part, and magnetic field induction vector $\mathbf{B}_p(Q_i, \mathbf{X}_a, \mathbf{X}_p, \boldsymbol{\delta}, t)$ created by all contours of passive part of hybrid shield in shielding space point Q_i

$$\mathbf{B}_{R}(Q_{i}, X_{a}, X_{p}, \boldsymbol{\delta}, t) = \mathbf{B}_{L}(Q_{i}, \boldsymbol{\delta}, t) + \dots$$

$$\dots + \mathbf{B}_{a}(Q_{i}, X_{a}, t) + \mathbf{B}_{p}(Q_{i}, X_{a}, X_{p}, \boldsymbol{\delta}, t).$$
 (15)

Definition of geometric inverse magneto static problem for magnetic field combined electromagnetic shielding system synthesis. Hybrid active-passive shielding using multi-circuit windings of passive shield and compensating windings of active shield, created compensating magnetic field directed against original magnetic field created by power line. Hybrid active-passive shielding system synthesis task is to calculate spatial location coordinates of passive shield multi-circuit windings and active shield compensating windings as well as compensating windings currents magnitudes and phases. When hybrid active-passive shielding system designing, first of all, we will design a software controller in of an open-loop form [30-33] coarse control based on quasi-static magnetic field mathematical model [6, 7]. Then we will synthesis stabilizing precision controller in closed-loop form control [34-40], based on closed-loop system dynamics equations, taking into account models of actuators and measuring devices, disturbances and measurement noise, and designed to improve control accuracy compared to open-loop control based on quasi-static magnetic field mathematical model.

Let us introduce required parameters vector X for design problem of hybrid system of active-passive shielding, the components of which are vector X_a compensation windings geometric dimensions values, as well as compensation windings currents amplitudes $A_{\omega i}$ and phases $\varphi_{\omega i}$ of active part of hybrid active-passive shielding system, as well as vector X_p of geometric dimensions, thickness and material of the shield of passive part of hybrid active-passive shielding system. Then, for given initial required parameters vector values X and for uncertainty parameters vector $\boldsymbol{\delta}$ of hybrid active-passive shielding system resulting magnetic field induction vector effective value $\mathbf{B}_{R}(\mathbf{X}, \boldsymbol{\delta}, P_{i})$ in shielding space point Q_i calculated by COMSOL Multiphysics software environment using the of the of the resulting magnetic field instantaneous induction value vector $\boldsymbol{B}_{R}(Q_{i},\boldsymbol{X}_{a},\boldsymbol{X}_{p},\boldsymbol{\delta},t)$ from (15).

In [16–18] magnetic field shielding system synthesis problem reduced to one scalar criterion optimizing problem, which calculated as linear convolution of induction values in shielding space different points. However, calculating problem correctly of weighting factors with help of which scalar optimization criterion formed in general form is an ill-posed problem and its solution requires special approaches [26–30]. In addition, in formulation of magnetic field shielding system designing problem uncertainties of initial magnetic field models and of control system parameters were not taken into account at all. Therefore, in contrast to works [16–18] robust hybrid active-passive shielding system synthesis problem reduced to vector game solution calculating [41]

$$\boldsymbol{B}_{R}(\boldsymbol{X},\boldsymbol{\delta}) = \langle \boldsymbol{B}_{R}(\boldsymbol{X},\boldsymbol{\delta},Q_{1}) \rangle. \tag{16}$$

In this vector game, it is necessary to find minimum of game payoff vector (16) from required parameters vector X for hybrid active-passive shielding system synthesis problem, but maximum of same game payoff vector (16) from uncertainty parameters vector δ for hybrid active-passive shielding system

Components of vector game payoff (17) are resulting magnetic field induction effective values $B_R(X, \delta, Q_i)$ at all of the shielding space considered points Q_i .

Components of the vector game payoff (16) are nonlinear functions of required parameters vector X and of uncertainty parameters vector δ of of a hybrid active-passive

shielding system synthesis problem [19] and calculated by COMSOL Multiphysics software environment.

Vector game solution algorithm. Let's consider algorithm for vector game solution (16) calculating. The works [41] consider various approaches to computing by vector games solutions based on various heuristic approaches. Unlike works [31, 32], in this work, in order to find unique solution of vector game from set of Pareto-optimal solutions, in addition to the vector payoff (16) also used information about binary relationships of local solutions preferences relative to each other.

A feature of solution calculated problem under consideration is vector payoff (16) multi-extremal nature, so that possible solutions considered region contains local minima and maxima. This is due to fact that when resulting magnetic field induction level minimizing in shielding space one point, induction level in another point increases due to under compensation or overcompensation of the original magnetic field. Therefore, to calculate vector game solution under consideration, it is advisable stochastic multi-agent particle swarm optimization (PSO) algorithms used [41].

To calculate vector games solutions of stochastic multi-agent heuristic optimization methods used causes certain difficulties, however, this direction continues to develop intensively using various heuristic techniques. For calculating original vector game solution (16) stochastic multi-agent PSO algorithm used based on set of particle swarms, number of which equal to number of components of vector game payoff (16).

When calculating one single global solution to vector game (16) of scalar games solutions that are components of game vector (16) calculated using individual swarms. To calculate one single global solution to the vector game (16) individual swarms exchange information with each other during local games optimal solutions calculation. In contrast to works [36–38], at each swarm particle movement step binary preference functions of local solution obtained by one particle of swarm and global solution obtained by all swarms used [41]. This approach allows calculated solution that minimizes maximum resulting magnetic field induction level value for all considered shielding space points.

PSO is a robust stochastic optimization method based on the motion and intelligence of swarms. In PSO, each individual is treated as a particle in the design space with position and velocity vectors that fly through the problem space following the current optimal particles. PSO is a population-based search algorithm. The advantages of PSO are that it is simple to implement and has few configurable parameters. PSO is initialized with a population of n random particles (solutions), which then searches for optima by updating generations. At each iteration, each particle is updated with the «best» solution (fitness) it has achieved so far, which is called «best». The other «best» solution, which is the global best solution achieved so far by any particle in the population, is called «gbest» [41].

The PSO algorithm is a gradient-free algorithm. The algorithm does not require the calculation of the gradient or the Hessian matrix of second derivatives. The PSO algorithm is actually an optimization algorithm based on random search. A significant advantage of the PSO algorithm is the ability to calculate the global extremum due to the exchange of information between individual particles during the search for local extrema using individual particles. In fact, the «particle swarm» is a widely used approach for searching for a global extremum with a multi-start.

However, the main disadvantage of the PSO algorithm compared to deterministic optimization methods based on gradient methods is the relatively long computation time. This is, firstly, due to the search for one optimum using a swarm of particles, which increases the search time by approximately a number of times equal to the number of particles in the swarm. The search time especially increases when solving a vector optimization problem using multiple swarms of particles, the number of swarms is equal to the number of components of the vector objective function. Naturally, each component of the objective function calculated using a swarm of particles.

Therefore, to speed up the calculation of the global optimum, it is advisable to use the PSO algorithm for a «rough» calculation of the position of the global optimum. It is advisable to calculate the refined position of the global optimum using deterministic algorithms based on gradient optimization methods, and possibly using the matrix of second derivatives – the Hessian matrix.

The expediency of such an approach is also due to the fact, that in the region of the extremum, the components of the gradient vector of the objective function tend to zero. And although the PSO algorithm is formally a gradient-free optimization method and does not require calculating the gradient of the objective function, the speeds of particle movement in the PSO algorithm, which are determined based on a random search, actually play the role of the gradient components of the objective function. Naturally, in the region of the extremum, these speeds of particle movement, calculated based on a random search, also tend to zero, which determines the use of optimization algorithms based on the second derivatives – the Hessian matrix.

Sequential Quadratic Programming (SQP) is one of the most successful methods for solving smooth nonlinear optimization problems with constraints. The two most significant features of this algorithm are the speed of convergence and accuracy. SQP finds the search direction using linear approximation of the constraints and quadratic approximation of the design objective functions.

Let us consider the application of SQP method to solve this problem. This method is a combination of the Gauss-Newton method with determination of the direction of motion using the quasi-Newton algorithm. SQP is one of the most successful methods for solving smooth nonlinear constrained optimization problems. The two most significant features of this algorithm are the speed of convergence and accuracy. SQP finds the search direction using a linear approximation of the constraints and a quadratic approximation of the design objective functions. The solution procedure is based on formulating and solving a quadratic subproblem in each iteration.

Let us first consider the minimization of the quadratic norm of L2, commonly called the unconstrained least squares problem

$$f(x) = \frac{1}{2} \sum_{i=1}^{l} f_i(x)^2 .$$
 (17)

The gradient of this objective function can be represented as follows

$$\nabla f(x) = \nabla F(x)F(x), \tag{18}$$

where $\nabla F(x) = (\nabla f_1(x),...,\nabla f_l(x))$ is the Jacobian of this function and it is assumed that the components of the objective function can be differentiated twice. Then the matrix of second derivatives of the objective function – the Hesse matrix can be written as follows

$$\nabla^2 f(x) = \nabla F(x) \nabla F(x)^T + B(x), \tag{19}$$

where

$$B(x) = \sum_{i=1}^{l} f_i(x) \nabla^2 f_i(x) \nabla^2 f_i(x).$$
 (20)

Then the iterative procedure for choosing the direction d_k of movement using Newton's method can be reduced to solving the linear system

$$\nabla^2 f(x_k) d + \nabla f(x_k) = 0. \tag{21}$$
 For the iterative finding of the vector of the sought

For the iterative finding of the vector of the sough parameters

$$x_{k+1} = x_k + \alpha_k d_k \tag{22}$$

where a recurrent equation d_k can be obtained in which is the solution to the optimization problem, and α_k is the experimentally determined parameter.

This algorithm uses the Gauss–Newton method, which is a traditional algorithm for solving the problem of the nonlinear least squares method, to calculate the direction d_k of motion (22). In general, the Gauss–Newton method allows you to obtain a solution to the problem of sequential quadratic programming using only first-order derivatives, but in real situations it often cannot obtain a solution. Therefore, to improve convergence, second-order methods are used, which use the matrix of second derivatives of the objective function – the Jacobian matrix when solving optimization problems without constraints. Second-order algorithms, compared with first-order methods, allow you to effectively obtain a solution in a region close to the optimal point, when the components of the gradient vector have sufficiently small values.

The main problem of applying the SQP method is the need to use special methods to ensure negative eigenvalues when approximating the Hessian matrix in the case of alternative approaches. Currently, the Levenberg-Marquardt algorithm is used for pseudo-inversion of the Hessian matrix (21).

Minimax problems are widely used in robust control. If it is necessary to find the minimum for some variables and the maximum for other variables of the same objective function, then a necessary condition for the optimality of this minimax problem is that the gradient of the objective function is equal to zero for all variables, regardless of whether the objective function is minimized or maximized. When solving this minimax problem numerically, to find the direction of movement, it is necessary to use the components of the gradient of the objective function for those variables for which maximization is performed, and it is necessary to use the components of the antigradient (i.e., the gradient taken with the opposite sign) for those variables for which minimization is performed.

Numerical solution of nonlinear programming problem (17) with constraints, with the exception of direct methods, involves the use of partial derivatives. Analytical expressions for derivatives (18) in the problems under consideration are usually impossible to obtain; therefore, derivatives are calculated using various schemes – a two-way scheme, a forward scheme, or a backward scheme, which are approximate numerical calculations of derivatives using difference schemes.

Simulation results. Unlike works [13–18], in this work spatial location coordinates of contours for multicircuit passive screen calculated as multi-criteria zerosum game (16) solution for initial magnetic field electromagnetic hybrid active-passive shielded. In process combined active and multi-loop passive shielding system

synthesis spatial location coordinates of 16 conductors for multi-circuit passive shield calculated. In addition, spatial location coordinates of two compensation windings, as well as currents and phases in these windings of active shielding system also calculated.

Let us consider combined shield operation to magnetic field reduced in residential building located near power lines with wires triangular arrangement. Figure 3 shows initial magnetic field induction distribution generated by power line with wires triangular arrangement.

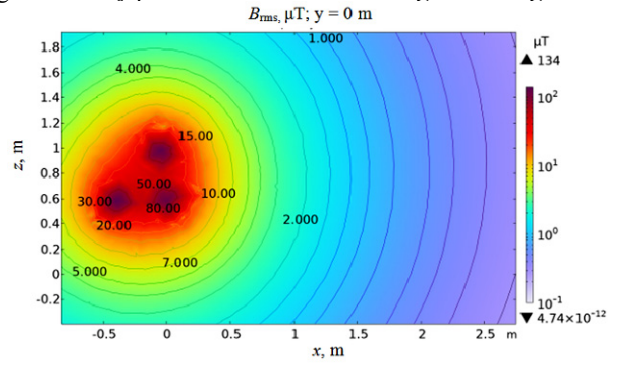


Fig. 3. Initial magnetic field induction distribution

As can seen from Fig. 3, initial magnetic field induction level in shielding space is more than 4 times higher than sanitary standards for population safe living of $0.5~\mu T$.

Figure 4 shows resulting magnetic field induction distribution when a multi-circuit passive shield operating only. As can see from Figure 4, resulting magnetic field induction level decreased by approximately 1.3 times, but exceeds sanitary standards by approximately 3 times.

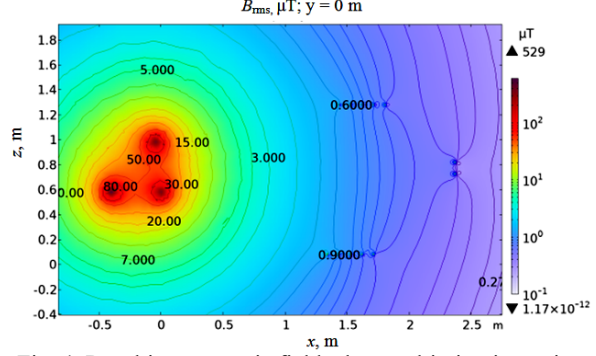


Fig. 4. Resulting magnetic field when multi-circuit passive shield operating only

Figure 5 shows the of the resulting magnetic field induction distribution when active shield with two compensating windings operating only. As can seen from Fig. 5, resulting magnetic field induction level decreased by approximately 8 times.

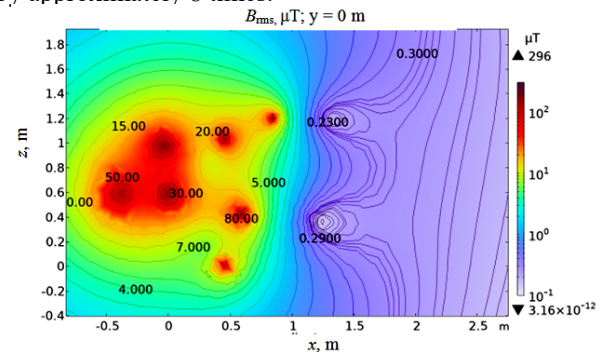


Fig. 5. Resulting magnetic field when active shielding system with two windings operating only

Figure 6 shows resulting magnetic field induction distribution during hybrid shield operation. As can seen from Fig. 6, resulting magnetic field induction level decreased by approximately 8.3 times. At the same time, resulting magnetic field induction level in shielding space does not exceed 0.24 $\mu T,$ which is more than two times less than induction level of industrial frequency magnetic field for population safe living.

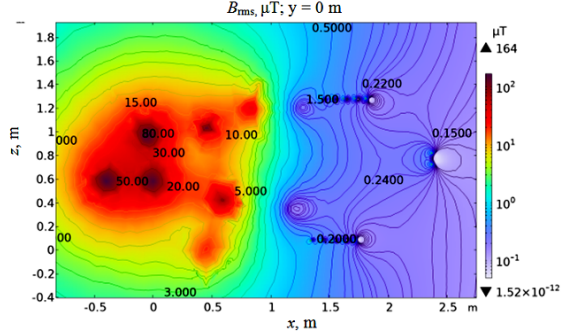


Fig. 6. Resulting field when hybrid shield working

Moreover, in comparison with active shield operation only, when combined shield operating, initial magnetic field shielding effective occurs in significantly larger shielding space.

Let us now consider resulting magnetic field induction distribution level along shielding space length based on three-dimensional magnetic field modeling.

First, let's consider resulting magnetic field threedimensional modeling results when multi-circuit passive shield operating only. Figure 7 shows the of magnetic field induction distribution along passive shield length for various coordinates along multi-circuit passive shield height and width.

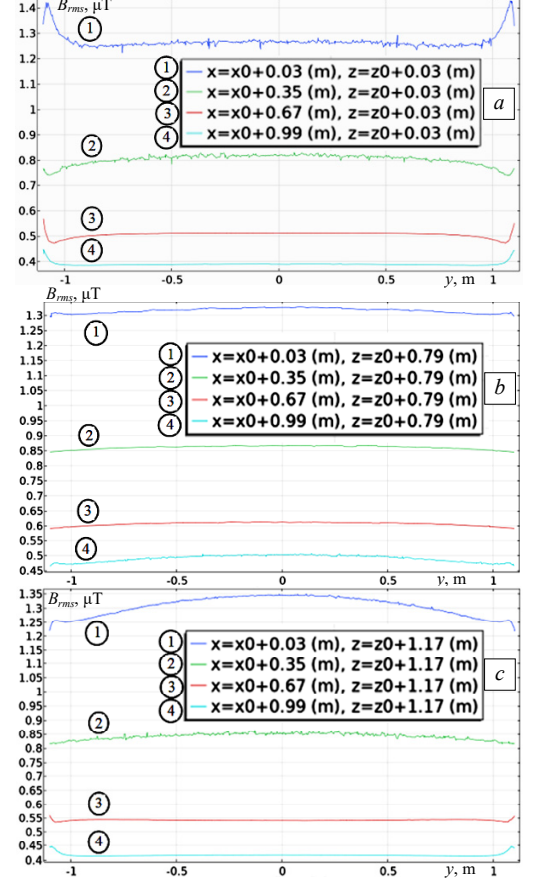


Fig. 7. Resulting magnetic field distribution level along shielding space length when multi-circuit passive shield operating only

As can seen from Fig. 7, shielding efficiency when multi-circuit passive shield using only remains almost constant along shield length and only slightly decreases at shielding area edges.

Let us now consider three-dimensional modeling results of resulting magnetic field when active shield operating only. Figure 8 shows resulting magnetic field induction distribution along length for various coordinates along shielding space height and width.

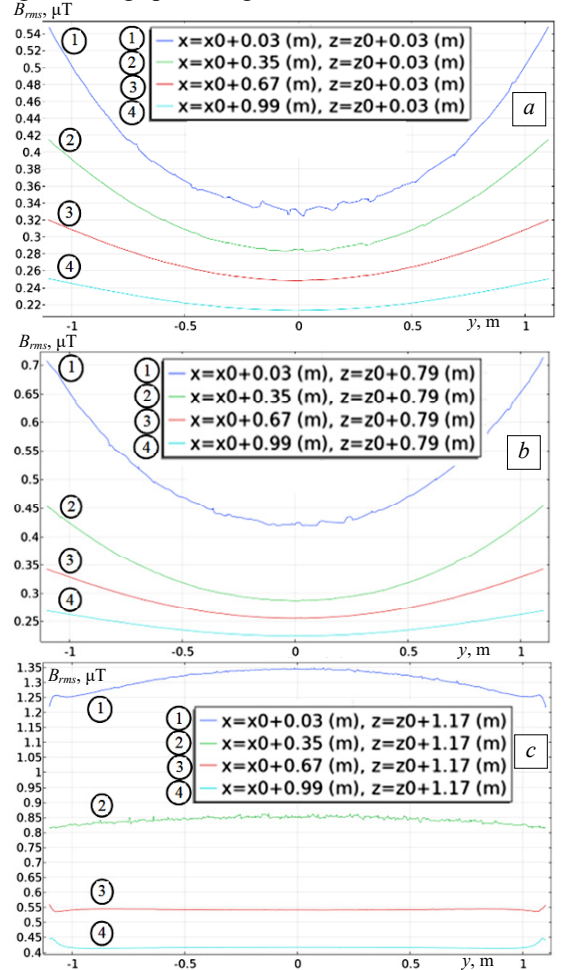


Fig. 8. Resulting magnetic field level distribution along shielding space length when active shield operating only

As can seen from Fig. 8, when active shield operating only in central part along shielding space length, resulting magnetic field induction level is in range $0.22-0.42~\mu T$. However, at shielding region edges, resulting magnetic field induction level increases by approximately 1.3-1.5 times to values of $0.27-0.7~\mu T$.

Let us now consider three-dimensional modeling results of resulting magnetic field during combined screen operation. Figure 9 shows resulting magnetic field induction distribution along length for various coordinates along shielding space height and width when combined shield operating.

As can seen from Fig. 9, when combined shield operates in central part along shielding space length, resulting magnetic field induction level slightly reduced compared to induction level when active screen operating only. In addition, at shielding area edges, resulting magnetic field induction level increases slightly less compared to induction level when active shield operating only. Thus, with the help of combined shield, resulting magnetic field induction level reduced in significantly larger space compared to active shield operation only.

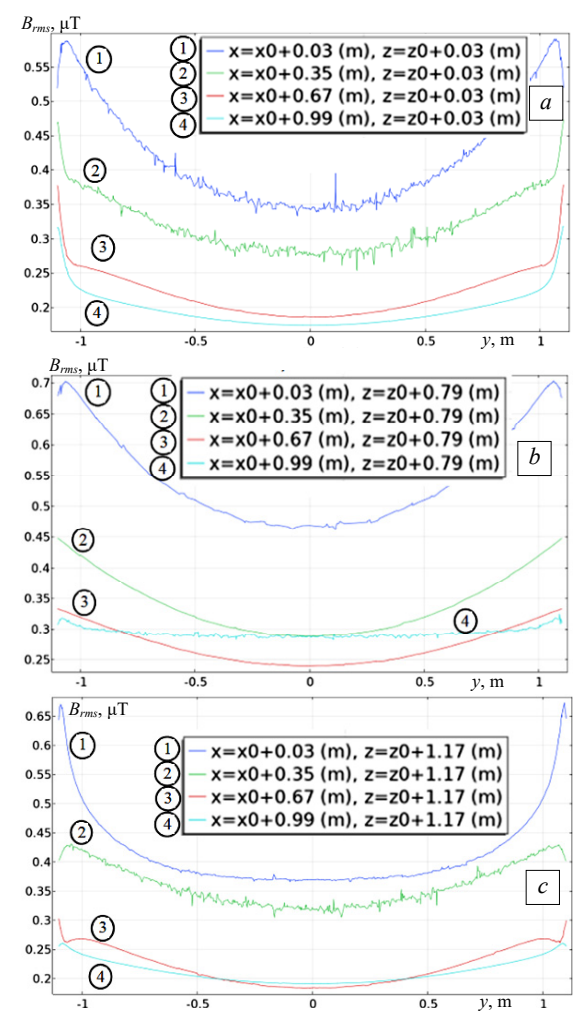


Fig. 9. Resulting magnetic field distribution level along shielding space length during combined screen operation

Combined hybrid active and multi-loop passive shielding system experimental setup description. To conduct experimental studies combined shield experimental setup developed. All experimental studies carried out on the magnetodynamic measuring stand at the Anatolii Pidhornyi Institute of Power Machines and Systems of the National Academy of Sciences of Ukraine [42].



Fig. 10. Multi-circuit passive shield

Experimental setup contains single-circuit power line setup with «Triangle» type wires arrangement, two compensation windings of active shielding system and a multi-circuit electromagnetic shield made of aluminum rod with 8 mm diameter. Figure 10 shows an experimental installation of such multi-circuit passive shield. Two magnetic field sensors installed inside passive shield.

As Fig. 11 shows, to implement two closed-loop control loops for two compensation windings of active shielding system with feedback on resulting magnetic field.

During control loops adjusting process, these sensors axes seted in such way as to maximum magnetic field induction value measured generated by compensation winding of corresponding compensating channel. This magnetic field

sensors axes installation makes it possible to minimize channels on each other influence when they work together.



Fig. 11. Magnetometer installation diagram



Fig. 12. Two compensating windings of active shielding system

Two more magnetic field installed sensors inside passive shield, which axes parallel directed coordinate axes. These two sensors used in system for resulting magnetic field space-time characteristics measuring. This measuring system used to control loops adjust of active shielding system of combined magnetic field shielding.

Figure 12 shows two compensation windings of active shielding system.

Figure 13 shows combined shielding control system. To measure resulting magnetic field inside shielding space a three-coordinate magnetometer type «TES 1394S triaxial ELF magnetic field meter» is used.



Fig. 13. Combined shielding control system

Experimental studies results. Let us consider experimental studies results of resulting magnetic field distribution dependences with combined multi-circuit electromagnetic shield consisting of two compensation windings of active shield and multi-circuit passive shield consisting of 16 circuits.

Let us now consider of experimentally measured distribution level of resulting magnetic field induction along shielding space length based on three-dimensional modeling of magnetic field distribution.

First, let us consider the experimentally measured results of resulting magnetic field when multi-circuit passive shield operating only. Figure 14 shows experimentally measured distributions of magnetic field induction along passive shield length for various coordinates along multi-circuit passive shield height and width.

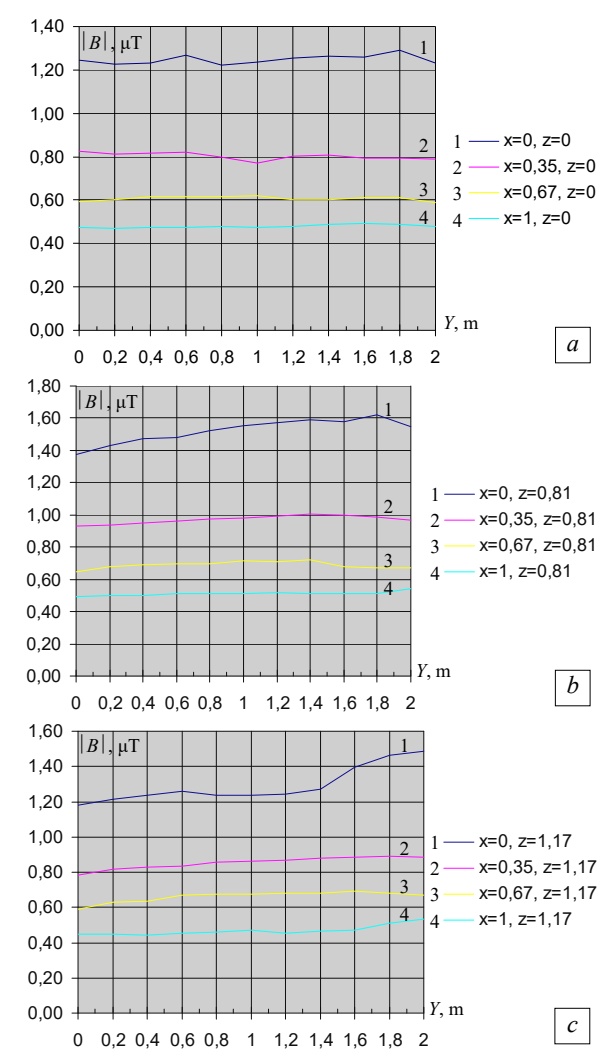


Fig. 14. Experimentally measured distributions of resulting magnetic field level along shielding space length when multicircuit passive shield operating only

As can seen from Fig. 14, shielding efficiency when multi-circuit passive shield using only remains almost constant along shielding space length and only slightly decreases along shielding area edges, which corresponds to calculated magnetic field distributions shown in Fig. 6.

Let us now consider experimentally measured values results of resulting magnetic field when active shield operating only. Figure 15 shows experimentally measured distributions of resulting magnetic field induction along length for various coordinates along shielding space height and width.

As can seen from Fig. 15, when active shield operating only in central part along shielding space length, experimentally measured levels values of resulting magnetic field induction distribution coincide with calculated magnetic field distributions shown in Fig. 8 with 20 % accuracy.

Let us now consider experimentally measured distributions of resulting magnetic field during operation of combined active and multi-loop passive shielding system. Figure 16 shows experimentally measured distributions of resulting magnetic field induction along length for various coordinates along shielding space height and width during of the combined shield operation.

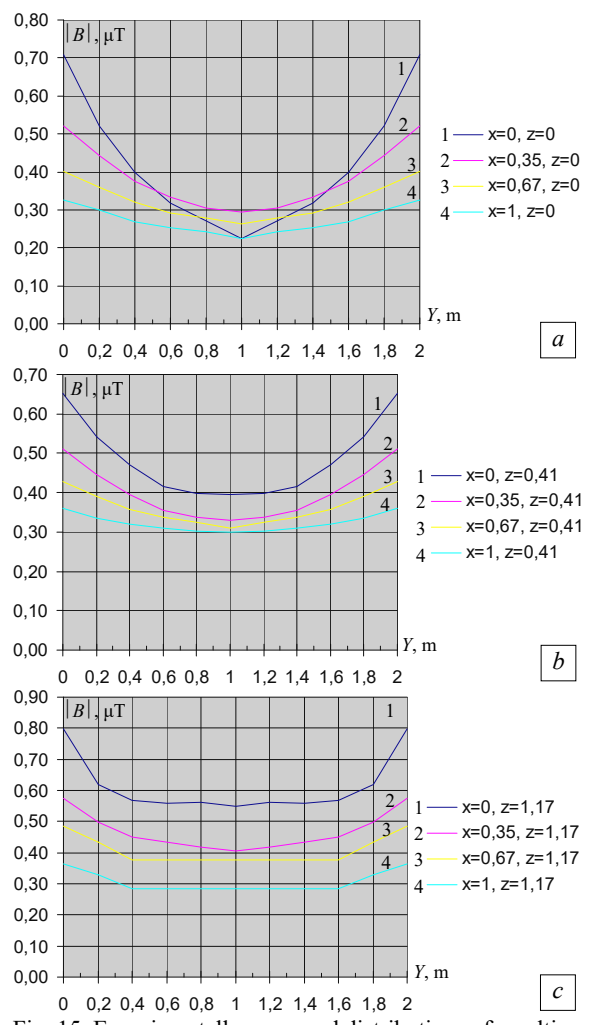


Fig. 15. Experimentally measured distributions of resulting magnetic field level along shielding space length when active shield operating only

As can seen from Fig. 16, when combined shield operating, the experimentally measured induction levels values of resulting magnetic field distribution coincide with calculated magnetic field distributions shown in Fig. 9 with 20 % accuracy.

Thus, based on three-dimensional modeling results and experimental studies, it has been established that with combined shield help resulting magnetic field induction level reduced in significantly larger space compared to active screen operation only.

Conclusions.

- 1. For the first time system synthesis methodology for robust combined active and multi-circuit passive shielding system to improve effectiveness of of industrial frequency magnetic field reduction in residential buildings space created by overhead power lines wires developed.
- 2. Developed system synthesis methodology for robust combined electromagnetic active and multi-circuit passive shielding system synthesis based on vector game solution. Vector game payoff calculated by finite element calculations system COMSOL Muliphysics. Vector game solution calculated based on hybrid optimization algorithm, which globally explores synthesis search space using particle swarm optimization and gradient-based sequential quadratic programming to rapidly calculated optimum synthesis point from Pareto optimal solutions taking into account binary preferences relationships used.

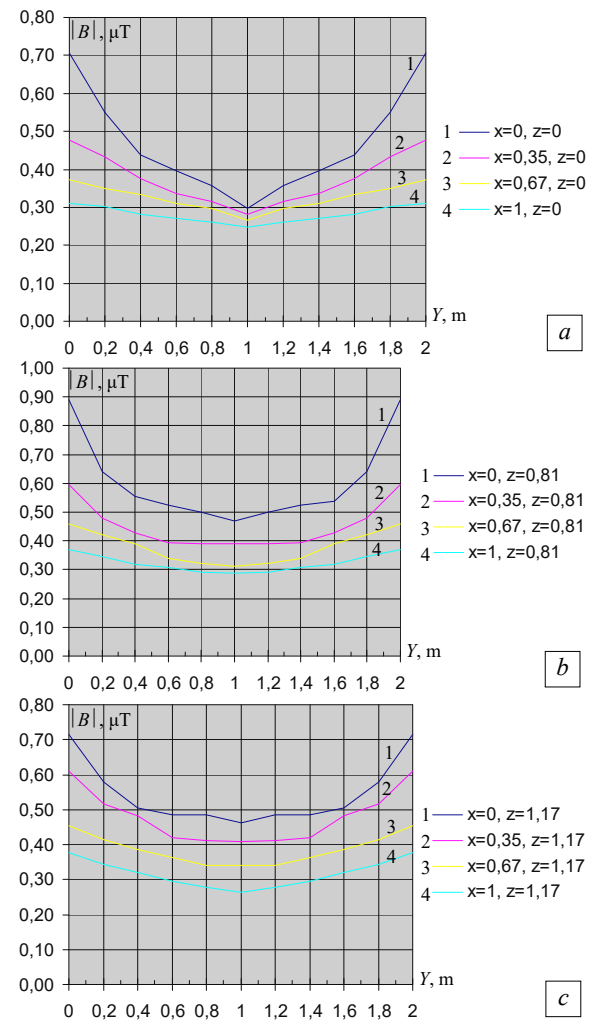


Fig. 16. Experimentally measured distributions along of shielding space length of resulting magnetic field level during of the combined shield operation

- 3. Performed theoretical studies results shown that shielding factor by only electromagnetic multi-circuit passive shield made from 1.5 mm thickness solid aluminum plate is about 2 units, only active shield made from winding form consisting of 20 turns is about 4 units. When combined electromagnetic passive and active shield used, shielding factor was more 10 units, which confirms its high efficiency, exceeding product shielding factors of passive and active shields.
- 4. Performed experimental studies results confirmed modeling and theoretical studies results. Experimentally measured induction levels values of resulting magnetic field distribution coincide with calculated magnetic field distributions with 20 % accuracy.
- 5. Practical used of developed combined active and multi-loop passive shielding system will allow magnetic field level reducing in residential building from phase wires triangular arrangement of overhead power lines to population safe level of 0.5 μ T.
- 6. In the future, it is necessary to implement such combined electromagnetic active and multi-circuit passive shielding systems to normalize the field in real residential building.

Conflict of interest. The authors declare that they have no conflicts of interest.

REFERENCES

- I. Sung H., Ferlay J., Siegel R.L., Laversanne M., Soerjomataram I., Jemal A., Bray F. Global Cancer Statistics 2020: GLOBOCAN Estimates of Incidence and Mortality Worldwide for 36 Cancers in 185 Countries. CA: A Cancer Journal for Clinicians, 2021, vol. 71, no. 3, pp. 209-249. doi: https://doi.org/10.3322/caac.21660.
- 2. Directive 2013/35/EU of the European Parliament and of the Council of 26 June 2013 on the minimum health and safety requirements regarding the exposure of workers to the risks arising from physical agents (electromagnetic fields). Available at: http://data.europa.eu/eli/dir/2013/35/oj (Accessed 20 February 2025).
- 3. The International EMF Project. Radiation & Environmental Health Protection of the Human Environment World Health Organization. Geneva, Switzerland, 1996. 2 p. Available at: https://www.who.int/initiatives/the-international-emf-project (Accessed 20 February 2025).
- **4.** Rozov V., Grinchenko V., Tkachenko O., Yerisov A. Analytical Calculation of Magnetic Field Shielding Factor for Cable Line with Two-Point Bonded Shields. *2018 IEEE 17th International Conference on Mathematical Methods in Electromagnetic Theory (MMET)*, 2018, pp. 358-361. doi: https://doi.org/10.1109/MMET.2018.8460425.
- 5. Rozov V.Y., Zavalnyi A.V., Zolotov S.M., Gretskikh S.V. The normalization methods of the static geomagnetic field inside houses. *Electrical Engineering & Electromechanics*, 2015, no. 2, pp. 35-40. doi: https://doi.org/10.20998/2074-272X.2015.2.07.
- **6.** Rozov V.Y., Pelevin D.Y., Kundius K.D. Simulation of the magnetic field in residential buildings with built-in substations based on a two-phase multi-dipole model of a three-phase current conductor. *Electrical Engineering & Electromechanics*, 2023, no. 5, pp. 87-93. doi: https://doi.org/10.20998/2074-272X.2023.5.13.
- 7. Rozov V.Yu., Reutskyi S.Yu., Pelevin D.Ye., Kundius K.D. Approximate method for calculating the magnetic field of 330-750 kV high-voltage power line in maintenance area under voltage. *Electrical Engineering & Electromechanics*, 2022, no. 5, pp. 71-77. doi: https://doi.org/10.20998/2074-272X.2022.5.12.
- Salceanu A., Paulet M., Alistar B.D., Asiminicesei O. Upon the contribution of image currents on the magnetic fields generated by overhead power lines. 2019 International Conference on Electromechanical and Energy Systems (SIELMEN). 2019. doi: https://doi.org/10.1109/sielmen.2019.8905880.
 Del Pino Lopez J.C., Romero P.C. Influence of different types of
- 9. Del Pino Lopez J.C., Romero P.C. Influence of different types of magnetic shields on the thermal behavior and ampacity of underground power cables. *IEEE Transactions on Power Delivery*, Oct. 2011, vol. 26, no. 4, pp. 2659-2667. doi: https://doi.org/10.1109/tpwrd.2011.2158593.
- 10. Hasan G.T., Mutlaq A.H., Ali K.J. The Influence of the Mixed Electric Line Poles on the Distribution of Magnetic Field. *Indonesian Journal of Electrical Engineering and Informatics (IJEEI)*, 2022, vol. 10, no. 2, pp. 292-301. doi: https://doi.org/10.52549/ijeei.v10i2.3572.
- 11. Victoria Mary S., Pugazhendhi Sugumaran C. Investigation on magneto-thermal-structural coupled field effect of nano coated 230 kV busbar. *Physica Scripta*, 2020, vol. 95, no. 4, art. no. 045703. doi: https://doi.org/10.1088/1402-4896/ab6524.
- 12. Ippolito L., Siano P. Using multi-objective optimal power flow for reducing magnetic fields from power lines. *Electric Power Systems Research*, 2004, vol. 68, no. 2, pp. 93-101. doi: https://doi.org/10.1016/S0378-7796(03)00151-2.
- 13. Barsali S., Giglioli R., Poli D. Active shielding of overhead line magnetic field: Design and applications. *Electric Power Systems Research*, May 2014, vol. 110, pp. 55-63. doi: https://doi.org/10.1016/j.epsr.2014.01.005.
- 14. Bavastro D., Canova A., Freschi F., Giaccone L., Manca M. Magnetic field mitigation at power frequency: design principles and case studies. *IEEE Transactions on Industry Applications*, May 2015, vol. 51, no. 3, pp. 2009-2016. doi: https://doi.org/10.1109/tia.2014.2369813.
- 15. Beltran H., Fuster V., García M. Magnetic field reduction screening system for a magnetic field source used in industrial applications. 9 Congreso Hispano Luso de Ingeniería Eléctrica (9 CHLIE), Marbella (Málaga, Spain), 2005, pp. 84-99.
- 16. Bravo-Rodríguez J., Del-Pino-López J., Cruz-Romero P. A Survey on Optimization Techniques Applied to Magnetic Field Mitigation in Power Systems. *Energies*, 2019, vol. 12, no. 7, art. no. 1332. doi: https://doi.org/10.3390/en12071332.
- 17. Canova A., del-Pino-López J.C., Giaccone L., Manca M. Active Shielding System for ELF Magnetic Fields. *IEEE Transactions on Magnetics*, March 2015, vol. 51, no. 3, pp. 1-4. doi: https://doi.org/10.1109/tmag.2014.2354515.

- 18. Canova A., Giaccone L. Real-time optimization of active loops for the magnetic field minimization. *International Journal of Applied Electromagnetics and Mechanics*, Feb. 2018, vol. 56, pp. 97-106. doi: https://doi.org/10.3233/jae-172286.
- 19. Canova A., Giaccone L., Cirimele V. Active and passive shield for aerial power lines. *Proc. of the 25th International Conference on Electricity Distribution (CIRED 2019)*, 3-6 June 2019, Madrid, Spain. Paper no. 1096.
- 20. Grinchenko V.S. Mitigation of three-phase power line magnetic field by grid electromagnetic shield. *Technical Electrodynamics*, 2018, no. 4, pp. 29-32. (Ukr). doi: https://doi.org/10.15407/techned2018.04.029.
- 21. Celozzi S. Active compensation and partial shields for the power-frequency magnetic field reduction. 2002 IEEE International Symposium on Electromagnetic Compatibility, Minneapolis, MN, USA, 2002, vol. 1, pp. 222-226. doi: https://doi.org/10.1109/isemc.2002.1032478.
- 22. Celozzi S., Garzia F. Active shielding for power-frequency magnetic field reduction using genetic algorithms optimization. *IEE Proceedings Science, Measurement and Technology*, 2004, vol. 151, no. 1, pp. 2-7. doi: https://doi.org/10.1049/ip-smt:20040002.
- 23. Celozzi S., Garzia F. Magnetic field reduction by means of active shielding techniques. WIT Transactions on Biomedicine and Health, 2003, vol. 7, pp. 79-89. doi: https://doi.org/10.2495/ehr030091.
- 24. Martynenko G. Analytical Method of the Analysis of Electromagnetic Circuits of Active Magnetic Bearings for Searching Energy and Forces Taking into Account Control Law. 2020 IEEE KhPI Week on Advanced Technology (KhPIWeek), 2020, pp. 86-91. doi: https://doi.org/10.1109/KhPIWeek51551.2020.9250138.
- 25. Popov A., Tserne E., Volosyuk V., Zhyla S., Pavlikov V., Ruzhentsev N., Dergachov K., Havrylenko O., Shmatko O., Averyanova Y., Ostroumov I., Kuzmenko N., Sushchenko O., Zaliskyi M., Solomentsev O., Kuznetsov B., Nikitina T. Invariant Polarization Signatures for Recognition of Hydrometeors by Airborne Weather Radars. Computational Science and Its Applications ICCSA 2023. Lecture Notes in Computer Science, 2023, vol. 13956, pp. 201-217. doi: https://doi.org/10.1007/978-3-031-36805-9 14.
- 26. Sushchenko O., Averyanova Y., Ostroumov I., Kuzmenko N., Zaliskyi M., Solomentsev O., Kuznetsov B., Nikitina T., Havrylenko O., Popov A., Volosyuk V., Shmatko O., Ruzhentsev N., Zhyla S., Pavlikov V., Dergachov K., Tserne E. Algorithms for Design of Robust Stabilization Systems. Computational Science and Its Applications ICCSA 2022. ICCSA 2022. Lecture Notes in Computer Science, 2022, vol. 13375, pp. 198-213. doi: https://doi.org/10.1007/978-3-031-10522-7 15.
- 13375, pp. 198-213. doi: https://doi.org/10.1007/978-3-031-10522-7 15.

 27. Ostroverkhov M., Chumack V., Monakhov E., Ponomarev A. Hybrid Excited Synchronous Generator for Microhydropower Unit. 2019 IEEE 6th International Conference on Energy Smart Systems (ESS), Kyiv, Ukraine, 2019, pp. 219-222. doi: https://doi.org/10.1109/ess.2019.8764202.
- 28. Ostroverkhov M., Chumack V., Monakhov E. Ouput Voltage Stabilization Process Simulation in Generator with Hybrid Excitation at Variable Drive Speed. 2019 IEEE 2nd Ukraine Conference on Electrical and Computer Engineering (UKRCON), Lviv, Ukraine, 2019, pp. 310-313. doi: https://doi.org/10.1109/ukrcon.2019.8879781.
- 29. Tytiuk V., Chornyi O., Baranovskaya M., Serhiienko S., Zachepa I., Tsvirkun L., Kuznetsov V., Tryputen N. Synthesis of a fractional-order Pl^AD^a-controller for a closed system of switched reluctance motor control. *Eastern-European Journal of Enterprise Technologies*, 2019, no. 2 (98), pp. 35-42. doi: https://doi.org/10.15587/1729-4061.2019.160946.
- 30. Shchur I., Turkovskyi V. Comparative Study of Brushless DC Motor Drives with Different Configurations of Modular Multilevel Cascaded Converters. 2020 IEEE 15th International Conference on Advanced Trends in Radioelectronics, Telecommunications and Computer Engineering (TCSET), Lviv-Slavske, Ukraine, 2020, pp. 447-451. doi: https://doi.org/10.1109/tcset49122.2020.235473.
- 31. Volosyuk V., Zhyla S., Pavlikov V., Ruzhentsev N., Tserne E., Popov A., Shmatko O., Dergachov K., Havrylenko O., Ostroumov I., Kuzmenko N., Sushchenko O., Averyanova Yu., Zaliskyi M., Solomentsev O., Kuznetsov B., Nikitina T. Optimal Method for Polarization Selection of Stationary Objects Against the Background of the Earth's Surface. International Journal of Electronics and Telecommunications, 2022, vol. 68, no. 1, pp. 83-89. doi: https://doi.org/10.24425/ijet.2022.139852.

- 32. Halchenko V., Trembovetska R., Bazilo C., Tychkova N. Computer Simulation of the Process of Profiles Measuring of Objects Electrophysical Parameters by Surface Eddy Current Probes. *Lecture Notes on Data Engineering and Communications Technologies*, 2023, vol. 178, pp. 411-424. doi: https://doi.org/10.1007/978-3-031-35467-0 https://doi.org/10.1007/978-3-031-35467-0 25.
- 33. Halchenko V., Bacherikov D., Filimonov S., Filimonova N. Improvement of a Linear Screw Piezo Motor Design for Use in Accurate Liquid Dosing Assembly. Smart Technologies in Urban Engineering. STUE 2022. Lecture Notes in Networks and Systems, 2023, vol. 536, pp. 237-247. doi: https://doi.org/10.1007/978-3-031-20141-7 22.
- 34. Maksymenko-Sheiko K.V., Sheiko T.I., Lisin D.O., Petrenko N.D. Mathematical and Computer Modeling of the Forms of Multi-Zone Fuel Elements with Plates. *Journal of Mechanical Engineering*, 2022, vol. 25, no. 4, pp. 32-38. doi: https://doi.org/10.15407/pmach2022.04.032.
- 35. Hontarovskyi P.P., Smetankina N.V., Ugrimov S.V., Garmash N.H., Melezhyk I.I. Computational Studies of the Thermal Stress State of Multilayer Glazing with Electric Heating. *Journal of Mechanical Engineering*, 2022, vol. 25, no. 1, pp. 14-21. doi: https://doi.org/10.15407/pmach2022.02.014.
- 36. Kostikov A.O., Zevin L.I., Krol H.H., Vorontsova A.L. The Optimal Correcting the Power Value of a Nuclear Power Plant Power Unit Reactor in the Event of Equipment Failures. *Journal of Mechanical Engineering*, 2022, vol. 25, no. 3, pp. 40-45. doi: https://doi.org/10.15407/pmach2022.03.040.
- 37. Rusanov A.V., Subotin V.H., Khoryev O.M., Bykov Y.A., Korotaiev P.O., Ahibalov Y.S. Effect of 3D Shape of Pump-Turbine Runner Blade on Flow Characteristics in Turbine Mode. *Journal of Mechanical Engineering*, 2022, vol. 25, no. 4, pp. 6-14. doi: https://doi.org/10.15407/pmach2022.04.006.
- 38. Kurennov S., Smetankina N., Pavlikov V., Dvoretskaya D., Radchenko V. Mathematical Model of the Stress State of the Antenna Radome Joint with the Load-Bearing Edging of the Skin Cutout. *Lecture Notes in Networks and Systems*, 2022, vol. 305, pp. 287-295. doi: https://doi.org/10.1007/978-3-030-83368-8 28.
- **39.** Kurennov S., Smetankina N. Stress-Strain State of a Double Lap Joint of Circular Form. Axisymmetric Model. *Lecture Notes in Networks and Systems*, 2022, vol 367 LNNS, pp. 36-46. doi: https://doi.org/10.1007/978-3-030-94259-5 4.
- 40. Smetankina N., Merkulova A., Merkulov D., Misiura S., Misiura I. Modelling Thermal Stresses in Laminated Aircraft Elements of a Complex Form with Account of Heat Sources. *Lecture Notes in Networks and Systems*, 2023, vol. 534 LNNS, pp. 233-246. doi: https://doi.org/10.1007/978-3-031-15944-2 22.
- **41.** Hashim F.A., Hussain K., Houssein E.H., Mabrouk M.S., Al-Atabany W. Archimedes optimization algorithm: a new metaheuristic algorithm for solving optimization problems. *Applied Intelligence*, 2021, vol. 51, no. 3, pp. 1531-1551. doi: https://doi.org/10.1007/s10489-020-01893-z.
- **42.** Baranov M.I., Rozov V.Y., Sokol Y.I. To the 100th anniversary of the National Academy of Sciences of Ukraine the cradle of domestic science and technology. *Electrical Engineering & Electromechanics*, 2018, no. 5, pp. 3-11. doi: https://doi.org/10.20998/2074-272X.2018.5.01.

Received 10.04.2025 Accepted 05.06.2025 Published 02.11.2025

- B.I. Kuznetsov¹, Doctor of Technical Science, Professor,
- T.B. Nikitina², Doctor of Technical Science, Professor,
- I.V. Bovdui¹, PhD, Senior Research Scientist,
- K.V. Chunikhin¹, PhD, Senior Research Scientist,
- V.V. Kolomiets², PhD, Assistant Professor,
- B.B. Kobylianskyi², PhD, Assistant Professor,
- ¹ Anatolii Pidhornyi Institute of Power Machines and Systems of the National Academy of Sciences of Ukraine,
- 2/10, Komunalnykiv Str., Kharkiv, 61046, Ukraine,
- e-mail: kuznetsov.boris.i@gmail.com (Corresponding Author)
- ² Bakhmut Education Research and Professional Pedagogical Institute V.N. Karazin Kharkiv National University,
- 9a, Nosakov Str., Bakhmut, Donetsk Region, 84511, Ukraine.

How to cite this article:

Kuznetsov B.I., Nikitina T.B., Bovdui I.V., Chunikhin K.V., Kolomiets V.V., Kobylianskyi B.B. Synthesis of combined shielding system for overhead power lines magnetic field normalization in residential building space. *Electrical Engineering & Electromechanics*, 2025, no. 6, pp. 40-50. doi: https://doi.org/10.20998/2074-272X.2025.6.06

Y. Laamari, N. Boukhennoufa, H. Benderradji, S. Allaoui

Fuzzy logic-based vector control of permanent magnet synchronous motor drives under inter-turn short-circuit fault conditions

Introduction. Permanent magnet synchronous motors (PMSMs) are widely used in industrial and automotive applications due to their high efficiency and power density. Problem. However, their performance can be significantly affected by faults such as inter-turn shortcircuits faults (ITSCFs) in the stator windings. These faults introduce oscillations in rotor speed and electromagnetic torque, increase total harmonic distortion (THD), and degrade the overall reliability of the system drive. Conventional field-oriented control (FOC) methods, particularly, those employing PI controllers, often struggle to maintain stability under such fault conditions. Goal. This study aims to develop and evaluate a fuzzy logic-based control strategy to enhance the fault tolerance of PMSM drives under ITSCFs conditions. Methodology. To achieve this, a mathematical model of the PMSM is developed to represent both healthy and faulty operating states. This model is integrated into a vector control framework where two types of speed controllers are compared: a conventional PI controller and a fuzzy PI controller. The proposed fuzzy logic controller is implemented within the FOC scheme and evaluated through simulation. Results. Simulation results demonstrate that the fuzzy vector control approach significantly reduces rotor speed and electromagnetic torque ripples under both healthy and faulty conditions, while maintaining stable torque output and minimizing THD. It consistently outperforms the conventional PI controller. Scientific novelty. Unlike traditional FOC methods, this study introduces a fuzzy logicenhanced control strategy specifically designed to improve PMSM performance under fault conditions. The integration of fuzzy logic with vector control offers superior dynamic response and enhanced resilience. Practical value. The proposed approach improves the robustness and reliability of PMSM drives, particularly in fault-sensitive applications such as industrial automation and electric vehicles. This contributes to extended system lifespan and improved operational stability. References 26, tables 2, figures 13.

Key words: permanent magnet synchronous motor, field-oriented control, inter-turn short-circuit, PI controller, fuzzy logic controller.

Синхронні двигуни з постійними магнітами (РМЅМs) широко використовуються в промисловості та автомобілебудуванні завдяки своїй високій ефективності та питомій потужності. Проблема. Однак на їх продуктивність можуть суттєво впливати такі несправності, як міжвиткові короткі замикання (ITSCFs) в обмотках статора. Ці несправності призводять до коливань швидкості ротора та електромагнітного моменту, збільшують коефіцієнт гармонічних спотворень (ТНД) та знижують загальну надійність приводу системи. Традиційні методи управління з орієнтацією по полю (FOC), зокрема, з використанням ПІ-регуляторів, часто не забезпечують стійкість у таких умовах. Мета. Дане дослідження спрямоване на розробку та оцінку стратегії управління на основі нечіткої логіки для підвищення стійкості до відмови РМЅМѕ в умовах ITSCFs. **Методологія**. Для досягнення цієї мети розроблено математичну модель PMSMs, яка описує як справні, так і несправні робочі стани. Ця модель інтегрована у систему векторного управління, де порівнюються два типи регуляторів швидкості: звичайний ПІ-регулятор та нечіткий ПІ-регулятор. Запропонований нечіткий логічний контролер реалізовано в рамках FOC схеми та оцінено за допомогою моделювання. Результати моделювання показують, що підхід з нечітким векторним управлінням значно знижує частоту обертання ротора і пульсації електромагнітного моменту як у справному, так і несправному стані, зберігаючи при цьому стабільний вихідний крутний момент і мінімізуючи сумарний ТНД. Він стабільно перевершує традиційний ПІ-регулятор. Наукова новизна. На відміну від традиційних FOC методів, це дослідження пропонує стратегію керування з покращеною нечіткою логікою, спеціально розроблену для покращення продуктивності PMSM в умовах несправності. Інтеграція нечіткої логіки з векторним управлінням забезпечує чудовий динамічний відгук та підвищену стійкість. Практична цінність. Пропонований підхід підвищує надійність та стійкість РМSMs, особливо у чутливих до відмов сферах, таких як промислова автоматика та електромобілі. Це сприяє збільшенню терміну служби системи та підвищенню експлуатаційної стабільності. Бібл. 26, табл. 2, рис. 13.

Ключові слова: синхронний двигун з постійними магнітами, полеорієнтоване керування, міжвиткове замикання, ПІ-регулятор, нечіткий логічний регулятор.

Introduction. Permanent magnet synchronous motors (PMSMs) have garnered significant attention in industrial applications, particularly in the traction and auxiliary machinery, due to their superior efficiency, high torque-toinertia ratio, and high power density [1–3]. However, during its operation, PMSMs are subjected to various stresses, including fluctuating power supply conditions, load variations, and thermal stresses on the stator winding that can lead to performance degradation and eventual failure. These effects are further accelerated when the motor is driven by inverter-based power systems [4, 5]. PMSM failures are typically classified into 3 categories: electrical, mechanical, and magnetic. Among these, stator inter-turn short-circuit faults (ITSCFs) are the most common electrical faults, accounting for approximately 30-40 % of all PMSM failures [6–8].

ITSCFs create imbalances in the phase currents, leading to rotor speed oscillations, fluctuations in electromagnetic torque, increased total harmonic distortion (THD), and mechanical vibrations which can accelerate the degradation on both mechanical and electrical components. Therefore, early detection and real-time compensation of these faults are critical for ensuring service continuity and enhancing motor longevity [2].

Several studies have been directed at fault detection and mitigation. For instance, authors [3] proposed a detection technique based on stator current analysis, while in [4] were utilized thermal sensors for fault identification. However, these methods primarily focus on fault detection rather than active compensation.

Furthermore, traditional control strategies, such as field-oriented control (FOC) paired with conventional PI controllers, tend to perform poorly under fault conditions due to their limited adaptability to dynamic system changes [5]. Most modern industrial processes require speed drives with great performance, good steady-state accuracy, high overload capability over the whole speed range and robust operation. In fact, many control techniques have been developed to achieve high efficiency. Among these techniques, FOC allows PMSM to be controlled like an independently excited DC machine providing natural flux-torque decoupling and enabling a rapid torque response [9, 10].

The FOC structure with conventional PI controllers is widely preferred in many applications [10, 11]. However, due to their fixed proportional gain and integral time

© Y. Laamari, N. Boukhennoufa, H. Benderradji, S. Allaoui

constant, the static and dynamic performance of PI controllers is significantly affected by parameter variations, load disturbances, and speed fluctuations. To overcome these limitations and improve the robustness of FOC, reducing its sensitivity to parametric variations, faults, and their effects, the implementation of modern and intelligent controllers has become more necessary [12, 13]. Recently, new control techniques for PMSM that are more competitive, able to surmount the nonlinearities and more robust were proposed in the literature such as adaptive control [13], fuzzy logic control [14-16], sliding mode control (SMC) [17, 18] and direct torque control (DTC) [19]. In most of these cited works, the PMSM models were considered without failures (healthy state). In [20] authors show guidelines for the search and choice of PMSM control strategies under different type of faults. They found that adaptive control based on the extended Kalman filter [21] is the best estimation system states, but a drawback complexity. SMC has been widely used for controlling nonlinear systems, providing excellent stability, robustness, and reliable performance even in the presence of uncertainties and external disturbances. Indeed, for the SMC as given in [22], the chattering phenomenon still remains the major problem of this method. On the other hand, various studies have shown that DTC offers several advantages over conventional FOC [19, 23]. However, DTC has notable drawbacks, including high flux and electromagnetic torque ripples, as well as variable switching frequency due to the use of hysteresis controllers [24]. To overcome these limitations, AI techniques, such as neural networks and fuzzy logic, have recently been introduced by researchers to enhance the performance of PMSM drive controllers [15-17]. The neural network technique offers high performance; however, it requires a training process, which can slow down the controller's response. In contrast, fuzzy logic control is an intelligent strategy that emulates human decision-making [16, 17]. Fuzzy logic controllers (FLC) are particularly effective in handling systems with uncertainties or parameter variations. The performance of FLC can be tuned through its internal components, including fuzzy rules, fuzzification, and defuzzification blocks.

Goal. The study aims to develop an advanced vector control strategy incorporating fuzzy logic to enhance fault tolerance in PMSM drives by replacing the conventional PI controller with a FLC. Instead, it relies on a set of linguistic rules derived from expert knowledge, allowing for adaptive and intelligent control. The primary objective is to evaluate the effectiveness of the FLC in terms of reducing torque and speed ripples while preserving overall system performance during fault conditions.

To demonstrate the effectiveness of the proposed method, a comparative study between fuzzy FOC and conventional FOC is conducted under short-circuit fault conditions in various operating scenarios. Simulation results confirm the superiority of fuzzy control in terms of robustness and efficiency in handling ITSCFs. A mathematical fault model of a PMSM driven by a pulse width modulation (PWM) inverter is utilized to analyze

 $\begin{bmatrix} v_{as} \\ v_{bs} \\ v_{cs} \\ 0 \end{bmatrix} = \begin{bmatrix} R_s & 0 & 0 & -R_{as2} \\ 0 & R_s & 0 & 0 \\ -R_{as2} & 0 & 0 & R_{as2} + R_f \end{bmatrix} \begin{bmatrix} i_{as} \\ i_{bs} \\ i_{cs} \\ i_f \end{bmatrix} + \begin{bmatrix} L_s & 0 & 0 & -L_{as2} + M_{a1a2} \\ 0 & L_s & 0 & -M_{a2b} \\ 0 & 0 & L_s & -M_{a2c} \\ -L_{as2} - M_{a1a2} & -M_{a2b} & -M_{a2c} \end{bmatrix} \frac{d}{dt} \begin{bmatrix} i_{as} \\ i_{bs} \\ i_{cs} \\ i_f \end{bmatrix} + \begin{bmatrix} p\Omega \varphi_f \sin \theta \\ p\Omega \varphi_f \sin(\theta - \frac{2\pi}{3}) \\ p\Omega \varphi_f \sin(\theta + \frac{2\pi}{3}) \\ -\mu p\Omega \varphi_f \sin \theta \end{bmatrix}, (3)$

where R_s , L_s are the resistance and self-inductance of healthy stator phase windings with $R_{as}=R_{bs}=R_{cs}=R_s$;

various inter-turn fault conditions and severity levels. In an open-loop framework, the system's basic behavior is observed. However, in a closed-loop configuration, the controller actively regulates the *d-q* currents, influencing the motor's fault response [12].

Modeling of PMSM under ITSCFs. Figure 1 shows the PMSM stator with an inter-turn fault, accounting for resistance, self-inductance, back electromotive force (EMF) and mutual inductance between faulty and healthy windings [25].

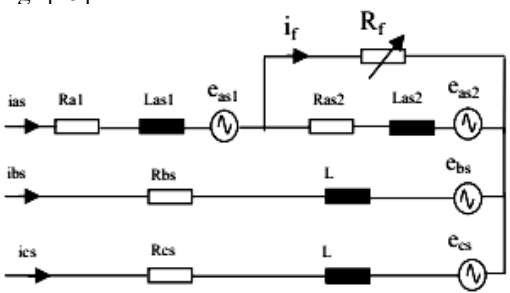


Fig. 1. PMSM stator with ITSCF in phase (as)

ITSCF refers to a fault among 2 stator windings within the same phase. To model this fault the affected phase (as) is divided into 2 sub-windings, representing the healthy and faulty branches. ITSCF is represented by a resistance whose value varies based on fault severity [25, 26]. As the fault resistance R_f approaches 0, the insulation failure progresses to a full inter-turn short-circuit. The fault current through R_f is denoted as i_f . To quantify the fault severity, a parameter μ is introduced, defined as the ratio of short-circuited turns N_f to the total number of turns in a phase N_s . Fault severity is characterized by 2 key parameters – the short-circuit percentage μ and the resistance (R_f). The resistances of healthy and faulty sections of the stator winding are:

$$R_{as1} = (1 - \mu)R_{as}; \ R_{as2} = \mu R_{as}; \ \mu = \frac{N_{as2}}{N_{as1} + N_{as2}} = \frac{N_f}{N_s}.$$
 (1)

To model the PMSM drive, the following assumptions are made: no magnetic saturation, negligible temperature effects, sinusoidal flux and magnetomotive force distribution, and the exclusion of higher harmonics [10]. Additionally, the following relationships are generally recognized:

$$\begin{cases} R_{s} = R_{as} = R_{as1} + R_{as2}; \\ L = L_{as1} + L_{as2} + 2M_{a1a2}; \\ M = M_{a1b} + M_{a2b} = M_{a1c} + M_{a2c}; \\ e_{as} = e_{as1} + e_{as2} = e_{as1} + e_{f}. \end{cases}$$
(2)

In general, the stator phases are connected in a star configuration, ensuring that: $i_{as}+i_{bs}+i_{cs}=0$. Under these conditions, the homopolar current component is 0, and the phase currents are limited solely by the cyclic inductance: $L_s=L-M$. Consequently, the voltage equations of PMSM with an ITSCF in phase (as), as shown in Fig. 1, can be expressed in the (abcf) reference frame as follows:

 R_{as2} , L_{as2} are the resistance and self-inductance of the faulty sub-coil (as2); M_{a1a2} , M_{a2b} , M_{a2c} are the mutual

inductances between sub-coil (as1) and coils (as2), (bs), and (cs), respectively; M_{a1b} , M_{a1c} are the mutual inductance between sub-coil (as1) and coils (bs) and (cs); M_{ab} is the mutual inductance between coils (as) and (bs).

Thus, (3) can be expressed in a more compact form:

$$[V_{abcf}] = [R_s][i_{abcf}] + [L_s] \frac{\mathrm{d}}{\mathrm{d}t}[i_{abcf}] + [E_{abcf}], \quad (4)$$

where $[V_{abcf}]$, $[i_{abcf}]$, $[E_{abcf}]$ are the stator voltage, current and back-EMF vectors, respectively.

Based on the power conservation principle, the electromagnetic torque under a short-circuit fault is given as:

$$C_{em} = \frac{e_{as}i_{as} + e_{bs}i_{bs} + e_{cs}i_{cs} - e_{f}i_{f}}{Q}.$$
 (5)

The motor's dynamic behavior is described by the following mechanical equation:

$$C_{em} - C_L - f\Omega = J \frac{\mathrm{d}\Omega}{\mathrm{d}t} \,, \tag{6}$$

where f is the friction coefficient; J is the rotor moment of inertia; C_L is the load torque; Ω is the rotor's mechanical speed. Identifying the inductances of a faulty motor is crucial, as they contain essential fault-related information. Two methods are employed to determine the faulty inductances of a PMSM by applying a simple percentage adjustment to the parameters of the healthy state [26].

In this study we adopt a method where the self-inductances of the faulty and healthy winding (as1, as2) are proportional to the square of the number of shorted turns. Additionally, the mutual inductance depends on the turn count of both sections [25]:

$$L_{as1} = (1 - \mu)^2 L_{as}; \quad L_{as2} = \mu^2 L_s;$$

$$M_{a1a2} = \mu(1 - \mu)L_s; \quad M_{a2b} - M_{a2c} = \mu M;$$

$$M_{a1b} = M_{a1c} = (1 - \mu)M,$$
(7)

where μ is the fraction of shorted turns.

Since the PMSM model is a multi-variable, non-linear and strongly coupled system. Hence, to surmount this difficulty and to obtain a model similar to that of the separately DC machine, the most popular control strategy of PMSM named FOC was established.

Proposed method. This approach involves replacing the conventional PI controller with a FLC in the FOC scheme for a PMSM drive, aiming to enhance performance under short-circuit faults in various operating conditions. FOC is the most used technique to drive the PMSM; it is based on the use of a transformation that takes machine's electrical variables from (abc) stationary referential into (d-q) rotating referential with the flux vector. Consequently, this makes it possible to control the flux with the stator current i_d , while, the component i_q allows to control the electromagnetic torque [9, 10]. When i_d =0, the relationship between C_{em} and i_q becomes linear, and PMSM will be equivalent to a DC motor with separate excitation. As shown in Fig. 2, FOC can achieve closed-loop speed control. The speed PI controller generates reference quadrature current i_q^* , or reference of the output torque:

$$C_{em} = 1.5 p i_q^* \varphi_f , \qquad (8)$$

where φ_f is the permanent magnet flux; p is the number of pole pairs of the motor.

To generate gating signals for the inverter, PWM is applied to produce the reference signals. Figure 2 shows the block diagram of the FOC for PMSM drive under ITSCF.

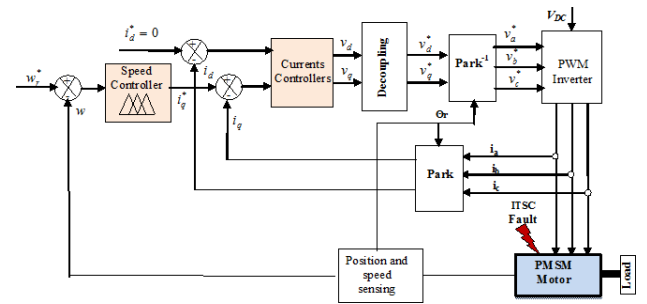


Fig. 2. Block diagram of the FOC for PMSM under faults

Classical PI speed controller. The PI controller is a feedback control loop method which is widely used in control systems in industries [13, 14]. It is defined by the following action law:

$$i_q^* = k_p(\omega_r^* - \omega) + k_i \int (\omega_r^* - \omega) dt , \qquad (9)$$

where k_p , k_i are the PI parameters which represent gains determined by pole placement method.

Fuzzy PI speed controller. Note that conventional PI controllers have certain limitations, such as overshoot and undershoot in the response, particularly when the system is affected by unknown nonlinearities [15, 16]. On the other hand, FLCs are able to overcome these disadvantages. Similar to human reasoning, FLC handles imprecise information through 3 steps: fuzzification, inference and defuzzification. Fuzzification converts crisp values into fuzzy values using membership functions. Inference applies rules to link inputs and outputs, while defuzzification converts the fuzzy output back to a crisp value. Figure 3 gives the whole framework of the FOC method containing 3 regulators, 2 conventional PI for the currents i_d and i_q (inner loops) and 1 regulator for the speed (outer loop). The proposed fuzzy PI speed controller is of Mamdani type with 3 linguistic variables: 2 inputs (error e and its variation de) and 1 output (control action current i_q^*). The error speed e and its change de are:

$$\begin{cases} e(k) = \omega_{ref(k)} - \omega(k); \\ de(k) = e(k) - e(k-1). \end{cases}$$
 (10)

In Fig. 3 gains k_e , k_{de} are scaling factors used to adjust controller input values for best performances.

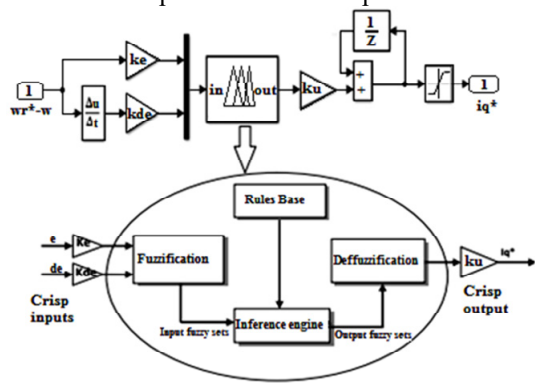


Fig. 3. Block framework of the fuzzy PI controller

The fuzzy PI control law is expressed as:

$$u(k) = u(k-1) + k_u du(k)$$
, (11)

where k_u is the control gain.

Each linguistic variable's universe of discourse is divided into 7 fuzzy subsets, defined by the following membership functions (Fig. 4): **NB** (Negative Big); **NM** (Negative Medium); **NS** (Negative Small); **ZE** (Zero); **PS** (Positive Small); **PM** (Positive Medium); **PB** (Positive Big).

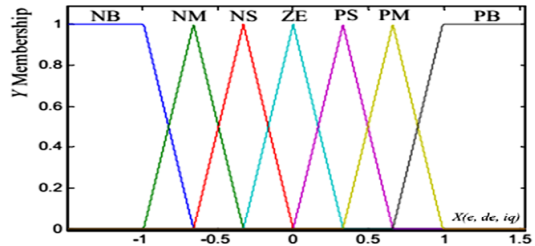


Fig. 4. Inputs and output FLC membership functions

Controller fuzzy rules are given in Table 1. Used rules have the following *If-Then* form:

 $R^{(l)}$: if e is A^l , and de is B^l , Then i_q^* is C^l , where (l) is the rule number; A^l , B^l are input membership functions; C^l is the output membership function.

Defuzzification process is based on the popular centre of gravity method.

Table 1

Speed fuzzy controller rules

-F							
de	NB	NM	NS	ZE	PS	PM	PB
e							
NB	NB	NB	NB	NM	NS	NS	ZE
NM	NB	NM	NM	NM	NS	ZE	PS
NS	NB	NM	NS	NS	ZE	PS	PM
ZE	NB	NM	NS	ZE	PS	PM	PB
PS	NS	NS	ZE	PS	PS	PM	PB
PM	NS	ZE	PS	PM	PM	PM	PB
PB	ZE	PS	PS	PM	PB	PB	PB

Simulation and results. All results presented here are based on the assumption that the fault parameters μ and R_f are known. The simulations are performed in MATLAB/Simulink environment. The nominal parameters of the PMSM used in this study are listed in Table 2. To analyze the motor's behavior under an inter-turn fault in the stator winding, both healthy and faulty operating conditions were considered.

Parameters of PMSM used in simulation

Table 2

uiation
Value
8
40
5
19
0.44
2.82
1000
0.108
0.0006
0.007
10

PMSM in healthy case. In this section, the performances of the vector control drive of PMSM, under healthy conditions are tested. In Fig. 5, 6 the rotor speed, the electromagnetic torque and the stator phase currents in the Park's frame for the healthy PMSM associated to the FOC with both classical PI and fuzzy PI speed controllers are respectively presented. The vector control robustness is tested under the application of a load torque at t=0.15 s followed by an application of a reversing speed from 100 rad/s to -100 rad/s at time t=0.25 s. It can be seen that obtained results with the classic PI speed regulator are almost similar to those obtained by the fuzzy PI regulator, but with a slight superiority of the later in terms of response time and load disturbance rejection. In addition, the three phase stator currents in (abc) reference frame as shown in Fig. 5,a and Fig. 6,a are balanced and sinusoidal.

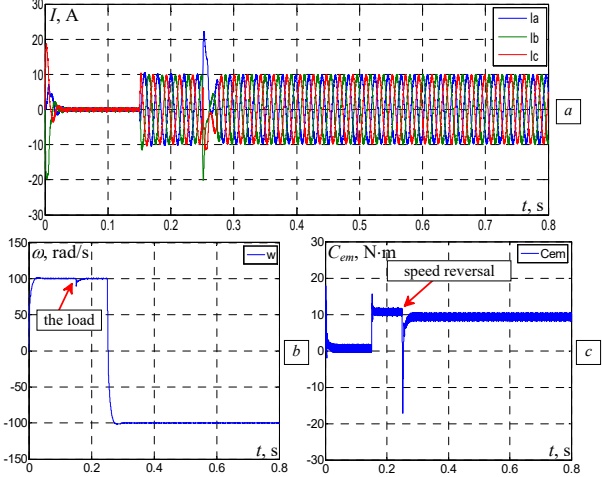


Fig. 5. Simulation results with *classical* PI speed controller in healthy case: *a*) stator phase currents; *b*) rotor speed; *c*) electromagnetic torque

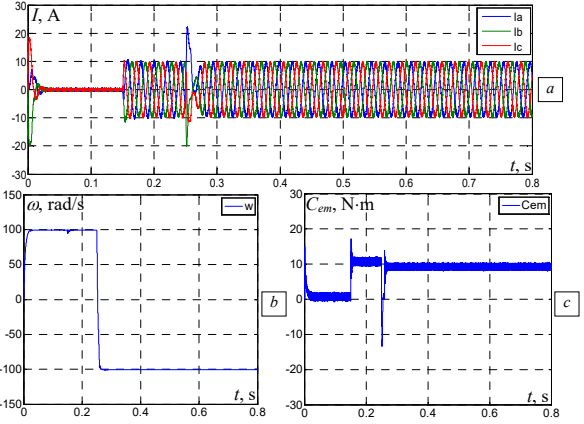
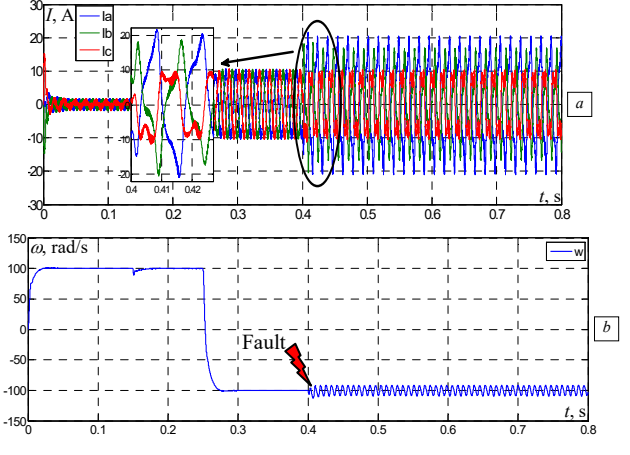


Fig. 6. Simulation results with *fuzzy* PI speed controller in healthy case: *a*) stator phase currents; *b*) rotor speed; *c*) electromagnetic torque

PMSM in faulty case. In this case, we will consider the FOC comportment of the PMSM drive with the presence of ITSCF. We test the robustness with the application of a load torque of 10 N·m at t=0.15 s followed by a speed reversing from 100 rad/s to -100 rad/s at time t=0.25 s as shown in Fig. 7,b,c and Fig. 8,b,c. Consider that the phase (as) is affected by a short-circuit fault introduced at t=0.4 s with μ =20 %, which corresponds to 32 turns out of 160 being faulty. The resistance R_f is fixed to 0.1 Ω . As shown in Fig. 7,a and Fig. 8,a the current magnitude in the faulty phase (as) is higher compared to the other healthy phases (bs, cs) and the unbalance of the phase currents becomes more important.



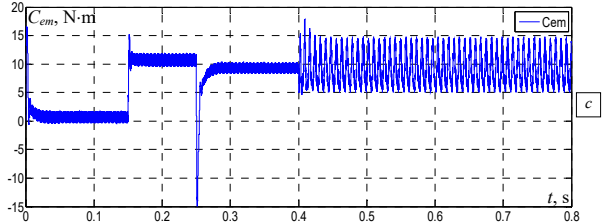
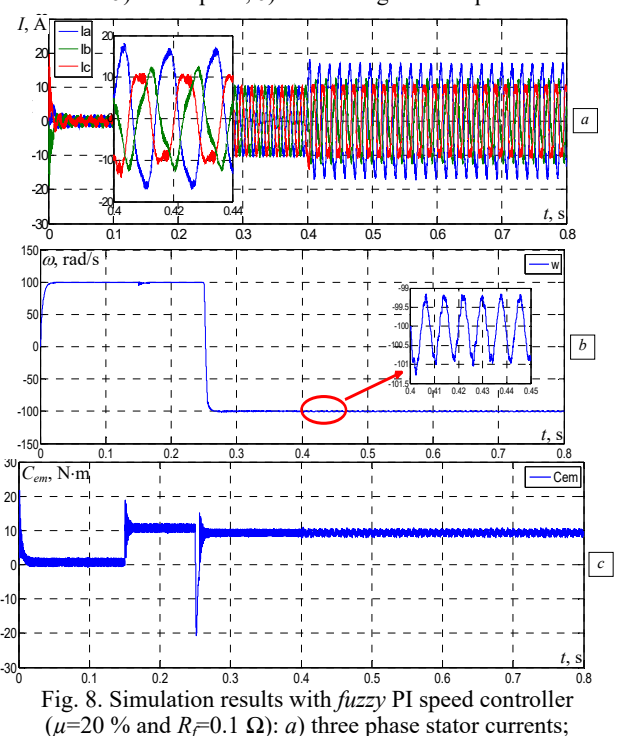


Fig. 7. Simulation results with *classical* PI speed controller $(\mu=20 \% \text{ and } R_f=0.1 \ \Omega)$: a) three phase stator currents; b) rotor speed; c) electromagnetic torque



Comparison and discussion. Figures 9, 10 show the rotor speed and electromagnetic torque for a healthy PMSM. For the fuzzy PI controller, the ripples magnitude is smaller compared to that obtained with the conventional PI controller. In what follows, and for comparison purposes, consider that the phase (as) is now affected by a short-circuit fault introduced at t=0.4 s with μ =50 %, which corresponds to 80 turns out of 160 being faulty.

b) rotor speed; c) electromagnetic torque

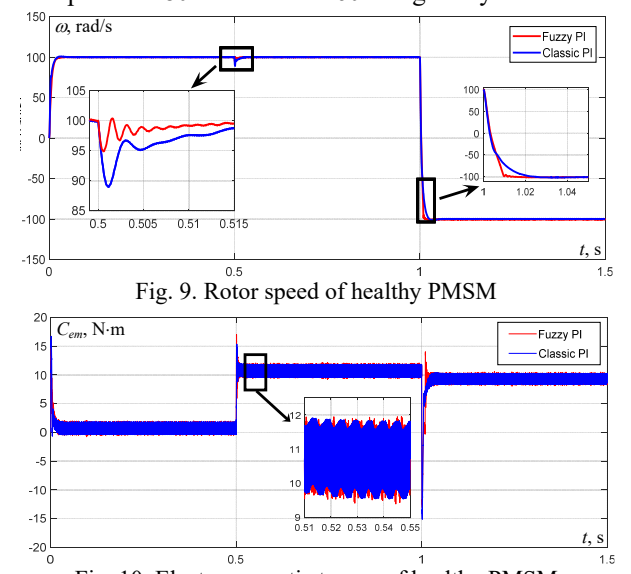


Fig. 10. Electromagnetic torque of healthy PMSM

Figures 11, 12 show the rotor speed and the electromagnetic torque, in which we note that the ripples increase significantly when μ increases to 50 % ITSCF with the fault resistance R_f =0.1 Ω . Comparing the classic PI controller with the fuzzy controller, we see that: 1) fuzzy control reduces efficiently ripples magnitude while utilizing the defective phase to maintain maximum torque capacity; 2) provides faster responses and more efficient load disturbance rejection in both cases, healthy and faulty ones. This control can be used in a situation where the fault severity is estimated to be safe to keep the motor running.

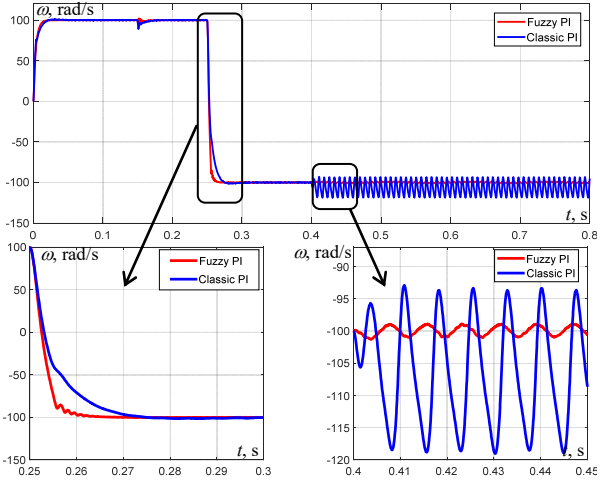


Fig. 11. Rotor speed of PMSM under short-circuit fault $(\mu=50 \% \text{ and } R_f=0.1 \Omega)$

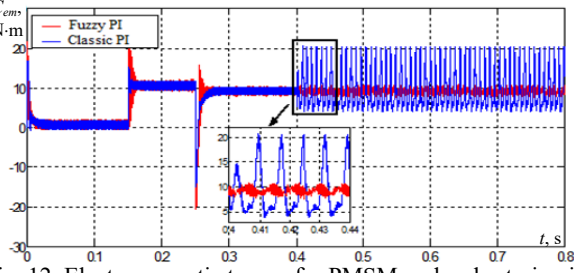


Fig. 12. Electromagnetic torque for PMSM under short-circuit fault (μ =50 % and R_f =0.1 Ω)

Figure 13 shows the rotor speed and electromagnetic torque spectra using MATLAB's fast Fourier transform (FFT) toolbox to analyze frequency components and THD.

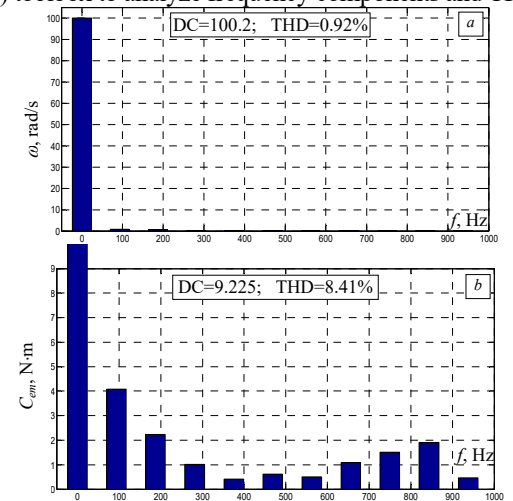


Fig. 13. Frequency analysis under ITSCF conditions in the fuzzy vector control (R_f =0.1 Ω and μ =50 %): a) rotor speed spectral analysis; b) electromagnetic torque spectral analysis

Under ITSCF conditions, harmonic frequencies appear, and their amplitude increases with the severity of the fault.

The results show that the fuzzy controller is more robust than the classical PI, exhibiting fewer ripples and lower THD.

Conclusions. In this study, the PMSM model, incorporating ITSCF in the stator winding, was integrate with vector control in a closed loop scheme using 2 types of controllers. The simulation results confirmed the superiority of the fuzzy PI controller over the conventional PI, especially in the presence of an ITSCF. Fuzzy logic based vector control ensures a high-quality dynamic response and robust control under load torque disturbances, speed reversals, and stator short faults. In addition, the FLC provides excellent dynamic and steady state responses for torque and motor speed, with reduced ripple content that can accelerate stator winding degradation. This advantage extends the winding's lifespan and enhances the predictive diagnosis of turn damage. In conclusion, it can be seen that our approach based on the FLC provides better results than the conventional method and makes the system much more robust to faults. In fact, the proposed scheme has the capability to reduce significantly the torque ripples and the fluctuations in the rotor speed. So, the controller does not just perform control tasks, but is also able to maintain protection when faults happening in the system and can be easily adapted to changes in machine parameters.

Conflict of interest. The authors declare that they have no conflicts of interest.

REFERENCES

- 1. Khaneghah M.Z., Alzayed M., Chaoui H. Fault Detection and Diagnosis of the Electric Motor Drive and Battery System of Electric Vehicles. Machines, 2023, vol. 11, no. 7, art. no. 713. doi: https://doi.org/10.3390/machines11070713.
 Niu G., Dong X., Chen Y. Motor Fault Diagnostics Based on Current
- Signatures: A Review. IEEE Transactions on Instrumentation and
 Measurement,
 2023,
 vol.
 72,
 pp.
 1-19.
 doi: https://doi.org/10.1109/TIM.2023.3285999.

 3.
 Hu R., Wang J., Mills A.R., Chong E., Sun Z. Current-Residual-Based
- Stator Interturn Fault Detection in Permanent Magnet Machines. IEEE Transactions on Industrial Electronics, 2021, vol. 68, no. 1, pp. 59-69. doi: https://doi.org/10.1109/TIE.2020.2965500.
- 4. Mohammed A., Melecio J.I., Djurovic S. Open-Circuit Fault Detection in Stranded PMSM Windings Using Embedded FBG Thermal Sensors. *IEEE Sensors Journal*, 2019, vol. 19, no. 9, pp. 3358-3367. doi: https://doi.org/10.1109/JSEN.2019.2894097
- 5. Sergakis A., Salinas M., Gkiolekas N., Gyftakis K.N. A Review of Condition Monitoring of Permanent Magnet Synchronous Machines: Techniques, Challenges and Future Directions. *Energies*, 2025, vol. 18, no. 5, art. no. 1177. doi: https://doi.org/10.3390/en1805117
- Mazzoletti M.A., Bossio G.R., De Angelo C.H. Interturn short-circuit fault diagnosis in PMSM with partitioned stator windings. IET Electric Power Applications, 2020, vol. 14, no. 12, pp. 2301-2311. doi:
- Pietrzak P., Wolkiewicz M. On-line Detection and Classification of PMSM Stator Winding Faults Based on Stator Current Symmetrical Components Analysis and the KNN Algorithm. *Electronics*, 2021, vol. 10, no. 15, art. no. 1786. doi: https://doi.org/10.3390/electronics10151786.
- 8. Huang W., Chen J., Hu J., Lv K., Liu H. Search-Coil Based Stator Interturn Fault Detection in Permanent Magnet Machines Running under Dynamic Condition. Electronics, 2023, vol. 12, no. 13, art. no. 2827. doi: https://doi.org/10.3390/electronics12132827
- Pietrzak P., Wolkiewicz M., Orlowska-Kowalska T. PMSM Stator Winding Fault Detection and Classification Based on Bispectrum Analysis and Convolutional Neural Network. IEEE Transactions on Industrial *Electronics*, 2023, vol. 70, no. https://doi.org/10.1109/TIE.2022.3189076. 5192-5202. pp.
- 10. Setiawan M.H., Ma'arif A., Saifuddin M.F., Salah W.A. A Comparative Study of PID, FOPID, ISF, SMC, and FLC Controllers for DC Motor Speed Control with Particle Swarm Optimization. International Journal of Robotics and Control Systems, 2025, vol. 5, no. 1, pp. 640-660. doi: https://doi.org/10.31763/ijrcs.v5i1.1764.
- 11. Khanh P.Q., Dat N.T., Anh H.P.H. Optimal Fuzzy-PI PMSM Speed Control Using Evolutionary DE Algorithm Implemented on DSP Controller. 2023 International Conference on System Science and Engineering (ICSSE), 2023, pp. 206-211. doi: https://doi.org/10.1109/ICSSE58758.2023.10227151.

- 12. Moussaoui L., Aouaouda S., Rouaibia R. Fault tolerant control of a permanent magnet synchronous machine using multiple constraints Takagi-Sugeno approach. Electrical Engineering & Electromechanics, 2022, no. 6, pp. 22-27. doi: https://doi.org/10.20998/2074-272X.2022.6.04
- 13. Chaabane H., Khodja D.E., Chakroune S., Hadji D. Model reference adaptive backstepping control of double star induction machine with extended Kalman sensorless control. Electrical Engineering Electromechanics, 2022, no. 4, pp. 3-11. doi: https://doi.org/10.20998/2074-
- 14. Zhang B., Niu P., Guo X., He J. Fuzzy PID control of permanent magnet synchronous motor electric steering engine by improved beetle antennae search algorithm. *Scientific Reports*, 2024, vol. 14, no. 1, art. no. 2898. doi: https://doi.org/10.1038/s41598-024-52600-8.
- 15. Sakri D., Laib H., Farhi S.E., Golea N. Sliding mode approach for control and observation of a three phase AC-DC pulse-width modulation rectifier. *Electrical Engineering & Electromechanics*, 2023, no. 2, pp. 49-56. doi: https://doi.org/10.20998/2074-272X.2023.2.08.

 16. Deng Y., Wang J., Li H., Liu J., Tian D. Adaptive sliding mode current
- control with sliding mode disturbance observer for PMSM drives. ISA Transactions. 2019. vol. 88. pp. 113-126. https://doi.org/10.1016/j.isatra.2018.11.039.
- 17. Petkar S.G., Thippiripati V.K. A Novel Duty-Controlled DTC of a Surface PMSM Drive With Reduced Torque and Flux Ripples. IEEE Transactions on Industrial Electronics, 2023, vol. 70, no. 4, pp. 3373-3383. doi: https://doi.org/10.1109/TIE.2022.3181405.
- 18. Bhuiyan E.A., Akhand M.M.A., Das S.K., Ali M.F., Tasneem Z., Islam M.R., Saha D.K., Badal F.R., Ahamed M.H., Moyeen S.I. A Survey on Fault Diagnosis and Fault Tolerant Methodologies for Permanent Magnet Synchronous Machines. International Journal of Automation and *Computing*, 2020, vol. 17, no. https://doi.org/10.1007/s11633-020-1250-3. no. pp.
- 19. Dan L. EKF-based fault detection and isolation for PMSM inverter. Sustainable Energy Technologies and Assessments, 2022, vol. 52, art. no. 101846. doi: https://doi.org/10.1016/j.seta.2021.101846.
- 20. Oualah O., Kerdoun D., Boumassata A. Comparative study between sliding mode control and the vector control of a brushless doubly fed reluctance generator based on wind energy conversion systems. Electrical Engineering & Electromechanics, 2022, no. 1, pp. 51-58. doi: https://doi.org/10.20998/2074-272X.2022.1.07.

 21. Zhang J., Zhan
- Inter-Turn Short-Circuit Fault. IEEE Transactions on Energy Conversion, pp. 2267-2275.
- 22. Guezi A., Bendaikha A., Dendouga A. Direct torque control based on second order sliding mode controller for three-level inverter-fed permanent magnet synchronous motor: comparative study. Electrical Engineering & Electromechanics, 2022, no. 5, pp. 10-13. doi: https://doi.org/10.20998/2074-
- 23. Bdewi M.Y., Mohammed A.M., Ezzaldean M.M. Design and Performance Analysis of Permanent Magnet Synchronous Motor for Electric Vehicles Application. Engineering and Technology Journal, 2021, vol. 39, no. 3A, pp. 394-406. doi: https://doi.org/10.30684/etj.v39i3A.1765.
- 24. Bensalem Y., Abbassi R., Jerbi H. Fuzzy Logic Based-Active Fault Tolerant Control of Speed Sensor Failure for Five-Phase PMSM. Journal of Electrical Engineering & Technology, 2021, vol. 16, no. 1, pp. 287-299. doi: https://doi.org/10.1007/s42835-020-00559-7.
- 25. Vaseghi B., Takorabet N., Nahid-Mobarakeh B., Meibody-Tabar F. Modelling and study of PM machines with inter-turn fault dynamic model-FEM model. Electric Power Systems Research, 2011, vol. 81, no. 8, pp. 1715-1722. doi: https://doi.org/10.1016/j.epsr.2011.03.017.
- 26. Zafarani M., Bostanci E., Qi Y., Goktas T., Akin B. Interturn Short-Circuit Faults in Permanent Magnet Synchronous Machines: An Extended Review and Comprehensive Analysis. IEEE Journal of Emerging and Selected Topics in Power Electronics, 2018, vol. 6, no. 4, pp. 2173-2191. doi: https://doi.org/10.1109/JESTPE.2018.2811538.

Received 08.04.2025 Accepted 21.05.2025 Published 02.11.2025

- Y. Laamari¹, PhD, Associate Professor,
- N. Boukhennoufa¹, PhD, Associate Professor,
- H. Benderradji¹, PhD, Associate Professor, S. Allaoui², PhD, Assistant Professor.
- ¹University of Batna2, Algeria,
- e-mail: y.laamari@univ-batna2.dz (Corresponding Author)
- ² Higher National School of Renewable Energies,
- Environment & Sustainable Development, Batna, Algeria

How to cite this article:

Laamari Y., Boukhennoufa N., Benderradji H., Allaoui S. Fuzzy logic-based vector control of permanent magnet synchronous motor drives under inter-turn short-circuit fault conditions. Electrical Engineering & Electromechanics, 2025, no. 6, pp. 51-56. doi: https://doi.org/10.20998/2074-272X.2025.6.07

M. Makhlouf, O. Laouar

New adaptive modified perturb and observe algorithm for maximum power point tracking in photovoltaic systems with interleaved boost converter

Introduction. In recent years, maximum power point tracking (MPPT) has become a critical component in photovoltaic (PV) systems to ensure maximum energy harvesting under varying irradiance and temperature conditions. Among the most common algorithms, perturb and observe (P&O) and incremental conductance (IC) are widely adopted due to their simplicity and effectiveness, **Problem.** Conventional P&O suffers from steady-state oscillations and slow dynamic response, while IC requires higher computational complexity and loses accuracy under rapidly changing conditions. These drawbacks limit overall tracking efficiency and system reliability. The goal of this work is the development and evaluation of a novel adaptive modified perturb and observe (AM-P&O) algorithm for a PV system with an interleaved boost converter. The proposed method dynamically adjusts the perturbation step size to achieve faster convergence and lessen steady-state oscillations to enhance tracking efficiency. Its performance is assessed through simulation with varying irradiance. It is then compared to traditional methods (P&O and IC) using quantitative metrics such as convergence time, oscillation magnitude, tracking efficiency, and computational cost. Methodology. The AM-P&O algorithm introduces an adaptive step size adjustment strategy, in which the perturbation magnitude is dynamically tuned according to the slope of the PV power-voltage curve. A detailed PV system and converter model was developed in MATLAB/Simulink, and simulations were performed under varying irradiance conditions. Performance metrics include tracking efficiency, convergence time, steady-state oscillation amplitude, and computational complexity. Results. The proposed AM-P&O achieves a better tracking, reduces convergence time by approximately 35 %, and decreases steady-state oscillations by nearly 90 % compared to conventional P&O. Under fast irradiance variations, the AM-P&O also demonstrates superior dynamic performance with lower computational burden compared to IC. Scientific novelty of this work lies in the adaptive perturbation mechanism, which balances fast convergence and reduced oscillations without increasing algorithmic complexity. Practical value. The AM-P&O provides a practical MPPT solution for PV systems, ensuring higher energy yield and improved stability in real-world applications, thereby supporting more efficient renewable energy integration into power networks. References 32, tables 8, figures 8.

Key words: photovoltaic system, maximum power point tracking, adaptive step size, modified perturb and observe algorithm, interleaved DC- DC converter, tracking efficiency.

Вступ. В останні роки відстеження точки максимальної потужності (МРРТ) стало критично важливим компонентом у фотоелектричних (PV) системах для забезпечення максимального збору енергії в умовах змінних освітленості і температури. Серед найбільш поширених алгоритмів, що широко застосовуються завдяки своїй простоті та ефективності, є алгоритми збурення і спостереження (Р&О) і збільшення провідності (ІС). **Проблема**. Звичайний Р&О схильний до коливань і повільного динамічного відгуку, в той час як ІС вимагає більш високої обчислювальної складності і втрачає точність при швидко мінливих умовах. Ці недоліки обмежують загальну ефективність відстеження та надійність системи. Метою даної роботи є розробка та оцінка нового адаптивного модифікованого алгоритму збурення і спостереження (AM-P&O) для PV системи з підвицуючим перетворювачем з чергуванням. Запропонований метод динамічно регулює розмір кроку збурення для досягнення більш швидкої збіжності і зменшення усталених коливань для підвищення ефективності відстеження. Його продуктивність оцінюється шляхом моделювання зі змінною освітленістю. Також він порівнюється з традиційними методами (P&O та IC) з використанням кількісних метрик, таких як час збіжності, амплітуда коливань, ефективність відстеження та обчислювальні витрати. Методологія. Алгоритм АМ-Р&О пропонує стратегію адаптивного регулювання розміру кроку, в якій амплітуда збурення динамічно налаштовується відповідно до нахилу кривої потужності-напруги PV системи. Детальна модель PV системи та перетворювача розроблена в MATLAB/Simulink, а моделювання виконано в умовах змінної освітленості. Метрики продуктивності включають ефективність відстеження, час збіжності, амплітуду коливань і обчислювальну складність. Результати. Запропонований АМ-Р&О досягає кращого відстеження, скорочує час збіжності приблизно на 35 % і зменицує усталені коливання майже на 90 % у порівнянні з традиційним Р&О. При швидких змінах освітленості АМ-Р&О також демонструє високі динамічні характеристики з менишм обчислювальним навантаженням у порівнянні з ІС. Наукова новизна роботи полягає у механізмі адаптивного збурення, який забезпечує баланс між швидкою збіжністю та зниженням коливань без збільшення складності алгоритму. **Практична значимість**. AM-P&O пропонує практичне рішення MPPT для PV систем, забезпечуючи більше вироблення енергії та покращену стабільність у реальних умовах експлуатації, сприяючи ефективнішій інтеграції відновлюваних джерел енергії в енергомережу. Бібл. 32, табл. 8, рис. 8.

Ключові слова: фотоелектрична система, відстеження точки максимальної потужності, адаптивний розмір кроку, модифікований алгоритм збурення та спостереження, DC-DC перетворювач з чергуванням, ефективність відстеження.

Introduction. Photovoltaic (PV) technology has seen rapid deployment worldwide as a cost effective, modular source of low carbon electricity. However, their output is nonlinear and strongly sensitive to environmental factors (irradiance, temperature, etc.) and operating conditions (partial shading, etc.) so the maximum power point tracking (MPPT) is vital but requires a robust, fast and low cost MPPT solution to improve MPPT energy yield [1–4].

Classical MPPT techniques such as perturb & observe (P&O) and incremental conductance (IC) remain widely used because of their simplicity and low implementation cost. Nonetheless they exhibit limitations, for example P&O tends to oscillate around the maximum power point (MPP) in steady state and can be misled by varying

environmental conditions, while IC depends strongly on step size selection. These limitations introduced new concepts as variable/adaptive step-size schemes, hybrid methods, and occasional global search strategies to handle PV curves under partial shading [5–10].

Partial shading and module mismatch can cause the PV characteristics to have multiple local maxima which mislead the conventional MPPT techniques. To address this and the conventional techniques limitations, researchers proposed two broad directions. The first was to make them more adaptive (variable step-size, prediction/estimation, constrained search windows) so they remain lightweight yet dynamic, while the second was to incorporate occasional or hybrid global optimizers (particle swarm optimization

© M. Makhlouf, O. Laouar

(PSO), grey wolf optimization (GWO), teaching learning based optimization etc.) that combine fast local search with less-frequent global exploration. Hybrid and metaheuristic approaches improve the global MPP (GMPP) at the cost of higher computational resources and complexity [3, 7].

Despite these efforts, a clear gap remains between simple low-cost controllers and advanced computationally intensive solutions. Many adaptive MPPT techniques either increase algorithmic complexity (difficult for low-cost microcontrollers) or still suffer from oscillations and delayed convergence under rapid irradiance fluctuations [6, 8, 11].

Discussion in light of recent literature (2020–2025). MPPT algorithms are evaluated primarily by their tracking efficiency and convergence time [12, 13]. Contemporary literature (2020–2025) shows that advanced AI-based methods typically achieve tracking efficiencies ~99 %, with very fast convergence, outperforming conventional methods [12, 13]. However, classical methods (like P&O and IC) remain popular for their simplicity and low implementation cost [12, 14]. In practice, the choice of MPPT involves trade-offs among efficiency, speed, complexity, and robustness to changing conditions (irradiance, shading, temperature) [12, 14].

P&O and IC are widely used «baseline» MPPT methods due to their simplicity and minimal sensor requirements [13, 14]. P&O works by perturbing the PV operating point and observing power changes. It is easy to implement but inherently oscillates around the MPP [13]. IC compares incremental and instantaneous conductance to decide the direction of tracking; it achieves smoother convergence and lower steady-state ripple than P&O which makes it a better choice [13, 15].

Empirical studies highlight these differences. For example, under varying irradiance (250–1000 W/m²), authors [15] found that IC reached ~98.7 % tracking efficiency with a 0.15 s convergence, versus ~95.2 % for P&O. IC also yielded much smaller power ripple (~1.2 kW vs. 3.8 kW) [15]. In general, P&O tends to overshoot and oscillate around the MPP, resulting in longer settling times, while IC responds more smoothly [13, 15]. Under uniform insolation both work reasonably, but under partial shading their limitations become severe: they often lock onto a local maximum rather than the GMPP, causing large energy losses (up to ~70 %) [10, 13].

To mitigate oscillations and improve speed, many adaptive or variable-step versions of P&O and IC have been proposed. These algorithms dynamically adjust the perturbation step based on PV conditions. For example, authors [5] introduced a variable-step P&O that uses multiple step sizes; simulations showed it reduced power ripple by $\sim\!80$ % and cut response time by $\sim\!30$ % compared to fixed-step P&O. Similarly, authors [3, 16] developed a 4-segment variable-step IC by dividing the $I\!-\!V$ curve into regions with optimized steps, it eliminated steady-state oscillation and greatly accelerated tracking under rapidly changing irradiance.

These adaptive schemes retain the basic simplicity of classical methods but add computational overhead for step-size logic. In practice, they offer faster convergence and lower ripple than their fixed-step counterparts while maintaining comparable steady-state efficiency. For instance, the improved IC was shown to achieve no oscillation and improved energy extraction under dynamic irradiance [3, 17].

AI-based (artificial neural network (ANN), fuzzy logic) and metaheuristic (PSO, GWO, whale optimization algorithm (WOA)) approaches use global-search or learning to overcome classical limits. These methods typically achieve very high tracking efficiency (often ≥97 %) and can handle multiple maxima, but they incur higher complexity and require more computation or training. Recent reviews report that AI and metaheuristic MPPTs routinely reach ~99 % of theoretical power [12, 18].

For example, a neural-network MPPT was shown to reach ~99.7 % efficiency on clear days (99.3 % on overcast), with much lower steady-state error and faster transient response than P&O or IC [18]. Fuzzy-logic controllers also perform strongly; a recent hybrid fuzzy-IC MPPT achieved ~97.7 % average efficiency and a convergence time of only 53.5 ms, outperforming conventional and other hybrid techniques [19]. Metaheuristics further push these metrics: WOA/GWO achieved ~98.9 % efficiency in simulation and measurement [20], and a chimp optimization algorithm reached ~99.63 % efficiency under shading [14].

However, these gains come at cost. AI and metaheuristic methods are computationally intensive: ANNs require off-line training and embedded hardware, fuzzy controllers need rule-tuning, and swarm algorithms iterate many function evaluations. Authors [12] note that classical methods have low computational cost while AI methods «demand more complex hardware/software». In terms of dynamic performance, metaheuristics may converge slower (~0.65 s for WOA in one study [21], versus <<0.1 s for some fast techniques) but they excel at finding the global optimum under variable conditions.

Hybrid methods combine the strengths of global optimization and local tracking. A common pattern is using a metaheuristic or AI for coarse tracking and a fast local method for fine adjustment. These techniques aim to achieve near-optimal efficiency with accelerated convergence. For instance, authors [19] proposed a P&O+PSO hybrid: it attained ~2 % higher efficiency than pure P&O (and a 0.2 ms faster convergence) under shading conditions. In [18] authors achieved by fuzzy-IC hybrid 97.7 % efficiency with only 53 ms settling time. Similarly, a modified hybrid predictive control and adaptive P&O (MPC+P&O) controller improved P&O's response by ~35 % and reduced overshoot by 28 % [13].

GWO/PSO hybrids exemplify this trade-off: authors' GWO-PSO method used GWO for exploration and PSO for exploitation. It required only two tuning parameters and converged quickly to the GMPP independently of initial conditions [15], outperforming standalone PSO or GWO. In general, global-local hybrids can achieve tracking efficiencies >98 % with fast convergence times, at the expense of doubled algorithmic complexity (and tuning of both components).

The recent literature (2020–2025) shows a clear hierarchy classical MPPTs are simple and low-cost but oscillatory and vulnerable to shading; adaptive classical methods improve dynamic behavior with modest complexity; intelligent/metaheuristic algorithms achieve very high efficiency and robust shading performance but are computationally demanding; and hybrid strategies combine global search with fast local refinement to optimize both convergence and accuracy. The choice

depends on application priorities: if simplicity and low cost dominate, classical or adaptive methods suffice; if maximal energy yield under complex conditions is needed, modern AI or hybrid schemes are preferable [12, 15].

Problem statement. Although many MPPT approaches have been proposed, practical PV systems impose the following challenges that are not fully solved by conventional P&O or IC:

- Rapid irradiance changes shift the MPP quickly fixedstep algorithms either fail to converge fast enough or produce large steady-state oscillations [5, 11].
- Under partial shading multiple local maxima appear simple hill-climbing techniques can be trapped in local MPPs. Global or hybrid searches can find the GMPP but add complexity and runtime overhead [3, 7].
- There is no universal optimally methods. Methods that maximize speed often increase oscillation or computational effort [2, 9].

The **goal** of the work is the development and evaluation of a novel adaptive modified perturb and observe (AM-P&O) algorithm for a PV system with an interleaved boost converter (IBC).

The proposed method dynamically adjusts the perturbation step size to achieve faster convergence and lessen steady-state oscillations to enhance tracking efficiency. Its performance is assessed through simulation with varying irradiance. It is then compared to traditional methods (P&O and IC) using quantitative metrics such as convergence time, oscillation magnitude, tracking efficiency, and computational cost.

Materials and methods. The AM-P&O algorithm was implemented in MATLAB/Simulink. A standard PV module model was used under dynamic irradiance conditions to evaluate the algorithm's response to rapid changes in solar input. The performance of AM-P&O was compared to conventional P&O and IC using tracking efficiency, convergence time, and steady-state oscillation as quantitative metrics. Simulations were conducted using continuous, variable sampling.

PV system modeling. PV cell can be represented by an equivalent electrical circuit that models its non-linear *I-V* characteristics under different irradiance *G* and temperature *T* conditions. The most widely used representation is the single-diode model [21] (Fig. 1). It is adopted for its balance between accuracy and simplicity. While the double-diode model offers improved accuracy, it requires additional parameters that are rarely found in datasheet (diffusion and recombination diode reverse saturation current, diffusion and recombination diode ideality factor) and increases computational complexity.

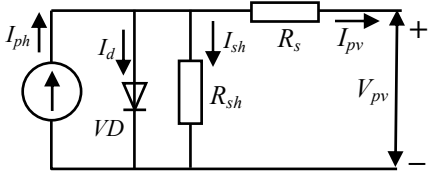


Fig. 1. PV cell single-diode equivalent model

The output current *I* of a single-diode model is:

$$I = I_{ph} - I_0 \left(\exp \left(\frac{q(V + IR_s)}{nkT} \right) - 1 \right),$$
 (1)

where I_{ph} is the photocurrent; I_0 is the diode reverse saturation current; R_s , R_{sh} are the series and shunt

resistances; n is the diode ideality factor; q is the electron charge; k is the Boltzmann constant; T is the temperature.

The photocurrent I_{ph} depends linearly on solar irradiance G and is affected by temperature T:

$$I_{ph} = \left[I_{sc,ref} + \alpha (T - T_{ref})\right] \frac{G}{G_{ref}}, \qquad (2)$$

where G is the incident irradiance; G_{ref} is the reference irradiance (often 1000 W/m²), α is the temperature coefficient of the current; T_{ref} is the reference temperature; $I_{sc,ref}$ is the short-circuit current under reference conditions.

The diode reverse saturation current I_0 varies exponentially with temperature as:

$$I_0 = I_{0,ref} \left(\frac{T}{T_{ref}}\right)^3 \exp\left[\frac{qE_g}{nk} \left(\frac{1}{T_{ref}} - \frac{1}{T}\right)\right], \quad (3)$$

where $I_{0,ref}$ is the reference current; E_g is the semiconductor band-gap energy.

Power converter modeling. The converter used is an IBC due to its ability to handle high input currents, reduce current ripple, and improve overall efficiency. It consists of multiple boost converters in parallel interleaved in operation with a phase shift (180° for two-phase IBC) (Fig. 2). The interleaving reduces input current ripple thus minimizes stress on the PV module and lower electromagnetic interference.

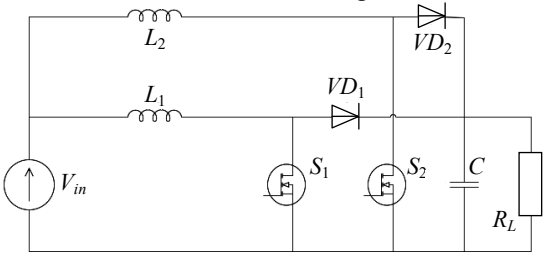


Fig. 2. Two-phase IBC circuit

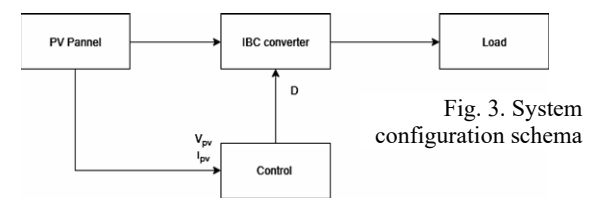
The two-phase IBC [22] used in this work comprises: two inductors L_1 , L_2 one per phase; two controlled switches S_1 , S_2 (typically MOSFETs or IGBTs); two diodes VD₁, VD₂; an output capacitor C; a load resistance R_L . We can arrive to the following result after using state space representation and using the state space averaging technique:

$$\frac{dX}{dt} = \begin{bmatrix} 0 & 0 & \frac{D-1}{L_1} \\ 0 & 0 & \frac{D-1}{L_2} \\ \frac{1-D}{C} & \frac{1-D}{C} & -\frac{1}{RC} \end{bmatrix} X + \begin{bmatrix} \frac{1}{L_1} \\ \frac{1}{L_2} \\ 0 \end{bmatrix} V_{in}; \quad (4)$$

$$X = \begin{bmatrix} i_{L1} \\ i_{L2} \\ V_0 \end{bmatrix}$$
 (5) $Y = C_{out} \cdot V_{in};$ (6) $C_{out} = [0 \ 0 \ 1],$ (7)

where X is the state vector; Y is the output vector; C_{out} is the output matrix; i_{L1} , i_{L2} are the inductor currents; V_0 is the output voltage; V_{in} is the input voltage; R is the load resistance; L_1 , L_2 are the inductance of both phases of the IBC; D is the duty cycle; C is the output capacitance.

The system consists of a PV panel connected to a two-phase IBC (Fig. 3). The PV voltage and current are measured and sent to the control block, which runs the MPPT algorithm. Based on these values, the control generates a duty ratio that drives the IBC to regulate the output and deliver maximum power to the load.



MPPT algorithms. For decades, researchers have focused on extracting the most power from PV systems, resulting in a wide range of MPPT techniques. These range from traditional methods (for example, P&O, IC and hill climbing) to more modern approaches like as fuzzy logic, neural networks, PSO and genetic algorithms. P&O is the most widely used MPPT technique due to its simplicity and low cost to implement. It perturbs the operating point of the PV and observes the power if power increases, perturbation continues in the same direction; if it decreases, the direction reverses.

It does however display oscillations around the MPP in steady state and can fail under rapidly changing irradiance. Furthermore, the fixed step size creates a trade-off, big step size allow for faster tracking but increased power loss due to oscillations while tiny step size reduce oscillations but hinder convergences.

Principle of operation of P&O. P&O is based on an iterative process that continuously adjusts the duty cycle of the DC-DC converter to extract the maximum amount of power possible from a PV [23].

The algorithm measures the new power and compares it to the last value. If power increases it continues perturbing in the same direction. If it decreases it perturbs in the opposite direction (see Table 1).

Power voltage cases for P&O algorithm

	Tower voltage cases for reco argorithm				
ſ	ΔP	ΔV	Action		
ĺ	> 0	> 0	Increase voltage		
ſ	> 0	< 0	Decrease voltage		
ſ	< 0	> 0	Decrease voltage		
ĺ	< 0	< 0	Increase voltage		

Principle of operation of IC. Its an algorithm that improves upon the conventional P&O by directly analyzing the slope of the power voltage curve of a PV panel. The core idea is that the derivative dP/dV is 0 at MPP, positive to the left and negative to the right. Unlike P&O which only observes the power, IC attempts to mathematically determine whether the current operating point is to the left or right of the MPP using both instantaneous and IC [24] (Table 2). Let:

$$P = I \cdot V$$
; (8); $dP/dV = I + V \cdot (dI/dV)$; (9)

For:

dP/dV = 0; (10) dI/dV = -I/V, (11) where I is the PV current; V is the PV voltage; P is the PV power.

Table 2

Table 1

IC principle

FF			
Action			
Stay at MPP			
Increase voltage			
Decrease voltage			
If ΔI =0: stay at MPP; if $\Delta I \neq 0$: perturb			

Proposed modified P&O algorithm. To overcome the trade-off due to the step size seen in traditional P&O and IC, an adaptive step-size strategy is introduced, in which it dynamically adjusts based on the P-V curve and rate of change of power. Algorithm description is next (Table 3). Let:

$$\Delta_1 = P(k) - P(k-1);$$
 (12) $\Delta_2 = V(k) - V(k-1).$ (13)

Adaptive step size:

$$\alpha(k) = \alpha_{\text{max}} \left[1 - \exp(-\mu \left| \frac{\Delta_{l}}{\Delta_{2}} \right|) \right], \tag{14}$$

where P is the PV power; V is the PV voltage; α_{max} is the maximum perturbation step, μ is the sensitivity coefficient (in this article we took μ =0.01); Δ_1 , Δ_2 are the difference of power and voltage.

Table 3 Power voltage cases for novel modified P&O algorithm

٠.	, situage subset for the ver into unition 1 each in				
	ΔP	ΔV	Duty cycle D		
	> 0	> 0	Increase by $\alpha(k)$		
	> 0	< 0	Decrease by $\alpha(k)$		
	< 0	> 0	Decrease by $\alpha(k)$		
	< 0	< 0	Increase by $\alpha(k)$		

Simulation setup. PV module parameters. The PV system model is developed using a commercially available PV module, with all key parameters carefully extracted directly from the manufacturer's datasheet. These parameters include characteristics such as rated power, open-circuit voltage, short-circuit current, temperature coefficients, and other essential electrical specifications. Table 4 summarizes the simulation model parameters used in this study of the different control methods for the PV panel.

Table 4

PV module parameters

Parameter	Value
Module	Zytech Solar ZT280P
Maximum power P_{max} , W	280.33
Cells per module	72
Open circuit voltage V_{oc} , V	45.25
Short-circuit current I_{sc} , A	8.4
Voltage at MPP V_{mpp} , V	35.62
Current at MPP I_{mpp} , A	7.87
Temperature coefficient of V_{oc} , %/°C	-0.3199
Temperature coefficient of I_{sc} , %/°C	0.0483
Model parameter	rs
Light-generated current I_L , A	8.475
Diode saturation current I_0 , A	$6.39 \cdot 10^{-11}$
Diode ideality factor	0.9562
Shunt resistance R_{sh} , Ω	194.59
Series resistance R_s , Ω	0.564

Converter parameters. The IBC used in the simulation is designed according to the power rating of the PV module and the desired DC bus voltage (Table 5).

Table 5

IBC converter parameters

Parameter	Value
Inductor per phase L, mH	4
Output capacitor C, µF	1000
Switching frequency f_s , kHz	10
Number of phases	2
Duty ratio range D	[0.1 - 0.9]

Load parameters. The load considered in this study consists of a 900 W electrical device connected in parallel with a rechargeable energy storage system (Table 6). The energy storage system is a Li-Ion battery, which is chosen for its high energy density, long cycle life, and efficient charge/discharge characteristics. This configuration allows the system to supply the load continuously while accommodating fluctuations in generation and consumption. The parallel configuration also allows for the analysis of transient responses and the impact of load variations on both the PV system and the battery performance.

Load parameters

Component	Parameter	Value
	Type	Li-Ion
	Nominal voltage, V	96
Battery	Rated capacity, Ah	50
	Initial state of charge, %	20
	Battery response time, s	30
Load	Rated power, W	900
Load	Connection	In parallel with the battery

Test scenarios. To evaluate the performance of the system, several test scenarios are considered, focusing on variations in environmental and operating conditions. The primary scenario involves changes in solar irradiance levels, simulating real-world fluctuations in sunlight intensity.

evaluation metrics. Performance System by efficiency, performance is evaluated tracking convergence steady-state oscillations, time, and computational cost, which together measure power extraction, speed, stability, and algorithm efficiency.

Results and discussion. In this simulation, the initial duty cycle variation (ΔD) was fixed at 0.01 across all methods, ensuring a consistent and fair basis for comparison. Figure 4 shows the irradiance profile applied during the simulation. The irradiance begins at 1000 W/m², at 0.6 s drops to 700 W/m², and then rises to 800 W/m² from 1.2 s to 1.8 s.

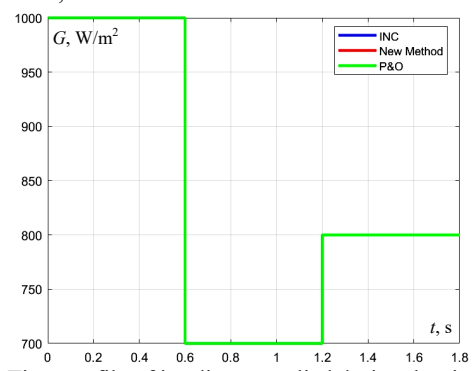


Fig. 4. Time profile of irradiance applied during the simulation

These irradiance variations are applied to assess the dynamic performance of the PV system, focusing on its voltage, current, and power response under rapidly changing solar conditions. Such an analysis offers valuable insight into the system's stability and efficiency when operating under realistic, time-varying irradiance profiles. Figure 5 illustrates the duty cycle performance comparison of 3 MPPT algorithms: IC, P&O, and the proposed method over a period of 1.8 s. The most notable characteristic is the dramatically different behavior patterns between the methods.

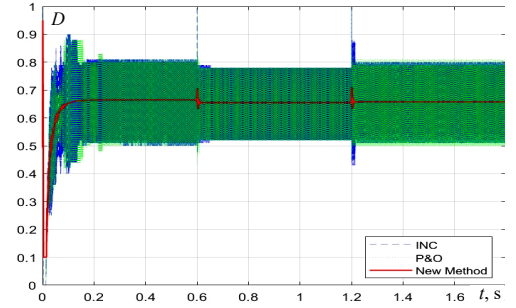


Fig. 5. Duty cycle variation obtained using IC, P&O and the proposed AM-P&O method

IC and P&O algorithms exhibit pronounced oscillations, with duty cycles fluctuating between 0.5 and 0.8 due to the fixed perturbation step (ΔD). In contrast, the proposed method demonstrates much greater stability, with only brief disturbances around 0.6 s and 1.2 s, after which it quickly returns to the steady operating point. This stable behavior highlights the effectiveness of the adaptive mechanism in minimizing oscillations, enabling more accurate MPPT, improved energy harvesting efficiency, and reduced power loss compared to traditional methods.

Figure 6 shows the PV power output of the 3 MPPT algorithms over a simulation period of 1.8 s. The results illustrate how effectively each method tracks the MPP under changing irradiance conditions. The output stabilizes around 1400 W initially, then drops to approximately 1000 W, and finally settles near 1132 W.

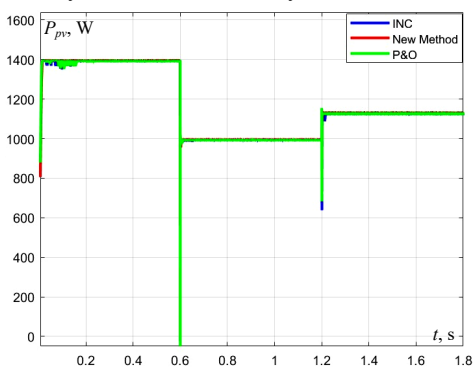


Fig. 6. Instantaneous PV power response under different MPPT algorithms IC, P&O and the proposed method

While all algorithms are able to follow the MPP transitions, the proposed method exhibits faster stabilization and smoother tracking compared to IC and P&O. Figure 7 presents the PV power output of the 3 MPPT algorithms over a 0.04-second window to provide a clearer view of their dynamic behavior.

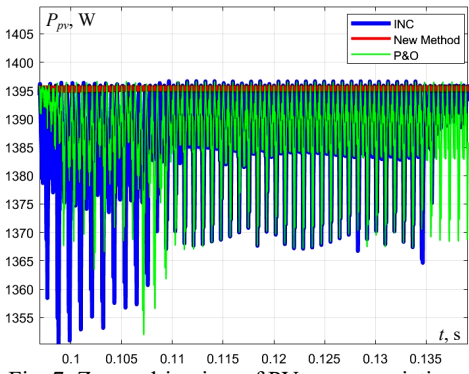


Fig. 7. Zoomed-in view of PV power variations under IC, P&O, and the proposed method

While all methods eventually reach the MPP, their responses differ noticeably in terms of oscillations. The proposed method delivers the most stable performance, keeping the output within just 1–2 W of the optimum. By comparison, the P&O algorithm shows moderate oscillations of about 15–20 W above and below the MPP due to its continuous P&O operation.

The IC algorithm exhibits the most significant oscillations, with power swings of 20–25 W around the MPP, particularly pronounced during the initial portion of the measurement period before somewhat stabilizing.

Overall, these results underline the superior stability and efficiency of the proposed method compared with conventional approaches.

Figure 8 compares the mean output power of the three MPPT algorithms. The proposed method delivers the highest performance at 955 W, followed by P&O at 949.5 W and IC at 946.5 W. Although the numerical differences may seem modest about 0.6 % higher than P&O and 0.9 % higher than IC this improvement translates into more efficient energy harvesting over extended operation. These results confirm the proposed method's superior capability to track the MPP while minimizing power losses.

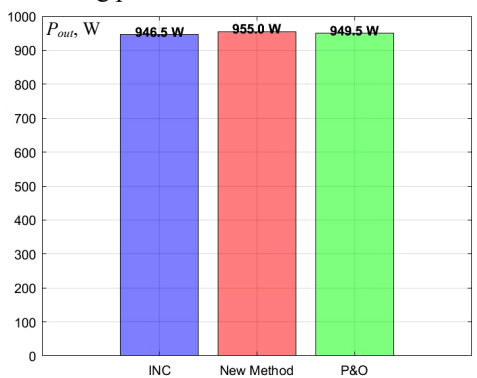


Fig. 8. Mean output power comparison of IC, P&O, and the proposed method

Analysis of trade-offs between speed, accuracy, and complexity. The comparison of the 3 MPPT methods (Tables 7, 8) highlights key trade-offs. P&O and IC respond quickly but exhibit higher oscillations (± 15 –25 W), leading to slightly lower mean power (949.5 W and 946.5 W) and reduced tracking accuracy. The proposed method achieves high accuracy and minimal oscillations (± 1 –2 W) with a higher mean power of 955 W, but at the cost of increased computational complexity. These results demonstrate that improved stability and energy harvesting efficiency can be obtained with more complex algorithms, while simpler methods offer faster but less precise tracking.

Table 7 Comparative table of the methods

MPPT		Computational
method	Duty cycle behavior	cost
P&O	High oscillations, fluctuates between 0.5 and 0.8	low
IC	High oscillations, fluctuates between 0.5 and 0.8	low
Proposed method	Stable, minor disturbances at ~0.6 s and 1.2 s	high

Table 8
Power comparative table of the methods

· ·				
MPPT method	Power oscillations	Mean output		
MIFFI Illeulou	around MPP	power, W		
P&O	moderate, ±15–20 W	949.5		
IC	significant, ±20–25 W	946.5		
Proposed method	minimal, ±1–2 W	955.0		

Conclusions. The proposed method achieved the highest mean output power at 955 W, outperforming both P&O (949.5 W) and IC (946.5 W) algorithms. More importantly, it demonstrated exceptional stability with minimal oscillations around the MPP, maintaining steady-state operation without the continuous perturbation's characteristic of conventional methods.

The duty cycle analysis revealed that traditional IC and P&O algorithms exhibit significant oscillatory behavior as they continuously search for the optimal operating point. In contrast, the proposed method quickly converges to a stable duty cycle and maintains it throughout the test period, indicating superior tracking precision and reduced power losses.

Under dynamic conditions with varying irradiance levels, the proposed method consistently followed the desired MPP while maintaining stable power output. The reduced oscillations and improved tracking stability translate to enhanced energy harvesting efficiency, making it particularly valuable for practical PV applications where consistent power generation is crucial.

Future work can focus on implementing the AM P&O algorithm on embedded hardware to validate its real-time performance and computational efficiency. Its structure also allows for integration with hybrid or predictive schemes to further enhance convergence under extreme irradiance fluctuations or partial shading conditions. Moreover, combining the proposed method with real-time irradiance estimation or forecasting techniques could further optimize energy extraction in grid-connected PV system.

Conflict of interest. The authors declare that they have no conflicts of interest.

REFERENCES

- *I.* Katche M.L., Makokha A.B., Zachary S.O., Adaramola M.S. A Comprehensive Review of Maximum Power Point Tracking (MPPT) Techniques Used in Solar PV Systems. *Energies*, 2023, vol. 16, no. 5, art. no. 2206. doi: https://doi.org/10.3390/en16052206.
- 2. Endiz M.S., Gökkuş G., Coşgun A.E., Demir H. A Review of Traditional and Advanced MPPT Approaches for PV Systems Under Uniformly Insolation and Partially Shaded Conditions. *Applied Sciences*, 2025, vol. 15, no. 3, art. no. 1031. doi: https://doi.org/10.3390/app15031031.
- **3.** Ali M.H., Zakaria M., El-Tawab S. A comprehensive study of recent maximum power point tracking techniques for photovoltaic systems. *Scientific Reports*, 2025, vol. 15, no. 1, art. no. 14269. doi: https://doi.org/10.1038/s41598-025-96247-5.
- 4. Alombah N.H., Harrison A., Mbasso W.F., Belghiti H., Fotsin H.B., Jangir P., Al-Gahtani S.F., Elbarbary Z.M.S. Multiple-to-single maximum power point tracking for empowering conventional MPPT algorithms under partial shading conditions. *Scientific Reports*, 2025, vol. 15, no. 1, art. no. 14540. doi: https://doi.org/10.1038/s41598-025-98619-3.
- 5. Sun C., Ling J., Wang J. Research on a novel and improved incremental conductance method. *Scientific Reports*, 2022, vol. 12, no. 1, art. no. 15700. doi: https://doi.org/10.1038/s41598-022-20133-7.
- **6.** Ye S.-P., Liu Y.-H., Liu C.-Y., Ho K.-C., Luo Y.-F. Artificial Neural Network Assisted Variable Step Size Incremental Conductance MPPT Method with Adaptive Scaling Factor. *Electronics*, 2021, vol. 11, no. 1, art. no. 43. doi: https://doi.org/10.3390/electronics11010043.
- 7. Singh Chawda G., Prakash Mahela O., Gupta N., Khosravy M., Senjyu T. Incremental Conductance Based Particle Swarm Optimization Algorithm for Global Maximum Power Tracking of Solar-PV under Nonuniform Operating Conditions. *Applied Sciences*, 2020, vol. 10, no. 13, art. no. 4575. doi: https://doi.org/10.3390/app10134575.
- **8.** Mahmod Mohammad A.N., Mohd Radzi M.A., Azis N., Shafie S., Atiqi Mohd Zainuri M.A. An Enhanced Adaptive Perturb and Observe Technique for Efficient Maximum Power Point Tracking Under Partial Shading Conditions. *Applied Sciences*, 2020, vol. 10, no. 11, art. no. 3912. doi: https://doi.org/10.3390/app10113912.
- 9. Amal Z. Advanced Perturb and Observe Algorithm for Maximum Power Point Tracking in Photovoltaic Systems with Adaptive Step Size. *Journal of Automation, Mobile Robotics and Intelligent Systems*, 2024, pp. 55-60. doi: https://doi.org/10.14313/JAMRIS/3-2024/22.
- 10. Djilali A.B., Bounadja E., Yahdou A., Benbouhenni H., Elbarbary Z.M.S., Colak I., Al-Gahtani S.F. Enhanced variable step sizes perturb and observe MPPT control to reduce energy loss in photovoltaic systems.

- *Scientific Reports*, 2025, vol. 15, no. 1, art. no. 11700. doi: https://doi.org/10.1038/s41598-025-95309-y.
- 11. Subudhi B., Pradhan R. A Comparative Study on Maximum Power Point Tracking Techniques for Photovoltaic Power Systems. *IEEE Transactions on Sustainable Energy*, 2013, vol. 4, no. 1, pp. 89-98. doi: https://doi.org/10.1109/TSTE.2012.2202294.
- 12. Boubaker O. MPPT techniques for photovoltaic systems: a systematic review in current trends and recent advances in artificial intelligence. *Discover Energy*, 2023, vol. 3, no. 1, art. no. 9. doi: https://doi.org/10.1007/s43937-023-00024-2.
- 13. Naima B., Belkacem B., Ahmed T., Benbouhenni H., Riyadh B., Samira H., Sarra Z., Elbarbary Z.M.S., Mohammed S.A. Enhancing MPPT optimization with hybrid predictive control and adaptive P&O for better efficiency and power quality in PV systems. Scientific Reports, 2025, vol. 15, no. 1, art. no. 24559. doi: https://doi.org/10.1038/s41598-025-10335-0.
- 14. Nagadurga T., Raju V.D., Barnawi A.B., Bhutto J.K., Razak A., Wodajo A.W. Global MPPT optimization for partially shaded photovoltaic systems. *Scientific Reports*, 2025, vol. 15, no. 1, art. no. 10831. doi: https://doi.org/10.1038/s41598-025-89694-7.
- 15. Chtita S., Motahhir S., El Hammoumi A., Chouder A., Benyoucef A.S., El Ghzizal A., Derouich A., Abouhawwash M., Askar S.S. A novel hybrid GWO–PSO-based maximum power point tracking for photovoltaic systems operating under partial shading conditions. Scientific Reports, 2022, vol. 12, no. 1, art. no. 10637. doi: https://doi.org/10.1038/s41598-022-14733-6.
- 16. Melhaoui M., Rhiat M., Oukili M., Atmane I., Hirech K., Bossoufi B., Almalki M.M., Alghamdi T.A.H., Alenezi M. Hybrid fuzzy logic approach for enhanced MPPT control in PV systems. *Scientific Reports*, 2025, vol. 15, no. 1, art. no. 19235. doi: https://doi.org/10.1038/s41598-025-03154-w.
- 17. Hussain M.T., Sarwar A., Tariq M., Urooj S., BaQais A., Hossain M.A. An Evaluation of ANN Algorithm Performance for MPPT Energy Harvesting in Solar PV Systems. Sustainability, 2023, vol. 15, no. 14, art. no. 11144. doi: https://doi.org/10.3390/su151411144.
- 18. Zemmit A., Loukriz A., Belhouchet K., Alharthi Y.Z., Alshareef M., Paramasivam P., Ghoneim S.S.M. GWO and WOA variable step MPPT algorithms-based PV system output power optimization. *Scientific Reports*, 2025, vol. 15, no. 1, art. no. 7810. doi: https://doi.org/10.1038/s41598-025-89898-x.

- 19. Timur O., Uzundağ B.K. Design and Analysis of a Hybrid MPPT Method for PV Systems Under Partial Shading Conditions. *Applied Sciences*, 2025, vol. 15, no. 13, art. no. 7386. doi: https://doi.org/10.3390/app15137386.
- 20. Elsafi A., Almohammedi A.A., Balfaqih M., Balfaqih Z., Sabri S. Comparative analysis of maximum power point tracking methods for power optimization in grid tied photovoltaic solar systems. *Discover Applied Sciences*, 2025, vol. 7, no. 9, art. no. 976. doi: https://doi.org/10.1007/s42452-025-07606-w.
- 21. Latreche K., Taleb R., Bentaallah A., Toubal Maamar A.E., Helaimi M., Chabni F. Design and experimental implementation of voltage control scheme using the coefficient diagram method based PID controller for two-level boost converter with photovoltaic system. Electrical Engineering & Electromechanics, 2024, no. 1, pp. 3-9. doi: https://doi.org/10.20998/2074-272X.2024.1.01.
- **22.** Hosseinpour M., Seifi E., Seifi A., Shahparasti M. Design and analysis of an interleaved step-up DC–DC converter with enhanced characteristics. *Scientific Reports*, 2024, vol. 14, no. 1, art. no. 14413. doi: https://doi.org/10.1038/s41598-024-65171-5.
- 23. Saberi A., Niroomand M., Dehkordi B.M. An Improved P&O Based MPPT for PV Systems with Reduced Steady-State Oscillation. *International Journal of Energy Research*, 2023, vol. 2023, art. no. 4694583. doi: https://doi.org/10.1155/2023/4694583.
- 24. Louarem S., Kebbab F.Z., Salhi H., Nouri H. A comparative study of maximum power point tracking techniques for a photovoltaic grid-connected system. *Electrical Engineering & Electromechanics*, 2022, no. 4, pp. 27-33. doi: https://doi.org/10.20998/2074-272X.2022.4.04.

Received 11.05.2025 Accepted 09.07.2025 Published 02.11.2025

M. Makhlouf¹, Doctor of Science, Lecturer,

O. Laouar², Master of Science, Student,

¹ Ecole National Polytechnique de Constantine, Algeria, e-mail: makhlouf.me@gmail.com (Corresponding Author).

²CentraleSupelec, Gif-sur-Yvette, Ile-de-France, France.

How to cite this article:

Makhlouf M., Laouar O. New adaptive modified perturb and observe algorithm for maximum power point tracking in photovoltaic systems with interleaved boost converter. *Electrical Engineering & Electromechanics*, 2025, no. 6, pp. 57-63. doi: https://doi.org/10.20998/2074-272X.2025.6.08

V.T.K. Nhi, B.T. Quy, H.H.B. Nghia, L.V. Dai

A robust hybrid control strategy for enhancing torque stability and performance in PMSM drives

Introduction. Recently, permanent magnet synchronous motors (PMSMs) have become essential in various high-performance applications, including electric vehicles and renewable energy systems. However, traditional control methods, such as PI controllers, often struggle to handle dynamic operating conditions and external disturbances, resulting in torque ripple and stability issues. Problem. The main issue with existing control strategies is their inability to maintain accurate torque control and system stability under fluctuating loads and varying motor parameters, which negatively impacts performance in real-world applications. Goal. This paper proposes a robust hybrid control strategy that integrates sliding mode control (SMC) with proportional resonant control (PRC), enhanced by Luenberger and Kalman observers. The goal is to improve torque stability, reduce errors, and optimize performance in PMSM drive systems. Methodology. The proposed method combines SMC and PRC to form an SMC-PRC controller, with Luenberger and Kalman observers integrated for effective load torque estimation. Results. The simulation experiments were carried out to compare the effectiveness of the proposed control strategy with that of traditional PI controllers. The results revealed that the SMC-PRC approach offers a notable improvement in overall control performance, including reduced tracking error, enhanced dynamic response, and better stability. Furthermore, the proposed method achieved faster settling times and maintained robust operation under varying system conditions. Scientific novelty. This work introduces a hybrid control approach that combines SMC and PRC with advanced state estimation techniques, providing a robust and efficient solution to PMSM control. Practical value. The proposed method is highly beneficial for applications under dynamic operating conditions, such as electric vehicles and renewable energy systems, improving system efficiency and stability. References 40, tables 7, figures 10.

Key words: permanent magnet synchronous motor, sliding mode control, proportional resonant control, integral absolute error, integral time absolute error, integral square error, Luenberger observer, Kalman filter.

Вступ. Останнім часом синхронні двигуни з постійними магнітами (РМЅМ) стали невід'ємною частиною різних високопродуктивних застосувань, включаючи електромобілі та системи відновлюваної енергії. Однак традиційні методи управління, такі як ПІ-регулятори, часто не справляються з динамічними робочими умовами та зовнішніми збуреннями, що призводить до пульсацій крутного моменту та проблем зі стабільністю. Основною **проблемою** існуючих методів управління є їх нездатність підтримувати точне управління крутним моментом і стійкість системи при коливаннях навантаження і параметрах двигуна, що змінюються, що негативно впливає на продуктивність в реальних ситуаціях. Мета. У цій статті пропонується надійна гібридна стратегія управління, що поєднує управління ковзним режимом (SMC) з пропорційнорезонансним управлінням (РКС), удосконалена за допомогою спостерігачів Люенбергера та Калмана. Мета полягає в тому, щоб підвищити стабільність крутного моменту, зменшити похибки і оптимізувати продуктивність систем приводу РМЅМ. Методологія. Пропонований метод об'єднує SMC та PRC для формування регулятора SMC-PRC, з інтегрованими спостерігачами Люенбергера та Калмана для оцінки ефективного крутного моменту навантаження. Результати. Проведено імітаційні експерименти порівняння ефективності запропонованої стратегії управління з ефективністю традиційних ПІ-регуляторів. Результати показали, що підхід SMC-PRC забезпечує помітне покращення загальних характеристик управління, включаючи зниження похибки стеження, покращення динамічного відгуку та підвищення стійкості. Крім того, пропонований метод забезпечує більш швидкий час встановлення і стійку роботу при умовах функціонування системи, що змінюються. **Наукова новизна**. У роботі представлений гібридний підхід до управління, що поєднує SMC та PRC з передовими методами оцінки стану, що забезпечує надійне та ефективне рішення для управління PMSM. **Практична значимість**. Запропонований метод ϵ корисним для застосування у динамічних умовах експлуатації, таких як електромобілі та системи відновлюваної енергії, підвишуючи їх ефективність та стійкість. Бібл. 40, табл. 7, рис. 10. Ключові слова: синхронний двигун з постійними магнітами, керування ковзним режимом, пропорційно-резонансне керування, інтегральна абсолютна похибка, інтегральна тимчасова абсолютна похибка, інтегральна квадратична похибка, спостерігач Люенбергера, фільтр Калмана.

Introduction. The permanent magnet synchronous motor (PMSM) is widely used in critical applications across various industries, including electric vehicles, industrial robotics, aerospace, and especially in the rapidly expanding renewable energy sector [1-3]. PMSMs offer key advantages such as high power density, exceptional efficiency, and a broad speed range, all of which contribute to their high reliability [4, 5]. PMSM control methods are generally categorized into 3 main approaches: field-oriented control (FOC), direct torque control (DTC) and V/F control [6, 7]. While DTC and V/F control are relatively simple to implement, they are prone to significant torque ripple and lower efficiency [8]. In contrast, FOC provides precise control of the magnetic field by adjusting the frequency, voltage, and inverter output position, which ensures stable torque, low noise, high power, and excellent dynamic performance [6, 9].

Linear control methods, such as PI control, PID control, and linear state feedback, have been commonly applied to control PMSMs. However, PMSMs exhibit numerous nonlinear characteristics, including system uncertainties and external disturbances, which increase

the complexity of controller design. These nonlinearities also make it more challenging to achieve the desired tracking performance in PMSM control systems [10]. To address these challenges, nonlinear control methods such as sliding mode control (SMC), fuzzy logic control, adaptive control, and model predictive control have gained popularity. For example, articles [11, 12] explore integrating a fuzzy event-trigger mechanism with supertwisting SMC to enhance sampling efficiency and tracking performance. Additionally, disturbance observer-based SMC has been introduced to counteract external disturbances in PMSM control [13].

As a result, sensorless control algorithms for PMSMs have become a key research area in motor control. These algorithms include high-frequency injection, extended Kalman filters (EKFs), model reference adaptive systems, and sliding mode observers (SMO) [14, 15]. Among these, SMO has become a preferred method due to its advantages in variable-structure control systems, simple implementation, and high robustness against parameter variations and external

© V.T.K. Nhi, B.T. Quy, H.H.B. Nghia, L.V. Dai

disturbances. Sensorless control methods primarily involve high-frequency signal injection [16] and the fundamental frequency model [17]. The high-frequency injection method involves injecting a high-frequency voltage or current into the system and analyzing the response to estimate rotor position, even when the motor is stationary or running at low speeds. However, this approach can introduce high-frequency noise, which impacts system performance. On the other hand, the fundamental frequency model is typically used for medium-to-high speed ranges, where the stator current is employed as input to an observer to determine rotor position. Common observers used in this method include the EKF [18, 19], model reference adaptive control [20], SMO [21] and a nonlinear flux observer [22, 23]. Among these, EKF has better convergence at low speeds but heavily depends on tuning the noise matrix to achieve high accuracy, requiring extensive simulation experiments to fine-tune suitable parameters [24].

Recently, optimization algorithms have been employed to determine the optimal values for the Q and Rmatrices in the EKF [24]. Several studies have utilized real-coded genetic algorithms in sensorless PMSM control systems to optimize the noise matrices of the EKF [25, 26]. Another approach involves the use of a normalized EKF, designed to improve the adaptability of the EKF to various control systems. This method integrates a swarm intelligence algorithm for offline parameter self-learning. However, these optimization algorithms come with high computational complexity, requiring large training datasets and multiple iterations to achieve optimal results, which results in extended training times. Additionally, ensuring that the training dataset sufficiently covers all possible operating conditions of the system remains a significant challenge in practical applications [24]. Some studies [27] have incorporated fuzzy logic into the EKF to adjust the O and R noise matrices in the sensorless control system of PMSM. However, the effectiveness of this method is heavily dependent on the accuracy of the fuzzy logic control rules. Furthermore, other research [24, 28, 29] has applied the Sage-Husa Kalman algorithm to sensorless control systems of PMSM and linear PMSMs. This approach uses the Sage-Husa noise estimator to compute R via regression methods and determine Q. However, the traditional Sage-Husa noise estimator may lead to observer divergence. As a result, recent improvements have focused on enhancing the stability and accuracy of the observer, while preserving the benefits of fast convergence and high adaptability [24].

This study proposes a linear state estimation approach for load estimation of PMSM based on an improved Luenberger observer and a Kalman filter, incorporating the principles of the SMC for speed loop control and 2 proportional resonant control (PRC) controllers for current loop control. The proposed system aims to create a robust motor control system for surface-mounted PMSM (SPMSM) with precise state estimation, strong speed control, and stable current control, optimized for high-performance applications in environments with noise and load variations. The Kalman filter is utilized to estimate unmeasured states and filter the measured signals. This filter is a common choice in industrial applications due to its optimal performance in linear systems with zero-mean, uncorrelated Gaussian noise.

Interestingly, the Kalman filter remains optimal even when the noise is non-Gaussian [30]. The Luenberger observer offers notable advantages, such as simplicity and low computational cost, particularly for linear systems. It is easy to implement and does not require complex calculations like the Kalman filter, allowing for quick and efficient state estimation. The estimated signal is then used for direct torque load compensation to enhance the system's instantaneous response. The SMC algorithm is introduced to reduce oscillation during sliding mode operation and improve system stability. This algorithm utilizes continuous control signals to replace traditional high-gain switching terms, thereby enhancing robustness against speed variations. Additionally, the algorithm integrates adaptive feedback gain correlated with the motor speed, mitigating the effects of speed fluctuations on system performance.

The **goal** of the paper is to propose a robust hybrid control strategy for PMSM drive systems, specifically targeting improved torque stability and overall system performance. By integrating SMC with PRC, the strategy seeks to minimize torque ripple and enhance system efficiency. The approach is further reinforced by the use of enhanced Luenberger state observer (LSP) and Kalman state observer (KSP) for accurate load torque estimation. The ultimate goal is to offer a more reliable, robust and efficient control solution, surpassing traditional PI controllers, particularly in environments with fluctuating loads and dynamic motor parameters.

Main contributions of this study are:

- 1. The proposal of a hybrid control strategy combining SMC and PRC, improving both torque stability and system performance, resulting in better performance than traditional PI controllers.
- 2. The integration of Luenberger and Kalman observers enhances load torque estimation and improves system reliability by accurately estimating unmeasured states.
- 3. The introduction of feed-forward compensation (FFC), which compensates for changes in load torque and disturbances, thus reducing delays and enhancing transient response.
- 4. Significant improvements in key performance metrics (integral of absolute error IAE, integral of time-weighted absolute error ITAE, integral of squared error ISE) based on simulation results, showing reductions of up to 94.614 % in IAE, 94.603 % in ITAE and 99.708 % in ISE compared to PI control.
- 5. A focus on applications in fluctuating load environments such as electric vehicles and renewable energy systems, where dynamic motor parameters and environmental changes often occur.

Mathematical model of PMSM. In the dq-axis reference frame, disregarding the magnetic saturation effect, the extended back electromotive force (EMF) model of a PMSM can be represented as follows [4, 6, 24, 31]:

This will can be represented as follows [4, 0, 24, 31].
$$\begin{bmatrix} u_d \\ u_q \end{bmatrix} = \begin{bmatrix} R_s + sL_d & -\omega_e L_q \\ \omega_e L_q & R_s + sL_d \end{bmatrix} \cdot \begin{bmatrix} i_d \\ i_q \end{bmatrix} + e_a \cdot \begin{bmatrix} 0 \\ 1 \end{bmatrix}, \quad (1)$$

where s is the Laplace operator; u_d , u_q are the stator voltages in the dq-axis; i_d , i_q are the components of the stator current in the dq-axis; R_s is the stator winding resistance; L_d , L_q are the dq-axis inductances; ω_e is the rotational speed of the magnetic flux; e_a is the magnitude of the extended EMF of the PMSM, described as [1, 2, 24]:

$$e_a = \left(L_d - L_q\right) \omega_e i_d - \left(L_d - L_q\right) \frac{\mathrm{d}i_q}{\mathrm{d}t} \tag{2}$$

Applying the inverse Park transformation to (1) yields the EMF model in the $\alpha\beta$ -axis coordinate system, expressed as follows [6, 24]:

expressed as follows [6, 24]:
$$\begin{bmatrix} u_{\alpha} \\ u_{\beta} \end{bmatrix} = \begin{bmatrix} R_s + sL_d & -\omega_e(L_d - L_q) \\ \omega_e(L_d - L_q) & R_s + sL_d \end{bmatrix} \cdot \begin{bmatrix} i_{\alpha} \\ i_{\beta} \end{bmatrix} + e_a \cdot \begin{bmatrix} -\sin\theta \\ \cos\theta \end{bmatrix}, (3)$$

where θ is the electrical rotor angle; u_{α} , u_{β} are the stator voltages in the $\alpha\beta$ -axis; i_{α} , i_{β} are the components of the stator current in the $\alpha\beta$ -axis.

The governing torque T_e equation can be derived from the input power equation of the windings. By simplifying this equation and applying the characteristics of the PMSM, the following expression is obtained [4, 32]:

$$T_{e} = \frac{3}{2} p \{ \varphi_{f} i_{q} + (L_{d} - L_{q}) i_{d} i_{q} \}, \tag{4}$$

where p is the number of pole pairs; φ_f is the rotor permanent magnet flux linkage.

In a PMSM, the permanent magnets are positioned on the rotor's surface, making the motor non-salient. Consequently, the reluctance paths along both the d-axis and q-axis are identical, resulting in equal inductances for both axes. For simplicity, the machine's inductance will be represented by $L_d = L_q = L_s$. Therefore, (4) can be written as [33, 34]:

$$T_e = \frac{3}{2} p \varphi_f i_q \,. \tag{5}$$

Using Newton's second law, the mechanical equation of the system can be derived as:

$$T_e = T_L + j \frac{\mathrm{d}\omega_r}{\mathrm{d}t} + B_m \omega_r \,, \tag{6}$$

where j is the total system inertia; T_L is the load torque; ω_r is the mechanical angular velocity of the rotor; B_m is the viscous friction coefficient of the motor.

The total system inertia accounts for the inertia of the PMSM and all coupling or fastening components connecting them. The first term in the equation corresponds to the torque required to accelerate the system without the effects of friction. The other 2 terms refer to the torque needed to overcome viscous friction and disturbance torque, respectively. Disturbance torque can originate from factors such as load torque, unmodeled friction, or other dynamic effects within the system.

Load torque identification method. FFC is a control technique that improves system response to rapid input signal changes without relying on feedback from the system. This method effectively reduces delays and helps the control system stabilize quickly when there are sudden changes in load torque, disturbances, or external factors. FFC works by providing a control signal based on the predicted behavior of the system. When there are changes in load torque or external disturbances, the FFC control signal is computed and applied immediately without waiting for feedback from the system's sensors or measurement devices. To apply FFC, we first need to develop the dynamic model of the system. For SPMSM, this model describes the relationship between the electromagnetic torque, load torque and frictional effects within the system. From (6) we rewrite the general equation for the SPMSM system as follows:

$$j\frac{\mathrm{d}\omega_r}{\mathrm{d}t} = T_e - \underbrace{T_L - T_D}_{T_{L_D}} - B_m\omega_r , \qquad (7)$$

where T_L is the load torque acting on the motor, caused by external factors like mechanical load; T_D is the disturbance torque, including unmeasured factors such as unmodeled friction or external disturbances affecting the system. Angular acceleration $d\omega_r/dt$ is a key factor in determining how the motor system responds to the applied torque. The above equation can be restructured to calculate angular acceleration easily:

$$\frac{\mathrm{d}\omega_r}{\mathrm{d}t} = \frac{1}{j} T_e - \frac{B_m}{j} \omega_r - \frac{1}{j} T_{L_D};$$

$$\frac{\mathrm{d}T_{L_D}}{\mathrm{d}t} = \tau_{L_D} T_{L_D} + w_{L_D},$$
(8)

where τ_{L_D} is the attenuation coefficient; w_{L_D} is the noise affecting the load. Determining $d\omega_l/dt$ helps understand the rate of change of the motor's rotational angle under the influence of various factors such as electromagnetic torque, load torque and friction. The system can measure the ω_r but cannot directly measure T_{L_D} . Therefore, the speed sensor will give the result:

$$\omega_{meas} = \omega_r + v_{mot \quad spd} , \qquad (9)$$

where ω_{meas} is the measured motor speed; v_{mot_spd} is the measurement noise.

From (8), (9) we can rewrite in the form:

$$\begin{bmatrix} \frac{\mathrm{d}\omega_{r}}{\mathrm{d}t} \\ \frac{\mathrm{d}T_{L_D}}{\mathrm{d}t} \end{bmatrix} = A \cdot \begin{bmatrix} \omega_{r} \\ T_{L_D} \end{bmatrix} + B \cdot T_{e} + C \cdot \begin{bmatrix} v_{mot_spd} \\ w_{L_D} \end{bmatrix};$$

$$\omega_{meas} = C \cdot \begin{bmatrix} \omega_{r} \\ T_{L_D} \end{bmatrix} + v_{mot_spd},$$
where $A = \begin{bmatrix} -B_{m}/j & -1/j \\ 0 & \tau_{L} \end{bmatrix}; B = \begin{bmatrix} 1/j \\ 0 \end{bmatrix}; G = \begin{bmatrix} 1 & 0 \\ 0 & 1 \end{bmatrix}; C = \begin{bmatrix} 1 & 0 \end{bmatrix}.$

From (7), it can be seen that the electromagnetic torque T_e must overcome the total load force and friction force to produce the angular acceleration of the motor. To calculate and control torque in the system, the drive system needs to respond to changes in the control signal and reference torque. The following equation can represent a dynamic model of the drive system:

$$\frac{\mathrm{d}T_e}{\mathrm{d}t} = \frac{1}{\tau_{\cdots}} \left(T_{e_ref} - T_e \right),\tag{11}$$

where T_{e_ref} is the reference torque that the system needs to achieve, provided by the controller, τ_m is the time constant of the drive system, which reflects the response speed of the drive system. This equation (11) means that the electromagnetic torque T_e will change over time and adjust to match the reference torque T_{e_ref} . The time response of the drive system is controlled τ_m , helping the system achieve stability when there are changes in the control signal.

FFC uses predictive models to react immediately to changes in load torque and disturbances. The FFC control signal u(t) is calculated in advance and applied directly to the system to minimize delays:

$$u(t) = K_{FFC} \cdot T_{L-D} + T_{e-ref} , \qquad (12)$$

where K_{FFC} is the gain constant for FFC. The FFC control signal u(t) is calculated from the estimated load torque and disturbance torque, allowing the electromagnetic

torque to reach the desired value without waiting for feedback from the system.

Therefore, the modified system structure is depicted in Fig. 1. FFC helps transient response and eliminates interference in the control system. Figure 1 illustrates the control diagram of the system, integrating FOC to effectively manage the SPMSM. The speed controller takes the reference speed ω_{r_ref} as input and combines it with one of the 2 observers, using the torque signal T to generate the i_{qT_ref} signal for motor control. This signal, along with the feedback current in the dq-axis, creates the reference currents Δi_d and Δi_q . The current controller then produces the voltage commands u_d and u_q , which are converted into a 3-phase signal and supplied to the space

vector pulse width modulation converter. The actual stator current i_q , the real position θ , obtained from the position sensor, and ω_r , derived from the derivative of the real position, are used as inputs for the feedback signal, the Luenberger observer, and the Kalman filter. The torque estimation methods are: discrete Luenberger observer in simulation 1 and discrete Kalman filter in simulation 2. These 2 simulations are independent of each other to test the response of the proposed controller against each observer. This design ensures that only one independent estimation method is active at any given time, thus avoiding data conflicts and facilitating the evaluation and comparison of the performance of both methods in a unified simulation framework.

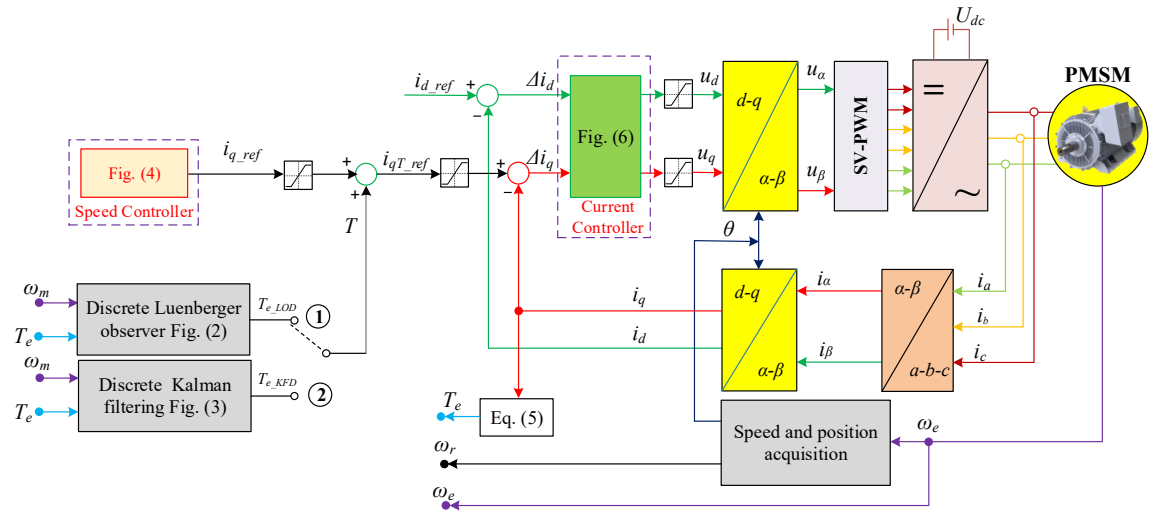


Fig. 1. Diagram of proposed control strategy

Design of discrete Luenberger observer. The basic structure of the Luenberger observer is shown in Fig. 2. Based on the mathematical model of the PMSM, the speed and torque of the PMSM, which are easy to measure, are typically used as inputs to reconstruct the motor's state. In Fig. 2 a feedback control is introduced, where the feedback signal is the difference between the estimated state and the actual state, such as the q-axis current. This feedback mechanism adjusts the observer to make the estimated value infinitely close to the actual value as time progresses. A linear state observer is constructed based on the mechanical equation of the system.

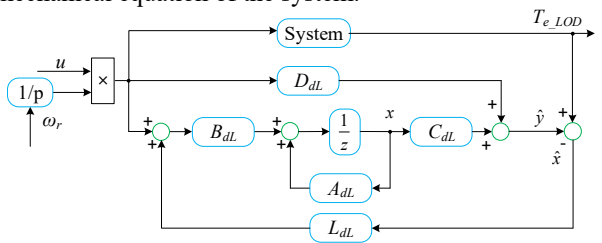


Fig. 2. Structure of the discrete Luenberger load observer

The plant in state-space form is presented in (13) [35–37]:

$$x = Ax + Bu + Gw;$$

$$y = Cx + Du + v,$$
(13)

where in the Luenberger observer the matrices A, B, C, D, G are the essential components in the state-space model of the system. These matrices describe the system dynamics and the relationship between the system's states, inputs and

outputs. With x representing the system states (such as speed and torque); u is the input, which is the actual motor torque T_e ; w is the disturbance acting on the system; y is the output, which signals like speed or torque can measure.

The state space representation of the Luenberger observer is established in (10), we see that (13) is a shortened form of (10) to simplify the control system design process. The load is already transformed into a state. The Luenberger observer equation is used to estimate the states of the system. It is based on the system's dynamic model and adjusts the estimated states based on the measured outputs and inputs. The equation is given by [35, 38]:

$$\frac{d\hat{x}}{dt} = A\hat{x} + Bu + L \cdot \left[y - (\hat{C}x + Du) \right];$$

$$\frac{d\hat{x}}{dt} = (A - LC) \cdot \hat{x} + \left[B \quad L \right] \cdot \begin{bmatrix} u \\ y \end{bmatrix};$$

$$\hat{y} = C\hat{x},$$
(14)

where \hat{x} is the estimated state of the system; L is the observer gain matrix; y is the measured output of the system.

The equation indicates that by designing the observer gains $L = [l_1 \quad l_2]^T$ such that the new system (A - LC) becomes stable and fast enough, the estimation error can be driven to zero by using the estimated speed as a feedback signal $(\Delta \omega_r = \omega_{r_ref} - \omega_r)$, where ω_{r_ref} is the reference value and ω_r is the response rate. The observer gains L can be determined using the pole placement method. The closed-loop system poles are placed at the desired locations, and then the new characteristic equation

is derived. By comparing the coefficients of the latest and old characteristic equations, the observer gains can be found. By converting the above continuous state function A, B, C, D into a discrete state A_d , B_d , C_d , D_d , G_d and reconstructing the estimation matrices using the existing observer gain L, the values of the Luenberger observers are then A_{dL} , B_{dL} , C_{dL} , D_{dL} , G_{dL} . Hence the new system matrices are rewritten as:

$$A_{d} = e^{At_{s}}; \qquad \rightarrow A_{dL} = e^{A_{d}t_{s}};$$

$$B_{d} = \int_{0}^{t_{s}} e^{A.t} B dt; \qquad \rightarrow B_{dL} = \int_{0}^{t_{s}} e^{A_{d}t} B_{d} dt;$$

$$C_{d} = C; \qquad \rightarrow C_{dL} = C_{d};$$

$$D_{d} = D; \qquad \rightarrow D_{dL} = D_{d};$$

$$L_{dL} = G_{dL}S,$$

$$(15)$$

where t_s is the sampling time; G_{dL} is the arbitrary matrix; S is obtained by solving the Sylvester equation.

The control parameters are given in Table 1.

Table 1

Discrete	parameter v	values of	the cont	roller

Parameters	Value	Parameters	Value
S _{1,2}	$-50 \pm j10$	D_d	$\begin{bmatrix} 0.006 & 0.009 \\ 0 & -0.003 \end{bmatrix}$
$ au_L$	0	$t_s(s)$	$0.2 \cdot 10^{-3}$
L	$\begin{bmatrix} 99.885 \\ -37.960 \end{bmatrix}$	A_{dL}	$\begin{bmatrix} 0.980 & -0.013 \\ 0.007 & 0.999 \end{bmatrix}$
A_d	$\begin{bmatrix} 1 & -0.013 \\ 0 & 1.0 \end{bmatrix}$	B_{dL}	$\begin{bmatrix} 0.013 & 0.019 \\ 0 & -0.007 \end{bmatrix}$
B_d	$\begin{bmatrix} 0.013 \\ 0 \end{bmatrix}$	C_{dL}	$\begin{bmatrix} 0.990 & -0.006 \\ 0.003 & 1.0 \end{bmatrix}$
C_d	$\begin{bmatrix} 0.990 & -0.006 \\ 0.003 & 1.0 \end{bmatrix}$	D_{dL}	$\begin{bmatrix} 0.006 & 0.009 \\ 0 & -0.003 \end{bmatrix}$

Design of discrete steady-state Kalman filtering. This section presents a simple discrete Kalman filter. The system in discrete state space is represented as [24, 39, 40]:

$$x_k = Ax_{k-1} + Bu_{k-1} + w_{k-1}; y_k = Cx_k + Du_k + v_k,$$
 (16)

where the subscript k-1, k are represented as the time step k-1 and k, respectively; x_k is the state vector; x_{k-1} is the vector state of the system; u_{k-1} is the system input; w_{k-1} is the process noise affecting the state; y_k is the output vector; v_k is the output vector at the time step k; v_k is the measurement noise affecting the output. The process noise w_k and measurement noise v_k are assumed to be white, zero-mean, uncorrelated, and have the following covariance properties [24, 39]:

$$w_k \approx (0, Q_k); \quad v_k \approx (0, R_k);$$

$$E \cdot \left[w_k v_j^T \right] = Q_k \delta_{k-1}; \quad E \cdot \left[v_k v_j^T \right] = R_k \delta_{k-1}; \quad E \cdot \left[w_k v_j^T \right] = 0, \tag{17}$$

where Q_k is the covariance matrix of the process noise; R_k is the covariance matrix of the measurement noise; δ_{k-1} is the Kronecker delta function (equals 1 if k=j, otherwise 0).

Kalman filter algorithm, including initialization, state propagation, covariance update, and Kalman gain calculation. The process of solving this algorithm is presented as follows.

Initialization. The first step is to initialize the filter by defining the initial state estimate \hat{x}_0^+ as the expected value of the initial state x_0 . Similarly, the state estimation error covariance matrix P_0^+ is initialized. These are described as [24, 39]:

$$\hat{x}_0^+ = E \cdot (x_0);$$

$$P_0^+ = E \cdot \left[(x_0 - \hat{x}_0^+) \cdot (x_0 - \hat{x}_0^+)^T \right].$$
(18)

State propagation. In this step, the filter propagates the state estimate forward in time. This is referred to as the prior state estimate in the literature. It is calculated using as [24, 39]:

$$\hat{x}_k^- = A \cdot \hat{x}_{k-1}^- + B \cdot u_{k-1}, \tag{19}$$

where \hat{x}_k^- is the prior state estimate.

Covariance update. The next step is to update the state estimation error covariance matrix P_k^- , which describes the uncertainty in the state estimate. The equation for this update is [24, 39]:

$$P_k^- = A \cdot P_{k-1}^- \cdot A^T + Q_{k-1}, \qquad (20)$$

 $P_k^- = A \cdot P_{k-1}^- \cdot A^T + Q_{k-1} \,,$ where Q_{k-1} is the process noise covariance matrix.

Kalman gain calculation. Finally, the Kalman gain K_k is computed to determine how much the state estimate should be corrected based on the measurement error. The formula for this is [24, 39]:

$$K_{k} = \frac{P_{k}^{-} \cdot C^{T}}{P_{k}^{-} \cdot C \cdot C^{T} + R_{k}}.$$
 (21)

The next step in the Kalman filter algorithm is the correction step, where the posterior state estimate \hat{x}_k^+ is updated based on the measurement. This process is described as [24, 39]:

$$\hat{x}_{k}^{+} = \hat{x}_{k}^{-} + K_{k} \cdot \left(y_{k} - C \cdot \hat{x}_{k}^{-} \right). \tag{22}$$

The term $y_k - C \cdot \hat{x}_k^-$ is called the residual or innovation, representing the difference between the actual measurement and the predicted output. After updating the state estimate, the error covariance matrix P_k^+ is updated by [24, 39]:

$$P_k^+ = (I - C \cdot K_k) \cdot P_k^-, \tag{23}$$

where I is the identity matrix; $C \cdot K_k$ represents the adjustment to the covariance based on the Kalman gain and output matrix. It is expected that P_k^+ will decrease over time because the term $(I - C \cdot K_k) < 1$. This reduces uncertainty in the state estimate as more measurements are processed. The noise covariance matrices Q_k (process noise) and R_k (measurement noise) significantly affect the Kalman gain K_k . When Q_k increases, the state estimation error covariance P_k^- increases, leading to a higher Kalman gain K_k . Lowering R_k also increases the Kalman gain K_k . With a higher Kalman gain, the algorithm puts more weight on the new measurement, leading to larger corrections in the state estimate. Conversely, if K_k is close to 0, the algorithm ignores new measurements and assumes the current estimate is accurate. By substituting the same data as in the subsection of «design of discrete Luenberger observer», it gets the control parameters for the Kalman filter shown in Table 2.

Discrete parameter values of the controller

Financial							
Parameter	Value	Parameter	Value	Parameter	Value		
\hat{x}_k^-	$\begin{bmatrix} 125.686 \\ 5.985 \end{bmatrix}$	P_k^+	$\begin{bmatrix} 0 & 0 \\ 0 & 0.084 \end{bmatrix}$	K_k	$\begin{bmatrix} 0.835 \\ -0.556 \end{bmatrix}$		
Q_{k-1}	$\begin{bmatrix} 0.001 & 0 \\ 0 & 0 \end{bmatrix}$	P_k^-	$\begin{bmatrix} 0.001 & 0 \\ 0 & 0 \end{bmatrix}$	\hat{x}_k^+	$\begin{bmatrix} 123.819 \\ 0.966 \end{bmatrix}$		

In embedded systems, due to limitations in memory and computational resources, it is often preferable to fix the Kalman gain to reduce processing costs. This means that parameters K_k and P_k are not updated continuously, which is only feasible under the assumption that the system and noise remain time-invariant. The steady-state Kalman filter, although not fully optimal, approaches optimality $k\rightarrow\infty$. Figure 3 illustrates that the Kalman gain converges to a stable value after approximately 50 and 500 time samples, with a sampling time of 0.2 ms. In the left plot, the Kalman gain increases rapidly from 0.81 to 0.835 within the first 30 steps and then stabilizes, indicating quick adaptation to the measured signal. Meanwhile, the right plot shows the Kalman gain decreasing from -0.6 to near 0 over 500 steps, reflecting an increasing trust in system predictions over time. These variations enable the Kalman filter to enhance the accuracy of state estimation and noise reduction, effectively supporting the control of PMSMs.

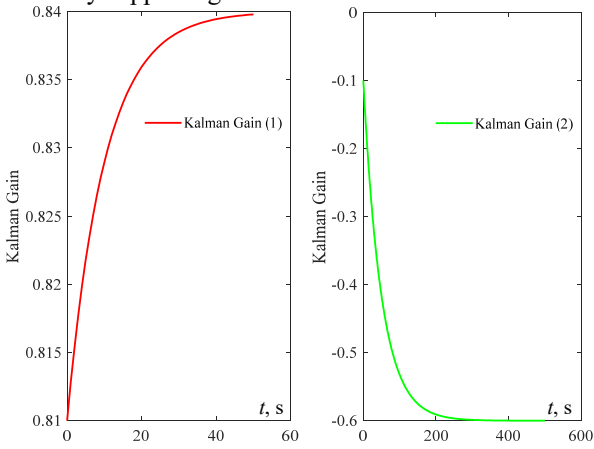


Fig. 3. Kalman gains captured during simulation

Proposed speed controller. To introduce the SMC design, we first define the system's state variables, which are crucial for implementing this control approach. By establishing these state variables, we can proceed to formulate the control law and analyze the system's behavior under SMC. Therefore, the system state is defined as:

$$\Delta \omega_r = \omega_{r_ref} - \omega_r;$$

$$x_1 = \frac{d(\Delta \omega_r)}{dt} = -\frac{d\omega_r}{dt}.$$
(24)

Additionally, the following equations can be obtained based on (6) and (24):

$$\frac{\mathrm{d}(\Delta\omega_r)}{\mathrm{d}t} = -\frac{\mathrm{d}\omega_r}{\mathrm{d}t} = -\frac{p}{j} \cdot \left(\frac{3}{2} \cdot p \cdot \varphi_f \cdot i_q - T_L\right);$$

$$\frac{\mathrm{d}x_1}{\mathrm{d}t} = -\frac{\mathrm{d}^2(\Delta\omega_r)}{\mathrm{d}t^2} = -\frac{\mathrm{d}\omega_r}{\mathrm{d}t} \cdot \frac{3}{2} \cdot \frac{p^2}{j} \cdot \varphi_f \cdot \frac{\mathrm{d}i_q}{\mathrm{d}t},$$
with $a = \frac{3}{2} \cdot \frac{p^2 \cdot \varphi_f}{j}$, $u = \frac{\mathrm{d}i_q}{\mathrm{d}t}$, the system (25) is

represented under the state space system as:

$$\frac{\mathrm{d}}{\mathrm{d}t} \begin{bmatrix} \Delta \omega_{\mathrm{r}} \\ x_{1} \end{bmatrix} = \begin{bmatrix} 0 & 1 \\ 0 & 0 \end{bmatrix} \cdot \begin{bmatrix} \Delta \omega_{\mathrm{r}} \\ x_{1} \end{bmatrix} + u \cdot \begin{bmatrix} 0 \\ -a \end{bmatrix}. \tag{26}$$

The sliding surface function is defined as:

$$s_s = c \cdot \Delta \omega_r + x_1 \,. \tag{27}$$

Differentiating (27) becomes:

$$\frac{\mathrm{d}s_s}{\mathrm{d}t} = c \cdot \frac{\mathrm{d}(\Delta\omega_r)}{\mathrm{d}t} + \frac{\mathrm{d}x_1}{\mathrm{d}t} = c \cdot x_1 - a \cdot u \ . \tag{28}$$

According to the SMC law, the control signal is expressed as:

$$u = \frac{1}{a} \cdot \left(c \cdot x_1 + e \cdot |X|^{\alpha} \cdot \operatorname{sgn}(s_s) + k \cdot s_s \right), \tag{29}$$

where u is the control signal; c, e, k are the control parameters respectively; X is the state variable of the system; s_s is the deviation (or error) of the system from the sliding surface; α is the adaptive switching power term.

The reference current for the q-axis can be expressed as:

$$i_{q_ref} = \int_{0}^{T} \frac{1}{a} \left(c \cdot x_1 + e \cdot |X|^{\alpha} \cdot \operatorname{sgn}(s_s) + k \cdot s_s \right) dt . \quad (30)$$

To analyze the stability of the controller, define the Lyapunov function:

$$L_{v} = s_{s}^{2} / 2. {(31)}$$

 $L_y = s_s^2 / 2$. (31) Substituting (27) and (28) into (31), it has follows as:

$$\frac{\mathrm{d}L_{y}}{\mathrm{d}t} = s_{s} \cdot \left(c \cdot \Delta \omega_{r} + \frac{\mathrm{d}x_{1}}{\mathrm{d}t} \right) = -e \cdot \left| X \right|^{\alpha} \cdot \left| s_{s} \right| + k \cdot s_{s}^{2} . \quad (32)$$

The derivative of the Lyapunov function L_{ν} gives us the above result, where dL_v/dt is the change in the Lyapunov function over time. Since the parameters satisfy e > 0, $\alpha > 0$, k > 0, then $dL_v/dt < 0$ will be established, ensuring that the system enters the sliding mode as long as the conditions are met. SMC speed control diagram is shown in Fig. 4.



Fig. 4. The proposed speed control diagram

Proposed current controller. PRC is an effective control method designed to improve accuracy in control systems, especially in systems that require the resolution of issues related to steady-state error at the fundamental frequency. Unlike traditional PI control methods, PRC control is capable of adjusting the signal at the fundamental frequency without producing a steady-state error. PRC has the following transfer function:

$$G_{PRC}(s) = k_p + \frac{2 \cdot k_i \cdot s}{s^2 \cdot \omega_e^2}, \qquad (33)$$

where k_p is the proportional gain; k_i is the integral gain; ω_e is the resonant frequency, which determines the frequency at which the PRC has the most effect.

When the angular frequency of the AC signal is given as ω_e , the magnitude of the transfer function $G_{PRC}(s)$ will be:

$$\left| G_{PRC}(s) \right|_{s=j\omega_e} = \sqrt{k_p^2 + \left(\frac{2 \cdot k_i \cdot \omega_c}{-\omega_e^2 + \omega_e^2} \right)^2} \ . \tag{34}$$

From (34), it can be observed that the magnitude of $G_{PRC}(s)$ becomes infinite, which allows the control of a

sinusoidal signal with the same frequency as the resonant frequency to achieve zero steady-state error control. However, in practical applications, due to issues in implementing the ideal PRC, this section uses an improved quasi-PRC, with its transfer function being:

$$G_{PRC}(s) = k_p + \frac{2 \cdot k_i \cdot \omega_e \cdot s}{s^2 + 2 \cdot \omega_c \cdot s + \omega_e^2}, \qquad (35)$$

where ω_c is the cutoff frequency of the quasi-resonant controller.

From (35), it can be seen that the controller has 3 design parameters: k_p , k_i and ω_c . For ease of analysis, assume that any 2 parameters are kept constant, and then observe how the variation of the 3rd parameter affects the system's performance. Figure 5 shows the corresponding changes in the Bode plot when only k_p , k_i and ω_c is changed, and analyzes the role of each parameter.

In Fig. 5,a, where k_p is changed, it can be seen that the magnitude outside the bandwidth increases as k_p increases, while the fundamental frequency does not increase significantly. This indicates that when k_p becomes too large, its effect on resonance is negligible. In Fig. 5,b, where only k_i is changed, it can be seen that as k_i

increases, the gain at the fundamental frequency increases, indicating that it plays a role in eliminating steady-state error. However, the increase in k_i also widens the bandwidth of the PRC, thus increasing the influence of resonance and amplifying unnecessary signals, which is detrimental to the overall stability of the system. In Fig. 5,c, where only ω_c is changed, it can be seen that as ω_c decreases, the gain at the fundamental frequency increases, and the bandwidth narrows. This indicates that it has good selectivity for the signal, and f_e determines the bandwidth of the controller. Therefore, to achieve a good control effect with the resonant controller, the principle of parameter tuning is to adjust k_p to eliminate the steadystate error of the system and adjust ω_c to suppress the impact of frequency fluctuations. The transfer function (33) is in the s-domain. When using PRC for digital control of a 3-phase PMSM system, to simplify the discretization process, only the resonant controller is discretized. Its implementation can be done using bilinear transformation, and the transformation formula is:

$$s = \frac{1}{t_s} \cdot \frac{1 - z^{-1}}{1 + z^{-1}} \,. \tag{36}$$

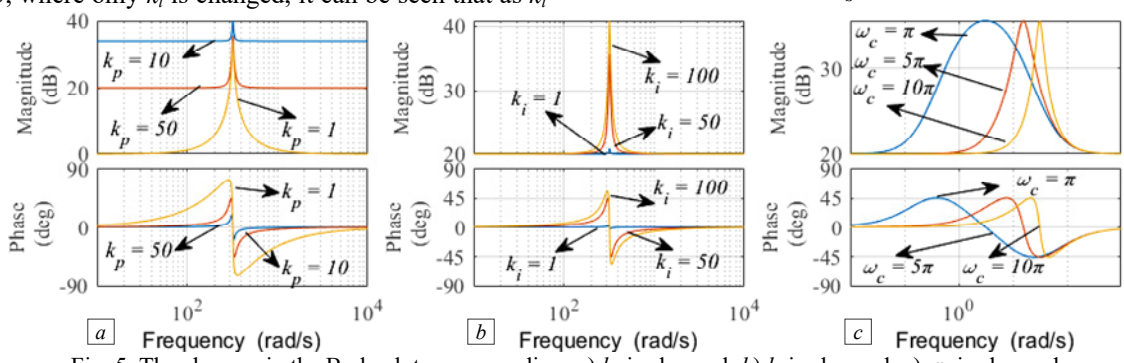


Fig. 5. The changes in the Bode plot corresponding: a) k_n is changed; b) k_i is changed; c) ω_c is changed

Substituting (36) into (35), it can become as follows:

$$G_{PRC}(z) = \frac{b_0 + b_1 z^{-1} + b_2 z^{-2}}{1 + a_1 z^{-1} + a_2 z^{-2}},$$
 (37)

in which:

$$a_1 = \frac{2\omega_e^2 t_s^2 - 8}{4 + 4\omega_c t_s + \omega_e^2 t_s^2}; \quad a_2 = \frac{4 - 4\omega_c t_s + \omega_e^2 t_s^2}{4 + 4\omega_c t_s + \omega_e^2 t_s^2};$$

$$b_0 = \frac{4 \cdot k_i \omega_c t_s}{4 + 4 \omega_e t_s + \omega_e^2 t_s^2}; \quad b_1 = 0; \quad b_2 = \frac{-4 k_i \omega_c t_s}{4 + 4 \omega_c t_s + \omega_e^2 t_s^2}.$$

After organizing, the difference equation of the controller is:

$$u_{d,q}(k) = b_0 e(k) + b_2 e(k-2) - a_1 y(k-1) - a_2 y(k-2)$$
. (38)

Equation (38) achieves steady-state control of the error signal. It can be seen that the control is relatively simple and easy to implement. The implementation block diagram of the PRC is shown in Fig. 6 and parameters are listed in Table 3.

Parameter of the PRC

Turumeter of the Title							
Parameter	Value	Parameter	Value				
k_p	5.775	ω_c	20				
k_i	1000	t_s	0.0001				

We have the resonant frequency matches the motor speed, thus achieving near-error-free tracking of the current. Compared to traditional PI control methods, the control system based on the PR controller does not contain feedforward compensation terms or decoupling terms related to

motor parameters. This reduces coordinate rotation, thereby simplifying the implementation of the control algorithm and improving the robustness of the control system.

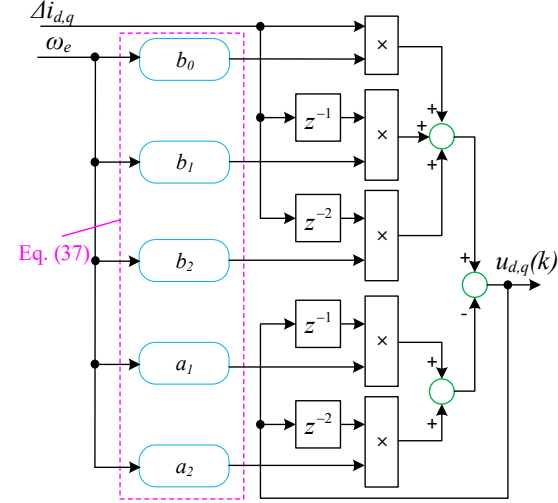


Fig. 6. Implementation block diagram of the PRC

Results and discussion. The simulation cases were conducted under steady-state conditions and assumed operating conditions to observe the control signals and performance between LSP and KSP under the influence of the proposed SMC-PRC controller and the traditional PI controller. The parameters of the SPMSM are listed in

Table 4. MATLAB/Simulink software was used to conduct 3 simulation experiments (Fig. 7), to demonstrate the operational capability of the SPMSM under all conditions and evaluate the effectiveness of the observation methods tested in this study. The data from the 3 conditions display key parameters, including the actual rotor speed, estimated

speed, reference speed, current components, dq-axis voltage $(i_d, i_q, u_d \text{ and } u_q)$, and 3-phase current (i_{abc}) . In each experimental case, the parameters were calculated and compared with the proposed SMC-PRC observer and the traditional PI controller. These values indicate the superiority of the proposed controller in this study.

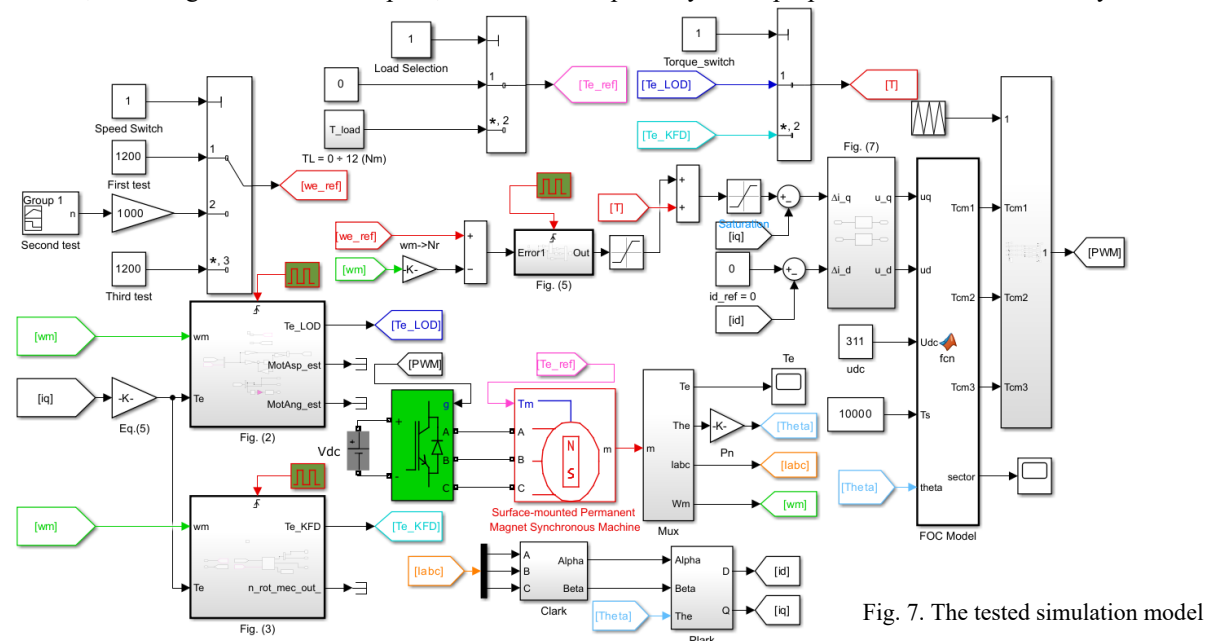


Table 4

The parameters of tested system

Parameter Value Parameter Value Rated power P_r , kW 9.4 d-axis inductance L_d , mH 2.2 4500 q-axis inductance L_q , mH 2.2 Rated speed n_r , rpm Rotor peak PM flux 4 0.12258 Number of pole pairs linkage φ_m , Wb Stator resistance R_s , Ω | 0.268 | Viscous friction B_m , N·s/m 0.001665 Total inertia j, kg·m² 0.0146 Rated torque T_r , N·m 20 DC-link voltage U_{dc} , V 360 Switching frequency f_s , kHz

Case study 1. In this experiment, 2 strategies (SMC-PRC and PI) were compared when the motor operated at a low speed of 50 rpm and under noload conditions. The simulation results showed that both control strategies were able to track the reference signal well (Fig. 8,a,b). However, during the startup process, the torque of SMC-PRC was lower compared to PI, with the startup values being 4.888 N·m and 12.994 N·m, respectively, as shown in Fig. 8,c,d. The startup currents also exhibited a significant difference: while SMC-PRC had a startup current of 6.649 A, PI had a much higher current - 17.671 A (Fig. 8,e,f). This indicates that SMC-PRC reduces the startup current by up to 62.382 %. Additionally, the 3-phase currents (Fig. 8,g,h), displayed distinct changes in both control strategies, with SMC-PRC providing a more stable current during startup.

The error indices IAE, ITAE, and ISE (Table 5) show that the SMC-PRC method significantly improves over PI, with IAE reduced by 10.837 %, ITAE -9.6 %, ISE -20.72 %.

Table 5 A comparison of the error indices in the case study 1

Observer type	SMC-PRC	PI	Ratios, %
IAE	0.3258	0.3654	10.837
ITAE	1.9548	2.1624	9.6
ISE	0.0176	0.0222	20.72

These results demonstrate that the use of the SMC-PRC controller not only helps reduce startup current but also enhances control performance, improving the accuracy and stability of the system compared to PI.

Case study 2. This test provides a comprehensive overview of the observed results when the speed command is increased from 2000 to 3000 rpm at 2 s and then reduced from 3000 rpm to 1000 rpm at 3 s, after which the motor stabilizes. The simulation results with both the SMC-PRC and PI controllers (Fig. 9) reveal significant differences in the control parameters throughout the operation. The speed of both controllers follows the reference signal almost exactly, but PI shows a slower settling time compared to SMC-PRC (Fig. 9,a,b). Based on the comparison of settling times between the 2 methods, SMC-PRC proves to be superior. Specifically, at 3000 rpm, the settling time of SMC-PRC is 2.089 s, which is shorter than PI's 2.265 s, and faster by approximately 0.176 s. At 2000 rpm, SMC-PRC has a settling time of just 0.165 s, while PI takes 0.568 s, faster by about 0.403 s. Finally, at 1000 rpm, SMC-PRC achieves a settling time of 3.186 s, while PI takes 3.63 s, faster by 0.444 s. In total, the settling time of SMC-PRC is 5.44 s, while PI's settling time is 6.463 s, with a difference of 1.023 s. Therefore, SMC-PRC is not only faster, but also enables the system to reach the reference speed more quickly and stably compared to PI. The torque in SMC-PRC during startup is 0.105 N·m, lower than PI's 0.343 N·m, indicating that SMC-PRC is more stable in the initial phase (Fig. 9,c,d). The startup currents i_q and i_d (Fig. 9,e,f) have values of 34.551 A and -15.355 A for SMC-PRC, significantly lower compared to PI's startup currents of 55.116 A and -17.964 A, indicating that SMC-PRC helps reduce the startup current by approximately 37.312% for i_d and 14.634% for i_q .

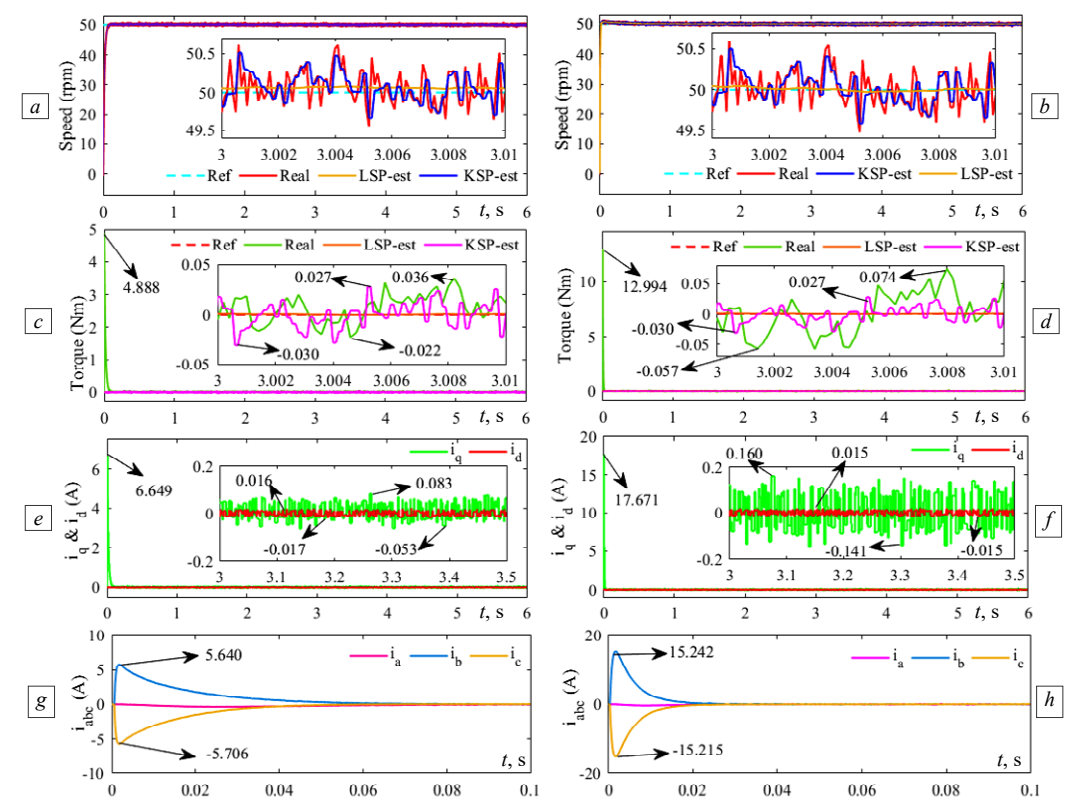


Fig. 8. Dynamic response of the system in the case study 1: a) and b) the rotor speed applying SMC-PRC and PI methods; c) and d) the electromagnetic torque applying SMC-PRC and PI methods; e) and f) the d- and q-axis current applying SMC-PRC and PI methods; g) and h) the 3-phase current applying SMC-PRC and PI methods

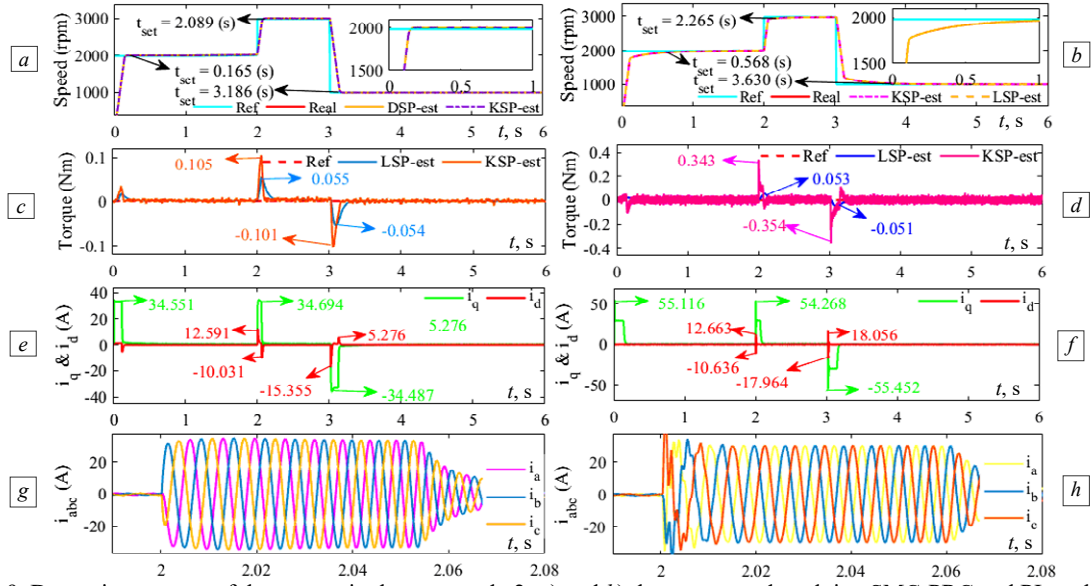


Fig. 9. Dynamic response of the system in the case study 2: a) and b) the rotor speed applying SMC-PRC and PI methods; c) and d) the electromagnetic torque applying SMC-PRC and PI methods; e) and f) the d- and q-axis current applying SMC-PRC and PI methods; g) and h) the 3-phase current applying SMC-PRC and PI methods

The 3-phase current images also show significantly greater stability in SMC-PRC compared to PI, where PI experiences strong oscillations in the phases. These results demonstrate that the SMC-PRC controller outperforms PI in reducing startup current and maintaining system stability.

The error indices IAE, ITAE, and ISE (Table 6) show significant improvements in the SMC-PRC method compared to PI, with IAE reduced by 94.614%, ITAE – 94.603%, and ISE – 99.708%. These results confirm that the use of the SMC-PRC controller not only helps reduce the startup current, but also enhances control performance, improving the accuracy and stability of the system compared to PI.

A comparison of the error indices in the case study 2

Observer type	SMC-PRC	PI	Ratios, %
IAE	0.548	10.182	94.614
ITAE	3.296	61.092	94.603
ISE	0.05	17.278	99.708

Case study 3. In this case, the simulation results were carried out by setting the speed to 2000 rpm and varying the load torque from 0 to 12 N·m at 3 s (Fig. 10). The results for both the SMC-PRC and PI control methods show significant differences in tracking the speed and current signals. Both methods maintain the speed close to the reference value, but SMC-PRC exhibits higher stability, especially during the

rapid speed change from 2.9 s to 3 s (Fig. 10,a,b). The torque in SMC-PRC stabilizes at around 12 N·m, while PI shows greater fluctuation, reaching approximately 12.53 N·m (Fig. 10,c,d). The currents in Fig. 10,e,f show large variations in both methods during startup. SMC-PRC starts with a significantly lower current about 18.558 A for i_q , while PI peaks at 20.229 A for i_q , indicating that SMC-PRC is more effective in reducing the startup current. Also, the 3-phase currents (Fig. 10,g,h), are more stable in SMC-PRC compared to PI, helping to minimize unnecessary oscillations. These results show that SMC-PRC not only reduces the startup current, but also improves the stability and overall performance of the system compared to PI.

The error indices IAE, ITAE, and ISE (Table 7) show that the SMC-PRC method significantly improves over PI, with IAE reduced by 74.18 %, ITAE – 74.18 %, and ISE – 93.333 %. These results confirm that the use of the SMC-PRC controller not only helps reduce the startup current but also enhances control performance, improving the accuracy and stability of the system compared to PI.

A comparison of the error indices in the case study 3

Observer type	SMC-PRC	PI	Ratios, %		
IAE	82.68	320.22	74.18		
ITAE	496.08	1921.32	74.18		
ISE	1139.33	17090.141	93.333		

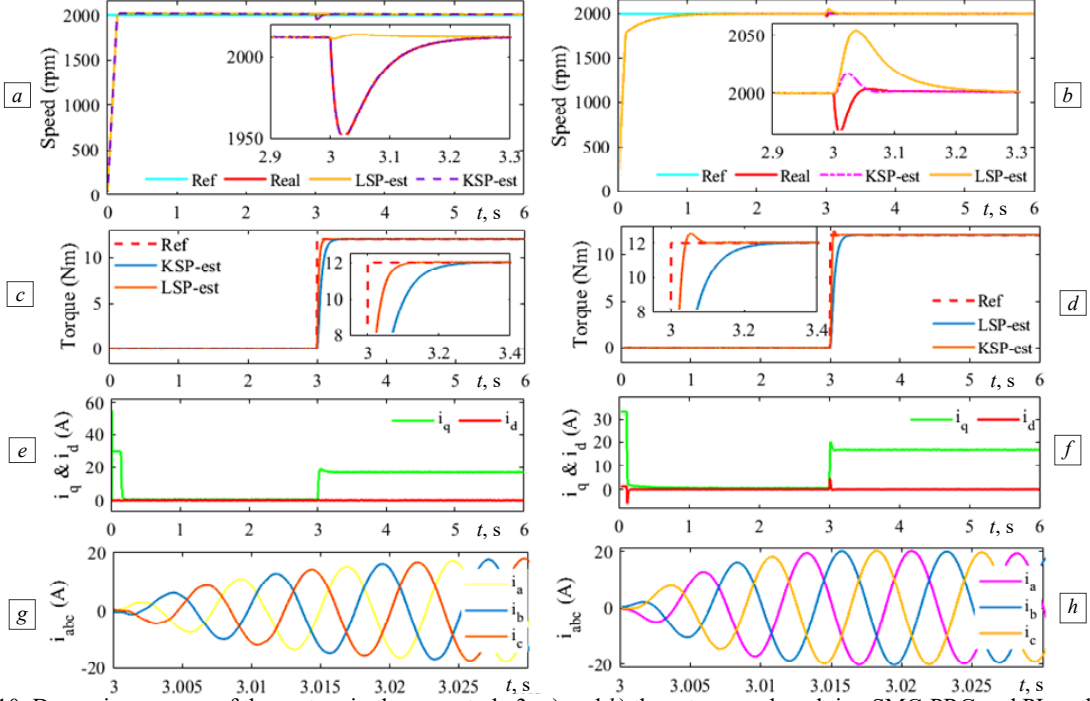


Fig. 10. Dynamic response of the system in the case study 3: a) and b) the rotor speed applying SMC-PRC and PI methods; c) and d) the electromagnetic torque applying SMC-PRC and PI methods; e) and f) the d- and q-axis current applying SMC-PRC and PI methods; g) and h) the 3-phase current applying SMC-PRC and PI methods

Conclusions. The purpose of this work was, firstly, to evaluate the performance of the use of field programmable gate array programmable logic circuits for the diagnosis of faults in an induction machine by introducing a fuzzy inference system into the algorithm of the analysis of the motor current signal analysis by taking the RMS signal of the stator phase current as the fault indicator signal. Secondly, to implement and validate the proposed hardware detection algorithm. The originality of our work has been to combine the performance of artificial intelligence techniques, the simplicity of motor current signal analysis algorithms and the execution power of programmable logic circuits, for the definition of a fault diagnosis structure for the induction machine achieving the best simplicity/performance and speed/performance ratios. Finally, the proposed solution has improved the performance of fault detection for the induction machine, especially in terms of hardware resource consumption, realtime online detection and speed of detection.

Conflict of interest. The authors declare that they have no conflicts of interest.

REFERENCES

I. Hassan A.M., Ababneh J., Attar H., Shamseldin T., Abdelbaset A., Metwally M.E. Reinforcement learning algorithm for improving speed response of a five-phase permanent magnet synchronous motor based model predictive control. *PLOS ONE*, 2025, vol. 20, no. 1, art. no. e0316326. doi: https://doi.org/10.1371/journal.pone.0316326.

- Hu J., Yao Z., Xin Y., Sun Z. Design and optimization of the jet cooling structure for permanent magnet synchronous motor. *Applied Thermal Engineering*, 2025, vol. 260, art. no. 125051. doi: https://doi.org/10.1016/j.applthermaleng.2024.125051.
 Liu F., Wang X., Sun L., Wei H., Li C., Ren J. Improved 3D hybrid
- 3. Liu F., Wang X., Sun L., Wei H., Li C., Ren J. Improved 3D hybrid thermal model for global temperature distribution prediction of interior permanent magnet synchronous motor. *Energy*, 2025, vol. 315, art. no. 134270. doi: https://doi.org/10.1016/j.energy.2024.134270.
- 4. Dien C.N., Nghia H.H.B. Optimizing Permanent Magnet Synchronous Motor Performance Considering Both Maximum Torque Per Ampere and Field Weakening. *International Journal of Intelligent Engineering & Systems*, 2025, vol. 18, no. 1, pp. 1121-1136. doi: https://doi.org/10.22266/jijes2025.0229.81.
- 5. Meng D., Wu Q., Zhang J., Li Y., Diao L. Restarting control of free-running interior permanent magnet synchronous motor under position sensorless control. *Alexandria Engineering Journal*, 2025, vol. 115, pp. 83-93. doi: https://doi.org/10.1016/j.aej.2024.11.111.
- 6. Liang Z., Cheng L., Cheng L., Li C. Rotor Position Estimation Algorithm for Surface-Mounted Permanent Magnet Synchronous Motor Based on Improved Super-Twisting Sliding Mode Observer. *Electronics*, 2025, vol. 14, no. 3, art. no. 436. doi: https://doi.org/10.3390/electronics14030436.
- 7. Alnaib I.I., Alsammak A.N. Optimization of fractional PI controller parameters for enhanced induction motor speed control via indirect field-oriented control. *Electrical Engineering & Electromechanics*, 2025, no. 1, pp. 3-7. doi: https://doi.org/10.20998/2074-272X.2025.1.01. Mesloub H., Boumaaraf R., Benchouia M.T., Golea A., Golea N.,
- Srairi K. Comparative study of conventional DTC and DTC_SVM based control of PMSM motor Simulation and experimental results. *Mathematics and Computers in Simulation*, 2020, vol. 167, pp. 296-307. doi: https://doi.org/10.1016/j.matcom.2018.06.003.

- 9. Nemouchi B., Rezgui S.E., Benalla H., Nebti K. Fractional-based iterative learning-optimal model predictive control of speed induction motor regulation for electric vehicles application. Electrical Engineering & *Electromechanics*, 2024, no. 5, https://doi.org/10.20998/2074-272X.2024.5.02 5. pp.
- 10. Lee J., You S., Kim W., Moon J. Extended state observer-actorcritic architecture based output-feedback optimized backstepping control for permanent magnet synchronous motors. Expert Systems Applications, 2025. vol. 270. art. no. https://doi.org/10.1016/j.eswa.2025.126542
- 11. Gu J., You S., Kim W., Moon J. Fuzzy Event-Triggered Super Twisting Sliding Mode Control for Position Tracking of Permanent Magnet Synchronous Motors Under Unknown Disturbances. IEEE Transactions on Industrial Informatics, 2023, vol. 19, no. 9, pp. 9843-9854. doi: https://doi.org/10.1109/TII.2022.3231410
- 12. Aib A., Khodja D.E., Chakroune S., Rahali H. Fuzzy current analysis-based fault diagnostic of induction motor using hardware cosimulation with field programmable gate array. Electrical Engineering & Electromechanics, 2023, no. 6. https://doi.org/10.20998/2074-272X.2023.6.01. 6,
- 13. Gil J., You S., Lee Y., Kim W. Nonlinear sliding mode controller using disturbance observer for permanent magnet synchronous motors under disturbance. Expert Systems with Applications, 2023, vol. 214, art. no. 119085. doi: https://doi.org/10.1016/j.eswa.2022.119085
- 14. Liu X., Wang Z., Wang W., Lv Y., Yuan B., Wang S., Li W., Li Q., Zhang Q., Chen Q. SMO-Based Sensorless Control of a Permanent Magnet Synchronous Motor. Frontiers in Energy Research, 2022, vol. 10, art. no. 839329. doi: https://doi.org/10.3389/fenrg.2022.839329.

 15. Yao G., Wang X., Wang Z., Xiao Y. Senseless Control of
- Permanent Magnet Synchronous Motors Based on New Fuzzy Adaptive Sliding Mode Observer. Electronics, 2023, vol. 12, no. 15, art. no. 3266. doi: https://doi.org/10.3390/electronics12153266.
- 16. Yousefi-Talouki A., Pescetto P., Pellegrino G., Boldea I. Combined Active Flux and High-Frequency Injection Methods for Sensorless Direct-Flux Vector Control of Synchronous Reluctance Machines. IEEE Transactions on Power Electronics, 2018, vol. 33, no. 3, pp. 2447-2457. doi: https://doi.org/10.1109/TPEL.2017.2697209.
- 17. Pasqualotto D., Rigon S., Zigliotto M. Sensorless Speed Control of Synchronous Reluctance Motor Drives Based on Extended Kalman Filter and Neural Magnetic Model. IEEE Transactions on Industrial Electronics, 2023, vol. 70, no. https://doi.org/10.1109/TIE.2022.3159962 2, pp. 1321-1330.
- 18. Jiang F., Sun S., Liu A., Xu Y., Li Z., Liu X., Yang K. Robustness Improvement of Model-Based Sensorless SPMSM Drivers Based on an Adaptive Extended State Observer and an Enhanced Quadrature PLL. IEEE Transactions on Power Electronics, 2021, vol. 36, no. 4, pp. 4802-4814. doi: https://doi.org/10.1109/TPEL.2020.3019533
- 19. Zhang Y., Yin Z., Bai C., Wang G., Liu J. A Rotor Position and Speed Estimation Method Using an Improved Linear Extended State Observer for IPMSM Sensorless Drives. IEEE Transactions on Power
- 20. Zhang G., Wang G., Xu D., Zhao N. ADALINE-Network-Based PLL for Position Sensorless Interior Permanent Magnet Synchronous Motor Drives. IEEE Transactions on Power Electronics, 2016, vol. 31, no. 2, pp. 1450-1460. doi: https://doi.org/10.1109/TPEL.2015.2424256.
- 21. Kim H., Son J., Lee J. A High-Speed Sliding-Mode Observer for the Sensorless Speed Control of a PMSM. IEEE Transactions on Industrial Electronics, 2011, vol. 58, no. 9, pp. 4069-4077. doi: https://doi.org/10.1109/TIE.2010.2098357.
- 22. Wu C., Sun X., Wang J. A Rotor Flux Observer of Permanent Magnet Synchronous Motors With Adaptive Flux Compensation. *IEEE* Transactions on Energy Conversion, 2019, vol. 34, no. 4, pp. 2106-2117. doi: https://doi.org/10.1109/TEC.2019.2932787
- 23. Xu W., Jiang Y., Mu C., Blaabjerg F. Improved Nonlinear Flux Observer-Based Second-Order SOIFO for PMSM Sensorless Control. IEEE Transactions on Power Electronics, 2019, vol. 34, no. 1, pp. 565-579. doi: https://doi.org/10.1109/TPEL.2018.2822769
- 24. Yingjun S., Zhenglong W., Yuanyuan F. An adaptive extended Kalman filter observer-for permanent magnet synchronous motor position sensorless control systems. Scientific Reports, 2025, vol. 15, no. 1, art. no. 11605. doi: https://doi.org/10.1038/s41598-025-85787-5
- 25. Salvatore N., Caponio A., Neri F., Stasi S., Cascella G.L. Optimization of Delayed-State Kalman-Filter-Based Algorithm via Differential Evolution for Sensorless Control of Induction Motors. IEEE Transactions on Industrial Electronics, 2010, vol. 57, no. 1, pp. 385-

- 394. doi: https://doi.org/10.1109/TIE.2009.2033489
- 26. Zerdali E., Barut M. The Comparisons of Optimized Extended Kalman Filters for Speed-Sensorless Control of Induction Motors. IEEE Transactions on Industrial Electronics, 2017, vol. 64, no. 6, pp. 4340-4351. doi: https://doi.org/10.1109/TIE.2017.2674579
- 27. Yin Z., Xiao L., Sun X., Liu J., Zhong Y. A speed and flux estimation method of induction motor using fuzzy extended Kalman filter. 2014 International Power Electronics and Application Conference and Exposition, 2014, pp. https://doi.org/10.1109/PEAC.2014.7037941. 693-698
- 28. Wang T., Huang S., Gao M., Wang Z. Adaptive Extended Kalman Filter Based Dynamic Equivalent Method of PMSG Wind Farm Cluster. IEEE Transactions on Industry Applications, 2021, vol. 57, no. 3, pp. 2908-2917. doi: https://doi.org/10.1109/TIA.2021.3055749
- 29. Zerdali E. Adaptive Extended Kalman Filter for Speed-Sensorless Control of Induction Motors. IEEE Transactions on Energy Conversion, 2019, vol. 34, no. 2, https://doi.org/10.1109/TEC.2018.2866383. pp.
- 30. Simon D. Optimal State Estimation: Kalman, H∞, and Nonlinear Approaches. John Wiley & Sons, https://doi.org/10.1002/0470045345. 2006. 526 p.
- 31. Saberi S., Rezaie B. Sensorless FCS-MPC-based speed control of a permanent magnet synchronous motor fed by 3-level NPC. Journal of Renewable Energy and Environment, 2021, vol. 18, no. 2, pp. 13-20. doi: https://doi.org/10.30501/JREE.2020.234039.1118
- 32. Abu Ibaid O.Z.I., Belhamdi S., Abid M., Chakroune S., Mouassa S., Al-Sagar Z.S. Wavelet packet analysis for rotor bar breakage in an inverter induction motor. Electrical Engineering & Electromechanics, 2023, no. 3, pp. 3-11. doi: https://doi.org/10.20998/2074-272X.2023.3.01
- 33. Kuvvetli I., Tap A., Ergenc A.F., Ergene L.T. An adaptive neurofuzzy inference system controller design of an SPMSM drive for multicopter applications. Transactions of the Institute of Measurement and Control, 2024, pp. 1-15. doi: https://doi.org/10.1177/01423312241286042
- 34. Kimouche A., Mekideche M.R., Chebout M., Allag H. Influence of permanent magnet parameters on the performances of claw pole machines used in hybrid vehicles. Electrical Engineering & Electromechanics, 2024, 3-8. no. pp. https://doi.org/10.20998/2074-272X.2024.4.01
- 35. Boudouani S., Yahdou A., Benbouhenni H., Boudjema Z., Almalki M.M., Alghamdi T.A. Enhanced speed sensorless control of IPMSM using integral synergetic observer. Measurement and Control, 2025, pp. 1-15. doi: https://doi.org/10.1177/00202940241312846.
- 36. Caramori G.M., De Almeira L.M.M., Da Costa C. Enhanced Position Estimation of PMSM Using the Luenberger Observer and PLL Algorithm: Design and Simulation Study. European Journal of Engineering and Technology Research, 2023, vol. 8, no. 6, pp. 37-44. doi: https://doi.org/10.24018/ejeng.2023.8.6.3122
- 37. Saifi R. Implementation of a new flux rotor based on model reference adaptive system for sensorless direct torque control modified for induction motor. Electrical Engineering & Electromechanics, 2023, no. 2, pp. 37-42. doi: https://doi.org/10.20998/2074-272X.2023.2.06
- 38. Moussaoui L., Aouaouda S., Rouaibia R. Fault tolerant control of a permanent magnet synchronous machine using multiple constraints Takagi-Sugeno approach. Electrical Engineering & Electromechanics, 2022, no. 6, pp. 22-27. doi: https://doi.org/10.20998/2074-272X.2022.6.04.
- 39. Dilys J., Stankevič V., Łuksza K. Implementation of Extended Kalman Filter with Optimized Execution Time for Sensorless Control of a PMSM Using ARM Cortex-M3 Microcontroller. Energies, 2021, vol. 14, no. 12, art. no. 3491. doi: https://doi.org/10.3390/en14123491.
- 40. Rouaibia R., Djeghader Y., Moussaoui L. Artificial neural network and discrete wavelet transform for inter-turn short circuit and broken rotor bars faults diagnosis under various operating conditions. Electrical Engineering & Electromechanics, 2024, no. 3, pp. 31-37. doi: https://doi.org/10.20998/2074-272X.2024.3.04.

Received 01.05.2025 Accepted 13.07.2025 Published 02.11.2025

V.T.K. Nhi¹, Postgraduate Student, Lecturer, B.T. Quy¹, PhD, H.H.B. Nghia¹, College Student, L.V. Dai¹, PhD,

¹ Faculty of Electrical Engineering Technology, Industrial University of Ho Chi Minh City, Vietnam, e-mail: levandai@iuh.edu.vn (Corresponding Author)

How to cite this article:
Nhi V.T.K., Quy B.T., Nghia H.H.B., Dai L.V. A robust hybrid control strategy for enhancing torque stability and performance in PMSM drives. Electrical Engineering & Electromechanics, 2025, no. 6, pp. 64-74. doi: https://doi.org/10.20998/2074-272X.2025.6.09

S.E. Rezgui, Z. Darsouni, H. Benalla

Nonlinear vector control of multiphase induction motor using linear quadratic regulator and active disturbances rejection control under disturbances and parameter variations

Introduction. This paper introduces a hybrid control strategy for multiphase induction motors, specifically focusing on the dual star induction motor (DSIM) by integrating active disturbances rejection control (ADRC) and linear quadratic regulator (LQR). Problem. Conventional PI-based indirect field oriented control (IFOC) of DSIM drives exhibit 3 critical shortcomings: 1) sensitivity to parameter variations, such as rotor resistance fluctuations; 2) sluggish transient response during rapid speed and torque changes; 3) slow disturbances rejection, such as sudden load torque variations. The goal of this work is to achieve enhanced reliability, precision and robustness of DSIM drives in high-performance demand applications such as automotive. Methodology. The proposed hybrid control architecture is structured as follows: 1) IFOC decoupling. The DSIM's stator currents are decomposed into 2 components using Park transformations, aligning the rotor flux vector to the d-axis. 2) The LQR is designed to optimize the outer speed/torque loop regulation by minimizing control efforts and state deviations. 3) ADRCs controllers are designed in the inner current loops. Each controller utilizes an extended state observer to estimate and compensate parameter variations and external disturbances in real time. Results. Simulations using MATLAB/Simulink validation on a 5 kW DSIM under multiple scenarios confirm the robustness of the proposed hybrid strategy. Scientific novelty. The contribution lies in the integration of ADRC and LQR in IFOC: The hierarchical fusion of ADRC (inner loops) and LQR (outer loop) uniquely leverages ADRC's and the LQR's real-time power to handle any disturbances and unmodeled dynamics. Practical value. The proposed technique demonstrates enhanced performances in speed's response, sudden load torque demands and parameter variations. It exhibited high robustness even under degraded conditions such as phase faults, making this strategy ideal for high-performance applications like electric vehicles, where stability and adaptability are critical. References 31, tables 2, figures 24. Key words: optimal control, active disturbances rejection control, indirect field-oriented control, multiphase induction motor, three-level neutral point clamped inverters.

Вступ. У статті розглядається гібридна стратегія управління багатофазними асинхронними двигунами, зокрема з фокусом на асинхронний двигун з подвійною зіркою (DSIM),шляхом залучення активного управління придушенням збурень (ADRC) та лінійно-квадратичного регулятора (LQR). Проблема. Традиційне непряме полеорієнтоване управління (IFOC) на основі ПІ-регулятора приводів DSIM має 3 критичні недоліки: 1) чутливість до змін параметрів, таких як коливання опору ротора; 2) інерційний перехідний процес при швидких змінах швидкості та крутного моменту; 3) повільне придушення збурень, таких як різкі зміни крутного моменту навантаження. **Метою** роботи є підвищення надійності, точності та стійкості приводів DSIM у високопродуктивних застосуваннях, таких як автомобілебудування. Методологія. Запропонована архітектура гібридного управління структурована таким чином: 1) Розв'язування ІFOC. Струми статора DSIM розкладаються на 2 складові з використанням перетворень Парка, вирівнюючи вектор потоку ротора осі d. 2) LOR призначений для оптимізації регулювання зовнішнього контуру швидкості/крутного моменту за рахунок мінімізації зусиль з управління та відхилень стану. 3) Контролери ADRC спроєктовані у внутрішніх струмових контурах. Кожен контролер використовує розширений спостерігач стану для оцінки та компенсації змін параметрів та зовнішніх збурень у реальному часі. Результати. Моделювання з використанням валідації у MATLAB/Simulink для 5 кВт DSIM у кількох сценаріях підтверджує надійність запропонованої гібридної стратегії. **Наукова новизна**. Внесок полягає в інтеграції ADRC і LOR в IFOC: ієрархічне злиття ADRC (внутрішніх контурів) і LQR (зовнішнього контуру) унікальним чином використовує потужність ADRC та LQR в реальному часі для обробки будь-яких збурень та немодельованої динаміки. Практична иінність. Запропонована методика демонструє покращені характеристики при реагуванні на швидкість, раптові вимоги до крутного моменту навантаження і зміни параметрів. Він показав високу надійність навіть за умов погіршення характеристик, таких як фазові замикання, що робить цю стратегію ідеальною для високопродуктивних застосувань, таких як електромобілі, де стабільність та адаптивність мають вирішальне значення. Бібл. 31, табл. 2, рис. 24.

Ключові слова: оптимальне керування, активне придушення перешкод, опосередковане полеорієнтоване керування, багатофазний асинхронний двигун, трирівневі інвертори з фіксованою нейтральною точкою.

Introduction. Three-phase induction motors have broad applications across industries and electric traction and have gained large attention in recent researches [1, 2]. However, multiphase motors have become favored in traction applications like electric vehicles and electric marine propulsion due to their superior features over threephase motors. They distribute power across more phases, reducing power per phase and torque ripples. Multiphase motors enhance fault tolerance and torque density with increased degrees of freedom and harmonic current reduction [3]. However, multiphase motors are inherently nonlinear systems due to their coupling between stator and rotor flux dynamics. As a result, achieving precise control over their dynamic performance during variations in speed and torque remains a challenging task. The choice of strategy depends on the specific application, computational resources, and performance requirements. To this end, innumerable control strategies have been developed to fully exploit multiphase induction motors performance across various operating points.

Starting with the most familiar strategies, namely scalar control, vector control, and direct torque control (DTC) [4-8], where authors [5] designed a flux and speed state observer for sensorless control of a dual star induction motor (DSIM) for direct vector control. A comparison with the sliding mode model reference adaptive system technique was conducted to evaluate speed and flux tracking during transients and parameter variations. The results demonstrated the observer's superior robustness against uncertainties, disturbances, and speed changes, while reducing torque ripple compared to model reference adaptive system. However, the proposed state observer still sensitive to parameters variations particularly in low speed. A novel vector control scheme for speed sensorless control of a dual stator induction generator in a grid-connected wind energy conversion system is presented in [6]. This work introduced a 9-zone space vector-based hybrid pulse width modulation (PWM), which optimally controlled

© S.E. Rezgui, Z. Darsouni, H. Benalla

grid and motor side converters, reducing torque pulsation, current ripple, and switching losses. Simulation and laboratory validation demonstrated that the proposed sensorless control outperformed conventional vector control schemes. However, while the hybrid PWM and sensorless control provide significant advantages, the work lacks parameter variation tests.

When conventional DTC scheme is extended for the multiphase motors, it can produce undesirable harmonics (5th and 7th order) in phase currents which cause losses in the motor winding, as a remedy, a simplified method of synthetic vectors generation is proposed in [7]. By using the mapped voltage vectors in d-q and x-y subspaces, dwell times are calculated to suppress the effect of some undesirable vectors and generate new synthetic vectors. These latter are achieved by both field programmable gate array and PWM module. Experimental results shown that with the proposed DTC the current's total harmonic distortion (THD) is reduced by ≈70 % when compared to that of traditional structure. The authors [8] proposed a modified DTC strategy that employs a 2-step approach to select the optimal vector for supplying the DSIM, effectively reducing harmonic currents. To address the steady-state torque error associated with the conventional 5-level hysteresis controller, they developed a 5-level torque regulator that replaces the zero-voltage vector with active voltage vectors and incorporates a PI controller within its structure to enhance steady-state performance.

More advanced techniques have been investigated, for instance, in [9], the authors presented a sensorless control system using super twisting sliding mode control for direct speed and flux control, which ensured robustness, finitetime convergence, and reduced chattering while eliminating speed and position sensors. The innovative torque-sharing algorithm enhanced performance across a wide speed range, including zero speed, preventing winding overload. However, the dependency on the observer of the rotor speed and winding fluxes was a notable problem, along with the need for load torque information for optimal torque sharing. Following the SMC context, authors [10] proposed a nonlinear integral backstepping control for DSIM, improving robustness under parameter variations by using both reduced and complete mathematical models. The control strategy ensured asymptotic global stability and effective load disturbance rejection. Simulation results validated the superiority of the complete model over the reduced one, showing better handling of internal parameter particularly rotor resistance, maintaining changes, decoupling between flux and torque. However, the increased complexity in implementing the complete model was a drawback compared to the simpler reduced model.

Model predictive control has gained a lot of interest from the AC motors control community due to its effectiveness in controlling multi-input, multi-output systems with constraints. Several enhanced model predictive control strategies have been developed with the aim of exploring more efficient solutions [11, 12]. The objectives include simplifying algorithms, designing optimal weighting factors, improving parameter robustness, and minimizing current or torque ripples. For example, in [13], the authors proposed a new modulation strategy in model predictive currents control (MPCC) that combines virtual vectors and space vector modulation for an

asymmetrical 6-phase induction motor. Compared to previous MPCC strategies, such as MPCC with virtual vectors and MPCC with finite set formulation, the proposed MPCC outperforms these methods in *x-y* current reduction and THD. Additionally, a robustness test confirmed the controller's stability under parameter variations.

Some works have been devoted to model reference adaptive control techniques for the DSIM speed control. An adaptive control technique based on the Landau stability theorem was applied in [14] to improve speed regulation. The controller adapts parameters over time using a closed-loop output error algorithm, ensuring robustness against motor parameter variations. Simulation results demonstrated satisfactory speed control, quick disturbance rejection, and smooth electromagnetic torque without peaks. Robustness tests under rotor resistance variations confirmed the method's efficiency in normal and severe conditions.

Other papers have opted to use AI-based strategies as fuzzy, neural network and neuro-fuzzy controllers. An adaptive fuzzy controller based on Lyapunov's stability algorithm was developed in [15]. The approach used a recalculation of the PI-fuzzy speed gains regulator in real time. MATLAB/Simulink simulations showed improved tracking performance and robustness against parameter variations compared to the conventional PI-fuzzy controller. However, tests were limited to medium speeds ($\pm 100 \text{ rad/s}$), the DSIM was not at full load, and keeping traditional PI current controllers make the system susceptible to disturbances. A sensorless 5-level DTC scheme based on neural networks and an extended Kalman filter for a DSIM was studied in [16]. To improve robustness and dynamic performance, artificial neural networks were employed, and extended Kalman filter was used to estimate rotor speed, reducing sensor requirements and installation costs. Simulation results in MATLAB demonstrated that the proposed control scheme provided highly satisfactory performance for the DSIM. However, the work necessitates tests at low speeds as well as evaluations of robustness against parameter variations. In [17], a neuro-fuzzy scheme was developed for speed control of a DSIM with improved performance. A 4-layer network was used to optimize the fuzzy elements by minimizing the squared error. Two 5level inverters with PWM techniques and indirect fieldoriented control (IFOC) were implemented. Simulation results showed the neuro-fuzzy controller provided better speed response, robustness to load disturbances, and parameter variations compared to a conventional inverter. Additionally, the 5-level inverter significantly reduced stator currents and pulsating electromagnetic torque. Another aspect of AI optimization techniques has been used with a synergetic control to improve the performance of vector control scheme of a DSIM in [18]. The optimal parameters in the speed loop are obtained based on the synergistic control theory and the particle swarm optimization. The results showed that synergetic control enhances the robustness of drive speed control, offering superior performance in load torque rejection and reducing torque vibrations caused by chattering.

Optimal control strategies, like the linear quadratic regulator (LQR), aim to minimize a defined cost function, such as energy consumption, torque ripple, or trajectory tracking errors, while adhering to system constraints. Although these techniques are not commonly applied to

multiphase motors, studies in [19–21] investigated their use for induction motors, showing promising potential for such strategies.

Finally, in [22], the authors proposed a control scheme for a DSIM using active disturbance rejection control (ADRC) without relying on current or speed sensors. By utilizing only DC voltage information and the switching states of the converters, voltage observers were employed to estimate the stator currents and rotor speed. It is noteworthy that ADRC was applied solely to the stator currents, while traditional PI controllers were retained for speed and flux control. However, despite the promising results, the system was not tested under conditions of parameter variation.

To ensure high robustness against external disturbances, such as load torque variations and changes in speed reference, and to improve the efficiency of the IFOC system in addressing internal disturbances, including variations in stator and rotor resistance as well as changes in the moment of inertia and even in degraded conditions such as phase fault, 2 advanced regulators will be utilized. The LQR regulator will be employed to regulate speed and torque, while the ADRC regulator will be used to control the reference voltages of the inverters. By adopting this approach, classical PI regulators will be avoided, thereby eliminating the performance limitations typically associated with these regulators.

The main problem addressed is: how can a hybrid LQR-ADRC strategy be designed and validated to replace conventional PI regulators in IFOC systems, ensuring superior robustness, efficiency, and fault tolerance under complex operational scenarios? By resolving this, the study aims to eliminate the performance limitations of PI-based systems while enhancing the reliability of multiphase motor drives in electric vehicles.

Mathematical methods and modeling.

Model of the DSIM. The DSIM is a type of a 3-phase

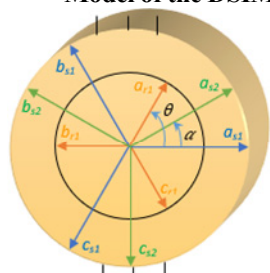


Fig. 1. Spatial distribution of fluxes in the DSIM

induction motors which contain dual stators coupled in star, the phase shift between the first and the second star is and the rotor windings are shorted. Figure 1 shows the distribution of fluxes axis of all windings.

By applying the Park transformation on the 3 windings of the DSIM, the system will be expressed as follows [3]:

$$V_{ds1} = R_{s}i_{ds1} + \frac{d\phi_{ds1}}{dt} - \omega_{s}\phi_{qs1};$$

$$V_{ds2} = R_{s}i_{ds2} + \frac{d\phi_{ds2}}{dt} - \omega_{s}\phi_{qs2};$$

$$V_{qs1} = R_{s}i_{qs1} + \frac{d\phi_{qs1}}{dt} + \omega_{s}\phi_{ds1};$$

$$V_{qs2} = R_{s}i_{qs2} + \frac{d\phi_{qs2}}{dt} + \omega_{s}\phi_{ds2};$$

$$0 = R_{r}i_{dr} + \frac{d\phi_{qs1}}{dt} - (\omega_{s} - \omega)\phi_{ds1};$$

$$0 = R_{r}i_{dr} + \frac{d\phi_{qs1}}{dt} - (\omega_{s} - \omega)\phi_{ds1},$$

$$(1)$$

where R_{s1} , R_{s2} are the resistances of the 1st and 2nd star; R_r is the rotor resistance; ω_s , ω are the angular velocities of the stator and the rotor; $V_{d,q(s,r)1,2}$, $i_{d,q(s,r)1,2}$, $\phi_{d,q(s,r)1,2}$ are the motor's voltages, currents and fluxes.

The stator fluxes expressions are given by:

$$\begin{cases} \phi_{ds1} = L_{s1}i_{ds1} + L_m(i_{ds1} + i_{ds2} + i_{dr}); \\ \phi_{ds2} = L_{s2}i_{ds2} + L_m(i_{ds1} + i_{ds2} + i_{dr}); \\ \phi_{qs1} = L_{s1}i_{qs1} + L_m(i_{qs1} + i_{qs2} + i_{qr}); \\ \phi_{qs2} = L_{s2}i_{qs2} + L_m(i_{qs1} + i_{qs2} + i_{qr}); \\ \phi_{dr} = L_ri_{dr} + L_m(i_{dr} + i_{ds1} + i_{ds2}); \\ \phi_{qr} = L_ri_{qr} + L_m(i_{qr} + i_{qs1} + i_{qs2}), \end{cases}$$
(2)

where L_{s1} , L_{s2} are the inductances of the 1st and 2nd star; L_r is the rotor inductance; L_m is the mutual inductance.

Using stator currents and rotor flux components, the equation for electromagnetic torque is:

$$T_{em} = p \frac{L_m}{L_r + L_m} (\phi_{dr}(i_{sq1} + i_{sq2}) - \phi_{qr}(i_{sd1} + i_{sd2}), \quad (3)$$

where p is the number of pole pairs.

Finally, the rotational equation is given by:

$$\frac{\mathrm{d}}{\mathrm{d}t}\Omega = \frac{1}{J}(T_{em} - T_L - F_r\Omega),\tag{4}$$

where Ω is the mechanical rotor speed; J is the moment of inertia; T_L is the load torque; F_r is the friction coefficient.

Modeling of the IFOC. The principle of fieldoriented control is to realize decoupling between the magnetic flux and the torque. Unlike the direct approach, IFOC calculates the rotor flux angle indirectly by using the shafts' speed information, which eliminates the need to directly measure the rotor flux position.

By aligning the d-axis with the rotor's flux, the orientation is achieved, resulting in the following [23]:

$$\phi_{qr} = 0 \rightarrow \phi_{dr} = \phi_r. \tag{5}$$

The new system can now be governed using the decoupling terms v^*_{ds1} and e_{ds1} as follows:

$$\begin{cases} V_{ds1}^* = v_{ds1}^* + e_{ds1}; & V_{ds2}^* = v_{ds2}^* + e_{ds2}; \\ V_{qs1}^* = v_{qs1}^* + e_{qs1}; & V_{qs2}^* = v_{qs2}^* + e_{qs2}, \end{cases}$$
 (6)

where.

$$\begin{cases} v_{ds1}^* = R_{s1}i_{ds1} + L_{s1} \frac{\mathrm{d}i_{ds1}}{\mathrm{d}t}; & v_{ds2}^* = R_{s1}i_{ds2} + L_{s1} \frac{\mathrm{d}i_{ds2}}{\mathrm{d}t}; \\ v_{qs1}^* = R_{s1}i_{qs1} + L_{s1} \frac{\mathrm{d}i_{qs1}}{\mathrm{d}t}; & v_{qs2}^* = R_{s1}i_{qs2} + L_{s1} \frac{\mathrm{d}i_{qs2}}{\mathrm{d}t}, \end{cases}$$
(7)

and:

$$\begin{cases} e_{ds1} = \omega_s (L_{s1} i_{qs1} + \tau_r \, \phi_r^* \omega_{sl}); \ e_{ds2} = \omega_s (L_{s2} i_{qs2} + \tau_r \, \phi_r^* \omega_{sl}); \\ e_{qs1} = \omega_s (L_{s1} i_{ds1} + \phi_r^*); \ e_{qs2} = \omega_s (L_{s2} i_{ds2} + \phi_r^*), \end{cases}$$
(8)

where $\tau_r = L_r/R_r$ is the rotor time constant; ω_{sl} is the slip frequency. The symbol (*) indicates the references.

The electromagnetic torque is:

$$T_{em} = p \frac{L_m}{L_r + L_m} (\phi_{dr}^* (i_{sq1} + i_{sq2})) = p \frac{L_m}{L_r + L_m} \phi_{dr}^* i_{sq}^*), (9)$$

Equation (9) shows that the electromagnetic torque is similar to that of a separately excited DC motor, which demonstrates that torque and flux are now decoupled.

The synchronous angular speed can be derived as:

$$\omega_s = \omega + \omega_{sl} = p\Omega + \frac{L_m R_r}{L_m + L_r} \frac{i_{qs}^*}{\phi_{dr}^*}, \qquad (10)$$

The complete scheme of the classical PI-based IFOC is presented in Fig. 2.

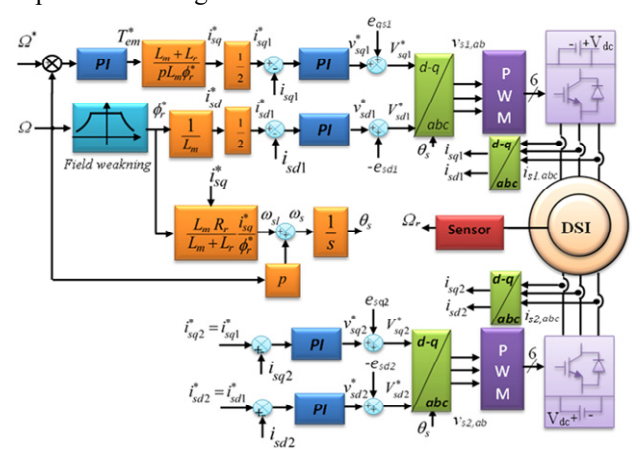


Fig. 2. Schematic of the classical IFOC with PI-based controllers fed by double 2-levels inverters

Design of the LQR. In this section, the LQR will be used as an advanced regulator to regulate speed and torque of the DSIM, in objective to ensure high robustness against phase fault, load torque variation, high precision within the shortest time possible without surpassing the motor capacity.

First, let's take the Laplace transform of (4) considering T_L as perturbation (i.e. $T_L = 0$) as follows:

$$\frac{\Omega}{T_{em}} = \frac{1}{Js + F_r} \,. \tag{11}$$

To define the LQR regulator, (11) must be converted into state-space representation. For this purpose, statespace variables are chosen so that:

$$\begin{cases} x_1 = \Omega; \\ x_2 = \dot{\Omega}, \end{cases}$$
 (12)

Using (4) in (12) will give:

$$\begin{cases} \dot{x_1} = x_2; \\ x_2 = 1/J = (T_{em} - T_L - F_r x_1). \end{cases}$$
 (13)

In matrix form it will be:

$$\begin{bmatrix} \dot{x}_1 \\ \dot{x}_2 \end{bmatrix} = \begin{bmatrix} 0 & 1 \\ -F_r/J & 0 \end{bmatrix} \begin{bmatrix} x_1 \\ x_2 \end{bmatrix} + \begin{bmatrix} 0 \\ 1 \end{bmatrix} T_{em} - \begin{bmatrix} 0 \\ 1/J \end{bmatrix} T_L. \quad (14)$$

The output of this system is

$$y = \begin{bmatrix} 1 & 0 \end{bmatrix} \begin{bmatrix} x_1 \\ x_2 \end{bmatrix}. \tag{15}$$

So, the matrixes A, B, C, D are then defined as:

$$\begin{bmatrix} A \end{bmatrix} = \begin{bmatrix} 0 & 1 \\ -F_r/J & 0 \end{bmatrix}, \begin{bmatrix} B \end{bmatrix} = \begin{bmatrix} 0 \\ 1 \end{bmatrix}, \begin{bmatrix} C \end{bmatrix} = \begin{bmatrix} 1 & 0 \end{bmatrix}, \begin{bmatrix} D \end{bmatrix} = 0.$$

The control law of the LQR regulator is defined as:

$$U_{lqr} = -K_{lqr}[x]. (16)$$

where K_{lqr} is the feedback gain of the regulator: $K_{lqr} = R \cdot B \cdot P \; ,$

$$K_{lar} = R \cdot B \cdot P , \qquad (17)$$

where R is the 1st controller matrix. In our case it has been set as:

$$R = 5 \begin{bmatrix} -50 & 50 \\ 1 & -50 \end{bmatrix};$$

P is the solution of the covariance equation (Ricatti equation) which is defined by:

$$A^{T} \cdot P + P \cdot A - P \cdot B \cdot R^{-1} \cdot B^{T} \cdot P + C^{T} \cdot Q \cdot C = 0.$$
 (18)
 Q is the 2nd controller matrix: $Q = 100$.

The matrixes R and Q represent a degree of freedom to adjust between minimization of the error and the effort of the control, in other way to control precision and response speed. The only inconvenient of this technique is to find a relationship between these 2 matrixes to ensure the desired robustness.

Substituting (16) in (18) will lead to a closed loop system such that:

$$[\dot{x}] = ([A] - [B \cdot K_{lqr}])[x].$$
 (19)

The new state space of the system will be:

$$\begin{cases} \left[\dot{x}\right] = \left|A_{lqr}\right| \left[x\right] \\ y = \left[C\right] \left[x\right] \end{cases}$$
 (20)

The structure of the LQR regulator used in the speed loop is depicted in Fig. 3.

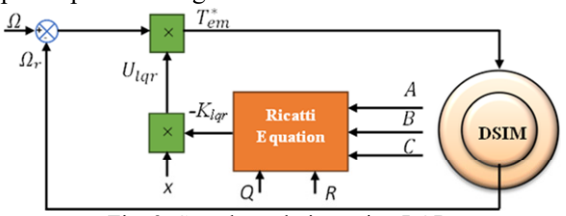


Fig. 3. Speed regulation using LQR

Modeling of the ADRC. ADRC is a robust control strategy designed to estimate and compensate for system uncertainties, external disturbances, and nonlinearities in real-time. By combining an extended state observer to estimate disturbances and a feedback controller to reject them, ADRC enhances the performance and stability of dynamic systems.

The ADRC control was first proposed by Han in 1990s as an alternative to PID controllers [24]. Since then, it has been used in flux or torque regulator in vector control [25-29]. We opted to apply it to the DSIM, in aim to improve torque response, reduce sensitivity to parameter variations, and ensure robust operation under load disturbances. The illustration of the used ADRC is shown on Fig. 4 [30].

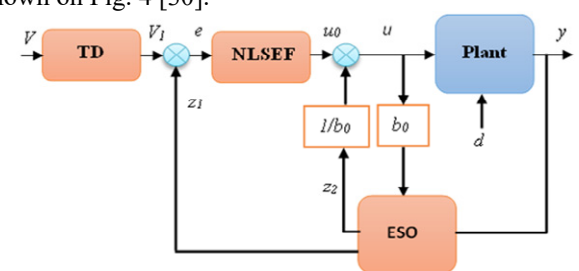


Fig. 4. Schematic description of the ADRC

According to this work, V_1 is the tracking signal for the current reference $i^*_{sdq(1,2)}$, while e is the error signal of the current loop. The term u_0 corresponds to the output of the nonlinear state error feedback, and u is the reference voltage adjusted by the estimated disturbance. Additionally, z_1 and z_2 are the tracking signal for $i_{sdq(1,2)}$ and the estimated disturbance, respectively. The tracking differentiator makes the feed-back error change gradually to solve the contradiction between rapidity and overshoot. And b_0 is a nominal control gain, it's an estimate of the system's input gain, which relates the control input to the system's dynamics.

Thus, 4 ADRC regulators will be used to control the DSIM currents, where their outputs will constitute the input voltages of the inverters. As it can be seen in Fig. 5, based on the current transfer function of the DSIM, the state formulation of current loop can be defined by:

$$\begin{cases} x_1 = i_{s1,2(dq)}(t); \\ x_2 = \dot{i}_{s1,2(dq)}(t). \end{cases}$$
 (21)

$$\begin{cases} x_1 = x_2; \\ \dot{x}_2 = \frac{1}{L_s} (u(t) - R_s x_2). \end{cases}$$
 (22)

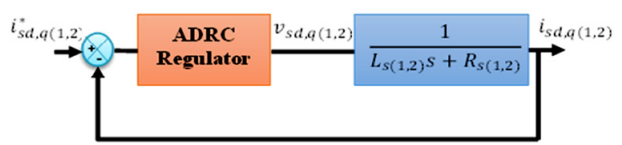


Fig. 5. Currents regulation using ADRC regulator

The current's matrixes of the system will be:

$$\begin{bmatrix} A \end{bmatrix} = \begin{bmatrix} 0 & 1 \\ -R_s/L_s & 0 \end{bmatrix}, \begin{bmatrix} B \end{bmatrix} = \begin{bmatrix} 0 \\ 1/L_s \end{bmatrix}, \begin{bmatrix} C \end{bmatrix} = \begin{bmatrix} 1 & 0 \end{bmatrix}, \begin{bmatrix} D \end{bmatrix} = 0 .$$

The ADRC regulator will be used to compensate the last system, so the new state space will be:

$$\begin{cases} \dot{x}_1 = x_2; \\ \dot{x}_2 = 1/L_s \left(u(t - R_s x_1 + z_2(t)); \right); \\ \dot{x}_3 = z_2(t). \end{cases}$$
 (23)

The control low of the previous system shown in (23) will be:

$$\begin{cases} u_0 = (i_{ref} - z_1) w_c^2 - 2 w_c z_2(t); \\ u(t) = \frac{1}{b_0} (u_0 - z_2(t)), \end{cases}$$
 (24)

where $w_c = 5000$ is the bandwidth of the observer; $b_0 = 5000$.

The extended state space of the previous system shown in (23) will be:

$$[\dot{x}] = \begin{bmatrix} 0 & 1 & 0 \\ R_s/L_s & 0 & 1 \\ 0 & 0 & 0 \end{bmatrix} \begin{bmatrix} x_1 \\ x_2 \\ x_3 \end{bmatrix} + \begin{bmatrix} 0 \\ 1/L_s \\ 0 \end{bmatrix} \frac{(u_0 - z(t))}{b_0} .$$
 (25)

While the output of the extended system is:

$$y(t) = \begin{bmatrix} 1 & 0 & 0 \end{bmatrix} \begin{bmatrix} x_1 \\ x_2 \\ x_3 \end{bmatrix}. \tag{26}$$

And the new matrixes are:

$$\begin{bmatrix} A_{ext} \end{bmatrix} = \begin{bmatrix} 0 & 1 & 0 \\ R_s / L_s & 0 & 1 \\ 0 & 0 & 0 \end{bmatrix}, B_{ext} = \begin{bmatrix} 0 \\ 1 / L_s \\ 0 \end{bmatrix}, C_{ext} = \begin{bmatrix} 1 & 0 & 0 \end{bmatrix}.$$

The scheme of the proposed strategy is shown in Fig. 6. **Simulation results and discussion.** In this section, we will evaluate the performance and robustness of the DSIM fed by dual 3-level neutral point clamped inverters.

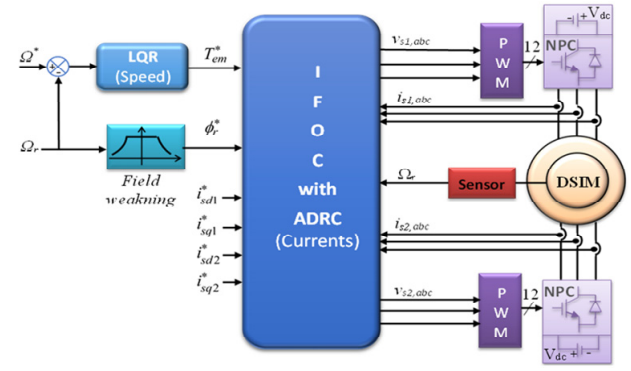


Fig. 6. Global control scheme of the proposed LQR-ADRC speed and current controllers connected to dual neutral point clamped inverters

Using MATLAB/Simulink, 2 control strategies were tested: the traditional IFOC with PI regulators, and an advanced approach combining IFOC with LQR for electromagnetic torque control and ADRC for current regulation. The simulations include tests to assess the system's ability to track speed references, handle external disturbances, and maintain stability under challenging conditions, such as phase faults and internal parameter variations. Additionally, a THD study is conducted to evaluate the system's harmonic suppression capabilities. The motor parameters used in this study are listed in Table 1 [31].

Table 1

DSIM	parameters
------	------------

Parameters	Value
Rated power P, kW	4.5
Line-to-line voltage V_n , V	380
Rated speed Ω_n , rad/s	288.29
Number of pole pairs <i>p</i>	1
Stator inductance L_s , mH	22
Rotor inductance L_r , mH	6
Mutual inductance L_m , H	0.4092
Stator resistance R_s , Ω	3.72
Rotor resistance R_r , Ω	2.12
Moment of inertia <i>J</i> , kg⋅m ²	0.00625
Friction coefficient F_r , m/(rad·s ⁻¹)	0.001

Test 1. Evaluation of reference tracking at variable speed. Figures 7, 8 illustrate the speed and torque responses of the DSIM controlled by the classical IFOC $(\varOmega_{PI},~T_{\mathit{em(PI)}})$ and the IFOC-based LQR-ADRC approach $(\Omega_{LQR-ADRC}, T_{em(LQR-ADRC)})$ under varying speed references. Initially, the motor operates with a speed reference of 100 rad/s, 300 rad/s, followed by a reduction to 200 rad/s, and finally reverses its rotation to -100 rad/s. These figures demonstrate the system's ability to track both positive and negative speed references with minimal delay, indicating robust and efficient speed control. At start, it's shown that the torque peak is the same for both techniques (≈56 N·m). After that, the variation in the speed reference causes transient scenarios in torque for both techniques. However, the LQR-ADRC demonstrates a faster stabilization time, with the presence of additional peaks ≈20 N·m, while the IFOC-PI shows a longer stabilization time with less peaks and torque ripples.

Figures 9, 10 show the direct and quadrature components of the flux (ϕ_{dr}, ϕ_{qr}) of the DSIM. It can be seen that the orientations are successfully achieved. However, the LQR-ADRC shows a stable decoupling

despite some ripples at speed reference changing, while the classical IFOC shows a longer and stable response.

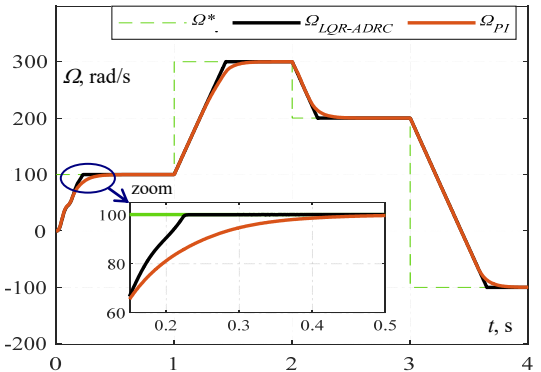


Fig. 7. Speed of the DSIM under variable speed reference

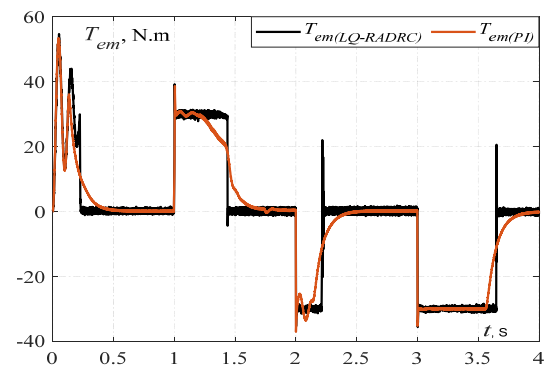


Fig. 8. Torque of the DSIM under variable speed reference

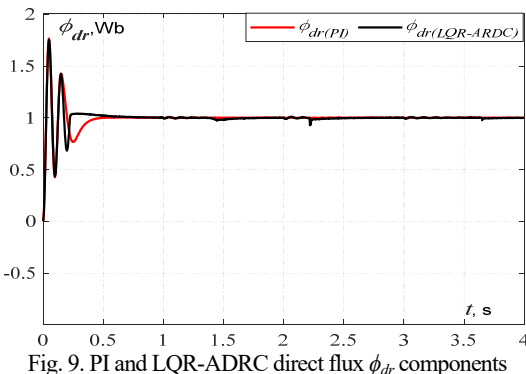


Fig. 9. PI and LQR-ADRC direct flux ϕ_{dr} components

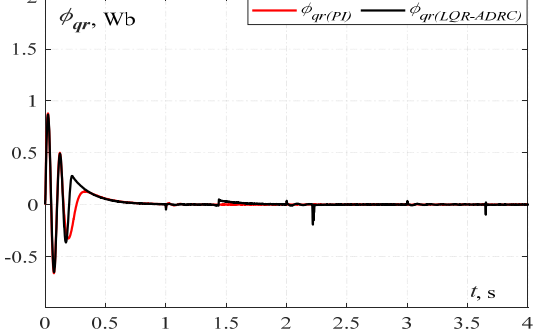


Fig. 10. PI and LQR-ADRC direct flux ϕ_{ar} components

Table 2 compares the 2 approaches in terms of stabilization time, overshoot, and precision. One can observe that the new approach (LQR-ADRC-based IFOC) surpasses the classical PI-IFOC in both precision and stabilization time, while maintaining 0 % overshoot. This demonstrates high robustness in tracking reference speeds.

Table 2 PI-based vs LQR-ADRC-based IFOC performance analysis

Criteria	Speed range,	Classical	LQR-ADRC
Citteria	rad/s	IFOC	based IFOC
	0→100	0.5	0.24
Stabilizing t, s	100→300	0.7	0.4
	300→200	0.45	0.25
	200→-100	1	0.65
Overshoot, %		0	0
Precision, %		99	99.98

Test 2. Performance against external disturbance. Here, the motor starts with 250 rad/s step reference. Then, a sequence of multiple load-torques are applied as the following: T_L =10 N·m at t = 1 s, T_L =20 N·m at t = 2 s, and T_L = -20 N·m at t = 3 s. From Fig. 11, the LQR-ADRC instantly rejects disturbances, while the PI-based IFOC has significantly longer rejection time. Figure 12 shows the LQR-ADRC's electromagnetic torque response is faster than classical IFOC.

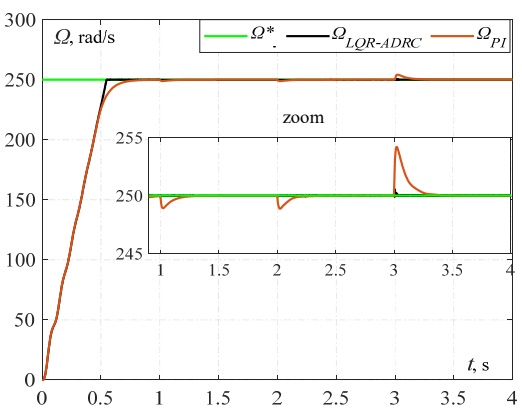


Fig. 11. Speed of the DSIM under load variation

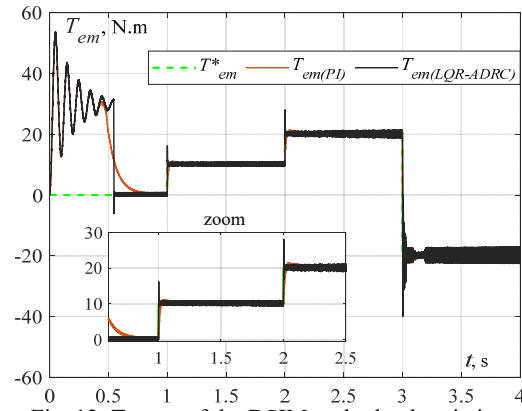


Fig. 12. Torque of the DSIM under load variation

Test 3. *THD comparison*. Figures 13, 14 show the currents of the 1st star of the DSMI. The waves form is regular in LQR-ADRC compared to classic IFOC.

Figures 15, 16 reveal a THD of 13.72 % with PI-based IFOC, compared to 5.18 % with LQR-ADRC-based IFOC. This demonstrates that the proposed approach is more effective at minimizing harmonics.

Following the 3 tests and the analysis of their results, which demonstrate that the LQR-ADRC outperforms the IFOC in most scenarios, further tests will be conducted to evaluate the robustness of this new approach. This time, the focus will be on phase faults and internal disturbances, such as variations in stator and rotor resistances and changes in the moment of inertia.

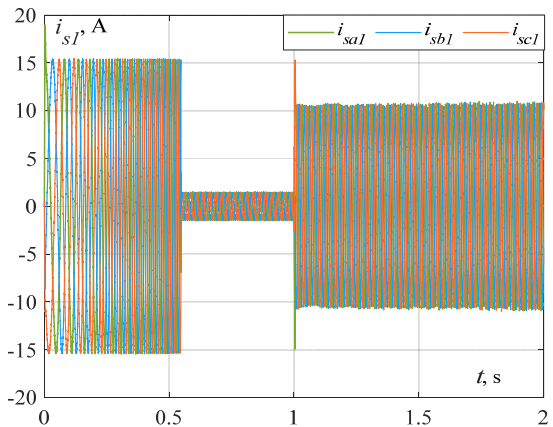


Fig. 13. Currents of the 1st star controlled by LQR-ADRC

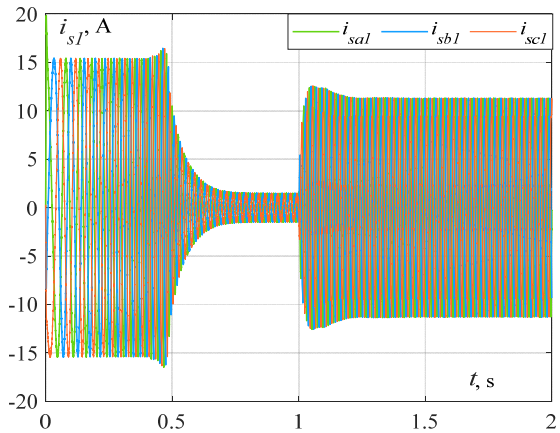
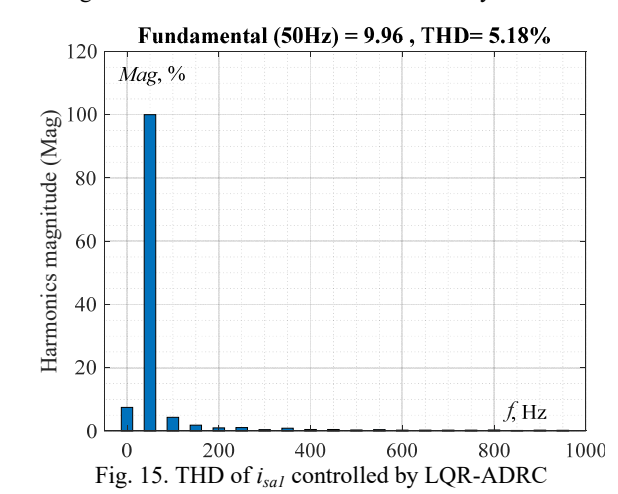
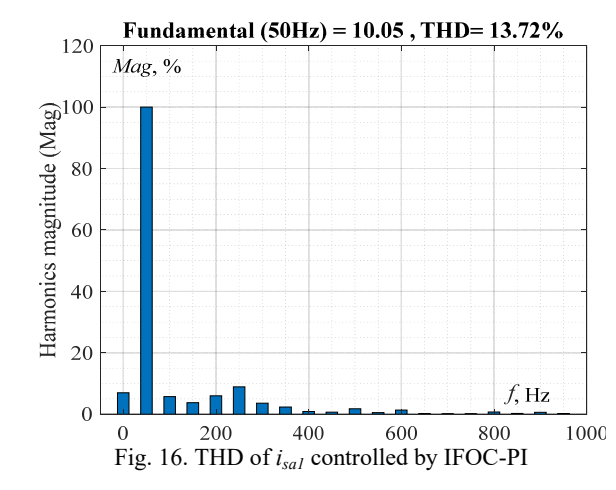


Fig. 14. Currents of the 1st star controlled by IFOC-PI





Test 4. Phase fault examination. In this test, the motor will start with a load torque T_L =20 N·m. It will then encounter several changes of reference speed and at t = 4 s, a phase fault will occur in the phase A of the 1st star. Figure 17 represents the speed response of the DSIM, while Fig. 18 shows the electromagnetic torque. Despite these severe conditions, the system continues to operate effectively without losing service continuity or compromising its stability. It demonstrates remarkable resilience, maintaining its robustness and consistent performance even under challenging circumstances.

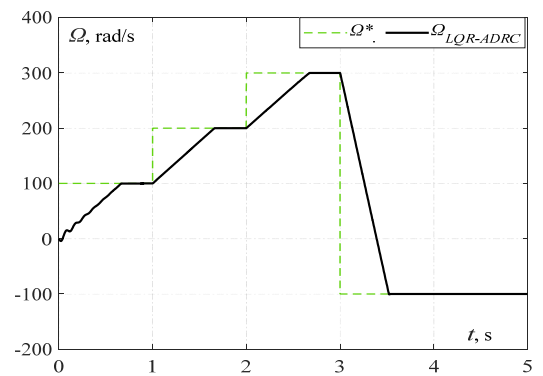


Fig. 17. Speed of the DSIM under variable speed, load torque and phase fault

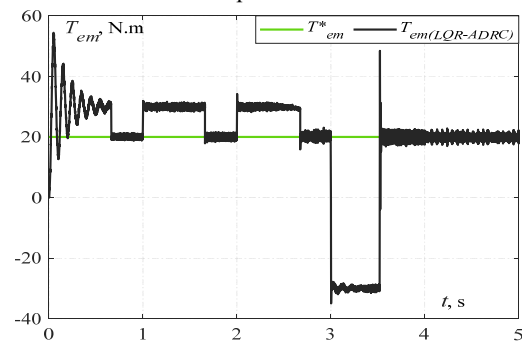
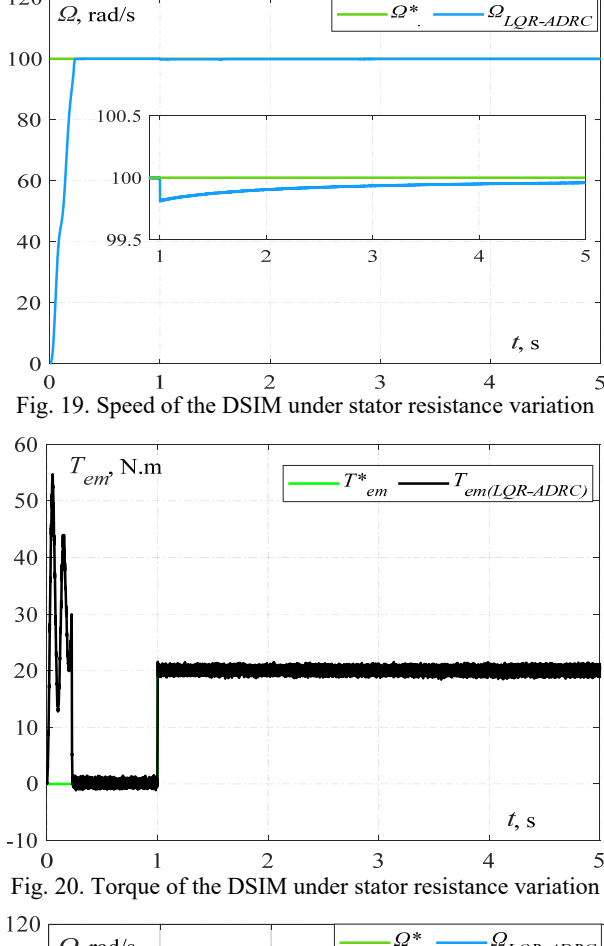


Fig. 18. Torque of the DSIM under variable speed, load torque and phase fault

Test 5. Robustness against internal parameters changing. The impact of parameters variation is a critical factor in the performance of the control system. These changes can affect the dynamics of the motor such as the rotor flux linkage, torque production, and current regulation.

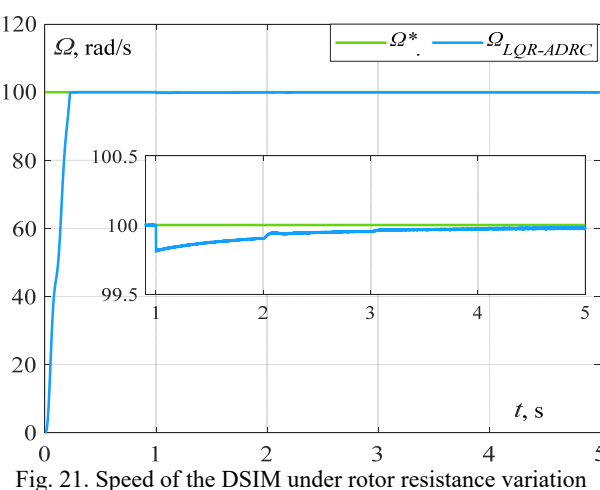
At this scenario, tests will be conducted against internal parameters such as R_s , R_r and J to evaluate the system's robustness. First the system will start with normal parameters. In all scenarios, the motor will operate at a reference speed of 100 rad/s, with a resistant torque of 20 N·m applied at t=1 s. The parameter will then be multiplied by 1.5 at t=2 s, by 2 at t=3 s, and by 2.5 at t=4 s, resulting in a 250 % increase.

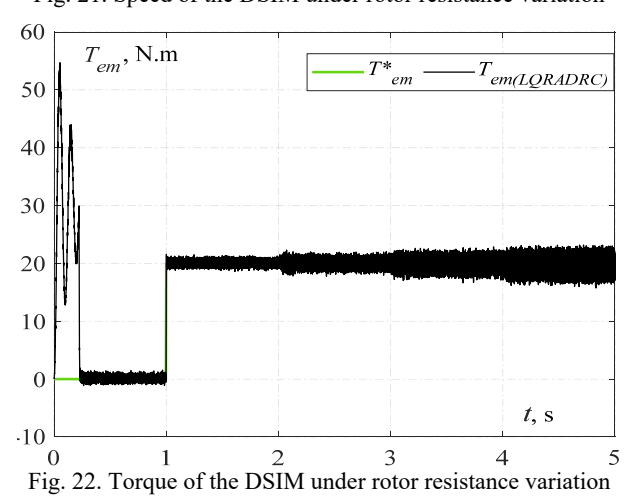
Figures 19–24 highlight that rotor resistance variations influence the transient dynamics without compromising the stability or balance of the stator currents thanks to the proposed controllers. Despite these variations, the control system maintains robust performance, as evidenced by the actual speed consistently aligning with the reference speed without noticeable deviations or delays. This indicates that the control strategy effectively compensates for the effects of resistance changes, ensuring stability and precision.



120

 Ω , rad/s





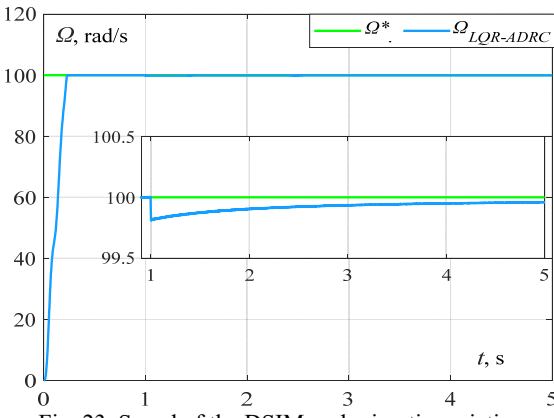


Fig. 23. Speed of the DSIM under inertia variation

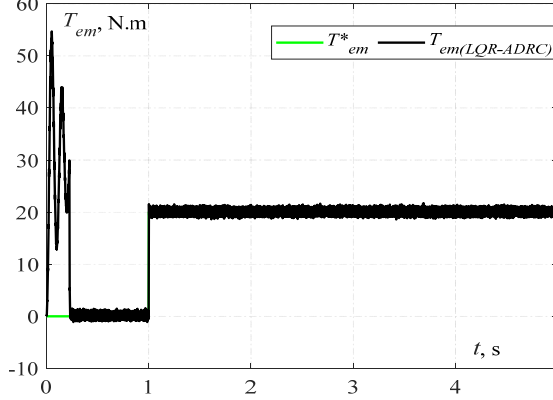


Fig. 24. Torque of the DSIM under moment of inertia variation

Conclusions. In this work, LQR regulator has been employed to regulate the speed of a DSIM, while ADRC regulators have been used to control the currents.

Several tests have been conducted and the results revealed that the LQR-ADRC-based IFOC control strategy significantly outperforms the classical PI-IFOC in terms of speed control, stabilization time, and robustness. The LQR-ADRC exhibits faster stabilization times across various speed transitions, with minimal current ripples and no overshoot, maintaining a high precision. It also shows superior performance under external disturbances, such as load torque variations, where it maintains speed response stability without significant deviations. In phase fault scenarios and internal parameter variations, the LQR-ADRC proves highly robust, maintaining precise speed control and stability even under degraded conditions. In conclusion, the LQR-ADRC-based IFOC emerges as a more efficient and robust control strategy, particularly in dynamic and challenging operational conditions.

Conflict of interest. The authors declare that they have no conflicts of interest.

REFERENCES

- 1. Volkov V.A., Antonov N.L. Refined calculation of energy modes of a frequency-regulated induction motor. Electrical Engineering & Electromechanics, 2024, no. https://doi.org/10.20998/2074-272X.2024.5.01
- 2. Chaib Ras A., Bouzerara R., Bouzeria H. An adaptive controller for power quality control in high speed railway with electric locomotives with asynchronous traction motors. Electrical Engineering & Electromechanics, 2024, no. https://doi.org/10.20998/2074-272X.2024.2.04.
- 3. Salem A., Narimani M. A Review on Multiphase Drives for Automotive Traction Applications. IEEE Transactions on Transportation Electrification, 2019, vol. 5, no. 4, pp. 1329-1348. doi: https://doi.org/10.1109/TTE.2019.2956355.

- **4.** Rinkeviciene R., Savickiene Z., Uznys D., Pitrenas A., Slepikas A. Scalar control of six-phase induction motor. *2017 Open Conference of Electrical, Electronic and Information Sciences (EStream)*, 2017, pp. 1-6. doi: https://doi.org/10.1109/eStream.2017.7950304.
- 5. Mossa M.A., Khouidmi H., Ma'arif A. Robust Flux and Speed State Observer Design for Sensorless Control of a Double Star Induction Motor. *Journal of Robotics and Control (JRC)*, 2022, vol. 3, no. 4, pp. 464-475. doi: https://doi.org/10.18196/jrc.v3i4.15667.
- 6. Chatterjee S., Chatterjee S. A novel speed sensor-less vector control of Dual Stator Induction machine with space vector based advanced 9-zone hybrid PWM for grid connected wind energy generation system. *Electric Power Systems Research*, 2018, vol. 163, pp. 174-195. doi: https://doi.org/10.1016/j.epsr.2018.02.021.
- 7. Pandit J.K., Aware M.V., Nemade R., Tatte Y. Simplified Implementation of Synthetic Vectors for DTC of Asymmetric Six-Phase Induction Motor Drives. *IEEE Transactions on Industry Applications*, 2018, vol. 54, no. 3, pp. 2306-2318. doi: https://doi.org/10.1109/TIA.2018.2789858.
- 8. Guedida S., Tabbache B., Nounou K., Benbouzid M. Direct torque control scheme for less harmonic currents and torque ripples for dual star induction motor. *Revue Roumaine des Sciences Techniques Série Électrotechnique et Énergétique*, 2023, vol. 68, no. 4, pp. 331-338. doi: https://doi.org/10.59277/RRST-EE.2023.4.2.
- **9.** Ayaz Khoshhava M., Abootorabi Zarchi H., Markadeh G. Sensorless Speed and Flux Control of Dual Stator Winding Induction Motors Based on Super Twisting Sliding Mode Control. *IEEE Transactions on Energy Conversion*, 2021, vol. 36, no. 4, pp. 3231-3240. doi: https://doi.org/10.1109/TEC.2021.3077829.
- 10. Abdallah A., Bouchetta A., Boughazi O., Baghdadi A., Bousserhane L.K. Double star induction machine using nonlinear integral backstepping control. *International Journal of Power Electronics and Drive Systems (IJPEDS)*, 2019, vol. 10, no. 1, pp. 27-40. doi: https://doi.org/10.11591/ijpeds.v10.i1.pp27-40.
- 11. Nemouchi B., Rezgui S.E., Benalla H., Nebti K. Fractional-based iterative learning-optimal model predictive control of speed induction motor regulation for electric vehicles application. Electrical Engineering & Electromechanics, 2024, no. 5, pp. 14-19. doi: https://doi.org/10.20998/2074-272X.2024.5.02.
- 12. Babes B., Hamouda N., Kahla S., Amar H., Ghoneim S.S.M. Fuzzy model based multivariable predictive control design for rapid and efficient speed-sensorless maximum power extraction of renewable wind generators. *Electrical Engineering & Electromechanics*, 2022, no. 3, pp. 51-62. doi: https://doi.org/10.20998/2074-272X.2022.3.08.
- 13. Gonzalez O., Ayala M., Romero C., Delorme L., Rodas J., Gregor R., Gonzalez-Prieto I., Duran M.J. Model Predictive Current Control of Six-Phase Induction Motor Drives Using Virtual Vectors and Space Vector Modulation. *IEEE Transactions on Power Electronics*, 2022, vol. 37, no. 7, pp. 7617-7628. doi: https://doi.org/10.1109/TPEL.2022.3141405.
- 14. Hadji C., Khodja D., Chakroune S. Robust Adaptive Control of Dual Star Asynchronous Machine by Reference Model Based on Landau Stability Theorem. Advances in Modelling and Analysis C, 2019, vol. 74, no. 2-4, pp. 56-62. doi: https://doi.org/10.18280/ama c.742-403.
- 15. Youb L., Belkacem S., Naceri F., Cernat M., Pesquer L.G. Design of an Adaptive Fuzzy Control System for Dual Star Induction Motor Drives. *Advances in Electrical and Computer Engineering*, 2018, vol. 18, no. 3, pp. 37-44. doi: https://doi.org/10.4316/AECE.2018.03006.
- 16. Lazreg M.H., Bentaallah. A. Sensorless Speed Control of Double Star Induction Machine With Five Level DTC Exploiting Neural Network and Extended Kalman Filter. *Iranian Journal of Electrical and Electronic Engineering*, 2019, vol. 15, no. 1, pp. 142-150. doi: http://doi.org/10.22068/IJEEE.15.1.142.
- 17. Bentouhami L., Abdessemed R., Kessal A., Merabet E. Control Neuro-Fuzzy of a Dual Star Induction Machine (DSIM) supplied by Five-Level Inverter. *Journal of Power Technologies*, 2018, vol. 98, no. 1, pp. 70-79.
- 18. Guermit H., Kouzi K., Bessedik S.A. Novel design of an optimized synergetic control for dual stator induction motor. COMPEL The International Journal for Computation and Mathematics in Electrical

- and Electronic Engineering, 2019, vol. 38, no. 6, pp. 1828-1845. doi: https://doi.org/10.1108/COMPEL-01-2019-0042.
- 19. Ebrahim O.S., Salem M.F., Jain P.K., Badr M.A. Application of linear quadratic regulator theory to the stator field-oriented control of induction motors. *IET Electric Power Applications*, 2010, vol. 4, no. 8, pp. 637-646. doi: https://doi.org/10.1049/iet-epa.2009.0164.
- 20. Swargiary M., Dey J., Saha T.K. Optimal speed control of induction motor based on Linear Quadratic Regulator theory. 2015 Annual IEEE India Conference (INDICON), 2015, pp. 1-6. doi: https://doi.org/10.1109/INDICON.2015.7443806.
- 21. Janous S., Talla J., Smidl V., Peroutka Z. Constrained LQR Control of Dual Induction Motor Single Inverter Drive. *IEEE Transactions on Industrial Electronics*, 2021, vol. 68, no. 7, pp. 5548-5558. doi: https://doi.org/10.1109/TIE.2020.2994885.
- 22. Oumar A., Ahmed Y., Cherkaoui M. Operating of DSIM without current and speed sensors controlled by ADRC control. *Mathematical Problems in Engineering*, 2022, pp. 1-8. doi: https://doi.org/10.1155/2022/9033780.
- 23. Khemis A., Boutabba T., Drid S. Model reference adaptive system speed estimator based on type-1 and type-2 fuzzy logic sensorless control of electrical vehicle with electrical differential. *Electrical Engineering & Electromechanics*, 2023, no. 4, pp. 19-25. doi: https://doi.org/10.20998/2074-272X.2023.4.03.
- 24. Huang Y., Xue W., Zhiqiang G., Sira-Ramirez H., Wu D., Sun M. Active disturbance rejection control: Methodology, practice and analysis. *Proceedings of the 33rd Chinese Control Conference*, 2014, pp. 1-5. doi: https://doi.org/10.1109/ChiCC.2014.6896585.
- 25. Kelam S. Nonlinear robust ADRC control of induction machine. *Przegląd Elektrotechniczny*, 2023, no. 3, pp. 211-217. doi: https://doi.org/10.15199/48.2023.03.37.
- 26. Chalawane H., Essadki A., Nasser T., Arbaoui M. A new robust control based on active disturbance rejection controller for speed sensorless induction motor. 2017 International Conference on Electrical and Information Technologies (ICEIT), 2017, pp. 1-6. doi: https://doi.org/10.1109/EITech.2017.8255226.
- 27. Oumar A., Chakib R., Cherkaoui M. Current Sensor Fault-Tolerant Control of DSIM Controlled by ADRC. *Mathematical Problems in Engineering*, 2020, art. no. 6568297. doi: https://doi.org/10.1155/2020/6568297.
- 28. Hezzi A., Ben Elghali S., Bensalem Y., Zhou Z., Benbouzid M., Abdelkrim M.N. ADRC-Based Robust and Resilient Control of a 5-Phase PMSM Driven Electric Vehicle. *Machines*, 2020, vol. 8, no. 2, art. no. 17. doi: https://doi.org/10.3390/machines8020017.
- 29. Vinh V.Q., Phat T.C., Giang N.H. An Adaptive Active Disturbance Rejection Controller (ADRC) for Induction Motor Drives. *International Journal of Electrical and Electronics Engineering*, 2024, vol. 11, no. 12, pp. 295-301. doi: https://doi.org/10.14445/23488379/IJEEE-V11II2P127.
- **30.** Han J. From PID to Active Disturbance Rejection Control. *IEEE Transactions on Industrial Electronics*, 2009, vol. 56, no. 3, pp. 900-906. doi: https://doi.org/10.1109/TIE.2008.2011621.
- 31. Darsouni Z., Rezgui S.E., Benalla H., Rebahi F., Boumendjel M.A.M. Ensuring service continuity in electric vehicles with vector control and linear quadratic regulator for dual star induction motors. *Electrical Engineering & Electromechanics*, 2025, no. 2, pp. 24-30. doi: https://doi.org/10.20998/2074-272X.2025.2.04.

Received 13.03.2025 Accepted 18.05.2025 Published 02.11.2025

- S.E. Rezgui¹, Doctor of Technical Sciences, Associate Professor, Z. Darsouni¹, PhD Student,
- H. Benalla¹, Full Professor,
- ¹ Laboratory of Electrical Engineering of Constantine (LEC), Technology Sciences Faculty,
- University Constantine 1 Freres Mentouri, Algeria,
- e-mail: rezgui.salaheddine@umc.edu.dz (Corresponding Author); darsounizakaria@gmail.com; benalla.hocine@umc.edu.dz

How to cite this article:

Rezgui S.E., Darsouni Z., Benalla H. Nonlinear vector control of multiphase induction motor using linear quadratic regulator and active disturbances rejection control under disturbances and parameter variations. *Electrical Engineering & Electromechanics*, 2025, no. 6, pp. 75-83. doi: https://doi.org/10.20998/2074-272X.2025.6.10

S.S. Sabry, O.Sh. Al-Yozbaky

Enhanced siting and sizing of distributed generation in radial distribution networks under load demand uncertainty using a hybrid metaheuristic framework

Introduction. Constant changes in electrical system loads lead to increased power losses and voltage drops, requiring effective strategies to improve grid performance amid changing power demands. Problem. Many studies assume constant loads when determining optimal locations for distributed generation (DG) units, when in reality, loads change throughout the day. These changes affect network performance and require efficient solutions that adapt to changes in loads demand to maintain system efficiency and stability. Goal. This research aims to optimize the locations and sizes of DG units to reduce power losses and optimize voltage profile, taking into account changes in loads hourly over a 24-hour period. Methodology. The study analyzes 24 hourly scenarios using 2 optimization techniques: the conventional particle swarm optimization (PSO) algorithm and the hybrid-dynamic PSO algorithm. A multi-objective function is adopted to reduce power losses and improve voltage profile at the same time. Results. The modified IEEE 33 bus system was used to verify the effectiveness of the proposed method. The hybrid-dynamic PSO algorithm has shown superior performance in reducing active and reactive losses compared to the traditional algorithm. It also contributed to a significant improvement in the voltage profile, demonstrating its high efficiency in dealing with changes in loads demand during time. Scientific novelty of this work lies in the integration of hourly load changes into the process of allocating DG units and using a hybrid-dynamic PSO algorithm that combines the benefits of PSO traditional and adaptation mechanisms, leading to realistic and more efficient improvement. Practical value. This methodology enhances the performance of the smart grid by reducing power losses and voltage deviation under daily load, ultimately reducing operational costs and improving grid reliability. References 28, tables 4, figures 10.

Key words. distributed generation, renewable energy, optimization algorithms, voltage stability, power losses minimization, uncertain loads demand.

Вступ. Постійні зміни навантаження електросистеми призводять до збільшення втрат потужності та падіння напруги, що вимагає розробки ефективних стратегій для підвищення продуктивності мережі в умовах змінного попиту на електроенергію. Проблема. У багатьох дослідженнях щодо оптимального розташування установок розподіленої генерації (DG) передбачається наявність статичних навантажень, хоча насправді навантаження змінюються впродовж дня. Ці зміни впливають на продуктивність мережі та потребують динамічних рішень, що адаптуються до змін навантаження у часі для підтримки ефективності та стабільності системи. Мета. Дане дослідження спрямоване на оптимізацію розташування та розмірів DG установок для зниження втрат потужності та оптимізації профілю напруги з урахуванням щогодинних змін навантаження протягом 24 годин. Методологія. У дослідженні аналізуються 24-годинні сценарії з використанням двох методів оптимізації: традиційного алгоритму оптимізації роєм часток (PSO) та гібридно-динамічного алгоритму PSO. Для зниження втрат потужності та одночасного покращення профілю напруги використовується багатоцільова функція. Результати. Для перевірки ефективності запропонованого методу використовувалася система шин IEEE 33. Гібридно-динамічний алгоритм PSO продемонстрував високу ефективність зниження активних і реактивних втрат порівняно з традиційним алгоритмом. Це також сприяло значному покращенню профілю напруги, продемонструвавши його високу ефективність за умов зміни навантаження у часі. Наукова новизна роботи полягає в інтеграції погодинних змін навантаження у процес розподілу DG установок та використання гібридно-динамічного алгоритму PSO, що поєднує переваги традиційних механізмів PSO та механізмів адаптації, що призводить до реалістичного та ефективнішого покращення. Практична цінність. Дана методологія підвищує продуктивність інтелектуальної мережі за рахунок зниження втрат електроенергії та відхилення напруги при добовому навантаженні, що знижує експлуатаційні витрати та підвищує надійність мережі. Бібл. 28, табл. 4, рис. 10.

Ключові слова. розподілена генерація, відновлювальна енергетика, алгоритми оптимізації, стабільність напруги, мінімізація втрат потужності, невизначені навантаження.

Introduction. Electrical energy is one of the pillars of

modern civilization and one of the basic requirements in the life of modern man. Transmission and distribution networks are one of the most prominent components of the electrical system. One of the main challenges facing the performance of distribution networks is the change in load demand, which leads to differences in active and reactive losses, as well as voltage drops and decreases in network stability [1, 2]. Optimal planning of distributed generation (DG) is one of the most important methods for reducing electrical losses [3] and improving voltage limits in distribution network [4]. However, the installation and operation of these generators require significant investment and operational costs, which calls for the use of standard optimization algorithms in order to ensure that the integration of DG with distribution networks is optimal [5].

DG is called by various terms such as local generation, integrated generation, scattered generation, or decentralized generation, and it generally refers to electrical energy sources (whether renewable or non-renewable) that are connected to the distribution network or directly to the consumption site [6, 7]. The concept of DG includes a variety of technologies, as shown in Fig. 1 [8], that produce energy at sites close to consumers. These systems can serve individual buildings [9] or be used in Microgrids [10]. They can also be operated with on-grid mode [11].

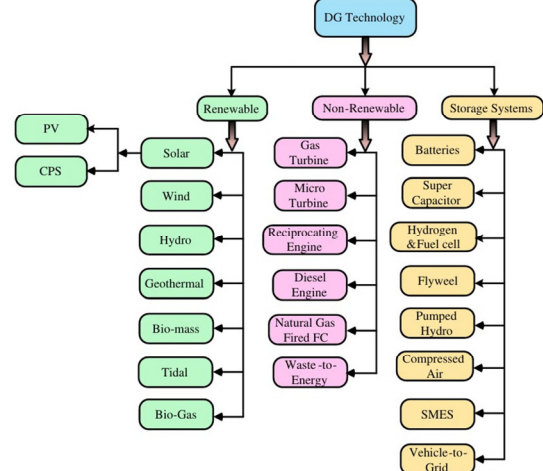


Fig. 1. Shows most of the DG techniques [8]

Methods for searching for the optimal solution to the problem of locating and scaling DG vary depending on the nature of the system studied, the complexity of the objectives and the constraints imposed, and these methods are generally divided into 3 main categories: analytical, numerical, and metaheuristic algorithms. Analytical methods [12] rely on explicit mathematical equations and

© S.S. Sabry, O.Sh. Al-Yozbaky

are often used in simplified systems with few buses and limited targets, but become impractical with the complexity of the network. Numerical methods [13], such as the Newton-Raphson method or linear programming, provide high accuracy but require accurate mathematical models and may suffer from falling into local solutions, and do not fit easily to multi-objectives or nonlinear variables. In contrast, intelligent optimization algorithms [14-20] have been more common in recent years, due to their ability to deal with complex models, multiple targets, and the nature of nonlinear or inaccurately defined constraints. Some studies have also tended to combine more than one algorithm for improved performance, or to use hybrid algorithms that combine artificial intelligence with traditional optimization. The literature shows that the choice of an optimization algorithm depends on several factors such as the number of DG units, load type, network model, and objective function, however, the general trend is leaning towards intelligent multi-objective optimization algorithms due to their flexibility and effectiveness in arriving at practical and workable solutions.

A review of the literature referred to above shows that most researchers have addressed the allocation of DG units based on fixed loads. Some evaluated the allocation of these units under time-varying loads, but the locations and sizes of DG units were often calculated at the average load only. Moreover, some researchers looked at multiple load models, but each allocation was made separately for each given load, rather than a standardized allocation that took into account loads over the time period (24 h) in our current study. Some studies have also shown allocation of DG units under loads and probabilistic generation. However, the majority of these studies relied on constant generation based on (average generation) from renewable energy sources, without taking into account the temporal change in production.

In order to simulate the full picture of the actual operating reality of the system, it is necessary to make an allocation of DG units for each time period separately, according to load variables. Hence, the optimal allocation is chosen from among all time assignments based on the desired objectives, such as maximizing system efficiency, reducing losses or optimizing voltage profile.

The main contributions of this research are the application of a modified hybrid metaheuristic optimization algorithm to determine the optimal allocation of DG units across 24 different scenarios, and the problem model was built based on multiple scenarios, so that each scenario represents specific load and generation conditions during a specific hour of the day. The methodology was implemented within a 24-hour time horizon, taking into account the regenerative generation pattern of solar generating units with the use of storage batteries to make the generation constant from the system. The hybriddynamic metaheuristic algorithm was also employed in the context of allocating the locations and sizes of DG, and their performance was evaluated in this context. Optimal allocation of DG units was achieved throughout the day, with the aim of reducing the multi-objective function (MOF). The study included the analysis and discussion of active power losses, reactive power losses, as well as voltage profiles at different buses. Total power losses were also calculated and discussed over the full day. Finally, the results of the study were compared with the results of another optimization algorithm, such as particle swarm optimization (PSO), in terms of optimal allocation of single and multiple DG units.

The **goal** of the paper is to optimize the locations and sizes of DG units to reduce power losses and optimize voltage profile, taking into account changes in loads hourly over a 24-hour period.

The formulation of the problem involves the use of backward forward sweep power flow analysis and the results associated with optimal location and size allocation of DG using an optimization algorithm approach, taking into account a set of constraints. Allocation means optimized for DG to introduce these generators into the system at an optimal point in terms of location and size. Figure 2 shows the diagram of the system. The first stage involves entering system data such as a 24-hour variable load. In the second phase, the optimal allocation of DG units is determined according to changes in load demand based on the minimum value of the objective function.

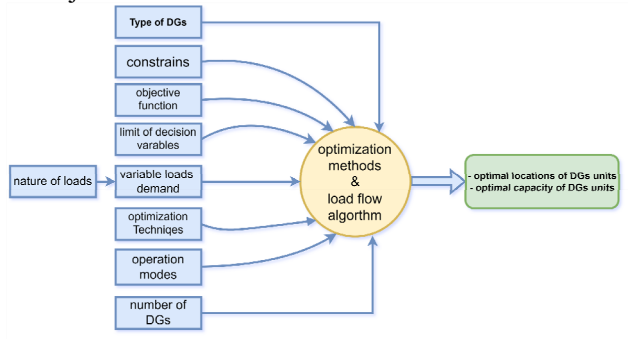


Fig. 2. Factors influencing the optimal location and sizing of DG

Load flow analysis. Power flow analysis technology is used for planning, operation, optimization, and monitoring of electrical power systems, as it contributes significantly to ensuring system stability, reliability and economic efficiency.

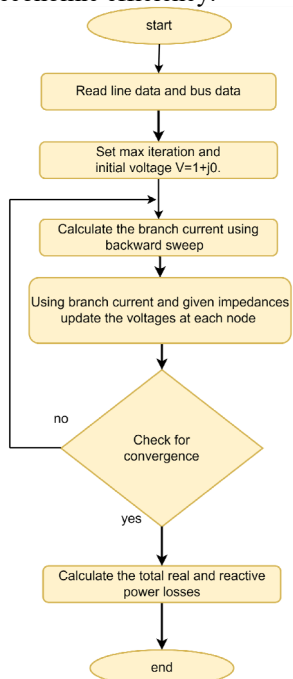


Fig. 3. Flow chart of backward forward sweep algorithm

However, traditional methods used in power flow analysis, such as the Newton-Raphson method and the Gauss-Seidel method, may not be suitable distribution networks and may not guarantee access to the solution (no convergence) for following reasons [21]:

- 1. Radioactive nature or weak entanglement in the network structure.
- 2. High resistance-to-reactance ratio.
- 3. Imbalance of the system.
- 4. The presence of DG sources.

The backward forward sweep algorithm [22] (Fig. 3) is an effective method used in power flow analysis for radial distribution networks, as it

is characterized by its ability to provide accurate results with speed of convergence and reduce the number of iterations required to reach the solution. For these reasons, this algorithm is the preferred choice in the analysis of distribution systems.

Steps of implementation of backward forward sweep algorithm.

1) Initializing. Set the current at each node to zero:

 $i_k = 0, \tag{1}$

where i_k is the complex current at node k.

Set the voltage of all nodes to 1 p.u.:

$$v_k = 1, (2)$$

where v_k is the complex voltage at node k.

2) Calculating the nodal current by using the complex power equation:

$$i_k = s_k^* / v_k^* \,, \tag{3}$$

where s_k is the complex power at node k [p.u.]; v_k is the voltage at node k [p.u.]; i_k is the calculated current at node k [p.u.]; symbol «*» denotes complex conjugate.

3) Backward sweep – branch current calculation. Calculate branch current flowing from node *k* to node *k*–1:

$$i_{k,k-1} = i_k + \sum i_{m,k} , \qquad (4)$$

where $i_{k, k-1}$ is the current in the branch from node k to k-1; $\Sigma i_{m,k}$ is the sum of branch currents from all downstream nodes connected to node k.

4) Perform forward sweep to update the node voltage according to the voltage drop equation across the lines:

$$v_{k+1} = v_k - z_{k,k+1} \cdot i_{k,k+1}, \tag{5}$$

where v_k is the voltage at node k; v_{k+1} is the voltage at the downstream node k+1; $z_{k,k+1}$ is the complex impedance of the line between nodes k and k+1; $I_{k,k+1}$ is the current in the branch between nodes k and k+1.

5) Check the stopping criterion, where the iterative process continues until reaching the acceptable variance between the calculated values in successive iterations:

$$\max \left| v_k^{n+1} - v_k^n \right| \le \varepsilon , \qquad (6)$$

where ε is the specified tolerance for convergence (typically 10^{-4} .)

Objective function. The main objective of the goal function is to reduce the multi-objective index to the lowest possible value.

MOF index is a combination of 3 main indicators – the Active Power loss Index (API), the Reactive Power loss Index (RPI) and the Voltage Deviation index (VD) [23]. Optimal allocation of DG units is achieved by minimizing the MOF value. This process is based on (7), where the coefficients $w_1 - w_3$ refer to the weights of API, RPI and VD:

$$MOF = w_1 \cdot API + w_2 \cdot RPI + w_3 \cdot VD$$
; (7)

$$\sum_{i=1}^{3} w_i = 1; (8)$$

where w_1 is the weight of API objective (w_1 =0.5); w_2 is the weight of RPI objective (w_2 =0.25); w_3 is the weight of VD objective (w_3 =0.25).

The relative weights of the 3 objectives (reducing real losses, reducing reactive losses and reducing voltage deviation) were determined using the analytic hierarchy process developed by T.L. Saaty, which is one of the most common multi-standard decision-making methods [24] is

common and accurate. This method is based on the principle of conducting even comparisons between goals using a numerical preferential scale that reflects the degree of relative importance between each pair, so that the judgments are translated into a comparison matrix used to extract the final weights through mathematical treatment based on normalization and analysis of eigenvalues. In this context, a logical assessment was adopted that the first goal (API) is twice as important as the other 2 goals (RPI and VD), while RPI and VD were considered equally important. According to this assessment, the comparison matrix is built to reflect these relationships (PLI > RPI = VD), with a preference ratio of (2:1). Based on these provisions, the final weights were derived to be approximately 0.5 for API and 0.25 for each of the RPI and VD. This distribution reflects the level of technical impact expected for each objective on grid performance and is consistent with the logic of improving the operational efficiency of electrical distribution systems, where priority is given to reducing real losses as directly related to economic losses in energy.

Active power loss index (API) is related to the objective of reducing active power losses [25, 26], and is calculated as the ratio between Actual Power Loss in the presence of DG (APLDG) to Actual Power Loss (APL) in the absence of DG:

$$API = APLDG / APL. (9)$$

Reactive power loss index (RPI) is the ratio of the Reactive Power Loss [27] when DG is present (*RPLDG*) to the Reactive Power Loss (*RPL*) without DG:

$$RPI = RPLDG / RPL. \tag{10}$$

Voltage deviation index (VD) is the 3rd target considered in this question [28], and is mainly used to monitor the power system. In real time, efforts across buses deviate from their stability limits, and can be adjusted within safe limits through optimal allocation of DG in the system, contributing to voltage profile optimization. The VD indicator in (11) should be minimal, because higher values indicate a greater deviation from the initial value:

$$VD = \max_{b=1}^{n} \left(\left(v_{ini} - v_b \right) / v_{ini} \right), \tag{11}$$

where n is the total number of buses in the system; $v_{ini} = 1.05$ p.u.

Constrains. The process of minimizing the objective function is constrained by equality constraints and inequality constraints.

Equality constraints express the balance of real and reactive power of DG within the electrical system:

$$\sum P_{Gi} - \sum P_{Di} - P_{loss} = 0; (12)$$

$$\sum Q_{Gi} - \sum Q_{Di} - Q_{loss} = 0 , \qquad (13)$$

where P_{Gi} is the active power generated by traditional resources; P_{Di} is the active power generated by DG units; P_{loss} is the active power losses in network; Q_{Gi} is the reactive power injected by traditional resources; Q_{Di} is the reactive power injected by DG units; Q_{loss} is the reactive power losses in network.

Inequality constraints include setting the minimum and upper limits of DG capacity to ensure that permissible operational levels are not exceeded, in addition to restricting the locations of connecting generation units to

specific locations to the network to achieve the best technical and economic performance:

$$P_{DG}^{\min} \le P_{DG} \le P_{DG}^{\max}; \tag{14}$$

$$Q_{DG}^{\min} \le Q_{DG} \le Q_{DG}^{\max}; \tag{15}$$

$$2 \le DG_{position} \le n_{bus} \,, \tag{16}$$

where P_{DG} is the active power output of the DG unit; P_{DG}^{\min} , P_{DG}^{\max} are the minimum and maximum limits of the DG's active power; Q_{DG} is the reactive power of the DG unit; Q_{DG}^{\min} , Q_{DG}^{\max} are the minimum and maximum allowable reactive power; $DG_{position}$ is the bus number where the DG is installed; n_{bus} is the total number of buses in the network.

Optimization algorithms. PSO is one of the popular algorithms used to solve multidimensional optimization problems. These algorithms mimic the behavior of flocks of birds and fish in search of food sources, where the positions of particles are updated based on their individual and collective experiences to arrive at optimal solutions. The presented models aim to compare the traditional algorithm with a dynamic hybrid version, which includes additional steps to improve the quality and speed of arriving at the optimal solution by introducing local search mechanisms and handling recessions. PSO algorithm and the improved or modified hybrid algorithm, called the hybrid-dynamic PSO algorithm, were used, where their parameters are dynamically adjusted as the algorithm progresses, in addition to introducing the concept of mutation to the results in case of stagnation to avoid the algorithm falling into the trap of local solutions. The choice of this particular algorithm among the rest of the optimization algorithms for the following reasons:

- 1. The ability to process dynamic and non-convex equation.
 - 2. The ability to process large and complex data sets.
- 3. The ability to explore initial search spaces effectively.
- 4. The speed of convergence towards optimal solutions compared to other methods specially when deals with multi-objectives that have overlap and conflict with each other.

In PSO, the starting particles are distributed randomly across the available search space, and out of all these particles, the best solution is identified. The locations of the particles are updated in the next step based on the previous locations and velocity values, the entire swarm takes actions to improve the value of the objective function and achieve the optimization in the next steps.

The best fitness (min, max) is determined to direct the rest of the particles towards this best solution. The velocity of the particle is updated according to the gap between his current position and the optimal position relative to all other particles (g_{best}), in the same manner, the position of the particle is constantly being updated by adding its current location to its movement.

The position and velocity of the particle are determined according to the following equation:

$$v_i^{k+1} = w v_i^k + c_1 r_1 \left(p_{besti} - s_i^k \right) + c_2 r_2 \left(g_{best} - s_i^k \right); \quad (17)$$

$$s_i^{k+1} = s_i^k + v_i^{k+1}; (18)$$

where v_i^k is the velocity of particle *i* at iteration *k*; s_i^k is the position of particle *i* at iteration *k*; p_{besti} is the best position

found by particle i (personal best); g_{best} is the best position found by the entire swarm (global best); w is the inertia weight – controls exploration vs. exploitation; c_1 , c_2 are the acceleration coefficients (cognitive and social components); r_1 , r_2 are the random numbers uniformly distributed in [0, 1].

The PSO algorithm depends on 3 basic steps that are performed during each iteration:

- 1. Evaluating each solution using the objective function to calculate the fitness value.
- 2. Updating the best position of the particle (p_{best}) and the best global position (g_{best}) .
 - 3. Updating the particle's velocity v_i and its position s_i .

These steps continue until stopping criteria are met, such as reaching a certain number of iterations or achieving a certain accuracy threshold. Despite its efficiency, traditional PSO suffers from some drawbacks when dealing with optimization problems, the most prominent of which is that it may stop at local maximum values (stuck in a local maximum), which reduces its ability to explore the entire search space. The parameters w, c_1 , c_2 affect the performance of the algorithm, as tuning inappropriate values can lead to early convergence towards a non-optimal solution or divergence which prevents the algorithm from reaching an optimal solution.

A number of attempts have been made to improve the PSO algorithm in order to find the most suitable control parameters. Numerous methods exist for the search of optimal parameters other than those with fixed values. The variable coefficient PSO or dynamic PSO with control parameters that decrease linearly is given in (19–21). The control parameters of PSO are:

$$w_k = w_{\text{max}} - \frac{k}{k_{\text{max}}} \cdot (w_{\text{max}} - w_{\text{min}}); \qquad (19)$$

$$c_{1k} = c_{1\max} - \frac{k}{k_{\max}} \cdot (c_{1\max} - c_{1\min});$$
 (20)

$$c_{2k} = c_{2\max} - \frac{k}{k_{\max}} \cdot (c_{2\max} - c_{2\min}),$$
 (21)

where w_k is the inertia weight at iteration k; w_{\min} is the final (minimum) inertia weight; w_{\max} is the initial (maximum) inertia weight; k is the current iteration number; k_{\max} is the total number of iterations; c_{1k} is the cognitive component at iteration k; c_{2k} is the social component at iteration k; $c_{1\max}$ is the initial (maximum) cognitive value; $c_{1\min}$ is the final (minimum) cognitive value; $c_{2\min}$ is the initial (minimum) social value; $c_{2\max}$ is the final (maximum) social value.

Local search and mutation were used on the initial results of the PSO algorithm for the following reasons.

- 1) Exploitation. PSO algorithm is good at exploration but may not be accurate in finding the local optimal solution. Local search comes to fine-tuning on the found solution.
- 2) Accelerate-convergence. Instead of waiting for PSO to reach the optimal solution across many generations, local search can quickly improve good solutions in each or after a certain number of generations.
- 3) *Increase precision*. Helps to exceed some PSO limits such as oscillating around g_{best} without further optimization, by optimizing locally around g_{best} or p_{best} .

- 4) *Diversity*. Mutation causes a random change in the location of some particles, preventing premature grouping of particles around imperfect solutions.
- 5) Escape from local optima. If particles stop improving, the mutation gives a random push to each other to exit that area and explore new areas.
- 6) Improved exploration. Especially in the later stages of PSO when particles begin to focus on a small area around the g_{best} .

The method used to determine the best location and value for DG using the hybrid-dynamic PSO algorithm is as follows.

Step 1 (Initialization).

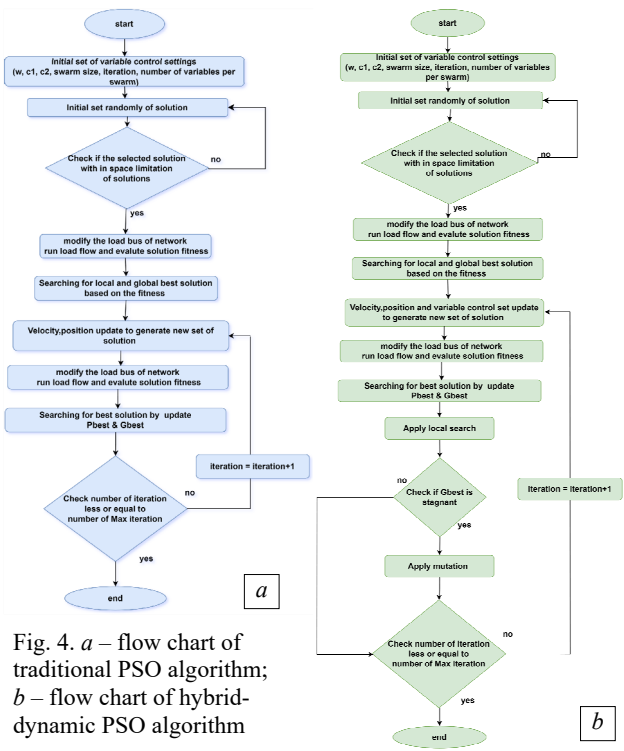
- 1. Number of iteration k.
- 2. Number of particles *n*.
- 3. Number of parameters per particle m.
- 4. Limitation of space solution.
- 5. Set the initial value of control set of PSO as shown in Table 1.
- 6. Set the initial value of each particle randomly with in the limit of space solution.
- Step 2. Modify the load bus by the initial set of particles.
 - Step 3. Run load flow and calculate APL, RPL, VD.
 - **Step 4.** Searching for p_{best} and g_{best} .
- **Step 5.** Update the velocity, position and variable control set to generate new set of solution.
 - **Step 6.** Evaluate the new solution.
 - **Step 7.** Searching for p_{best} and g_{best} .
 - Step 8. Apply local search.
- **Step 9.** Check if g_{best} is stagnant? If yes apply mutation, if don't check no. of iteration if less or equal to no. of max. iteration.
 - Step 10. Update the number of iterations.
- **Step 11.** If number of iterations less than or equal number of max iterations then go to step 5.

Table 1

PSO coefficients used in the simulation

Parameter	Value
Number of particles <i>n</i>	50
Number of iterations k_{max}	50-150
Number of parameters per particles <i>m</i>	2
Cognitive component c_1	0.5-2.5
Social component c_2	0.5-2.5
Inertia weight w	0.4-0.9

The traditional PSO algorithm (Fig. 4,a) begins by initializing the basic parameters, including the inertia weight w, acceleration coefficients c_1 , c_2 , swarm size, number of iterations and number of variables. A set of solutions is then randomly generated within the search space. The validity of the solutions is then checked. If the condition is met, the network loads are adjusted, and the load flow is run to evaluate the validity of the solutions. This is followed by a search for the best local and global solutions (p_{best} and g_{best}) based on the calculated validity values. The positions and velocities of the particles are then updated to generate a new set of solutions. This cycle continues with the network loads being updated, solutions being evaluated, and the best solutions being updated, with the number of iterations gradually increasing until the maximum number of iterations is reached, at which point the algorithm terminates.



The hybrid-dynamic PSO algorithm (Fig. 4,b) follows similar steps to the traditional algorithm, starting with initializing the basic settings and generating a random set of solutions. After verifying that the solutions adhere to the permissible space limits, the network loads are adjusted, and the load flow is run to assess the validity. The best local and global solutions are searched according to the validity criteria. After updating the speed and location variables, an additional optimization step is applied, which involve applying a local search to improve the quality of the discovered solutions. If the global solution g_{best} stagnates and does not improve across iterations, a mutation is applied to break this stagnation and stimulate the search for better solutions. The system continues iterating, updating solutions and increasing the number of iterations until a specified maximum number is reached, at which point the algorithm terminates. This hybrid-dynamic approach contributes to accelerating convergence to the optimal solution and increasing the efficiency of the search process.

Test system. Modified IEEE 33 bus distribution system was adopted to test the proposed method. Figure 5 shows the single line diagram of the distribution system, at base load, the total active power is 3715 kW, the reactive power is 2300 kVAr.

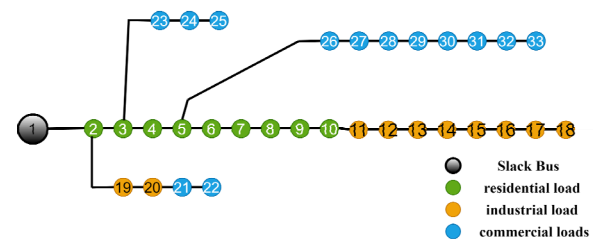


Fig. 5. Modified IEEE 33 bus test system

Limitations. The study's limitations refer to the specific aspects of its design or methodology that had an impact on or influenced the interpretation of the study's conclusions. Below are limitations of this work:

- 1) Load flow method. By backward forward sweep because this method is suitable for distribution networks of radial nature.
 - 2) Operation mode. On grid operation mode.
- 3) *Network type*. Modified IEEE 33 bus test system radial distribution network.
- 4) *Type of DG*. Renewable energies that they have the ability to inject active power only.
- 5) *Number of DG*. Single and multiple distribution generation units.
- 6) Load type. Variable load and load model is constant power.
 - 7) System condition. Balanced 3 phase system.
- 8) *Optimization method*. Metaheuristic method and the algorithm is hybrid dynamic PSO.
 - 9) *Objective function*:
 - minimize active power losses;
 - minimize voltage deviation at each bus;
 - maximize voltage stability.
- 10) *Decision variable*. Optimal location and value of DG with unity power factor.

Result and discussion. To validate the proposed approach and its effectiveness in the analysis and optimization methods presented, the study was applied to the modified IEEE 33 bus test system under different scenarios, including:

- Base case. System operation without integration of any DG.
- *1st case*. Integration of one DG unit at the optimal location within the network.
- 2nd case. Integration of 2 DG units at their optimal locations.
- 3rd case. Integration of 3 DG units at their optimal locations.

IEEE 33 bus model with variable load demand was chosen as the base case for loss evaluation and power flow analysis without DG, and the analysis was done using backward/forward sweep. The total losses in active and reactive power among the studied cases are shown in Fig. 6, and Fig. 7 shows load demands during 24 hours.

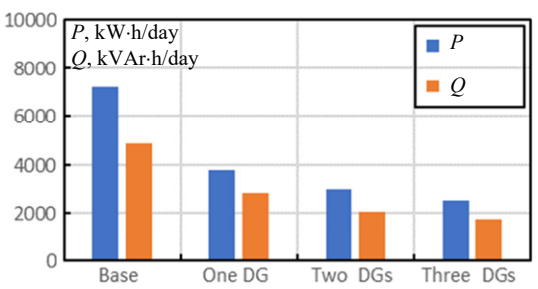


Fig. 6. Active and reactive power losses during 24 h in the 3 cases in addition to the basic case

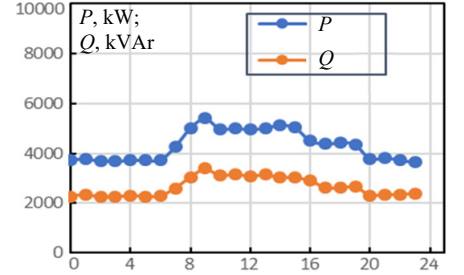


Fig. 7. Active and reactive load demand during 24 h

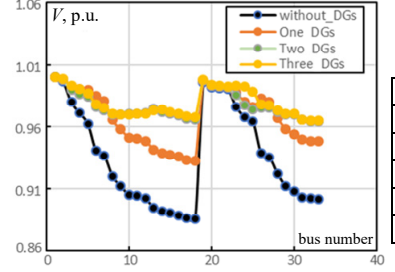
Initially with base case, energy losses for active and reactive power were measured at 7196.054 kW·h/day and 4887.774 kVAr·h/day, the minimum voltage value recorded for bus number 18 was 0.8459 p.u. In the 1st scenario, where a single DG unit was embedded, the optimal size of the unit was calculated to be 3079.71 kW at bus number 6, which caused total active and reactive energy losses to drop to 3799.023 kW·h/day and 2794.019 kVAr·h/day. In the next case, the system was embedded with 2 DG units, where 2 units of 1056.946 kW and 1322.302 kW were placed at buses number 13 and 30, respectively. This led to active energy losses of 2980 kW·h/day and reactive power losses of 2050 kVAr·h/day.

In case 3, where 3 DG units were considered, 957.925 kW, 1262.393 kW and 1231.201 kW units were put in buses 14, 24 and 30, respectively, which brought the total active losses down to 2506.591 kW·h/day and the reactive losses down to 1750 kVAr·h/day. Figure 6 shows how the inclusion of several DG units into distribution systems provides greater improvements on the reduction of active and reactive losses than single generation unit systems.

The changes within the average bus voltage for employing the optimal size and location of the DG in various scenarios with basic case is illustrated in Fig. 8. The application of the optimal distribution generator enhances the performance of all the bus voltages in terms of stability in comparison with the base case.

Table 2 presents the statistical results of 100 running of proposed method for MOF along 24 h with 3 DG along with the corresponding minimum, maximum, mean and standard deviation values. Additionally, the success rate (SR) is reported, which indicates the percentage of runs that achieved a solution within 2 % of minimum objective function value among all running.

The high effectiveness of the algorithm attributed to its inherent optimization capabilities and the adequacy of the selected number of particles and iterations in the PSO algorithm for consistently reaching the optimal solution.



The results of statistical analysis

Statistical indices Result Minimum 0.291

Maximum 0.310

Mean 0.291

Standard deviation 0.003

Success rate (SR) 0.96

Table 2

Fig. 8. Average voltage's buses during 24h in the 3 cases in addition to the basic case

The PSO algorithm was chosen and preferred over the rest of the algorithms based on previous studies that outweighed it over the rest of the algorithms for many reasons, including the ease of understanding its work and the simplicity of the way it is based on it, in addition to that it can be suitable for large and complex networks and speed of convergence to the optimal solution.

Despite the many advantages of this algorithm, it can fall into the trap of local solutions. In this research, this study proposed to use a simple algebraic method to overcome this problem, which is the method of adjusting the algorithm parameters in a dynamic way so that it makes the algorithm strong in terms of exploration, exploitation and choosing the best global solution.

To ensure the effectiveness of the proposed method, a comparison was made between it and the regular PSO algorithm with fixed parameters in a statistical way.

To increase competition between the 2 methods, a few particles were used repeats to combine 3 DG units to observe the difference between the 2 methods and which of them can get closer to the optimal solution in light of the small number of particles and iterations (Table 3).

Statistical result comparison of PSO and hybrid-dynamic PSO

	1	3 3
Statistical indices	PSO result	Hybrid-dynamic PSO result
Minimum	0.351	0.291
Maximum	0.372	0.310
Mean	0.362	0.291
Standard deviation	0.012	0.003
Success rate (SR)	0.18	0.96

Figures 9, 10 show the convergence of the proposed hybrid-dynamic PSO algorithm, which is characterized by its ability to explore a good region of the search space in the early iterations, and quickly reach the optimal solution. Figures 9, 10 show a comparison between the performance of 2 algorithms for optimization of location and the optimal size of DG units in electrical distribution networks, based on the value of a MOF.

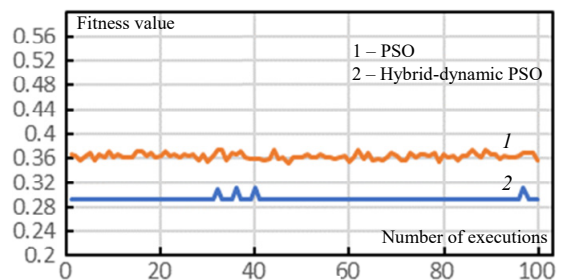


Fig. 9. The fluctuation of solutions across different executions

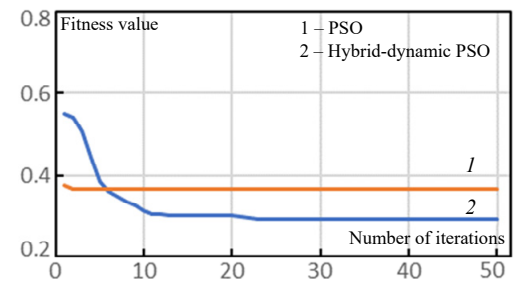


Fig. 10. The convergence of the solution to the optimal value along to iterations

By tracking objective function changes across a number of executions, the traditional PSO algorithm shows a continuous fluctuation in value, with results centered at relatively high levels (≈ 0.36), indicating poor stability and the likelihood of falling into local solutions without being able to improve them effectively. In contrast, the hybrid-dynamic PSO algorithm shows more stable performance, maintaining a relatively low value of the objective function (≈ 0.29) with a very limited number of sudden changes, indicating has a better ability to explore and converge towards the optimal solution. This superior performance demonstrates that the use of a hybrid-dynamic PSO algorithm contributes to improved search efficiency, reduced losses, and more reliable results in distribution network optimization applications.

In Table 4 the proposed methodology is compared with other methodologies, that using PSO algorithm to find the optimal location and size for DG. Note that when using more than 1 DG in different locations, it leads to an improvement in the results, as the 2nd case required injecting less power than the 1st case, and this led to improvements over the 1st case in terms of reducing total losses and improving voltage deviation and stability.

Table 4

Summary of the results obtained by following the proposed methodology

Summary of the results obtained by following the proposed methodology				
Number of DG	No DG	One DG	2 DG	3 DG
Best location of DG	-	Bus 6	Bus 13 Bus 30	Bus 14 Bus 24 Bus 30
Best capacity of DG, kW	-	3079.710@ Bus 6	1056.946@ Bus 13 1322.302@ Bus 30	957.925@ Bus 14 1262.393@ Bus 24 1231.201@ Bus 30
Total capacity of DG, kW	-	3079.710	2379.248	3451.519
Active energy loss, kW·h/day	7196.054	3799.023	2980	2506.591
Active energy loss reduction, %	-	0.472	0.586	0.652
Reactive energy loss, kVAr·h/day	2792.894	2794.019	2050	1750
Reactive energy loss reduction, %	_	0.4.28	0.582	0.642
Min voltage profile	0.8459	0.8959	0.9318	0.9337
Min voltage profile at bus no.	18	18	18	18
Min voltage profile at hour	9	9	9	9
Max voltage profile	0.9970	0.9989	0.9985	0.9991
Max voltage profile at bus no.	2	2	2	2
Max voltage profile at hour	23	23	23	23
	1 1	4 DC '4 '	.1 1 1 . 1 . 1	111 , 1,

^{*}Note: the symbol «@» refers to the bus number that DG unit with right capacity should be connected to it

The results show that the integration of DG units in the distribution network contributes significantly to improving the performance of the system in terms of reducing electrical losses and improving voltage profiles. When only 1 DG unit was added, the active losses (P_{loss}) during 24 h decreased from 7196.054 kW·h/day to 3799.023 kW·h/day, achieving a reduction of 47.2 %.

With the addition of 2 DG units, the P_{loss} during 24 h reduction rate improved to 58.6 %, while it reached 65.2 % when 3 DG units were used. As for reactive losses (Q_{loss}) during 24 h also a clear improvement is recorded, decreasing by 42.8 % with 1 DG unit, rising to 58.2 % and 64.2 % with 2 and 3 DG units respectively. On the other hand, the addition of DG units led to a clear

improvement in the minimum voltage profile, with the lowest voltage rising from 0.8459 without DG units to 0.8959 with 1 unit, and reaching 0.9318 and 0.9337 with 2 and 3 units respectively, indicating enhanced voltage stability. Note that the lowest voltage value was fixed at bus 18 and 9AM, while the highest voltage value was achieved at bus 2 and 11PM across all scenarios. In addition, it is clear that increasing the number of DG units not only reduces overall losses, but also contributes to a more balanced load distribution across the network. With the use of a 1 DG unit, the entire power was concentrated in one location 3079.71 kW at bus 6, resulting in a significant improvement in performance, but the improvement was limited compared to multi-unit of DG. When 2 DG units were added, power injection capacities were distributed between bus 13 and bus 30, allowing for more effective reduction in losses, as losses were further reduced even though the total power injection capacity was less than the single capacity per unit. By integrating 3 DG units distributed over buses 14, 24 and 30 achieve a more uniform distribution of generation power capacities, which is clearly reflected in the improvement of loss and voltage profile. This highlights the importance of the spatial distribution of DG units and the optimal capacity of each unit, as the multi-point injected reduces long electrical paths that cause greater losses, and enhances voltage stability across the grid. Therefore, the use of more than one DG unit with optimal locations and sizes provides a more improvement that exceeds the improvement of a single unit with a large capacity concentrated, which effectively contributes to raising the efficiency of the network.

Future works. Dynamic planning requires consideration of a long time period to determine the optimal locations for DG. Other future work below:

- 1. Island operation. It is recommended to develop models for intentional island operation with the integration of energy storage systems.
- 2. *Improving optimization algorithms*. Improving the tuning of parameters of metaheuristic optimization algorithms such as PSO and GA to achieve greater efficiency.
- 3. Achieving accuracy and computational efficiency. In order to improve the accuracy of convergence and computational efficiency, hybrid techniques should be further studied by combining analytical methods, optimization algorithms, and computational methods.

Conclusions. This paper presents an effective method to optimize the allocation of DG units based on the variable daily load profile. The performance of this methodology was tested using the IEEE 33 Bus test system, where a set of scenarios covering different periods during the day were analyzed to study the effect of variable load on the selection of the best location and capacity for DG.

The locations and sizes of DG units were determined based on the lowest values resulting from a MOF, which helped improve the overall performance of the network. The results showed the effectiveness of the proposed approach in reducing overall system losses along hourly loads demand, as well as improving voltage levels at buses.

In this context, the hybrid-dynamic PSO algorithm was used to determine the optimal distribution of generating units. The results showed that this algorithm significantly reduced both active and reactive power

losses compared to the traditional PSO algorithm. The hybrid algorithm also showed a higher ability to improve the lowest voltages in the grid.

In addition, the analyses showed that a significant reduction in total active power losses across all scenarios studied when using the hybrid method, compared to the decrease achieved when using the traditional algorithm. The same applied to reactive power losses, where the hybrid method showed significantly better results.

These results highlight the importance of the proposed approach based on the hybrid-dynamic PSO algorithm, especially in its ability to reduce losses and enhance voltage stability, making it a promising candidate for application in modern smart electricity grids that require flexibility and high dynamic response.

Acknowledgement. The authors would like to thank University of Mosul, College of Engineering, Electrical Department, for the support given during this work.

Conflict of interest. The authors declare that they have no conflicts of interest.

REFERENCES

- I. Shaheen A.M., Elsayed A.M., Ginidi A.R., Elattar E.E., El-Sehiemy R.A. Effective Automation of Distribution Systems With Joint Integration of DGs/ SVCs Considering Reconfiguration Capability by Jellyfish Search Algorithm. IEEE Access, 2021, no. 9, pp. 92053-92069. doi: https://doi.org/10.1109/ACCESS.2021.3092337.
- 2. Shaheen A., Elsayed A., Ginidi A., El-Sehiemy R., Elattar E. Improved Heap-Based Optimizer for DG Allocation in Reconfigured Radial Feeder Distribution Systems. *IEEE Systems Journal*, 2022, vol. 16, no. 4, pp. 6371-6380. doi: https://doi.org/10.1109/JSYST.2021.3136778.
- 3. Srinivas D. Optimal Planning of Type-1DGs in EV Incorporated Radial Distribution Network. *International Journal on Recent and Innovation Trends in Computing and Communication*, 2024, vol. 11, no. 11, pp. 1152-1161. doi: https://doi.org/10.17762/ijritcc.v11i11.10675.
- 4. Othman R.A., Yehya Al-Yozbaky O.S.A.-D. Influence of reactive power compensation from PV systems on electrical grid. *International Journal of Power Electronics and Drive Systems (IJPEDS)*, 2023, vol. 14, no. 2, pp. 1172-1183. doi: https://doi.org/10.11591/ijpeds.v14.i2.pp1172-1183.
- 5. Shi Q., Li F., Kuruganti T., Olama M.M., Dong J., Wang X., Winstead C. Resilience-Oriented DG Siting and Sizing Considering Stochastic Scenario Reduction. *IEEE Transactions on Power Systems*, 2021, vol. 36, no. 4, pp. 3715-3727. doi: https://doi.org/10.1109/TPWRS.2020.3043874.
- 6. Yuvaraj T., Ravi K., Devabalaji K.R. Optimal Allocation of DG and DSTATCOM in Radial Distribution System Using Cuckoo Search Optimization Algorithm. *Modelling and Simulation in Engineering*, 2017, vol. 2017, art. no. 2857926. doi: https://doi.org/10.1155/2017/2857926.
- 7. Suresh M.C.V., Belwin E.J. Optimal DG placement for benefit maximization in distribution networks by using Dragonfly algorithm. *Renewables: Wind, Water, and Solar*, 2018, vol. 5, no. 1, art. no. 4. doi: https://doi.org/10.1186/s40807-018-0050-7.
- 8. Alajmi B.N., AlHajri M.F., Ahmed N.A., Abdelsalam I., Marei M.I. Multi-objective Optimization of Optimal Placement and Sizing of Distributed Generators in Distribution Networks. *IEEJ Transactions on Electrical and Electronic Engineering*, 2023, vol. 18, no. 6, pp. 817-833. doi: https://doi.org/10.1002/tee.23784.
- 9. Al-Kaoaz H.N.A., Al-Yozbaky O.S.A.Y. Influence of natural clouds on the performance of solar cell systems in Iraq. *Bulletin of Electrical Engineering and Informatics*, 2023, vol. 12, no. 4, pp. 1867-1880. doi: https://doi.org/10.11591/eei.v12i4.4703.

- 10. Li X., Jones G. Optimal Sizing, Location, and Assignment of Photovoltaic Distributed Generators with an Energy Storage System for Islanded Microgrids. *Energies*, 2022, vol. 15, no. 18, art. no. 6630. doi: https://doi.org/10.3390/en15186630.
- 11. Ntombela M., Musasa K., Leoaneka M.C. Power loss minimization and voltage profile improvement by distributed generation(DG) sizing and placement. 2022 IEEE PES/IAS PowerAfrica, 2022, pp. 1-5. doi: https://doi.org/10.1109/PowerAfrica53997.2022.9905254.
- 12. Gopiya Naik S.N., Khatod D.K., Sharma M.P. Analytical approach for optimal siting and sizing of distributed generation in radial distribution networks. *IET Generation, Transmission & Distribution*, 2015, vol. 9, no. 3, pp. 209-220. doi: https://doi.org/10.1049/iet-gtd.2014.0603.
- 13. Rider M.J., López-Lezama J.M., Contreras J., Padilha-Feltrin A. Bilevel approach for optimal location and contract pricing of distributed generation in radial distribution systems using mixed-integer linear programming. *IET Generation, Transmission & Distribution*, 2013, vol. 7, no. 7, pp. 724-734. doi: https://doi.org/10.1049/iet-gtd.2012.0369.
- 14. Rocha L., Castro R., de Jesus J.M.F. An improved particle swarm optimization algorithm for optimal placement and sizing of STATCOM. *International Transactions on Electrical Energy Systems*, 2016, vol. 26, no. 4, pp. 825-840. doi: https://doi.org/10.1002/etep.2110.
- 15. Bhullar S., Ghosh S. Optimal Integration of Multi Distributed Generation Sources in Radial Distribution Networks Using a Hybrid Algorithm. *Energies*, 2018, vol. 11, no. 3, art. no. 628. doi: https://doi.org/10.3390/en11030628.
- *16.* Gumus T.E. Thevenin equivalent based stability index for identifying optimal location of DGs by using HFPSO algorithm. *Measurement*, 2025, vol. 249, art. no. 116970. doi: https://doi.org/10.1016/j.measurement.2025.116970.
- 17. Saud M.N.M., Rasid M.M. Adaptive hybrid differential evolution particle swarm optimization algorithm for optimization distributed generation in distribution networks. *Jurnal Teknologi*, 2025, vol. 87, no. 2, pp. 203-216. doi: https://doi.org/10.11113/jurnalteknologi.v87.19769.
- 18. Cikan M., Cikan N.N., Kekezoglu B. Determination of optimal island regions with simultaneous DG allocation and reconfiguration in power distribution networks. *IET Renewable Power Generation*, 2025, vol. 19, no. 1, art. no. e12942. doi: https://doi.org/10.1049/rpg2.12942.
- 19. Hidayat R., Lomi A., Budi Sulistiawati I. Implementasi Metode Artificial Bee Colony Untuk Penempatan Distributed Generator Pada Penyulang Rayon Tanjung. *Jurnal JEETech*, 2024, vol. 5, no. 2, pp. 113-125. (Id). doi: https://doi.org/10.32492/jeetech.v5i2.5202.
- 20. Hadjidj N., Benbrahim M., Ounnas D., Mouss L.H. Global maximum power point tracking method for photovoltaic systems using Takagi-Sugeno fuzzy models and ANFIS approach. *Electrical Engineering & Electromechanics*, 2025, no. 2, pp. 31-38. doi: https://doi.org/10.20998/2074-272X.2025.2.05.
- 21. Meena N.K., Swarnkar A., Gupta N., Niazi K.R. Multi-objective Taguchi approach for optimal DG integration in

- distribution systems. *IET Generation, Transmission & Distribution*, 2017, vol. 11, no. 9, pp. 2418-2428. doi: https://doi.org/10.1049/iet-gtd.2016.2126.
- 22. Jena S., Mishra A., Rastogi V. Network Topology Based Back/Forward Sweeping for Load Flow of Radial Distribution Systems. International Journal of Advanced Research in Electrical, Electronics and Instrumentation Engineering, 2014, vol. 3, no. 11, pp. 12914-12920. doi: https://doi.org/10.15662/ijareeie.2014.0311018.
- 23. Nageswari D., Kalaiarasi N., Geethamahalakshmi G. Optimal Placement and Sizing of Distributed Generation Using Metaheuristic Algorithm. Computer Systems Science and Engineering, 2022, vol. 41, no. 2, pp. 493-509. doi: https://doi.org/10.32604/csse.2022.020539.
- 24. Bajaj M., Singh A.K., Alowaidi M., Sharma N.K., Sharma S.K., Mishra S. Power Quality Assessment of Distorted Distribution Networks Incorporating Renewable Distributed Generation Systems Based on the Analytic Hierarchy Process. *IEEE Access*, 2020, vol. 8, pp. 145713-145737. doi: https://doi.org/10.1109/ACCESS.2020.3014288.
- 25. Han Z., Li J., Wang Q., Lu H., Xu S., Zheng W., Zhang Z. Deep learning-aided joint DG-substation siting and sizing in distribution network stochastic expansion planning. *Frontiers in Energy Research*, 2023, vol. 10, art. no. 1089921. doi: https://doi.org/10.3389/fenrg.2022.1089921.
- 26. Labed M.A., Zellagui M., Benidir M., Sekhane H., Tebbakh N. Optimal hybrid photovoltaic distributed generation and distribution static synchronous compensators planning to minimize active power losses using adaptive acceleration coefficients particle swarm optimization algorithms. *Electrical Engineering & Electromechanics*, 2023, no. 6, pp. 84-90. doi: https://doi.org/10.20998/2074-272X.2023.6.15.
- 27. Abbas A., Qaisar S.M., Waqar A., Ullah N., Al Ahmadi A.A. Min-Max Regret-Based Approach for Sizing and Placement of DGs in Distribution System under a 24 h Load Horizon. *Energies*, 2022, vol. 15, no. 10, art. no. 3701. doi: https://doi.org/10.3390/en15103701.
- 28. Akbar M.I., Kazmi S.A.A., Alrumayh O., Khan Z.A., Altamimi A., Malik M.M. A Novel Hybrid Optimization-Based Algorithm for the Single and Multi-Objective Achievement With Optimal DG Allocations in Distribution Networks. *IEEE Access*, 2022, vol. 10, pp. 25669-25687. doi: https://doi.org/10.1109/ACCESS.2022.3155484.

Received 04.05.2025 Accepted 12.07.2025 Published 02.11.2025

S.S. Sabry ¹, MSc, Student, O.Sh. Al-Yozbaky ¹, PhD, Associate Professor, ¹ Department of Electrical Engineering, College of Engineering, University of Mosul, Iraq, e-mail: sayf.23enp22@student.uomosul.edu.iq; o.yehya@uomosul.edu.iq (Corresponding Author)

How to cite this article:

Sabry S.S., Al-Yozbaky O.Sh. Enhanced siting and sizing of distributed generation in radial distribution networks under load demand uncertainty using a hybrid metaheuristic framework. *Electrical Engineering & Electromechanics*, 2025, no. 6, pp. 84-92. doi: https://doi.org/10.20998/2074-272X.2025.6.11

C.D. Tran, M. Kuchar, P.D. Nguyen

Improved speed sensorless control for induction motor drives using rotor flux angle estimation

Introduction. In the typical field-oriented control (FOC) method, the variation of machine resistance is not considered when calculating the rotor flux angle. This omission affects the accuracy of the control method during motor operation, leading to potential performance degradation. Problem. Neglecting stator resistance variations in the voltage model-based FOC technique can cause rotor flux angle estimation deviation. This inaccuracy impacts motor speed control, especially under varying operating conditions where resistance changes due to temperature fluctuations. Goal. This paper aims to improve the accuracy of rotor flux angle estimation in the voltage model-based FOC technique by incorporating a real-time stator resistance estimation process. Methodology. The proposed research integrates a model reference adaptive system to estimate the stator resistance and replaces the rated resistance value in the rotor flux angle calculation algorithm of the FOC technique. The effectiveness of the method is evaluated by using MATLAB/Simulink simulations, where the estimated resistance value is compared with the actual resistance value, and the motor speed control performance is analyzed. Simulation results demonstrate that the proposed method significantly enhances the accuracy of rotor flux angle estimation by adapting to changes in stator resistance. This improvement ensures better motor speed control performance, reducing deviations between the actual and reference speeds under different operating conditions. Scientific novelty of this research lies in integrating real-time stator resistance estimation into the rotor flux angle calculation process of the voltage model-based FOC technique, addressing a key limitation in typical FOC approaches. **Practical** value. By improving the accuracy of rotor flux angle estimation, the proposed method enhances the stability and efficiency of motor speed control. This ensures better performance in industrial applications where precise motor control is essential under varying operating conditions. References 27, figures 11.

Keywords: induction motor drive, field-oriented control, model reference adaptive system, stator resistance.

Вступ. У типовому методі управління з орієнтацією по полю (FOC) зміна опору машини не враховується під час розрахунку кута потоку ротора. Цей недолік впливає на точність методу керування під час роботи двигуна, що призводить до потенційного зниження продуктивності. Проблема. Нехтування змінами опору статора у методі FOC на основі моделі напруги може призвести до відхилення оцінки кута потоку ротора. Ця неточність впливає на керування швидкістю двигуна, особливо в умовах експлуатації, коли опір змінюється через коливання температури. **Метою** даної роботи ϵ підвищення точності оцінки кута потоку ротора в методі FOC на основі моделі напруги шляхом включення процесу оцінки опору статора в реальному часі. Методика. Пропоноване дослідження інтегрує адаптивну систему з еталонною моделлю для оцінки опору статора та замінює номінальне значення опору в алгоритмі розрахунку кута потоку ротора методом FOC. Ефективність методу оцінюється за допомогою моделювання MATLAB/Simulink, де розрахункове значення опору порівнюється з фактичним значенням опору, а потім аналізується характеристика керування швидкістю двигуна. Результати моделювання показують, що запропонований метод значно підвищує точність оцінки кута потоку ротора за рахунок адаптації змін опору статора. Це покращення забезпечує більш ефективне управління швидкістю двигуна, зменшуючи відхилення між фактичною та заданою швидкостями у різних робочих умовах. Наукова новизна даного дослідження полягає в інтеграції оцінки опору статора в реальному часі в процес розрахунку кута потоку ротора методом FOC на основі моделі напруги, що усуває ключове обмеження типових підходів FOC. Практична значимість. Підвишуючи точність оцінки кута потоку ротора, запропонований метод підвишує стабільність та ефективність управління швидкістю двигуна. Це забезпечує більш високу продуктивність у промислових застосуваннях, де точність управління двигуном необхідна в змінних робочих умовах. Бібл. 27, рис.11.

Ключові слова: привод асинхронного двигуна, полеорієнтоване управління, адаптивна система еталонної моделі, опір статора.

Introduction. The rotor flux angle is a crucial factor in the functioning and vector control methods of induction motors (IMs). It indicates the alignment of the rotor's magnetic field concerning the stator's magnetic field, and precise estimation of this angle is vital for achieving peak motor performance. Within the IM model, the rotor flux angle is integral in separating torque and flux control, enabling accurate and independent tuning of torque and flux during motor operation [1–5].

Problems and the relevance. The field-oriented control (FOC) method [6–9] is a widely used approach for determining the rotor flux angle. However, this method's control strategy relies heavily on the machine parameters, particularly the stator resistance. Furthermore, variations in stator resistance are not accounted for when computing the rotor flux angle, thereby impacting the precision of the control method during operation.

Review of recent publications about rotor flux estimation. Model reference adaptive systems (MRAS) have been extensively developed to calculate the rotor flux and its angle in IMs [10–13]. Two elementary models are utilized in the MRAS method: the current model (CM, the adaptive model) and the voltage model (VM, the reference model). The CM, sensitive to rotor resistance parameters

[14, 15], relies on the stator current signal and rotor speed to ascertain the rotor flux angle. Conversely, the VM, which depends on the stator resistance parameter [16, 17], uses both voltage and current signals to estimate rotor flux. A significant challenge in MRAS modeling is the variation in stator resistance due to temperature fluctuations, which can impact motor precision. As the stator winding temperature changes, the resistance alters, necessitating an adaptive approach to estimate this parameter accurately. These adaptive mechanisms bolster the resilience of MRAS models, mainly during low-speed functions where the precise determination of stator resistance is vital for sustaining performance [18, 19]. When the stator resistance is not accurately estimated, it leads to errors in the calculated stator flux, affecting the torque output and stability of the motor drive [20]. The authors [21] considered a rotor flux estimator based on the MRAS model, which also depends on the stator resistance (R_s) of the motor, and found that the estimated R_s value is susceptible to changes in IM parameters. This estimated R_s serves as an input to the speed estimator. The relationship between temperature-induced resistance changes and control accuracy is further supported by the findings in [22, 23], highlighting the challenges in

© C.D. Tran, M. Kuchar, P.D. Nguyen

maintaining accurate rotor speed and flux estimates in the face of R_s drift. The estimated R_s is considered a solution to improve the reliability of the flux estimate.

The goal of the paper. This study introduces an enhanced rotor flux-based model reference adaptive system (RF-MRAS) to estimate the rotor flux and determine the R_s of the IM. This estimated resistance is then used to update the R_s in the rotor flux angle calculation within the FOC technique, which traditionally overlooks variations in R_s [24, 25]. The proposed approach enhances the precision of rotor flux angle estimation, accommodating changes in stator resistance during motor speed regulation and ensuring alignment between the actual and target speeds across various operational scenarios. Furthermore, simulation results have confirmed the validity of this analysis.

Mathematical models for IMs within the $[\alpha/\beta]$ coordinate framework. The connection between the electrical parameters of an IM is influenced by several nonlinear factors [26]. These parameters include the stator current, flux linkage, and voltage. To study the dynamic performance of the IM, a mathematical model is formulated within the static coordinate framework $[\alpha/\beta]$. This model illustrates the interaction between the voltage, current, and flux linkage of both the stator and rotor. The primary mathematical equations defining the IM system are:

$$\begin{bmatrix} \boldsymbol{u}_{s}^{s} \\ 0 \end{bmatrix} = \begin{bmatrix} A \begin{bmatrix} \boldsymbol{i}_{s}^{s} \\ \boldsymbol{\psi}_{r}^{s} \end{bmatrix} + \begin{bmatrix} \boldsymbol{B} \end{bmatrix} \frac{\mathrm{d}}{\mathrm{d}t} \begin{bmatrix} \boldsymbol{i}_{s}^{s} \\ \boldsymbol{\psi}_{r}^{s} \end{bmatrix}, \tag{1}$$

with matrices:

$$[A] = \begin{bmatrix} R_s & 0 \\ -L_m/T_r & 1/T_r - j\omega_r \end{bmatrix}; [B] = \begin{bmatrix} \frac{L_sL_r - L_m^2}{L_r}L_s & L_m/L_r \\ 0 & 1 \end{bmatrix},$$

where u_s^s is the stator voltage vector; i_s^s is the stator current vector; ψ_r^s is the rotor flux vector; $T_r = L_r/R_r$ is the time rotor constant; R_s , R_r are the stator and rotor resistances; L_s , L_r , L_m are the stator, rotor and mutual inductances; ω_r is the rotor angular velocity.

A. Apply the typical VM to calculate rotor flux in the FOC technique corresponding to speed sensorless control. A speed sensorless induction motor drive (IMD) using the FOC technique consists of voltage/current sensors [27] integrated into the converter. The IMD consists of key components: the IM for converting electrical into mechanical energy, with rotor flux dynamics crucial for speed control; the applicationdependent load; the inverter power supply, a 3-phase voltage source inverter for AC voltage and frequency to manage speed and torque; and the sensing system for indirect speed estimation. The FOC controller separates torque and flux components of stator current for independent motor control, regulated by a PI controller. A new rotor flux controller estimates rotor flux. Figure 1 shows these components' interconnection.

Rotor flux calculation in IM is essential to control strategies, especially in sensorless applications. Rotor flux using a VM is advantageous because it does not depend on rotor parameters. The block diagram for estimating rotor flux vector components using the VM is depicted in Fig. 2.

Equation (2) describes the rotor flux estimation:

$$\frac{\mathrm{d}}{\mathrm{d}t} \begin{bmatrix} \psi_{r\alpha(VM)} \\ \psi_{r\beta(VM)} \end{bmatrix} = \frac{L_r}{L_m} \begin{bmatrix} u_{s\alpha} \\ u_{s\beta} \end{bmatrix} - \frac{L_r}{L_m} R_{s_est} \begin{bmatrix} i_{s\alpha} \\ i_{s\beta} \end{bmatrix} - a_1 \frac{\mathrm{d}}{\mathrm{d}t} \begin{bmatrix} i_{s\alpha} \\ i_{s\beta} \end{bmatrix};$$
with $a_1 = \left(L_s L_r - L_m^2 \right) / L_m,$

where $\psi_{r\alpha(VM)}$, $\psi_{r\beta(VM)}$ are the rotor flux components in the VM on the coordinate axis $[\alpha/\beta]$.

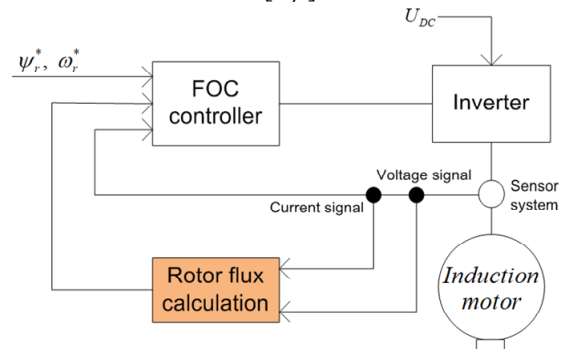
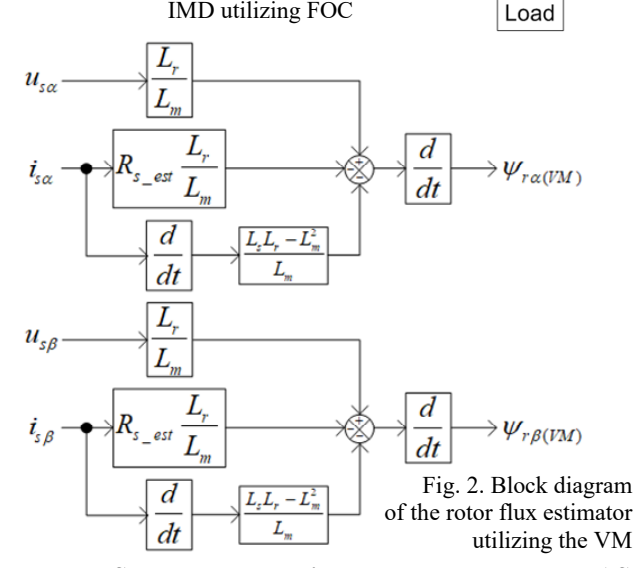


Fig. 1. Block diagram of a speed sensorless IMD utilizing FOC



B. Sensorless technique based on RF-MRAS. Figure 3 shows the rotor flux-based speed observer in the improved RF-MRAS model for speed estimation.

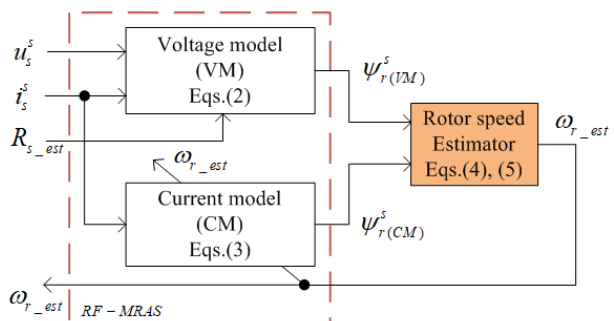


Fig. 3. Block diagram of the speed estimation using RF-MRAS

This improved model consists of the reference model (VM), represented in (2), and the adaptive model (CM), based on the relationship between the stator current, the rotor flux, and the rotor speed represented in (3), together with an adaptive mechanism to minimize the error between the 2 models, as shown in (4, 5):

$$\frac{\mathrm{d}}{\mathrm{d}t} \begin{bmatrix} \psi_{r\alpha(CM)} \\ \psi_{r\beta(CM)} \end{bmatrix} = \begin{bmatrix} -1/T_r & -\omega_{r_est} \\ \omega_{r_est} & -1/T_r \end{bmatrix} \begin{bmatrix} \psi_{r\alpha(CM)} \\ \psi_{r\beta(CM)} \end{bmatrix} + \frac{L_m}{T_r} \begin{bmatrix} i_{s\alpha} \\ i_{s\beta} \end{bmatrix}, (3)$$

where $\psi_{r\alpha(CM)}$, $\psi_{r\beta(CM)}$ are the rotor flux components in CM on the coordinate axis $[\alpha/\beta]$.

Equation (4) shows the discrepancy, termed as the error, between the outputs of the 2 estimators:

 $\xi_{RF-MRAS} = \psi_{r\alpha(CM)} \cdot \psi_{r\beta(VM)} - \psi_{r\beta(CM)} \cdot \psi_{r\alpha(VM)}$ The RF-MRAS technique estimates speed via the PI controller:

$$\omega_{r_est} = K_p \cdot \xi_{\omega_{RF-MRAS}} + K_i \int \xi_{\omega_{RF-MRAS}} dt , \quad (5)$$

where K_n , K_i are the gain constants for the proportional and integral components, respectively.

C. Stator resistance estimation using RF-MRAS. During motor operation, temperature increases affect the stator resistance, altering the R_s parameter of (2) in section A of the VM and causing rotor flux estimation errors. This research proposes a method to estimate R_s integrated with speed estimation. Figure 4 illustrates the fundamental block diagram of the R_s estimator based on RF-MRAS, which includes a reference function $f(\mathbf{i}_s^s, \mathbf{u}_s^s, R_{s_est})$ and an adaptive function $f(\mathbf{i}_s^s, \omega_{r_est})$. The PI controller processes the deviation between them. The output, R_{s_est} , adjusts to minimize the error.

The parameter R_{s_est} is expected to enhance the precision of the rotor flux estimation approach, which depends on the RF-MRAS model. The PI stage determines the R_s value:

$$\xi_{R} = [\psi_{r\alpha(RF)} - \psi_{r\alpha(CM)}]i_{s\alpha} + [\psi_{r\beta(RF)} - \psi_{r\beta(CM)}]i_{s\beta}; \quad (6)$$

$$R_{s_est} = K_{p}f(\xi_{R}) + K_{i}\int_{S}f(\xi_{R})dt. \quad (7)$$

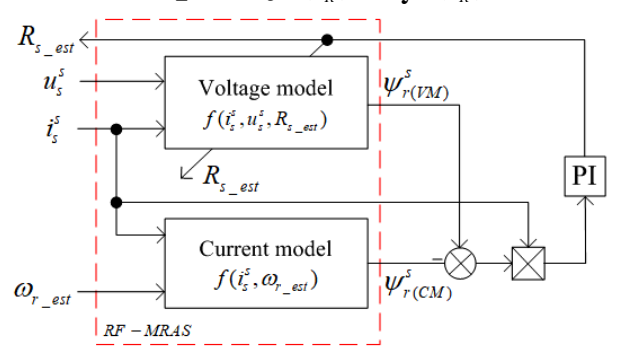


Fig. 4. Block diagram of the estimating stator resistance using RF-MRAS

Simulation results. The performance of the improved method is assessed through simulations of the IMD. The parameters for IM are: pole pairs - 2; rated speed – 1420 rpm; $R_s = 3.179 \Omega$; $R_r = 2.118 \Omega$; $L_s = 0.209 H$; $L_r = 0.209 \text{ H}; L_m = 0.192 \text{ H}.$

The sensitivity to changes in motor parameters was tested at a low-speed reference speed value increasing from 0 rpm to 300 rpm at 0.5 s. The motor was operated at a load of 14.8 N·m after 1 s (full load). Two cases considered the influence of the stator resistance on the VM-based flux estimator. The stator resistance was assumed to be unchanged and increased by 20 % from the nominal value, while the other parameters remained the same.

The 1st case simulated the operation of the IMD corresponding to the improved FOC method with rotor flux based on the VM. Figure 5 shows the performance of the motor when R_s is constant, showing the reference speed and the motor's actual speed; the control system maintained the motor speed closely following the reference value in a stable manner despite small overshoots during starting and at maximum load. The stator current stabilizes quickly after speed and load changes, with a slight initial spike when the speed changes, indicating that the system responds quickly and sensitively. Figures 6, 7 show that the components of the rotor flux vector components in $[\alpha/\beta]$ from the CM also remain accurate and well maintained, ensuring efficient operation of the system.

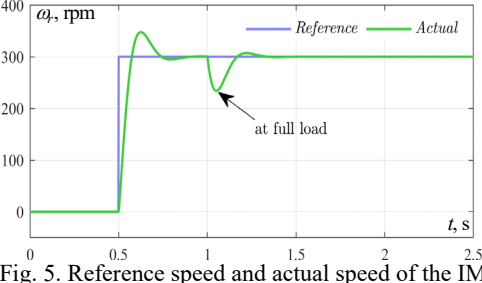
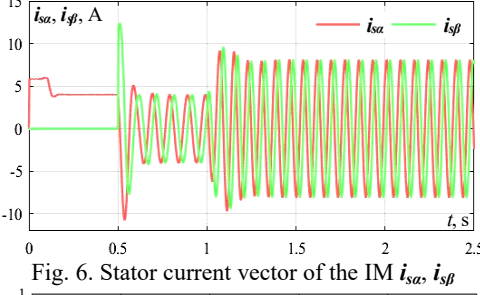


Fig. 5. Reference speed and actual speed of the IM



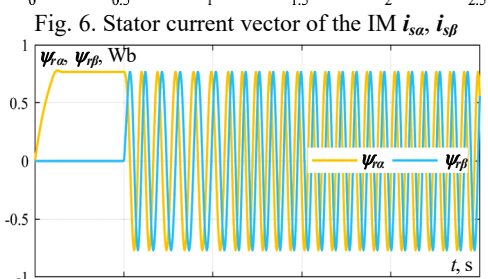


Fig. 7. Rotor flux vector from the VM for improved FOC technique: Ψ_{ra} , Ψ_{rb}

In the 2nd case, when the stator resistance increases by 20 % from the nominal value at 1.3 s, this change affects the rotor flux and rotor speed in the RF-MRAS technique. Although the initial change in R_s leads to a deviation between the reference value and the estimated value, the estimator has shown good adaptability, accurately adjusting to the change in R_s . The simulation results show (Fig. 8) that the difference between the actual and estimated stator resistance is negligible. The rotor flux and stator current vectors remain stable (Fig. 9, 10). Although the estimated speed in Fig. 11 still closely follows the actual speed and is very close to the reference speed, ensuring high accuracy in both the transient and steady-state responses.

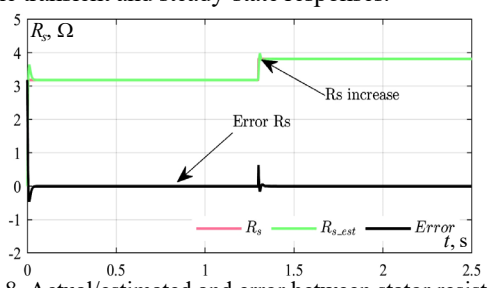


Fig. 8. Actual/estimated and error between stator resistance using RF-MRAS

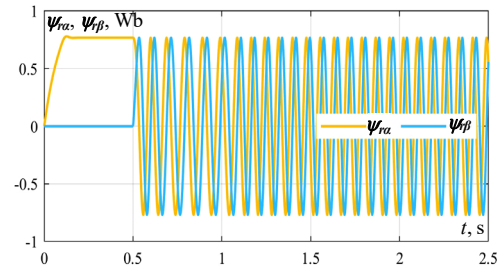


Fig. 9. Rotor flux vector based on improved FOC technique using RF-MRAS: $\Psi_{r\alpha}$, $\Psi_{r\beta}$

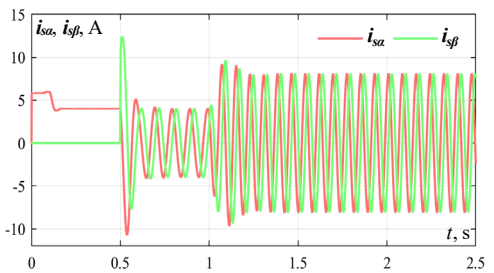


Fig. 10. Stator current vector of the IM based on improved FOC using RF-MRAS: $i_{s\alpha}$, $i_{s\beta}$

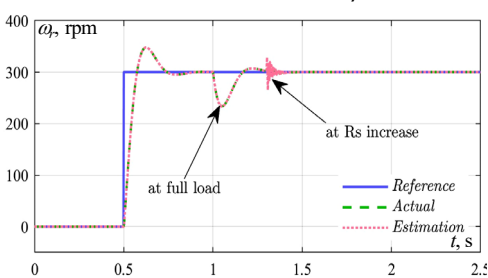


Fig. 11. Reference/actual/estimated speed of the IM based on improved FOC using RF-MRAS

The improved FOC system works well in both cases, ensuring accurate speed and fast response. When R_s changes, the system takes some time to adjust but still provides the accuracy of the speed estimate. The difference between the actual R_s and the estimated R_s is negligible, proving the stability of the estimator.

Conclusions. The proposed method focuses on accurately estimating the R_s to improve the accuracy of estimated speed in sensorless control systems and aims at a more comprehensive approach. Specifically, the method improves the accuracy of the rotor flux angle, which is the core element of FOC in motor speed control. Since the rotor flux angle plays an important role in ensuring the separation of torque and flux control, any deviation in this value due to the change in R_s can cause deterioration in the control performance. Therefore, optimizing both the estimation of R_s and the flux angle will significantly improve the accuracy and stability of the vector control system, not only under normal operating conditions but also when R_s changes significantly due to the influence of temperature or other environmental factors. The simulation results show that the proposed method can adapt to the change in R_s , ensuring that both the rotor speed and the flux angle are accurately estimated, thus improving the performance of sensor and sensorless control systems.

Acknowledgment. This research is funded by Ton Duc Thang University under grant no. FOSTECT.2024.20.

Conflict of interest. The authors declare that they have no conflicts of interest.

REFERENCES

- I. Kasula S., Shrestha B., Katwal K., Dahal R. Implementation of Indirect Field Oriented Control Using Space Vector Pulse Width Modulation for the Control of Induction Motor. *International Journal on Engineering Technology*, 2023, vol. 1, no. 1, pp. 139-152. doi: https://doi.org/10.3126/injet.v1i1.60936.
- 2. Chaabane H., Khodja D.E., Chakroune S., Hadji D. Model reference adaptive backstepping control of double star induction machine with extended Kalman sensorless control. *Electrical Engineering & Electromechanics*, 2022, no. 4, pp. 3-11. doi: https://doi.org/10.20998/2074-272X.2022.4.01.
- 3. Mehbodniya A., Kumar P., Changqing X., Webber J.L., Mamodiya U., Halifa A., Srinivasulu C. Hybrid Optimization Approach for Energy Control in Electric Vehicle Controller for Regulation of Three-Phase Induction Motors. *Mathematical Problems in Engineering*, 2022, vol. 2022, pp. 1-13. doi: https://doi.org/10.1155/2022/6096983.
- 4. Bach D.H., Tran C.D. An improved voltage model based on stator resistance estimation for FOC technique in the induction motor drive. *Advances in Electrical and Electronic Engineering*, 2024, vol. 22, no. 2, pp. 107-114. doi: https://doi.org/10.15598/aeee.v22i2.5745.
- 5. Malyar V.S., Hamola O.Y., Maday V.S., Vasylchyshyn I.I. Mathematical modelling of starting modes of induction motors with squirrel-cage rotor. *Electrical Engineering & Electromechanics*, 2021, no. 2, pp. 9-15. doi: https://doi.org/10.20998/2074-272X.2021.2.02.
- 6. Saady I., Karim M., Bossoufi B., Motahhir S., Adouairi M.S., Majout B., Lamnadi M., Masud M., Al-Amri J.F. Optimization for a Photovoltaic Pumping System Using Indirect Field Oriented Control of Induction Motor. *Electronics*, 2021, vol. 10, no. 24, art. no. 3076. doi: https://doi.org/10.3390/electronics10243076.
- 7. Khadar S., Abu-Rub H., Kouzou A. Sensorless Field-Oriented Control for Open-End Winding Five-Phase Induction Motor With Parameters Estimation. *IEEE Open Journal of the Industrial Electronics Society*, 2021, vol. 2, pp. 266-279. doi: https://doi.org/10.1109/OJIES.2021.3072232.
- 8. Ojha K., Sharma S., Tirole R. Performance analysis and speed control using indirect vector controlled for induction motor drives. *International Journal of Technical Research & Science*, 2023, vol. 8, no. 6, pp. 18-23. doi: https://doi.org/10.30780/IJTRS.V08.I06.004.
- 9. Tran C.D., Kuchar M., Nguyen P.D. Research for an enhanced fault-tolerant solution against the current sensor fault types in induction motor drives. *Electrical Engineering & Electromechanics*, 2024, no. 6, pp. 27-32. doi: https://doi.org/10.20998/2074-272X.2024.6.04.
- 10. El Merrassi W., Abounada A., Ramzi M. Advanced speed sensorless control strategy for induction machine based on neuro-MRAS observer. *Materials Today: Proceedings*, 2021, vol. 45, pp. 7615-7621. doi: https://doi.org/10.1016/j.matpr.2021.03.081.
- 11. Demir R., Yildiz R., Barut M. Speed-Sensorless Predictive Torque Control of the IM Based on MRAS. Ömer Halisdemir Üniversitesi Mühendislik Bilimleri Dergisi, 2023, vol. 12, no. 1, pp. 126-133. doi: https://doi.org/10.28948/ngumuh.1208031.
- 12. Gholipour A., Ghanbari M., Alibeiki E., Jannati M. Speed sensorless fault-tolerant control of induction motor drives against current sensor fault. *Electrical Engineering*, 2021, vol. 103, no. 3, pp. 1493-1513. doi: https://doi.org/10.1007/s00202-020-01179-0.
- 13. Tran C.D., Truong M.N. Sensorless Control for Induction Motor Drive Applying CB-MRAS Integrating Stator Resistance Estimation. International Review on Modelling and Simulations (IREMOS), 2024, vol. 17, no. 4, pp. 215-221. doi: https://doi.org/10.15866/iremos.v17i4.24107.
- 14. Adamczyk M., Niczyporuk S., Orlowska-Kowalska T. Current Sensor Fault-Tolerant Induction Motor Drive with

- Online Rotor Resistance Adaptation. 2022 IEEE 20th International Power Electronics and Motion Control Conference (PEMC), 2022, pp. 546-552. doi: https://doi.org/10.1109/PEMC51159.2022.9962895.
- 15. Bednarz S.A., Dybkowski M. Estimation of the Induction Motor Stator and Rotor Resistance Using Active and Reactive Power Based Model Reference Adaptive System Estimator. Applied Sciences, 2019, vol. 9, no. 23, art. no. 5145. doi: https://doi.org/10.3390/app9235145.
- 16. Özdemir S. A new stator voltage error-based MRAS model for field-oriented controlled induction motor speed estimation without using voltage transducers. *Electrical Engineering*, 2020, vol. 102, no. 4, pp. 2465-2479. doi: https://doi.org/10.1007/s00202-020-01043-1.
- 17. Adamczyk M., Orlowska-Kowalska T. Self-Correcting Virtual Current Sensor Based on the Modified Luenberger Observer for Fault-Tolerant Induction Motor Drive. *Energies*, 2021, vol. 14, no. 20, art. no. 6767. doi: https://doi.org/10.3390/en14206767.
- 18. Salomon C.P., Sant'Ana W.C., Borges da Silva L.E., Lambert-Torres G., Bonaldi E.L., de Oliveira L.E.L., Borges da Silva J.G. Induction Motor Efficiency Evaluation Using a New Concept of Stator Resistance. IEEE Transactions on Instrumentation and Measurement, 2015, vol. 64, no. 11, pp. 2908-2917. doi: https://doi.org/10.1109/TIM.2015.2437632.
- 19. Benlaloui I., Fezzani A., Orlowska-Kowalska T., Chriff-Alaoui L., Drid S. Online Short-Circuit Fault Detector of the Induction Motor Winding Based on MRAS Technique. *IEEE Transactions on Industrial Electronics*, 2025, vol. 72, no. 7, pp. 7426-7441. doi: https://doi.org/10.1109/TIE.2024.3508086.
- 20. Xiu C., Yao F., Zheng J. Comparative Analysis of Two Speed-Estimation Methods for Dual Three-Phase Induction Motor with Stator Resistance Online Identification. *Electronics*, 2021, vol. 10, no. 23, art. no. 2951. doi: https://doi.org/10.3390/electronics10232951.
- 21. Khan Y.A., Verma V. Stator resistance estimation for MRAS-based speed sensorless vector-controlled switched reluctance motor drive. *Electrical Engineering*, 2021, vol. 103, no. 4, pp. 1949-1963. doi: https://doi.org/10.1007/s00202-020-01203-3.
- 22. Juan J., Cui Y., Wang K. Speed sensorless adaptive rotor flux orientation control of induction motor drive. *Preprint submitted to International Journal of Robust and Nonlinear Control*, October 8, 2023, pp. 1-21. doi: https://doi.org/10.22541/au.169686035.54584096/v1.

- 23. Pham Van T., Vo Tien D., Leonowicz Z., Jasinski M., Sikorski T., Chakrabarti P. Online Rotor and Stator Resistance Estimation Based on Artificial Neural Network Applied in Sensorless Induction Motor Drive. *Energies*, 2020, vol. 13, no. 18, art. no. 4946. doi: https://doi.org/10.3390/en13184946.
- 24. Tran C.D., Brandstetter P., Kuchar M., Ho S.D. A Novel Speed and Current Sensor Fault-Tolerant Control Based on Estimated Stator Currents in Induction Motor Drives. International Review of Electrical Engineering (IREE), 2020, vol. 15, no. 5, pp. 344-351. doi: https://doi.org/10.15866/iree.v15i5.17937.
- 25. Zellouma D., Bekakra Y., Benbouhenni H. Field-oriented control based on parallel proportional—integral controllers of induction motor drive. *Energy Reports*, 2023, vol. 9, pp. 4846-4860. doi: https://doi.org/10.1016/j.egyr.2023.04.008.
- 26. Li Y.M., Wang Y.B., Yan Q.F., Huang W. Modeling and Simulation of Asynchronous Motor in αβ Coordinate System Based on Matlab. *Advanced Materials Research*, 2013, vol. 756-759, pp. 4646-4651. doi: https://doi.org/10.4028/www.scientific.net/AMR.756-759.4646. 27. Tran C.D., Kuchar M., Sotola V., Nguyen P.D. Fault-Tolerant Control Based on Current Space Vectors against Total Sensor Failures. *Sensors*, 2024, vol. 24, no. 11, art. no. 3558. doi: https://doi.org/10.3390/s24113558.

Received 16.03.2025 Accepted 22.05.2025 Published 02.11.2025

C.D. Tran¹, Doctor on Electrical Engineering,
M. Kuchar², Professor, Doctor on Electrical Engineering,
P.D. Nguyen^{2,3}, PhD Student,

¹ Power System Optimization Research Group,
Faculty of Electrical and Electronics Engineering,
Ton Duc Thang University, Ho Chi Minh City, Vietnam,
e-mail: trandinhcuong@tdtu.edu.vn (Corresponding Author)

² Department of Applied Electronics,
Faculty of Electrical Engineering and Computer Science,
VSB-Technical University of Ostrava, Czech Republic,

e-mail: martin.kuchar@vsb.cz; phuong.nguyen.duy.st@vsb.cz

Faculty of Engineering and Technology,
Saigon University, Ho Chi Minh City, Vietnam,

e-mail: phuong.nd@sgu.edu.vn

How to cite this article:

Tran C.D., Kuchar M., Nguyen P.D. Improved speed sensorless control for induction motor drives using rotor flux angle estimation. *Electrical Engineering & Electromechanics*, 2025, no. 6, pp. 93-97. doi: https://doi.org/10.20998/2074-272X.2025.6.12

A. Toualbia, A.B. Djilali, R. Taleb, N. Mansour, M. Souaihia, H. Saidi

Application perturb and observe maximum power point tracking with interconnection and damping assignment passive-based control for photovoltaic system using boost converter

Introduction. Power generation from renewable sources, such as photovoltaic (PV) power, has become increasingly important in replacing fossil fuels. A PV system's maximum power point (MPP) moves along its power-voltage curve in response to environmental changes. Despite the use of maximum power point tracking (MPPT) algorithms, the displacement of the MPP results in a decrease in PV system performance. Problem. Perturb & Observe (P&O) MPPT algorithm is a simple and effective algorithm, it can suffer from some drawbacks, such as oscillations around the MPP, slow tracking of rapid changes in irradiance, and reduced efficiency under temperature variation condition. The new MPPT control strategy for a solar PV system, based on passivity control, is presented. The goal of this study is to enhance the efficiency and stability of MPPT in PV systems by integrating the P&O algorithm with Interconnection and Damping Assignment Passivity-Based Control (IDA-PBC). Methodology. The new MPPT P&O PBC strategy aims to extract maximum power from the PV system in order to improve its efficiency under some conditions such as the variations of the temperature, the irradiation and the load. IDA-PBC is employed to design a Lyapunov asymptotically stable controller using the Hamiltonian structural properties of the open-loop model of the system. Also, with minimization of the energy dissipation in boost converter of the PV system to illustrate the modification of energy and generate a specify duty cycle applied to the converter. The results with MATLAB clearly demonstrate the advantages of the proposed MPPT P&O PBC, showcasing its high performance in effectively reducing oscillations in various steady states of the PV system, ensuring minimal overshoot and a faster response time. Scientific novelty. Key contributions include methodological improvements such as dynamic adjustment of the cycle for boost converter and a new approach to partner selection, which significantly optimizes the algorithm's performance. Practical value. A comparative analysis of the proposed MPPT controller against conventional algorithms shows that it offers a fast dynamic response in finding the maximum power with significantly less oscillation around the MPP. References 46, tables 2, figures 13.

Key words: photovoltaic generator, boost converter, passivity-based control, port-controlled Hamiltonian, maximum power point tracking.

Вступ. Генерація електроенергії з відновлюваних джерел, таких як фотоелектричні (РV) системи, набуває все більшого значення як заміна викопного палива. Точка максимальної потужності (МРР) РУ системи зміщується вздовж кривої залежності потужності від напруги в залежності від навколишнього середовища. Незважаючи на використання алгоритмів відстеження точки максимальної потужності (MPPT), зсув MPP призводить до зниження продуктивності PV системи. **Проблема**. MPPT алгоритм Perturb & Observe (P&O) ϵ простим і ефективним алгоритм, але він може мати недоліки, такі як коливання біля MPP, повільне відстеження швидких змін освітленості та зниження ефективності в умовах коливань температури. Представлено нову стратегію управління MPPT для сонячної PV системи, засновану на пасивному управлінні. **Метою** дослідження ϵ підвищення ефективності та стабільності MPPT у PV системах шляхом інтеграції алгоритму P&O з пасивним керуванням на основі міжз'єднання та призначення демпфування (IDA-PBC). Методологія. Нова стратегія MPPT P&O PBC спрямована на отримання максимальної потужності з PV системи для підвищення її ефективності в певних умовах, таких як коливання температури, випромінювання та навантаження. IDA-PBC використовується для розробки асимптотично стійкого регулятора Ляпунова з використанням гамільтонових структурних властивостей моделі системи з відкритим контуром. Також, з мінімізацією розсіювання енергії у підвищувальному перетворювачі PV системи, щоб проілюструвати зміну енергії та сформувати заданий робочий цикл, що застосовується до перетворювача. Результати, отримані в МАТLAB, показали переваги запропонованої стратегії МРРТ Р&О РВС, демонструючи її високу ефективність щодо зниження коливань у різних стаціонарних станах РУ системи, забезпечуючи мінімальне перерегулювання та швидший час відгуку. Наукова новизна. Ключові досягнення включають методологічні удосконалення, такі як динамічне налаштування циклу для підвищувального перетворювача, і новий підхід до вибору партнерів, що значно оптимізує продуктивність алгоритму. Практична цінність. Порівняльний аналіз МРРТ-контролера з традиційними алгоритмами показує, що він забезпечує швидкий динамічний відгук при пошуку максимальної потужності зі значно менишми коливаннями біля МРР. Бібл. 46, табл. 2, рис. 13.

Ключові слова: фотоелектричний генератор, підвищувальний перетворювач, пасивне керування, гамільтоніан з керуванням портами, відстеження точки максимальної потужності.

Introduction. The transition away from fossil fuelbased energy sources has been accelerated by concerns about global warming and the depletion of traditional resources. As a result of this shift, governments and industries worldwide are exploring alternative energy solutions to meet growing demands sustainably [1]. The current era is characterized by the fast renewable energy sources (RESs) growth as a key component of addressing the escalating global energy demand. The move toward RESs is driven by a number of reasons, including environmental concerns, modern technologies economic viability [2]. A growing number of RESs are emerging across the globe, including biogas, wave energy, solar energy, and wind energy. Solar energy in particular is projected to fulfill one-third of the world's electricity demand by 2060. Unlike other RESs, such as wind and hydroelectric energy, solar energy is not limited

by geographic availability, making it abundantly accessible worldwide.

Generally, solar energy stands out as the most reliable and effective solution for mitigating the issue of global warming [1, 2]. Its abundant availability, renewable nature, and environmentally friendly attributes make it a key player in efforts to combat climate change. Additionally, solar power systems produce no greenhouse gas emissions during operation, unlike traditional fossil fuel-based energy sources, thereby significantly reducing the carbon footprint associated with energy production. This underscores the importance of harnessing solar energy as a sustainable alternative to conventional power sources in the fight against global warming [3].

Moreover, photovoltaic (PV) panels are distinguished by their ease of use and installation, cost-

© A. Toualbia, A.B. Djilali, R. Taleb, N. Mansour, M. Souaihia, H. Saidi

effectiveness, and minimal maintenance requirements [4]. They find applications in various sectors such as water pumping systems, aeronautical applications, and battery chargers [5]. These features contribute to the widespread adoption of PV technology across different industries and sectors. The PV panel yields energy is subject to the temperature influence and solar irradiation, resulting in the nonlinear behavior of the panel [6]. This nonlinear behavior arises due to the complex interaction between the panel temperature, incident solar radiation, and the material properties of the PV cells [7, 8]. Achieving a PV panel's maximum power point (MPP) under climatic changes, while ensuring reliability and cost-effectiveness, has been a substantial research challenge. Consequently, numerous studies have been conducted to explore potential solutions to this issue [9, 10].

Energy consumption has increased due to the widespread use of electricity. The problem of energy conversion and storage has led to research and development of new supply sources [11, 12]. This interest grew in response the inevitable exhaustion of fossil fuels, their environmental impact, and the waste they generate. In the era of sustainable development, PV is rapidly progressing due to its significant potential as a RES capable of producing electricity by converting a portion of solar irradiation through a PV cell [13, 14]. PV panels have specific nonlinear electrical characteristics and, therefore, a special operating point called the MPP. Among the most widely employed MPP tracking (MPPT) algorithms in the PV literature is the extreme algorithm known as Perturb & Observe (P&O). This algorithm works by continuously perturbing the PV operating point and monitoring the resulting variation in electrical output or current to determine the direction that leads to the MPP. Despite its simplicity and common usage, P&O may exhibit fluctuations around the MPP under certain conditions, leading to suboptimal performance in dynamic environments.

According to [15], P&O control forces the operating point to oscillate about the MPP at steady state due to the periodic MPP search procedure repetition, causing the system to continuously oscillate to the MPP. This behavior contributes to power transfer losses. In cases of infrequent climate changes, especially abrupt changes in irradiation levels, this algorithm may track in the wrong direction and generate further power loss. Authors [16] proposed modular solutions using a PI controller for PV-DC choppers to monitor the MPPT algorithm. Conventional analysis of the system's stability and dynamic performance is difficult, making it necessary to operate the system at a chosen point and proceed with successive linearization to simplify the nonlinearity issues [17]. The work [17] introduces an MPPT technique based on the Interconnection and Damping Assignment Passivity-Based Control (IDA-PBC). The primary principle of the IDA-PBC controller is to regulate the overall power of the system to maintain stability around an equilibrium point [18]. According to published works, IDA-PBC controllers have shown promising results in various applications because they ensure stability and optimize performance in dynamic systems. Table 1 compares conventional, modern and hybrid categories MPPT control algorithms, highlighting their advantages and disadvantages.

Our contribution is focused on the application of the P&O-MPPT in conjunction with the IDA-PBC, using the

boost converters. There are several key objectives served by this combination.

Table 1

Advantages and disadvantages of MPPT control

	Advantages and dis	sadvantages of MP	P1 control
Type	Algorithm	Advantages	Disadvantages
S	P&O [19],	Easy to	Steady state
hm	incremental	implement,	oscillation, no
)rrit	resistance [20],	simple structure,	guarantee for
lgc	climbing [21],	and low-cost	convergence, drift
al a	incremental		problem, reduced
ons	conductance [22],		efficiency
nti	voltage/short circuit		
nve	current [23], hill and		
Conventional algorithms	fractional open		
	circuit [24]		
	Particle swarm	Robust, no	Large search
Modern algorithms	optimization (PSO)	steady-state and	space, high cost
ith	[25], grey wolf	transient	
g01	optimization [26],	oscillations, high	
al	cuckoo search [27],	tracking	
ern	fuzzy logic control	efficiency, and	
po	[28], sliding mode	few parameters	
Σ	control [29], particle	require turning	
	swarm [30]		
35	P&O-humpback	Higher tracking	High cost,
thn	whale [31],	accuracy	difficult to control
ori	P&O-ant-colony	reduced power	
alg	optimization [32],	oscillation, and	
Hybrid algorithms	P&O-PSO [33]	tracking	
ybr		efficiency is	
Ħ.		higher than 98 %	

It facilitates the efficient capture of the MPP of solar panels even under fluctuating climate conditions and varying loads. This capability ensures optimal energy extraction from the solar array.

By reducing undulations around the MPP, the system's stability is significantly enhanced. This stability is crucial for maintaining consistent and reliable power generation from the PV system.

The integration of IDA-PBC with the boost converters leads to a reduction in energy losses. As a result, not only does the system become more efficient, but also costs are reduced, making the system more economically viable.

Additionally, this approach improves the system's response time, allowing it to adapt quickly to changes in environmental conditions or load requirements. This responsiveness ensures that the system operates at peak performance levels, maximizing energy production. Moreover, the boost converter's ability to raise voltage levels further enhances the system's efficiency by minimizing the need for a series connection of solar panels. This feature simplifies system design and installation while also reducing overall system costs.

By integrating the P&O-MPPT with IDA-PBC, this work provides a comprehensive solution to optimize PV system performance. With its ability to address power capture efficiency, stability, energy losses, response time, and system complexity, this approach holds significant promise for advancing solar energy utilization.

The **goal** of this study is to enhance the efficiency and stability of MPPT in PV systems by integrating the P&O algorithm with IDA-PBC. Unlike previous approaches that relied on traditional P&O [19], incremental resistance [20], climbing [21], incremental

conductance [22], voltage/short circuit current [23], hill and fractional open circuit [24], this study introduces a novel strategy combining passivity theory and dynamic voltage tracking to improve convergence speed and reduce power oscillations.

PV system modeling. Figure 1 depicts the system under study. It consists of a PV generator (PVG) that supplies power to a load through a boost converter, which acts as an impedance stage. The boost converter and the load together influence the PVG (PVG operating point under changing climatic conditions). IDA-PBC is proposed to address the P&O voltage output behavior issue at steady-state caused by load variations.

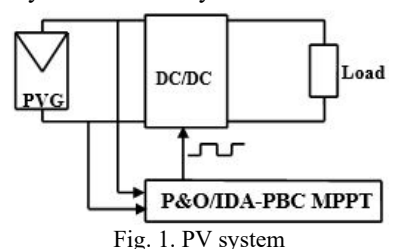


Figure 2 shows a PV cell single-diode model, operating within the 1st quadrant of the current-voltage characteristics [34, 35].

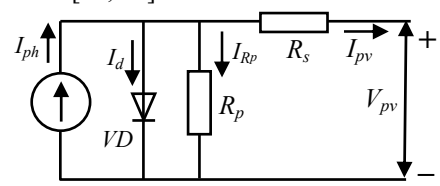


Fig. 2. Electrical equivalent model of PV module

The mathematical model for the same situation is:

$$I = I_{ph} - I_0 \left[\exp \left(\frac{q(V + I \cdot R_s)}{A \cdot k \cdot T} \right) - 1 \right] - \frac{V + I \cdot R_s}{R_p}, \quad (1)$$

where I_{ph} is the cell photocurrent; I_0 is the diode saturation current; R_s is the series resistance; R_p is the shunt resistance; q is the electron charge; I is the PV cell current; V is the PV cell output voltage; k is the Boltzmann constant; A is the diode ideality factor; T is the temperature.

Figure 3 illustrates the boost converter scheme. Output voltage V_{ch} is linked to its input voltage V [36, 37]:

$$V_{ch}/V = 1/(1-\mu),$$
 (2)

where μ is the carrier signal controlling the energy switch duty cycle in the boost converter.

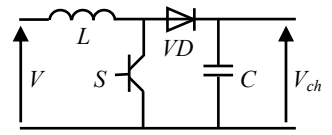


Fig. 3. The boost converter scheme

The boost converter model is:

$$\begin{cases} \dot{x}_1 = -\frac{1}{L}\mu x_2 + \frac{1}{L}V; \\ \dot{x}_2 = -\frac{1}{R_{ch}}x_2 + \frac{1}{C}\mu x_1, \end{cases}$$
 (3)

where $x_1 = I_L$ is the inductor current, which corresponds to the PVG current; $x_2 = V_{ch}$ is the boost converter output voltage, which corresponds to the load voltage.

Traditional P&O MPPT algorithm. Several techniques are commonly utilized for MPPT in PV systems. Among these techniques are:

- 1) P&O. This technique involves perturbing the operating point of the PV and observing the resulting change in energy output. The operating point is then adjusted accordingly to approach the MPP.
- 2) Incremental conductance. This strategy utilizes the incremental conductance of the PV system to determine the direction in which the operating point should be adjusted to approach the MPP. It is particularly effective in tracking the MPP under rapidly changing environmental conditions.
- 3) Constant voltage. In this approach, the voltage across the PV system is maintained at a constant value, and the current is adjusted accordingly to maximize power output. This method is suitable for applications where maintaining a stable voltage is critical.
- 4) Constant current. Similar to the constant voltage technique, the constant current technique maintains a constant current output from the PV system and adjusts the voltage to maximize energy output. It is often used in applications where a stable current supply is required.

These MPPT techniques vary in their complexity, performance under different operating conditions, and hardware requirements. Researchers continue to explore and develop MPPT methods to ameliorate the PV systems efficiency and reliability [38, 39].

The P&O method is widely regarded as the simplest and most useful MPPT technique in the field of PV systems due to its straightforwardness and ease of application. The fundamental principle of P&O involves applying a perturbation to the voltage of the operating point and then observing the resultant impact on power. If the energy increases, the P&O control is moving the search in the correct direction (right) to track the true MPP. It is evident that the disturbance has shifted the operating point toward this MPP. The P&O algorithm will persist in disturbing the voltage in the similar way. Conversely, if the energy decreases, the disturbance has moved the operating point away from the true MPP, necessitating a reversal in direction [40].

Figure 4 shows the P&O control flowchart [41]. The P&O offers the advantage of being straightforward to implement in software or into microcontrollers. However, as drawbacks, it oscillates around the MPP, which introduces power losses and presents slow response times in reaching the MPP. It may even track in the wrong direction under rapid changes in irradiance.

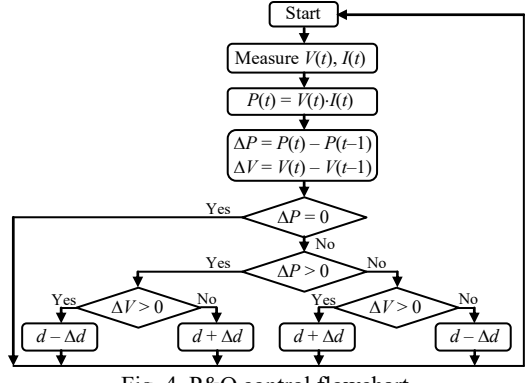


Fig. 4. P&O control flowchart

The enhanced P&O MPPT algorithm, as proposed, builds upon the conventional algorithm by incorporating an IDA-PBC controller. This controller aims to minimize the error between the PV voltage and the voltage produced by the MPPT block. The models are simulated, and the different results are presented next.

Proposed MPPT design strategy. The enhanced IDA-PBC is presented here for a DC-DC boost converter using a P&O algorithm, modeled using a passivity-based control Hamiltonian system framework. The proposed nonlinear regulator guarantees system stability and rapid response even under significant load disturbances and variations in illumination levels. This enhancement builds upon the traditional P&O method, offering improved performance and robustness in PV systems.

Model of DC-DC converter with IDA-PBC control. The PBC establishes a regulator design methodology aimed at stabilizing the system by rendering it passive [42, 43]. This approach ensures a stable and well-behaved system response. The IDA-PBC approach involves identifying the system's natural energy function, referred to as H(x), where the inductor and capacitor total energy are represented by the Hamiltonian function.

The port-controlled Hamiltonian system is derived from the following equation:

$$\begin{cases} \dot{x} = [J(x) - R(x)]\nabla H + g(x)u; \\ v = g^{T}(x)\nabla H. \end{cases}$$
 (4)

Stabilization in the IDA-PBC control is attained by targeting the closed-loop dynamics [44]:

$$\begin{cases} \dot{x} = \begin{bmatrix} J_d(x) - R_d(x) \end{bmatrix} \nabla H_d; \\ y = g^T(x) \nabla H_d, \end{cases}$$
 (5)

where $H_d(x)$ is the desired total power function that reaches its minimum at x^* , while $J_d = -J_d^T$ and $R_d = R_d^T \ge 0$ are the wanted interconnection and damping matrices respectively.

The boost converter depicted in Fig.3 is represented by its averaged model, which is given by:

$$\begin{pmatrix} L & 0 \\ 0 & C \end{pmatrix} \dot{x} = \begin{pmatrix} 0 & -\mu \\ \mu & 0 \end{pmatrix} - \begin{pmatrix} 0 & 0 \\ 0 & \frac{1}{R_{Ch}} \end{pmatrix} x + \begin{pmatrix} V \\ 0 \end{pmatrix}, \quad (6)$$

where:

$$x = \begin{pmatrix} x_1 \\ x_2 \end{pmatrix} = \begin{pmatrix} L \cdot i \\ C \cdot V_{ch} \end{pmatrix} = D \begin{pmatrix} i_L \\ V_{ch} \end{pmatrix}. \tag{7}$$

The control objective is to maintain internal stability while regulating the generator voltage to the desired optimal value. This entails stabilizing the desired equilibrium point x^* . So that the wanted equilibrium point is [45]:

$$x^* = (x_1^*, x_2^*) = \left(\frac{L \cdot V^2}{R \cdot E}, C \cdot V_d\right),$$
 (8)

where V_d is the output MPPT-P&O voltage delivered to the passivity block command system. The boost converter dynamic can be expressed in the form of port-controlled Hamiltonian (4). To achieve this, the Hamiltonian function of the boost can be described as [46]:

$$H(x) = \frac{1}{2} \frac{x_1^2}{L} + \frac{1}{2} \frac{x_2^2}{C} = \frac{1}{2} x^T D^{-1} x;$$
 (9)

and

$$J = \begin{pmatrix} 0 & -\mu \\ \mu & 0 \end{pmatrix}, \quad R = \begin{pmatrix} 0 & 0 \\ 0 & 1/R_{Ch} \end{pmatrix}, \quad E = \begin{pmatrix} V \\ 0 \end{pmatrix}.$$

Hence, the damping matrix is modified as bellow:

$$R_d = R + R_a, (10)$$

where R_a is the damping matrix added by the controller.

The aim is to represent the boost converter dynamics as the Port-Hamiltonian system:

$$\dot{x} = \left[J_d(\mu) - R_d \right] \frac{\partial H_d}{\partial x} (x). \tag{11}$$

The new $H_d(x)$ exhibits a local minimum at the desired equilibrium point x^* . That:

$$H_d = H + H_a, \tag{12}$$

 $H_d = H + H_a$, (12) The primary aim of the IDA-PBC is to determine a command $\mu(x)$, R_a , $J_a(\mu)$ and a vector K(x) satisfying the partial differential equation:

$$\left[J_d(\mu) - R_d\right] K(x) = R_a \frac{\partial H}{\partial x}(x) + gE, \qquad (13)$$

where:

$$K(x) = \frac{\partial H_a}{\partial x}(x). \tag{14}$$

Verifying:

$$\frac{\partial K}{\partial x}(x) = \left[\frac{\partial K}{\partial x}(x)\right]^T. \tag{15}$$

From (16), result

$$\dot{H}_{d} = -\left[\frac{\partial H_{d}}{\partial x}(x)\right]^{T} R_{d} \frac{\partial H_{d}}{\partial x}(x) \le 0.$$
 (16)

It has an asymptotically stable equilibrium at x^* if:

$$\left[\frac{\partial H_d}{\partial x}(x)\right]^T R_d \frac{\partial H_d}{\partial x}(x) = 0 \Rightarrow x = x^*.$$
 (17)

The desired power function is expressed as:

$$\dot{H}_d = \frac{1}{2} \left(x - x^* \right)^T D^{-1} \left(x - x^* \right). \tag{18}$$

The coefficient matrices and vector are:

$$J_a(x) = 0 ; (19)$$

$$R_a = \begin{bmatrix} r_1 & 0 \\ 0 & r_2 \end{bmatrix}; \tag{20}$$

$$\dot{H}_{d} = \frac{1}{2} (x - x^*)^T D^{-1} (x - x^*).$$
 (21)

$$\frac{\partial H}{\partial x}(x) = D^{-1}x$$
 and $K(x) = \frac{\partial H_a}{\partial x}(x) = -D^{-1}x^*$.

Inserting (14) into (11) results to

$$[J_d \quad R_d] D^{-1} x^* = -[J_a - R_a] D^{-1} x + gE . \quad (22)$$

From (22), the dynamic duty ratio is:

$$\mu = \frac{1}{V_{d}} \left(r_{1} \left(i - i^{*} \right) + V_{PV} \right). \tag{23}$$

Using (23) we can compute the converter duty cycle required to maximize the power from the PVG.

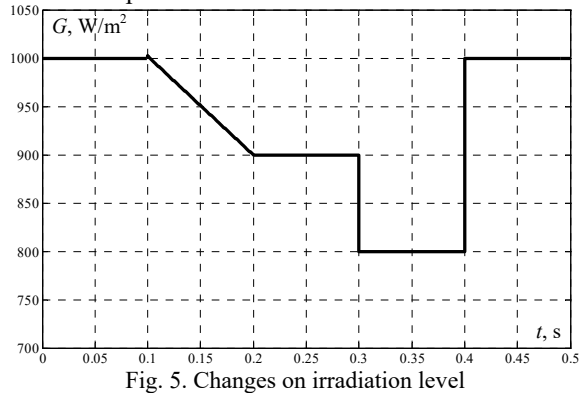
Results. To assess the enhanced PV performance (Fig. 1), MATLAB software was used. The PV system parameters are listed in Table 2. A comparative study was undertaken to evaluate 3 different MPPT techniques: P&O, P&O with PI control, and P&O with an IDA-based PBC algorithm. This comparison focuses on the efficiency

and dynamic response characteristics of each technique during a simulation time t = 0.5 s. Notably, all results were obtained under a dynamic load condition of 40Ω .

Table 2
The PVG module parameters

Parameters	Rated value
Short-circuit current I_{cc} , A	3.24
Maximum energy P_{max} , W	62.2
Open-circuit voltage V_{co} , V	24.93
Current I_{mp} at P_{max} , A	3.04
Voltage V_{mn} at P_{max} , V	20.21

Influence of variation in solar irradiation. The variation in irradiation levels is modeled according to the function shown in Fig. 5, while the temperature remains constant at 25 °C throughout the simulations. The results of the simulations for power, voltage and current are depicted individually for each of the 3 MPPT algorithms in Fig. 6–8, respectively. Additionally, it is worth mentioning that the variation in irradiation levels, as represented by the function in Fig. 5, plays a significant role in determining the PV system performance under different conditions. By keeping the temperature fixed at 25 °C, the focus of the analysis is directed toward the impact of irradiation level changes on the system's power generation capabilities.



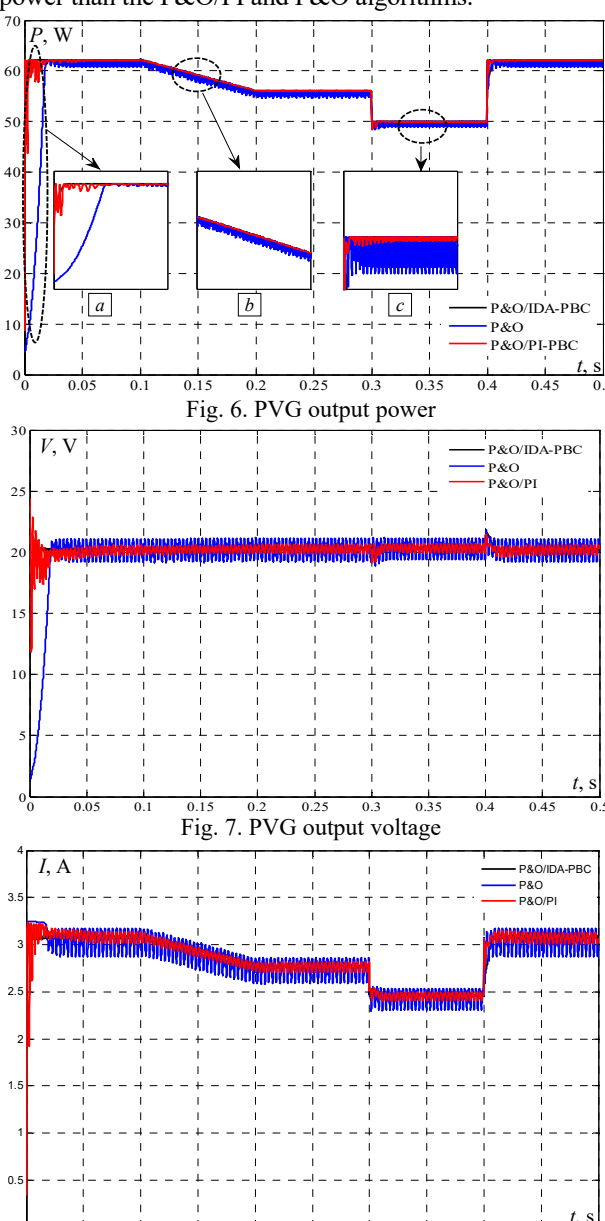
Furthermore, the simulation results presented in Fig. 6–8 offer a comprehensive comparison of the effectiveness and efficiency of the MPPT algorithms under consideration. By examining the variations in power, voltage and current across different irradiation levels, insights can be gained into the dynamic response and overall performance characteristics of each MPPT technique.

Overall, these simulation results provide valuable information for optimizing the operation of PV systems under varying environmental conditions, thereby contributing to the advancement of RES technologies.

In Fig. 6 (zoom *a*), it can be observed that the output energy of the PVG controlled by the P&O/IDA-PBC reaches the MPP at 4.2 ms, compared to the P&O/PI and P&O, which achieve the same MPP at 20 ms and 25 ms, respectively. The P&O/IDA-PBC provides the best tracking of maximum power and voltage compared to the P&O/PI and P&O.

As can be seen in Fig. 6 (zoom b), the P&O/PI and P&O continue to perturb the system in the same direction, resulting in large energy losses during the linear decrease in radiation levels from 1000 W/m² to 900 W/m². However, the P&O/IDA-PBC overcomes this behavior by significantly reducing undulations around the MPP, thus

minimizing energy losses. At the end of the simulation time (0.4-0.5 s) in Fig. 6 (zoom c), as the irradiation level increases to 1000 W/m^2 , it can be observed that the P&O/IDA-PBC controls the PVG to maintain more stable power than the P&O/PI and P&O algorithms.

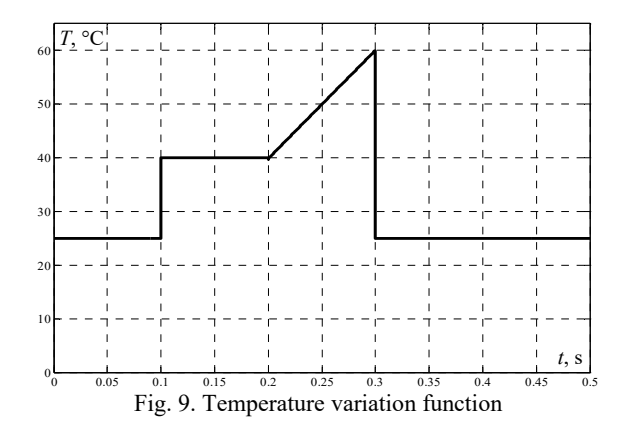


The percentage reduction in energy of the PVG output power is 2.49 % (P&O), 0.43 % (P&O/PI) and 0.014 % (P&O/IDA-PBC).

Fig. 8. PVG output current

As shown in Fig. 7, the ripple rates in PVG voltage are 6.43 % (P&O), 5.19 % (P&O/PI) and 0.44 % (P&O/IDA-PBC). For the PVG current, these rates are 6.18 %, 1.95 % and 0.29 %, respectively. The proposed strategy demonstrates the best control performance of the PV system, as it achieves the fastest MPPT speed with the least fluctuations and energy losses under the influence of variations in solar irradiation.

Influence of temperature variations. The variation in temperature is modeled according to the function illustrated in Fig. 9, while the solar irradiation remains constant at 1000 W/m² throughout the simulations.



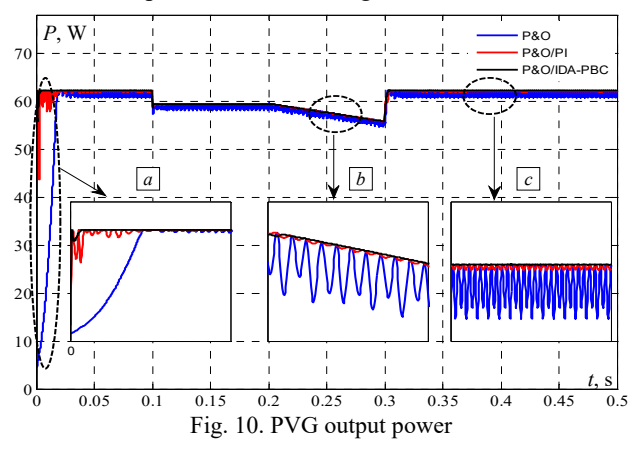
Figures 10–12 show the simulation results for the PV system's output power, voltage and current, controlled by the 3 algorithms under consideration. These results provide insights into how changes in temperature impact the performance of the MPPT and its ability to optimize the energy output of the PV system.

Moreover, the simulation results comparison obtained from the 3 MPPT algorithms allows for a comprehensive evaluation of their efficiency and effectiveness under varying temperature conditions.

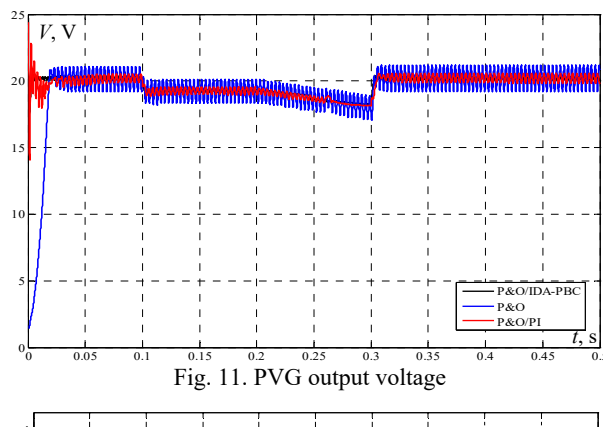
In Fig. 10 (zoom *a*), the MPP is reached after 4.2 ms for the P&O/IDA-PBC and after 20 ms and 25 ms for the other MPPTs. These results show that the P&O/IDA-PBC converges very quickly to the MPP compared to the P&O/PI and P&O.

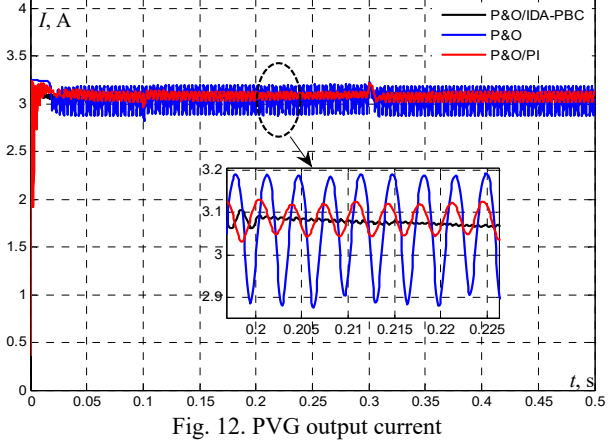
At the time interval 0.2–0.3 s in Fig. 10 (zoom b), when the temperature increases linearly from 40 °C to 60 °C, it can be noticed that the P&O/IDA-PBC algorithm tracks the MPP in the correct direction and exhibits fewer oscillations compared to the P&O/PI and P&O.

Figure 10 (zoom c) shows that at the simulation interval 0.4–0.5 s, the efficiency of the system controlled by P&O/IDA-PBC is 99.97 %, compared to 99.7 % (P&O/PI) and 97.59 % (P&O). This demonstrates that the PVG output power oscillation in P&O/IDA-PBC is more reduced compared to the P&O algorithm.



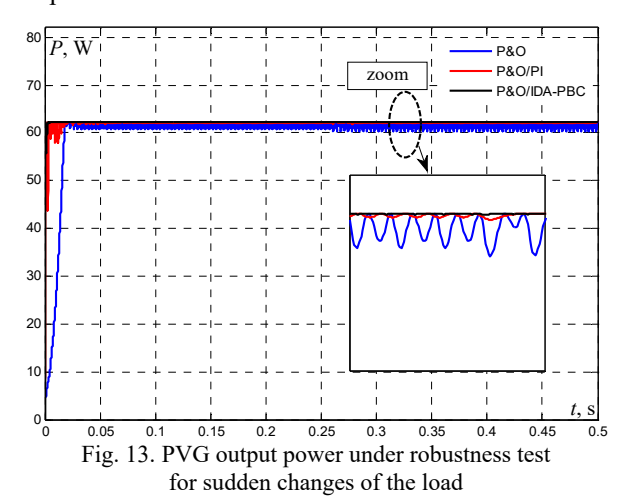
In Fig. 11 the ripple PVG voltage rate are 5.09 % (P&O), 2.52 % (P&O/PI) and 0.74 % (P&O/IDA-PBC). In Fig. 12, the ripple PVG current rate are 6.51 % (P&O), 1.62 % (P&O/PI) and 0.48 % (P&O/IDA-PBC). These results also prove that enhancing P&O with a PBC strategy significantly reduces oscillations and is more efficient than the P&O.





Abrupt increase in load. The performance evaluation of the system during a load variation at a fixed temperature of 25 °C and irradiation of 1000 W/m² is shown in Fig. 13. An abrupt increase in the load was applied by adding a resistor of 5 Ω at t = 0.26 s.

The results show that the use of P&O/IDA-PBC is the most effective compared to P&O and P&O/PI. As shown in Fig. 13 (zoom), the P&O/IDA-PBC ensures a very fast convergence to the MPP, with almost no oscillations around the MPP and, hence, less losses. It is to remark that when the value of the load increases, the decrease in power is important. Furthermore, the system controlled by P&O/IDA-PBC has 99.99 % efficiency compared with the P&O and P&O/PI algorithms are 96.95 % and 99.57 % respectively. It can be concluded that the P&O/IDA-PBC exhibits superior characteristics compared to P&O and P&O/PI.



Conclusions. Multiple MPPT algorithms were employed to optimize the PVG energy output. Among these algorithms, the P&O exhibits drawbacks such as inadequate support for sudden variations in irradiation levels and oscillations in power around the actual MPP. The passivity-based control strategy represents a viable approach for enhancing the P&O algorithm.

This work demonstrates the feasibility of leveraging passivity-based control strategies to enhance the characteristics of the P&O technique. Passivity theory has been applied in detail to the boost converter, which serves as an adjustment stage between the load and the PVG. The P&O delivers the measured reference voltage to the designed passivity block in order to significantly improve system efficiency. By applying passivity theory, we developed a P&O variant based on passivity, named the P&O/IDA-PBC technique.

Simulations were performed by comparing the efficiency of the studied system using 3 types of MPPTs: P&O/PI, classical P&O, and the proposed P&O/IDA-PBC. The results support that IDA-PBC greatly improves P&O performance, reduces power losses caused by ripples in the power of the operating MPP, and considerably increases convergence time. It is also worth noting that P&O/IDA-PBC is more robust than P&O/PI and classical P&O, as demonstrated by a set of tests, including temperature dependence on irradiation levels, abrupt variations in irradiation, and changes in load.

According to the simulated results, it can be concluded that the P&O/IDA-PBC method can correctly track the MPP under various operating conditions, providing the best efficiency in tracking the MPP, minimizing power loss, reducing oscillations around the MPP, and ensuring a more stable operating point compared to classical P&O and P&O/PI. Future work involves the practical implementation using the process in the loop technique to test and validate the proposed P&O/IDA-PBC method performance.

Conflict of interest. The authors declare that they have no conflicts of interest.

REFERENCES

- I. Ruffini A., Salerno A., Simões F. Net-zero emissions: Main technological, geopolitical, and economic consequences of the new energy scenario. SSRN Electronic Journal, 2022. doi: https://doi.org/10.2139/ssrn.3998525.
- **2.** Halkos G.E., Gkampoura E.-C. Reviewing Usage, Potentials, and Limitations of Renewable Energy Sources. *Energies*, 2020, vol. 13, no. 11, art. no. 2906. doi: https://doi.org/10.3390/en13112906.
- 3. Awasthi A., Shukla A.K., Murali Manohar S.R., Dondariya C., Shukla K.N., Porwal D., Richhariya G. Review on sun tracking technology in solar PV system. *Energy Reports*, 2020, vol. 6, pp. 392-405. doi: https://doi.org/10.1016/j.egyr.2020.02.004.
- 4. Reindl K., Palm J. Installing PV: Barriers and enablers experienced by non-residential property owners. *Renewable and Sustainable Energy Reviews*, 2021, vol. 141, art. no. 110829. doi: https://doi.org/10.1016/j.rser.2021.110829.
- 5. Al-Amayreh M.I., Alahmer A., Manasrah A. A novel parabolic solar dish design for a hybrid solar lighting-thermal applications. *Energy Reports*, 2020, vol. 6, pp. 1136-1143. doi: https://doi.org/10.1016/j.egyr.2020.11.063.
- 6. Djilali A., Yahdou A., Bounadja E., Mehedi F. Stopping the Drift Problem in the Tracking of Maximum Power Point for Photovoltaic System by Using Modified Variable Step Size Incremental Conductance Method. *European Journal of Electrical Engineering*, 2020, vol. 22, no. 3, pp. 273-283. doi: https://doi.org/10.18280/ejee.220308.

- 7. Necaibia S., Kelaiaia M.S., Labar H., Necaibia A., Castronuovo E.D. Enhanced auto-scaling incremental conductance MPPT method, implemented on low-cost microcontroller and SEPIC converter. *Solar Energy*, 2019, vol. 180, pp. 152-168. doi: https://doi.org/10.1016/j.solener.2019.01.028.
- 8. Jedari Zare Zadeh M., Fathi S.H. A New Approach for Photovoltaic Arrays Modeling and Maximum Power Point Estimation in Real Operating Conditions. *IEEE Transactions on Industrial Electronics*, 2017, vol. 64, no. 12, pp. 9334-9343. doi: https://doi.org/10.1109/TIE.2017.2711571.
- 9. Alik R., Jusoh A. Modified Perturb and Observe (P&O) with checking algorithm under various solar irradiation. *Solar Energy*, 2017, vol. 148, pp. 128-139. doi: https://doi.org/10.1016/j.solener.2017.03.064.
- 10. Belkaid A., Colak I., Kayisli K. Implementation of a modified P&O-MPPT algorithm adapted for varying solar radiation conditions. *Electrical Engineering*, 2017, vol. 99, no. 3, pp. 839-846. doi: https://doi.org/10.1007/s00202-016-0457-3.
- Al-Majidi S.D., Abbod M.F., Al-Raweshidy H.S. A novel maximum power point tracking technique based on fuzzy logic for photovoltaic systems. *International Journal of Hydrogen Energy*, 2018, vol. 43, no. 31, pp. 14158-14171. doi: https://doi.org/10.1016/j.ijhydene.2018.06.002.
 John R., Mohammed S.S., Zachariah R. Variable step size Perturb
- and observe MPPT algorithm for standalone solar photovoltaic system. 2017 IEEE International Conference on Intelligent Techniques in Control, Optimization and Signal Processing (INCOS), 2017, pp. 1-6. doi: https://doi.org/10.1109/ITCOSP.2017.8303163.
- 13. Lachtar S., Bouraiou A., Djaafri O., Maouedj R. Smooth Sliding Mode-Based MPPT Algorithm for Photovoltaic Applications. 2019 1st Global Power, Energy and Communication Conference (GPECOM), 2019, pp. 253-258. doi: https://doi.org/10.1109/GPECOM.2019.8778484.
 14. Yilmaz U., Kircay A., Borekci S. PV system fuzzy logic MPPT method and PI control as a charge controller. Renewable and Sustainable Energy Reviews, 2018, vol. 81, pp. 994-1001. doi: https://doi.org/10.1016/j.rser.2017.08.048.
- 15. Li H., Yang D., Su W., Lu J., Yu X. An Overall Distribution Particle Swarm Optimization MPPT Algorithm for Photovoltaic System Under Partial Shading. IEEE Transactions on Industrial Electronics, 2019, vol. 66, no. 1, pp. 265-275. doi: https://doi.org/10.1109/TIE.2018.2829668.
- 16. Xu D., Wang G., Yan W., Yan X. A novel adaptive command-filtered backstepping sliding mode control for PV grid-connected system with energy storage. Solar Energy, 2019, vol. 178, pp. 222-230. doi: https://doi.org/10.1016/j.solener.2018.12.033.
- 17. Al-Dhaifallah M., Nassef A.M., Rezk H., Nisar K.S. Optimal parameter design of fractional order control based INC-MPPT for PV system. Solar Energy, 2018, vol. 159, pp. 650-664. doi: https://doi.org/10.1016/j.solener.2017.11.040.
- 18. Ferdous S.M., Shafiullah G.M., Oninda M.A.M., Shoeb M.A., Jamal T. Close loop compensation technique for high performance MPPT using ripple correlation control. 2017 Australasian Universities Power Engineering Conference (AUPEC), 2017, pp. 1-6. doi: https://doi.org/10.1109/AUPEC.2017.8282429.
- 19. Lashab A., Sera D., Guerrero J.M. A Dual-Discrete Model Predictive Control-Based MPPT for PV Systems. *IEEE Transactions on Power Electronics*, 2019, vol. 34, no. 10, pp. 9686-9697. doi: https://doi.org/10.1109/TPEL.2019.2892809.
- 20. Rezk H., Fathy A. Performance Improvement of PEM Fuel Cell Using Variable Step-Size Incremental Resistance MPPT Technique. Sustainability, 2020, vol. 12, no. 14, art. no. 5601. doi: https://doi.org/10.3390/su12145601.
- 21. Jately V., Azzopardi B., Joshi J., Venkateswaran B.V., Sharma A., Arora S. Experimental Analysis of hill-climbing MPPT algorithms under low irradiance levels. *Renewable and Sustainable Energy Reviews*, 2021, vol. 150, art. no. 111467. doi: https://doi.org/10.1016/j.rser.2021.111467.
- 22. Bakar Siddique M.A., Asad A., Asif R.M., Rehman A.U., Sadiq M.T., Ullah I. Implementation of Incremental Conductance MPPT Algorithm with Integral Regulator by Using Boost Converter in Grid-Connected PV Array. *IETE Journal of Research*, 2023, vol. 69, no. 6, pp. 3822-3835. doi: https://doi.org/10.1080/03772063.2021.1920481.
- 23. Ibrahim H.H., Elsaharty M.A., Guerrero J.M., Walid Ghoneim A.M. A Smart MPPT Algorithm with a Power Independent Tracking

- System. 2022 International Conference on Electrical, Computer and Technologies (ICECET). 2022. 1-8. Energy https://doi.org/10.1109/ICECET55527.2022.9872662.
- 24. Sarkar P.R., Minai A.F., Bhaskar M.S., Pachauri R.K., Sashikant. Examination of MPPT Algorithm on Three Step DC-DC Converter. 2022 IEEE 9th Uttar Pradesh Section International Conference on Electrical, Electronics and Computer Engineering (UPCON), 2022, pp. 1-6. doi: https://doi.org/10.1109/UPCON56432.2022.9986394
- 25. Hayder W., Ogliari E., Dolara A., Abid A., Ben Hamed M., Sbita L. Improved PSO: A Comparative Study in MPPT Algorithm for PV System Control under Partial Shading Conditions. Energies, 2020, vol. 13, no. 8, art. no. 2035. doi: https://doi.org/10.3390/en13082035.
- 26. Motamarri R., Bhookya N., Chitti Babu B. Modified grey wolf optimization for global maximum power point tracking under partial shading conditions in photovoltaic system. International Journal of Circuit Theory and Applications, 2021, vol. 49, no. 7, pp. 1884-1901. doi: https://doi.org/10.1002/cta.3018.
- 27. Abo-Elyousr F.K., Abdelshafy A.M., Abdelaziz A.Y. MPPT-Based Particle Swarm and Cuckoo Search Algorithms for PV Systems. Green and Technology, 379-400. 2020, pp. Energy https://doi.org/10.1007/978-3-030-05578-3 14.
- 28. Hassan T., Abbassi R., Jerbi H., Mehmood K., Tahir M.F., Cheema K.M., Elavarasan R.M., Ali F., Khan I.A. A Novel Algorithm for MPPT of an Isolated PV System Using Push Pull Converter with Fuzzy Logic Controller. Energies, 2020, vol. 13, no. 15, art. no. 4007. doi: https://doi.org/10.3390/en13154007.
- 29. Zhang Y., Wang Y.-J., Yu J.-Q. A Novel MPPT Algorithm for Photovoltaic Systems Based on Improved Sliding Mode Control. Electronics, 2022, vol. 11, no. 15, art. no. 2421. https://doi.org/10.3390/electronics11152421.
- 30. Díaz Martínez D., Trujillo Codorniu R., Giral R., Vázquez Seisdedos L. Evaluation of particle swarm optimization techniques applied to maximum power point tracking in photovoltaic systems. International Journal of Circuit Theory and Applications, 2021, vol. 49, no. 7, pp. 1849-1867. doi: https://doi.org/10.1002/cta.2978.
- 31. Premkumar M., Sumithira T.R. Humpback whale assisted hybrid maximum power point tracking algorithm for partially shaded solar photovoltaic systems. Journal of Power Electronics, 2018, vol. 18, no. 6, pp. 1805-1818. doi: https://doi.org/10.6113/JPE.2018.18.6.1805.
- 32. El-Helw H.M., Magdy A., Marei M.I. A Hybrid Maximum Power Point Tracking Technique for Partially Shaded Photovoltaic Arrays. Access, 2017, vol. 5, pp. 11900-11908. https://doi.org/10.1109/ACCESS.2017.2717540.
- 33. Harrag A., Messalti S. PSO-based SMC variable step size P&O MPPT controller for PV systems under fast changing atmospheric conditions. International Journal of Numerical Modelling: Electronic Networks, Devices and Fields, 2019, vol. 32, no. 5, art. no. e2603. doi: https://doi.org/10.1002/jnm.2603.
- 34. Wang L., Wei X., Shao Y., Zhu T., Zhang J. MPPT of PV array using stepped-up chaos optimization algorithm. Turkish Journal of Electrical Engineering & Computer Sciences, 2015, vol. 23, pp. 1748-1760. doi: https://doi.org/10.3906/elk-1404-176.
- 35. Moradi M.H., Reisi A.R. A hybrid maximum power point tracking method for photovoltaic systems. Solar Energy, 2011, vol. 85, no. 11, pp. 2965-2976. doi: https://doi.org/10.1016/j.solener.2011.08.036
- 36. Enrique J.M., Andújar J.M., Bohórquez M.A. A reliable, fast and low cost maximum power point tracker for photovoltaic applications. Solar Energy, 2010, vol. 84, no. 1, pp. 79-89. doi: https://doi.org/10.1016/j.solener.2009.10.011.

- 37. Rezk H., Eltamaly A.M. A comprehensive comparison of different MPPT techniques for photovoltaic systems. Solar Energy, 2015, vol. 112, pp. 1-11. doi: https://doi.org/10.1016/j.solener.2014.11.010.
- 38. Hadjidj N., Benbrahim M., Ounnas D., Mouss L.H. Global maximum power point tracking method for photovoltaic systems using Takagi-Sugeno fuzzy models and ANFIS approach. Electrical Engineering & Electromechanics, 2025, no. 2, pp. 31-38. doi: https://doi.org/10.20998/2074-272X.2025.2.05.
- 39. Boudia A., Messalti S., Zeghlache S., Harrag A. Type-2 fuzzy logic controller-based maximum power point tracking for photovoltaic system. Electrical Engineering & Electromechanics, 2025, no. 1, pp. 16-22. doi: https://doi.org/10.20998/2074-272X.2025.1.03.
- 40. Bounechba H., Boussaid A., Bouzid A. Experimental validation of fuzzy logic controller based on voltage perturbation algorithm in battery storage photovoltaic system. Electrical Engineering & Electromechanics, 2024, no. 5, pp. 20-27. doi: https://doi.org/10.20998/2074- 272X.2024.5.03.
- 41. Romashko V.Y., Batrak L.M., Abakumova O.O. Obtaining the maximum power from the source using step-up and step-down type pulse regulators that work on battery. Electrical Engineering & 2024, Electromechanics, no. pp. 44-47. https://doi.org/10.20998/2074-272X.2024.3.06.
- 42. Sira-Ramirez H., Ortega R. Passivity-based controllers for the stabilization of DC-to-DC power converters. Proceedings of 1995 34th IEEE Conference on Decision and Control, 1995, vol. 4, pp. 3471-3476. doi: https://doi.org/10.1109/CDC.1995.479122
- 43. Seleme S.I.J., Morais L.M.F., Rosa A.H.R., Torres L.A.B. Stability in passivity-based boost converter controller for power factor correction. European Journal of Control, 2013, vol. 19, no. 1, pp. 56-64. doi: https://doi.org/10.1016/j.ejcon.2012.03.001.
- 44. Zeng J., Zhang Z., Qiao W. An Interconnection and Damping Assignment Passivity-Based Controller for a DC-DC Boost Converter With a Constant Power Load. IEEE Transactions on Industry Applications, 2014, vol. 50, no. 4, pp. 2314-2322. doi: https://doi.org/10.1109/TIA.2013.2290872.
- 45. Rodriguez H., Ortega R., Escobar G. A robustly stable output feedback saturated controller for the Boost DC-to-DC converter. Proceedings of the 38th IEEE Conference on Decision and Control, 1999, vol. 3, pp. 2100-2105. doi: https://doi.org/10.1109/CDC.1999.831229.
- 46. Baazouzi K., Bensalah A.D., Drid S., Chrifi-Alaoui L. Passivity voltage based control of the boost power converter used in photovoltaic system. Electrical Engineering & Electromechanics, 2022, no. 2, pp. 11-17. doi: https://doi.org/10.20998/2074-272X.2022.2.02.

Received 05.04.2025 Accepted 19.05.2025 Published 02.11.2025

A. Toualbia¹, Associate Professor,

A.B. Djilali¹, Associate Professor,

R. Taleb¹, Professor,

N. Mansour², Associate Professor, M. Souaihia¹, Associate Professor,

H. Saidi¹, Associate Professor,

¹ Electrical Engineering Department, Faculty of Technology, Laboratoire Génie Electrique et Energies Renouvelables (LGEER). Hassiba Benbouali University of Chlef, Algeria, e-mail: as.toualbia@univ-chlef.dz (Corresponding Author).

² College of Engineering, University of Bahrain, Bahrain.

How to cite this article:

Toualbia A., Djilali A.B., Taleb R., Mansour N., Souaihia M., Saidi H. Application perturb and observe maximum power point tracking with interconnection and damping assignment passive-based control for photovoltaic system using boost converter. Electrical Engineering & Electromechanics, 2025, no. 6, pp. 98-105. doi: https://doi.org/10.20998/2074-272X.2025.6.13

